Spectroscopic Investigation of the Three Lowest Doublet States of LiSr

Von der Fakultät für Mathematik und Physik
der Gottfried Wilhelm Leibniz Universität Hannover
zur Erlangung des akademischen Grades

Doktor der Naturwissenschaften
– Dr. rer. nat. –

genehmigte Dissertation von

Master of Science
Erik Schwanke

2019

Referent:
Prof. Dr. Eberhard Tiemann
Korreferentin:
Prof. Dr. Silke Ospelkaus
Korreferent:
Prof. Dr. Asen Pashov

Datum der Promotion:
15. Juli 2019

Zusammenfassung

Zweiatomige Moleküle mit einem Alkali- und einem Erdalkaliatom werden derzeit untersucht, um sie in späteren Experimenten zur Erforschung verschiedener physikalischer Phänomene zu nutzen. Diese Arbeit beschreibt die Aufnahme und Interpretation des nahinfraroten Spektrums eines Gases von LiSr-Molekülen. Die geringe reduzierte Masse von LiSr bedingt eine vergleichsweise geringe Liniendichte im thermischen Emissionsspektrum.

Das thermische Emissionsspektrum wird ausführlich besprochen. Es zeigt deutliche Vibrationsbanden, die aufgrund der Spin-Rotationskopplung zwei unterschiedliche Rotationsspektren erkennen lassen. Weiterhin wird eine Methode zur schnellen Zuordnung von Rotationsquantenzahlen vorgestellt, die durch die Verwendung von Laserstrahlung zur gezielten Anregung der Moleküle ermöglicht wird.

Die Zusammenführung des thermischen Emissionsspektrums mit den Spektren verschiedener Laserexperimente erlaubt eine umfassende Beschreibung der Rotationsleitern der niedrigsten Vibrationszustände $v'' = 0, 1, 2$ und $v' = 0, 1$ des $(2)^2\Sigma^+$–$X(1)^2\Sigma^+$-Systems. Im $(2)^2\Sigma^+$-Zustand wurden mehrere starke Störungen gefunden, die einer Kopplung zwischen den $(2)^2\Sigma^+$- und $(1)^2\Pi$-Zuständen zugeschrieben werden. Ein Modell zur Beschreibung dieses gekoppelten Systems wird entwickelt. Hiermit wird auch eine Beschreibung einiger Vibrationsniveaus des $(1)^2\Pi$- Zustandes erreicht.

Schlagworte: Optische Spektroskopie, Molekülspektrum, Alkali-Erdalkali-Moleküle

Abstract

Molecules consisting of an alkali and an alkaline earth atom are currently investigated with the aim of using them in experiments to explore diverse physical phenomena. This thesis is concerned with the observation and analysis of the infrared spectrum of LiSr in the gas phase. The moderate reduced mass of LiSr implies a relatively low density of the thermal emission lines. Individual transition lines can be discerned in the spectrum and enable the tracing of rotational branches in the thermal emission spectrum.

An analysis of the thermal emission spectrum of LiSr is presented. The spectrum displays clearly visible vibrational bands. Their line structure shows two distinguishable rotational systems due to spin-rotation coupling. A method to readily find the assignment of rotational quantum numbers by using laser radiation to excite the molecular sample at different frequencies is demonstrated.

Using the thermal emission spectrum together with laser-induced fluorescence spectra from different laser experiments allowed a thorough description of the rotational energy ladders of the lowest vibrational states $v'' = 0, 1, 2$ and $v' = 0, 1$ of the $(2)^2\Sigma^+$–$X(1)^2\Sigma^+$ system. It was found that several large perturbations occur in the $(2)^2\Sigma^+$ state. These perturbations are attributed to a coupling of the $(2)^2\Sigma^+$ to the $(1)^2\Pi$ and a model to describe the coupled system is established here, which includes a description of a few vibrational levels in the $(1)^2\Pi$ state.

Keywords: Optical Spectroscopy, molecular spectrum, alkali-alkaline earth-molecules

List of Publications

Some of the ideas, methods and results presented in this thesis have already been published in the following articles:

- Erik Schwanke et al. 'Laser and Fourier transform spectroscopy of $^{7}Li^{88}Sr$'. In: *Journal of Physics B: Atomic, Molecular and Optical Physics* 50.23 (14th December 2017), p. 235103. DOI: 10.1088/1361-6455/aa8ca0
- Julia Gerschmann et al. 'Laser and Fourier-transform spectroscopy of KCa'. In: *Physical Review A* 96.3 (6th September 2017), p. 032505. DOI: 10.1103/PhysRevA.96.032505

Contents

Introduction

Physicists are currently utilizing diatomic molecules to investigate a vast range of physical phenomena. Examples include characterizing collisions in the quantum regime [Yan+19], measuring upper limits of the electron's electric dipole moment [Cai+17] or exploring dipole-dipole interactions in many-body systems [Yan+13]. Further proposals, for example using molecular transitions for sensitive measurements of the proton-to-electron mass ratio [DeM+08] or the fine structure constant [CFK09] have not yet been realized experimentally. An extensive review of applications of molecules in various research topics is [Saf+18].

Many of these experiments were done with molecules consisting of two alkali metal atoms at a low temperature and they have brought many insights about cold atomic or molecular ensembles and how to manipulate them in the laboratory. Translating these principles to different types of molecules would allow to realize other experimental schemes to explore diverse subjects, like chemical processes at ultracold temperatures or the behaviour of bosons, fermions or interacting dipoles arranged in lattice geometries [BRY17; GB17]. A step in that direction is to work with molecules consisting of an alkali metal atom (group IA of the periodic table) and an alkaline earth metal atom with one valence electron more than an alkali metal atom (group IIA of the periodic table). This endows the molecule in its ground state with a magnetic dipole moment in addition to their permanent electric dipole moment [PHE16].

There are proposals for using such molecules to measure the proton-to-electron mass ratio [Kaj+13; Kaj+14], which requires precise information of transition energies between molecular states. To aquire this information, knowledge about the structure of these diatomics, their quantum states and energy landscape is essential.

For various molecules in this class, ab-initio calculations have been published (e.g. [PHE16]). They give a good approximation of the potential energy curves but are not accurate enough to be used as basis for experimental work. Several molecules were also investigated experimentally. Examples include rovibronic spectroscopy of vaporous ensembles (e.g. [DIn+94]), often in conjunction with laser-induced fluorescence spectroscopy (e.g. [BM82]), photoionization spectroscopy (e.g. [BD97]), photoassociation spectroscopy (e.g. [Nem+09]) or spectroscopy of the diatomics formed on helium nanodroplets (e.g. [Pot+15]). A list of references for the ab-initio and experimental works is given in Appendix E.

A first step towards the characterization of alkali-alkaline earth molecules is to use spectroscopic information to describe the molecular level structure. This information can then be used to find an accurate model for the potential energy curves of their electronic states. A description of the electronic, vibrational and rotational states of the molecule can be derived from these curves. Understanding these states serves as a basis to investigate the molecular hyperfine structure, which involves the nuclear spins. This information will be needed for later applications like slowing [Tru+17b; Pet+18] and trapping [Tru+17a] the molecules, cooling them with laser light [And+18; McC18] or transferring them into their absolute ground state via stimulated Raman adiabatic passage [Vit+17].

Different spectroscopic methods allow to reveal different aspects of the molecular energy

structure. For example, fluorescence spectroscopy can potentially reveal a wide vibrational spectrum in one experimental run (see e.g. [Iva+11b]). Photoassociation spectroscopy [SW99] probes the electronic potential curves, starting near the atomic asymptote, but requires a high experimental effort to advance deeper into the potential well when compared with thermal emission spectroscopy, which provides a broad spectrum of energy levels near the potential bottom. All these methods can be combined to learn more about the potential energy curves [Cia+18].

It can be expected from the ab-initio works that many of the alkali-alkaline earth diatomics have reasonably strong transitions between their lowest electronic states in the near-infrared region of the electromagnetic spectrum. The strongest transitions usually take place between two $^2\Sigma^+$ states (e.g. [Pot+17]). Investigating the rovibronic[a] spectra associated with these transitions allows insight into the rotational and vibrational energy levels of these electronic states. Because many states and transitions are involved in the formation of these spectra, it is challenging to work out the underlying molecular configuration. Especially for molecules with larger reduced mass, the spectra would consist of many overlapping lines, which are difficult to disentangle.

The present work is concerned with the interpretation of the near-infrared spectrum of LiSr. Due to its relatively small reduced mass, a comparatively well-resolved spectrum can be expected. By investigating this molecule, different analytical and experimental methods can be applied and tested with regards to their feasibility in the study of the more dense spectra of other group IA-group IIA diatomics. There exist several ab-initio calculations concerned with LiSr [GAD10; Gop+11; Gop+13; PHE16; Pot+17; Zei+18] and two experimental publications [Ste16; Sch+17b] concerned with its near-infrared spectrum. [Sch+17b] presents methods and results that are also found in this thesis but were expanded upon since then. A comparison of the spectroscopic constants derived here and those from these published works will be given on page 104 near the end of this work.

This thesis is structured as follows: First, an overview of the basic structure of the spectrum of a diatomic molecule will be given. The experimental setup used to investigate the LiSr spectrum will be described afterwards. Then the approach to find transition frequencies will be outlined, followed by a discussion of the features of the observed LiSr spectrum. Next, the process to find molecular parameters that model the observed spectrum with the Dunham expansion will be explained. In the course of this examination it will be seen that the spectrum cannot be sufficiently explained as a simple rovibronic spectrum, but that it has systematic perturbations. In order to explain these, the following chapters are concerned with the discussion of the coupling between two electronic states and the application of a coupling model to the spectrum. The last two chapters summarize the findings, discuss their limits and examine possible ways to overcome them.

[a] Usually, the word 'rovibronic' refers to rotational, vibrational and electronic transitions or spectra. The combined vibrational and electronic transitions or spectra are called 'vibronic', whereas 'rovibrational' refers to rotational and vibrational transitions or spectra.

Chapter 1

Spectra of Diatomic Molecules

In order to infer a molecule's structure from its corresponding electromagnetic spectrum, the principles governing the emission or absorption of electromagnetic radiation by a molecule have to be applied. This chapter will briefly summarize the important concepts used to describe the rovibrational states of a diatomic molecule and the transitions between them. For a more didactic or in-depth encounter with the contents of this chapter, please refer to the available literature, e.g. the textbooks [Her50; BC03; TS55; LF86].

Energy units

Throughout this thesis, frequencies and molecular constants will be given in units of wavenumbers [cm^{-1}]. They can be converted to SI units with Planck's constant h and the speed of light in vacuum c:

$$1\,\mathrm{cm}^{-1} \mathrel{\widehat{=}} \frac{c\,[\mathrm{cm/s}]}{1\,\mathrm{cm}} \approx 30\,\mathrm{GHz} \tag{1.0.1a}$$

or

$$1\,\mathrm{cm}^{-1} \mathrel{\widehat{=}} \frac{h[\mathrm{J\,s}] \cdot c\,[\mathrm{cm/s}]}{1\,\mathrm{cm}} \approx 124\,\mu\mathrm{eV}, \tag{1.0.1b}$$

depending on the context. This first chapter will explicitly mention the factor of hc in front of constants that will later be written without it.

1.1 Energies of Molecular Quantum States

For the interpretation of the spectra, the molecules can adequately be described in the Born-Oppenheimer approximation, which separates the nuclear motion and the electronic motion, so that the kinetic energies of the nuclei and electrons can simply be added. The state of a molecule is described by a wave function $|\psi\rangle$, which is defined by different quantum numbers. In this thesis, the bases of Hund's coupling cases (a) and (b) are used for the molecular states with appropriate quantum numbers. In these bases, the wave function $|\psi\rangle$ is expressed as

$$|\psi\rangle = |\Lambda, \Sigma, S, \Omega, J, v\rangle \qquad \text{for Hund's case (a)}$$

and

$$|\psi\rangle = |\Lambda, (N, S)J, v\rangle \qquad \text{for Hund's case (b).}$$

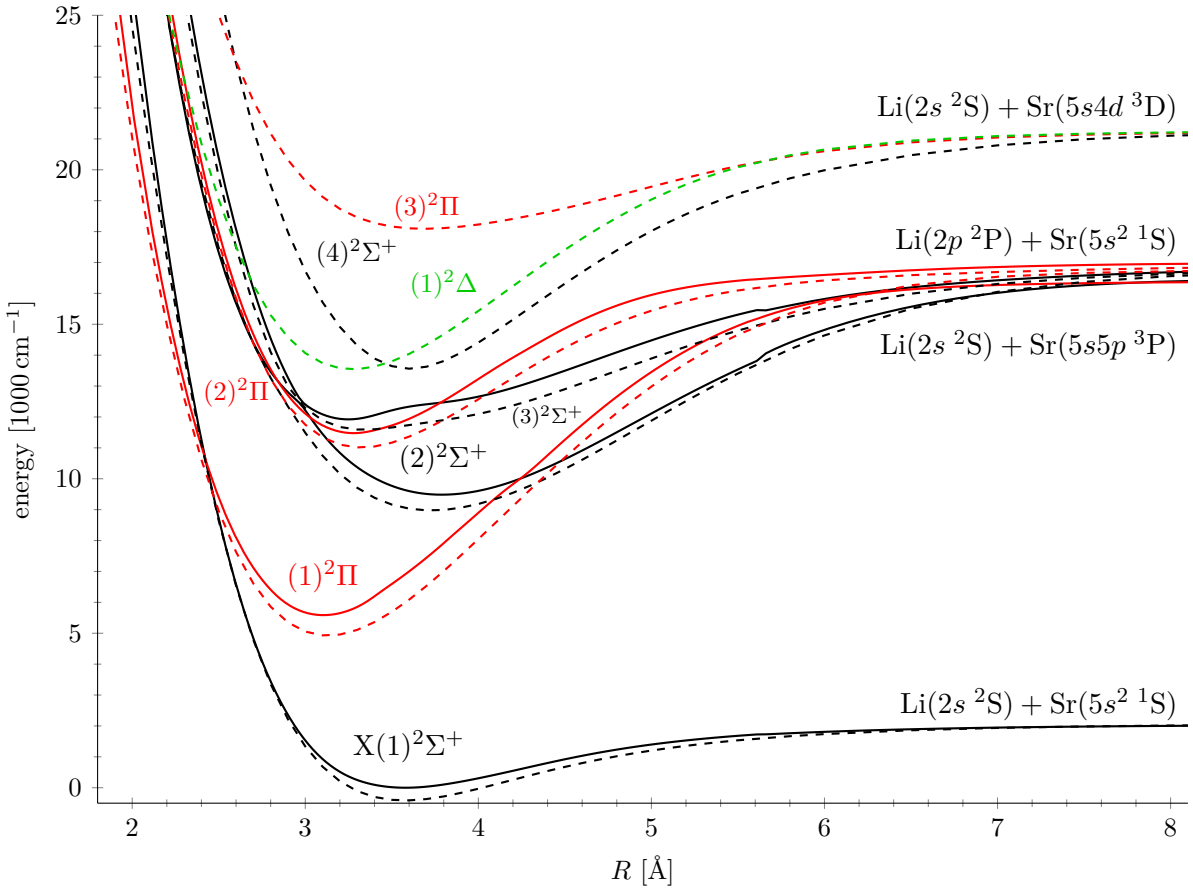

Figure 1.1: Potential energy curves of LiSr doublet states from [Gop+13] (solid) and [Pot+17] (dashed). $^2\Sigma^+$ curves are drawn in black, $^2\Pi$ curves in red and the only available $^2\Delta$ curve in green. The asymptotic atomic levels are given on the right. The fact that the first excited states of Li and Sr have a similar energy leads to many molecular states in LiSr that are close in energy. See the text for an explanation of the term symbols.

Λ is the quantum number for the projection of the electronic angular momentum $\vec{L}$ on the internuclear axis[a]. $\vec{S}$ is the electronic spin, with associated quantum number S and with its projection on the internuclear axis given by Σ. In Hund's case (b), $\vec{N}$ is the total angular momentum without spin and $\vec{J} = \vec{N} + \vec{S}$ is the total angular momentum without the nuclear spins. In Hund's case (a), $\Omega = \Lambda + \Sigma$ corresponds to the projection of $\vec{J}$ on the internuclear axis. With these quantum numbers, the term symbols $^{2S+1}\Lambda^{\pm}_{\Omega}$ are used to label electronic states. The quantum number v gives the vibrational state of the nuclear motion. Chapter 5 will show that the spin angular momentum is coupled to the molecular rotation and the observed spectrum can be described more intuitively in Hund's coupling case (b). For this reason, Hund's coupling case (b) is used in this chapter to discuss the properties of the molecular states.

1.1.1 Electronic Energy

The electronic energy depends on the internuclear distance R. The minimum of the potential energy curve of an electronic state, hcT_e, is at the equilibrium distance R_e for that state. Electronic states with the same projection quantum number Λ and multiplicity

[a] States with $\Lambda = 0$ are labeled Σ states, states with $\Lambda = 1$ are called Π states, then come $\Delta, \Phi, \Gamma, \mathrm{H}...$

$(2S+1)$ are numbered according to the energy of the state. The absolute electronic ground state will be further marked by X.

Figure 1.1 displays potential energy curves of several LiSr doublet states from two ab-initio works [Gop+13; Pot+17]. The spectrum in question features transitions to the electronic ground state $X(1)^2\Sigma^+$, so only transitions from Σ or Π states need to be considered, as explained in Section 1.3 below. Chapter 4 will discuss what LiSr spectra can be expected from these potential energy curves.

1.1.2 Vibrational Energy

The nuclei vibrate in the potential given by the electronic potential energy curves. Near the bottom of the potential well, the vibration can be approximated by the harmonic oscillator. The vibrational energy is then

$$E_{\text{vib}} = h\nu_e(v + 1/2) = \hbar c\,\omega_e(v + 1/2), \tag{1.1.1}$$

with $\omega_e = \nu_e/c$. The equidistant energy spacing is $\hbar c\omega_e$. Because of the anharmonic shape of the electronic potential, vibrational levels with higher v grow closer in energy. This can be described by introducing terms proportional to $(v + 1/2)^n$ with $n \geq 2$ and appropriate sign.

1.1.3 Rotational Energy

In first order, a diatomic molecule can be treated as a quantum mechanical rigid rotator with the energy

$$E_{\text{rot}} = \frac{\hbar^2}{2\,\mu\,R_e^2} J(J+1) = hc\,B_e\,J(J+1). \tag{1.1.2}$$

The constant depending on the internuclear equilibrium distance R_e, and the reduced mass μ, is known as the rotational constant B_e. Due to centrifugal effects, a rotating molecule's internuclear distance grows with the rotational quantum number J. This leads to a slow decrease in the rotational energy for higher J, which can be modelled with further terms proportional to $[J(J+1)]^n$, where $n \geq 2$.

For Σ states, Hund's case (b) is an appropriate choice. Here, the rotation of the molecule is given by the quantum number N and the following chapters will therefore use N instead of J for the rotational quantum numbers and energy expressions. Generally, the rotational energy in Hund's case (b) scales with $N(N+1) - \Lambda^2$, but this thesis is mainly concerned with states for which $\Lambda = 0$. Since Hund's case (a) uses J as the rotational quantum number, the value for the rotational constant will be different in order to parametrize the same observed rotational energy levels.

In a vibrating molecule, the expectation value of R can differ from R_e. Therefore, the rotational constant B_v has to be used for a rotating molecule with vibrational quantum number v.

1.1.4 Spin-Rotation Coupling

Because of the unpaired electron, the ground state of LiSr can be in two possible spin states. Due to the coupling of the spin to the rotation of the nuclei, these states are not degenerate in energy and their energy difference grows with the rotational quantum number.

In Hund's case (b), the spin is decoupled from the nuclear rotation and this energy can simply be added to the rovibrational energy. Following convention, the states with $J = N + 1/2$ are labeled with F_1 and the states with $J = N - 1/2$ are labeled with F_2. It will become important in Chapter 6 that, in the system under consideration, they correspond to the rotation-independent e/f symmetry (see Figure 1.2). This label describes a symmetry of $^{+}/_{-}(-1)^{J-1/2}$ for an uneven number of electrons and is discussed alongside other types of symmetry in [LF86, Section 2.2.2].

The energies of these states in Hund's case (b) depend on the spin-rotation constant γ and the nuclear rotation:

$$E_{\mathrm{F}1}(N) = +hc \cdot \gamma/2 \cdot N \qquad \text{for } \mathrm{F}_1 \tag{1.1.3a}$$

$$E_{\mathrm{F}2}(N) = -hc \cdot \gamma/2 \cdot (N+1) \qquad \text{for } \mathrm{F}_2 \tag{1.1.3b}$$

1.2 Dunham Expansion

Section 1.1.3 and Section 1.1.2 mentioned that the rotational and vibrational energies both change in a nonlinear manner when reaching higher quantum numbers. Also, the rotational and vibrational motions affect each other. These phenomena can be described by the Dunham expansion [TS55, pp. 9-11] that models the rovibrational energies with

$$E(v, N) = hc \sum_{m,n} \mathrm{Y}_{mn} [v + 1/2]^m [N(N+1)]^n. \tag{1.2.1}$$

The factors Y_{mn} are called Dunham coefficients. They can in principle be added to an infinite series describing the energy levels. The first terms approximate the molecular constants at the equilibrium distance R_e,

$$\mathrm{Y}_{00} \approx T_e, \tag{1.2.2a}$$

$$\mathrm{Y}_{10} \approx \omega_e, \tag{1.2.2b}$$

$$\mathrm{Y}_{01} \approx B_e \tag{1.2.2c}$$

and the Kratzer relation

$$\mathrm{Y}_{02} \approx -4 \frac{(\mathrm{Y}_{01})^3}{(\mathrm{Y}_{10})^2}. \tag{1.2.2d}$$

Dunham coefficients for different isotopologues of molecules with no electric charge and reduced masses μ_A and μ_B can be approximated via the relation

$$\mathrm{Y}_{mn}^{(A)} = \mathrm{Y}_{mn}^{(B)} \left(\frac{\mu^{(A)}}{\mu^{(B)}} \right)^{-\frac{m+2n}{2}}. \tag{1.2.3}$$

The Dunham series does not consider the spin-rotation coupling. Since the spin-rotation coupling constant γ can also depend on the rovibrational state [Ste+13], it will be expanded in a similar fashion:

$$\gamma(v, N) = \sum_{m,n} \gamma_{mn} [v + 1/2]^m [N(N+1)]^n \tag{1.2.4}$$

Contrary to the form of the Dunham series, this expansion has no physical justification and its form is merely to remember the effect of a parameter by association with the Dunham series. Further mentions of the Dunham model in this thesis are meant to include this representation of the spin-rotation coupling unless stated otherwise.

The total rovibronic energy and the energy of spin-rotation coupling for a state $|v, N, S\rangle$ is given by equations (1.1.3), (1.2.1) and (1.2.4):

$$E_{\mathrm{F1}}(v, N) = hc \sum_{m,n} \Big(\mathrm{Y}_{mn} + \frac{\gamma_{mn}}{2} \cdot N \Big) [v + 1/2]^m [N(N+1)]^n \qquad \text{for } \mathrm{F}_1 \tag{1.2.5a}$$

$$E_{\mathrm{F2}}(v, N) = hc \sum_{m,n} \Big(\mathrm{Y}_{mn} - \frac{\gamma_{mn}}{2} \cdot (N+1) \Big) [v + 1/2]^m [N(N+1)]^n \qquad \text{for } \mathrm{F}_2 \tag{1.2.5b}$$

The transition frequencies are obtained by subtracting the energy of the lower state from the energy of the higher state.

1.3 Rovibronic Transitions

The observed electromagnetic spectrum represents transitions between two rovibrational molecular states[b] $|\psi'\rangle$ and $|\psi''\rangle$. The stronger a transition, the higher is the observed intensity of the corresponding transition line in an emission spectrum. When the Born-Oppenheimer approximation is valid, the molecular states can be expressed as the product

$$|\psi\rangle = |v\rangle \cdot |\Lambda, (NS)J\rangle \,. \tag{1.3.1}$$

Transitions between rotational states are subject to selection rules, which means that the transition strength is zero if the rotational quantum numbers do not change by certain amounts during the transition.

1.3.1 Vibrational Transitions

Transitions between vibrational states of different electronic states have no selection rules. In principle, all vibrational transitions are allowed. The relative intensity of a transition between a vibrational state in the electronic ground state, v'', and a vibrational state in an electronically excited state, v', is approximated by the Franck-Condon factor (FCF), which is calculated by squaring the overlap integral of the vibrational wave functions:

$$\mathrm{FCF}(v' \to v'') = \left| \int_0^\infty \psi^*(v') \psi(v'') \, \mathrm{d}R \right|^2 = \left| \left\langle v' \middle| v'' \right\rangle \right|^2 \tag{1.3.2}$$

[b] When discussing molecular spectroscopy, $|\psi'\rangle$ marks the state with higher energy and $|\psi''\rangle$ the state lower in energy. The frequencies and transition strengths are the same in both directions.

1.3.2 Rotational Transitions

Within the scope of in the dipole approximation, transitions that change angular momenta can be described by the dipole matrix element between two states[c] $|\Lambda', (N', S')J', M'\rangle$ and $|\Lambda'', (N'', S'')J'', M''\rangle$ for the interaction of a dipole moment $\vec{\mu}$ with the electric field $\vec{E}$ (the electric part of an electromagnetic wave, i.e. light). This dipole matrix element gives the strength of the transition. It is zero for certain combinations of quantum numbers in the two involved states. In these cases, a dipole transition cannot take place. Investigating the dipole matrix element mathematically yields selection rules that describe which transitions are possible and which are forbidden. For the experimental observations described in Chapter 2, the assumption can be made that only linearly polarized light with the component E_0 is observed. The expression for the dipole moment in this case is discussed in more detail in Appendix A, where equation (A.9) gives a transition strength of

$$\left|\left\langle \Lambda', (N', S')J', M'\middle|\mu_0 \cdot E_0\middle|\Lambda'', (N'', S'')J'', M''\right\rangle\right|^2 \propto \sum_{m=-1}^{1}\left[\delta_{S'S''} \times (2J'+1)(2J''+1)(2N'+1)(2N''+1)\times \begin{pmatrix} J' & 1 & J'' \\ -M' & 0 & M'' \end{pmatrix}^2 \begin{pmatrix} N' & 1 & N'' \\ -\Lambda' & m & \Lambda'' \end{pmatrix}^2 \begin{Bmatrix} N' & J' & S'=1/2 \\ J'' & N'' & 1 \end{Bmatrix}^2\right], \quad (1.3.3)$$

written with Wigner 3-j and 6-j symbols. Here, M is the projection of J onto an axis in a laboratory frame. Appendix A further examines the properties of these symbols and what selection rules can be derived from equation (1.3.3). They are given in equations (A.11). For the following chapters, these selection rules are important:

Electronic Transitions

The only allowed transitions between electronic states are those with

$$\Lambda \to \Lambda, \Lambda \pm 1. \quad (1.3.4)$$

Since the electronic ground state is $X(1)^2\Sigma^+$, only transitions to Σ or Π states are allowed.

Spin

The spin is not affected by $\vec{\mu}$, therefore in all transitions $|\psi'\rangle \to |\psi''\rangle$, the spin S or its projection onto the internuclear axis S_z do not change:

$$S \to S \quad (1.3.5a)$$

$$S_z \to S_z \quad (1.3.5b)$$

[c] Note that these states have only angular momentum quantum numbers and are independent of the radial part of their wave functions.

Thus, the observed transitions will not involve changing the spin. Appendix A also explains that $F_{1/2} \to F_{2/1}$ transitions are weaker for large N than $F_{1/2} \to F_{1/2}$ transitions. Since the former type of transitions was never assigned in this work, all transitions will be assumed to be only of the latter type. In this approximation, all selection rules $N' \to N''$ imply also $J' \to J''$ of the same form.

Rotational Transitions

For rotational states, only dipole transitions with

$$N \to N,\, N \pm 1 \tag{1.3.6a}$$

except

$$N = 0 \nrightarrow N = 0 \tag{1.3.6b}$$

are allowed. In the case of an electronic $\Sigma \to \Sigma$ transition, the only rotational transitions with non-vanishing transition dipole moment are of the type

$$N \to N \pm 1. \tag{1.3.7}$$

Figure 1.2 illustrates the rovibronic transitions between the first two $^2\Sigma^+$ states.

1.4 Rovibronic Spectra

1.4.1 P and R Bands

All rotational transitions allowed by (1.3.7) together form a spectrum with two rotational branches. The so-called P branch has transitions with $N'' = N' + 1$ and the R branch has transitions with $N'' = N' - 1$. The different rotational constants of the two electronic systems let these branches appear as a shaded band and can be characterized with the Fortrat parabola [Her50, p. 171ff.], which describes the transition frequencies in terms of the square of the rotational quantum number[d]. The rotational transition frequencies f are given by:

$$f_{\mathrm{P}}^{\mathrm{F}_1} = (B_e' - B_e'')\, N'^2 + (B_e' - 3B_e'')\, N' - 2B_e'' + \left(\frac{\gamma' - \gamma''}{2}\right) N' - \gamma''/2 \tag{1.4.1a}$$

$$f_{\mathrm{P}}^{\mathrm{F}_2} = (B_e' - B_e'')\, N'^2 + (B_e' - 3B_e'')\, N' - 2B_e'' - \left(\frac{\gamma' - \gamma''}{2}\right) N' + \gamma' - \gamma'/2 \tag{1.4.1b}$$

$$f_{\mathrm{R}}^{\mathrm{F}_1} = (B_e' - B_e'')\, N'^2 + (B_e' + B_e'')\, N' + \left(\frac{\gamma' - \gamma''}{2}\right) N' + \gamma''/2 \tag{1.4.1c}$$

$$f_{\mathrm{R}}^{\mathrm{F}_2} = (B_e' - B_e'')\, N'^2 + (B_e' + B_e'')\, N' - \left(\frac{\gamma' - \gamma''}{2}\right) N' - \gamma'/2 \tag{1.4.1d}$$

[d] See Figure 4.2 for an illustration.

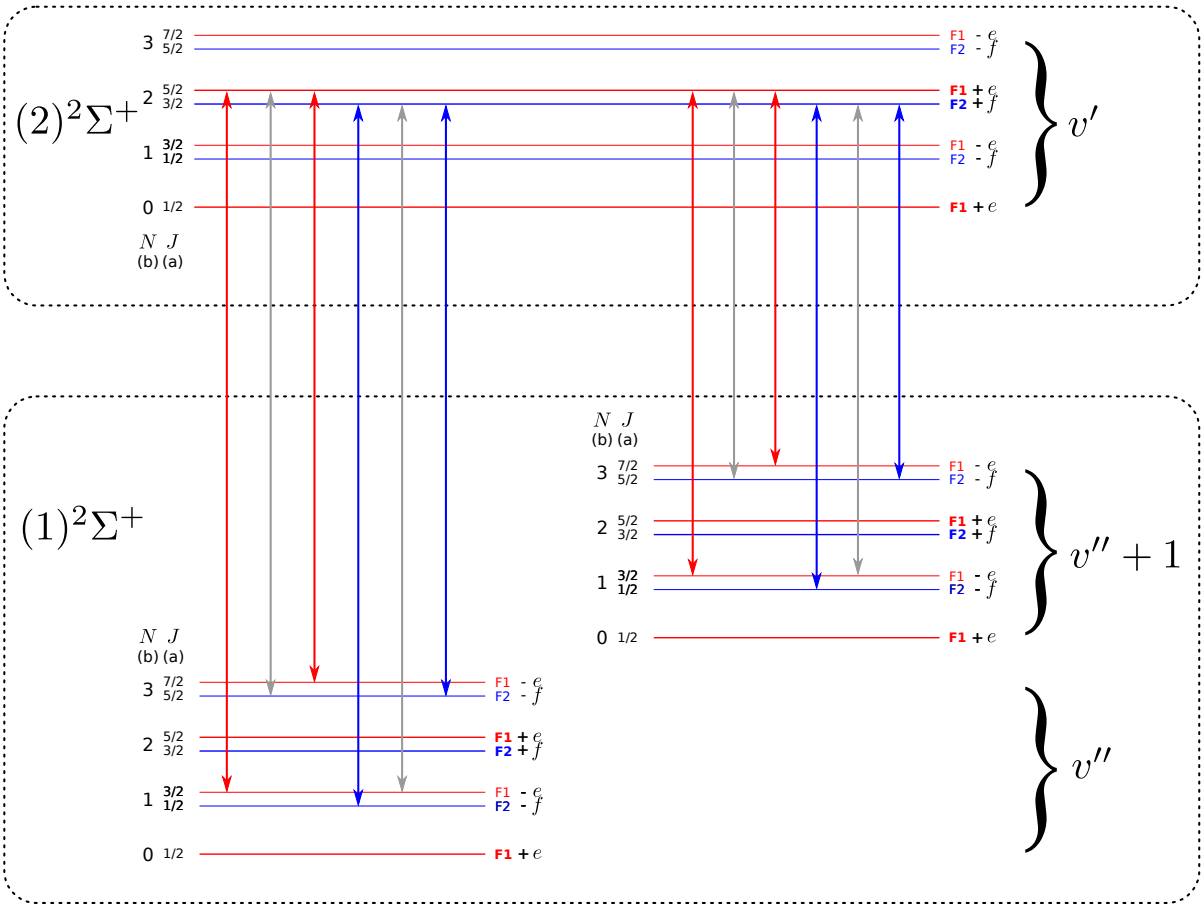

Figure 1.2: Rovibronic transitions between the first two $^2\Sigma^+$ states in Hund's cases (a) and (b). Red energy levels and arrows represent the F_1 system and blue ones depict F_2. Transitions between the spin system are drawn grey, they are not relevant in this thesis. Since transitions can take place between arbitrary vibrational states, the $(2)^2\Sigma^+$ states can decay to several vibrational levels. The energy spacing of the vibrational levels with v'' and $v''+1$ in the $X(1)^2\Sigma^+$ state is usually much larger than the rotational energy spacing. Note that the parity for F_1 and F_2 is always e or f, respectively.

The distance $\Delta f = f(N') - f(N'-1)$ grows as:

$$\Delta f_{\mathrm{P}}^{\mathrm{F_1}} = 2\left(B'_e - B''_e\right)N' - 2B''_e + \left(\frac{\gamma' - \gamma''}{2}\right) \tag{1.4.2a}$$

$$\Delta f_{\mathrm{P}}^{\mathrm{F_2}} = 2\left(B'_e - B''_e\right)N' - 2B''_e - \left(\frac{\gamma' - \gamma''}{2}\right) \tag{1.4.2b}$$

$$\Delta f_{\mathrm{R}}^{\mathrm{F_1}} = 2\left(B'_e - B''_e\right)N' + 2B''_e + \left(\frac{\gamma' - \gamma''}{2}\right) \tag{1.4.2c}$$

$$\Delta f_{\mathrm{R}}^{\mathrm{F_2}} = 2\left(B'_e - B''_e\right)N' + 2B''_e - \left(\frac{\gamma' - \gamma''}{2}\right) \tag{1.4.2d}$$

The absolute value of the distance Δf_{RP} between the R and P lines belonging to the same upper rotational state $|N'\rangle$ is (neglecting the centrifugal corrections):

$$\Delta f_{\mathrm{RP}}^{\mathrm{F_1}} = f_{\mathrm{R}}^{\mathrm{F_1}}(N') - f_{\mathrm{P}}^{\mathrm{F_1}}(N') = 2B''_e(2N'+1) + \gamma'' \tag{1.4.3a}$$

$$\Delta f_{\mathrm{RP}}^{\mathrm{F_2}} = f_{\mathrm{R}}^{\mathrm{F_2}}(N') - f_{\mathrm{P}}^{\mathrm{F_2}}(N') = 2B''_e(2N'+1) + \gamma'' - \gamma' \tag{1.4.3b}$$

As mentioned in Section 1.3, the P and R bands occur separately for the F_1 and F_2 systems. The spin-rotation coupling is strong enough to deform the rotational spectrum, so that four bands (F_1 P, F_1 R, F_2 P, F_2 R) can be resolved. The effect of the spin-rotation coupling on Δf or Δf_{RP} is not resolvable with the methods employed in this work, though. Since $\gamma \ll B_e$, the terms with the spin-rotation coupling constants in equations (1.4.2) and equation (1.4.4) are negligible. The frequency difference between the R and P lines is then

$$\Delta f_{\mathrm{RP}} = 2B''_e(2N' + 1). \tag{1.4.4}$$

1.4.2 Vibrational Bands

The energy spacing of the vibrational transitions is usually much larger than the spacing of rotational transitions. Because the energy levels and transition energies of vibrational and rotational states can simply be added, a spectrum given by equations (1.4.1) is found for every vibrational transition $v' \to v''$. This structure is called the (v'–v'') band. For low vibrational quantum numbers, the spacing of these bands is very regular but, depending on the vibrational frequencies of the two electronic states, several bands can be interwoven. The intensity of the rotational spectrum of a band is scaled with the associated Franck-Condon factor[e].

1.4.3 Intensity Distribution of Rotational Spectra

If a molecular sample is in thermal equilibrium, then its emission spectrum depends on the absorption coefficient $\alpha(f)$ according to Kirchhoff's radiation law. Absorption or emission of light can only take place for frequencies that correspond to the energy difference of an intramolecular transition. Apart from the rotational factor (1.3.3) and Franck-Condon factor (1.3.2), the intensity of a rotational emission line depends on the population of the samples' energy levels. For the thermal emission spectrum, the population distribution can be approximated by

$$(2N'' + 1) \cdot \exp\left(-\frac{hcB''_v N''(N'' + 1)}{k_B T}\right) \tag{1.4.5}$$

for a given v''. In other words, it is proportional to the number of energetically degenerate energy levels of the rigid rotor multiplied with the Boltzmann distribution for the ground state. Equation (1.4.5) ignores here the slightly different degeneracy for P and R transitions.

The overall intensity distribution of the rotational branches of a vibrational band is given by the product of equations (1.3.2), (1.3.3) and (1.4.5). The spectrum can have overlapping lines, for which the intensity is added at their common frequencies.

[e] The Franck-Condon factor also depends on N in principle, which further influences the intensity distribution of the band.

Chapter 2

Experimental Setup

This chapter will describe the steps taken to acquire the infrared spectrum of LiSr. Two types of spectra were recorded. One is a broadband thermal emission spectrum that shows transitions between states following a thermal population distribution. The other is a spectrum of the fluorescence of one rovibronic state excited by a laser tuned to an observed transition frequency. The latter type of spectrum will be called 'LIF spectrum' (laser induced fluorescence) in this thesis. All spectra were recorded by a Fourier-transform spectrometer (FTS). The general experimental setup for both kinds of spectra is the same. Registering a spectrum without the laser beam produces a regular thermal emission spectrum. With the laser running, a LIF spectrum is superimposed on the thermal emission spectrum.

2.1 Heat Pipe

The molecules were prepared in a heat pipe, which is a widely-used experimental setup for molecular spectroscopy (see e.g. [VC69; NBM80; Iva+11b; Szc+18]). The molecules are inside a heat-resistant metal pipe within an oven. The pipe is made of 1.4841 steel, which is suitable for temperatures up to 1150 °C. A sketch of the heat pipe and the oven is given in the centre of Figure 2.1. The oven is heated with heating coils whose winding direction alternates, so that their current should not produce a magnetic field. In practice, a small field remains. A magnetic field measurement in the oven suggested that during periods of strong heating, a magnetic field of less than 2 G builds up at the heat pipe position. The current is weaker when the target temperature merely needs to be held constant, so an even weaker magnetic field can be expected. The energetic splitting of atomic levels of both ^{7}Li and ^{88}Sr in a magnetic field of a few gauss are small enough to be neglected because the Doppler broadening of transition lines (see Section 3.1) has a much greater effect on the line shape [Sta10; Hil+14].

There are uncoated windows of BK7 glass at both ends of the pipe through which the sample can be observed. The heat pipe is filled with a buffer gas and its ends are cooled with water. The buffer gas slows the molecules' diffusion towards the cold ends by shortening their mean free path. This prevents the molecular vapour to reach the colder windows and covering them with a metal film. On the inside, the heat pipe is covered with a steel mesh. With this mesh, metal that condenses in the cooler parts of the heat pipe is moved back into the heated region by capillary force. Thereby, the losses of metal by condensation are limited. Once a heat pipe is prepared with a LiSr sample, it can usually be used for months[a], with no changes in the emission spectrum.

[a] For a regular measurement day, the oven is switched on in the morning and switched off in the evening. The heat pipe experiences many heating-cooling cycles during its lifetime.

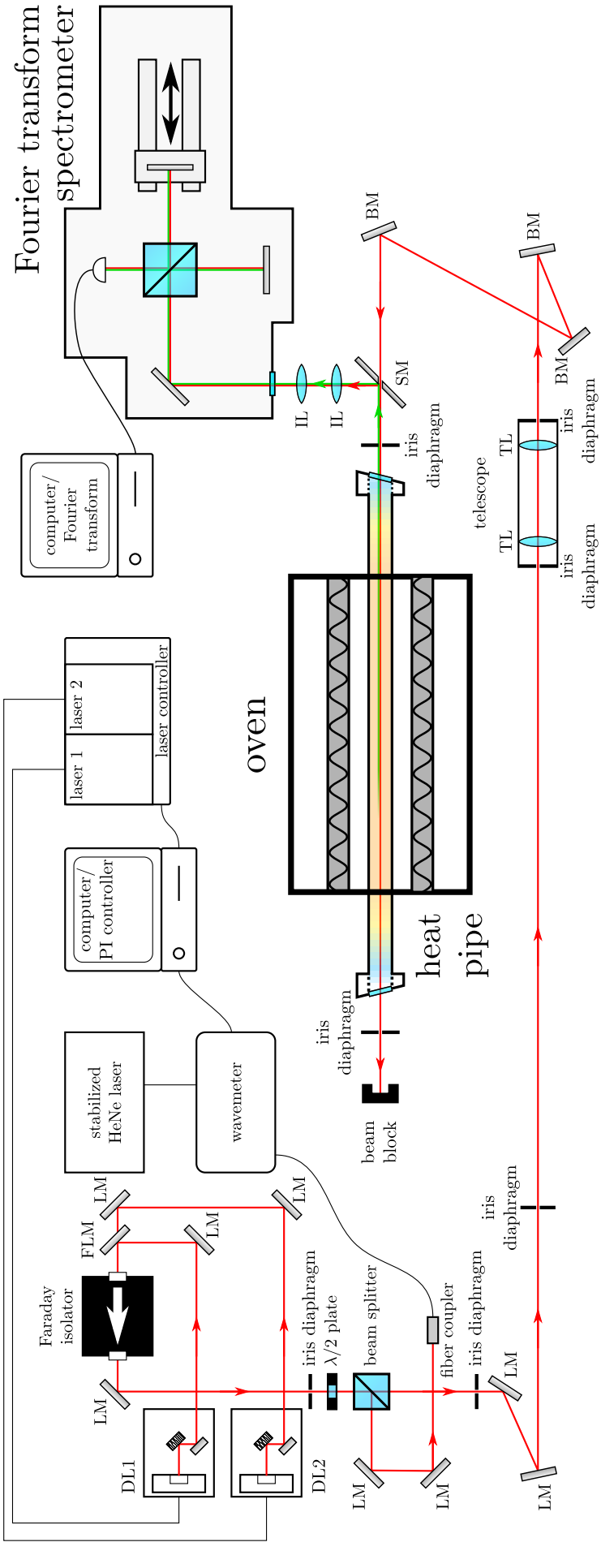

Figure 2.1: Setup of the heat pipe, Fourier-transform spectrometer (FTS) and lasers, not to scale. The hot section of the heat pipe is imaged into the FTS with the slotted mirror (SM) and two imaging lenses (IL1, IL2). The interferogram is recorded by a computer, which also transforms it into the frequency spectrum.
There are two laser heads (DL1 and DL2) that can be used with laser diodes. The laser beam paths coincide after the flippable mirror (FLM). The laser beams are partially injected into a wavelength meter. The wavelength measurement is used to stabilize the laser's frequency via a computer. The main part of the beam goes through a telescope and enters the heat pipe from the direction in which it is observed.
The laser beam travels about 3 m before it exits the heat pipe. In order to alleviate the large effect of small changes at its origin, for example when tuning the frequency, several mirrors and pairs of iris diaphragms were installed along the beam path to allow a quick adjustment of the beam direction for each major stage. BM: beam mirror, TL: telescope lens, LM: laser mirror

The heat pipes usually have to be changed because the mesh is deformed and protrudes into the hollow pipe. Imaging the mesh into the spectrometer adds a significant black body spectrum to the observed molecular spectrum. The mesh position cannot be corrected without potentially destroying the sample. The steel used for the mesh is not an especially heat resistant alloy (1.4401 steel), so there may be room for improvement here, although the lifetime of a LiSr heat pipe is more than satisfying.

2.2 Preparing the Molecular Sample

LiSr was prepared in the the gas phase by putting granules of lithium together with chunks of strontium in the centre of the heat pipe and heating both metals to 915 °C. This approach is uncomplicated in the case of LiSr. As [Iva+11b] suggests, the success of simply heating the metals to produce the desired diatomic molecules depends on their chemical properties. For other combinations of elements, more elaborate setups may be needed. Especially require combinations of other metals need more specific temperature conditions. The vapour pressures for alkali and alkaline earth metals differs usually by several orders or magnitude (see Figure 2.2). For the observation of the spectrum of a alkali-alkaline earth molecule in the heat pipe, different temperatures in different sections of the heat pipe (see [Ger+17; Szc+18]) might be required. It should be noted that the vapour pressure of lithium is similar to that of the alkaline earth metals (compare Figure 2.2), whereas the vapour pressure of the other alkali metals is significantly higher. So lithium and strontium can be expected to behave similarly during the heating process.

Before being filled with the metals, the heat pipe was baked out at temperatures up to 1000 °C until the pressure stabilized around 2×10^{-6} mbar to 3×10^{-6} mbar. After it had cooled down again, it was filled with argon to slightly over atmospheric pressure to prevent air leaking into the heat pipe.

Strontium pieces were cut to size under a nitrogen atmosphere and transported to the heat pipe. The transport vessel was open and connected to the nitrogen supply so that the whole time nitrogen streamed around the sample, displacing air. The heat pipe was opened on one side and the strontium deposited in its middle. After that, it was evacuated again and heated to 250 °C. After reaching around 10^{-5} mbar, the procedure was repeated to fill lithium in the middle of the heat pipe. Because of the low melting point of lithium, the heat pipe was then evacuated at room temperature until a pressure of 2×10^{-6} mbar to 3×10^{-6} mbar was again reached.

The heat pipe was filled with approximately 2 g lithium and 25 g strontium. These amounts were chosen to approximate the stoichiometric ratio of lithium and strontium, that is, about $^{7}/_{88}$. In that way, every Li atom is supplied with a Sr atom to form LiSr, but this very optimistic approach disregards all other possible reactions.

The creation of the molecules and the subsequent measurements took place under a buffer gas atmosphere. Before heating the metallic sample, the heat pipe was filled with argon until the pressure inside was 30 mbar and then the heat pipe was closed off from the pump and vacuum tubes. During the initial phase of the experiment series, pressures ranging from 10 mbar to 40 mbar were used until the value of 30 mbar was finally chosen. Experience shows that the pressure range from 20 mbar to 30 mbar can be used without

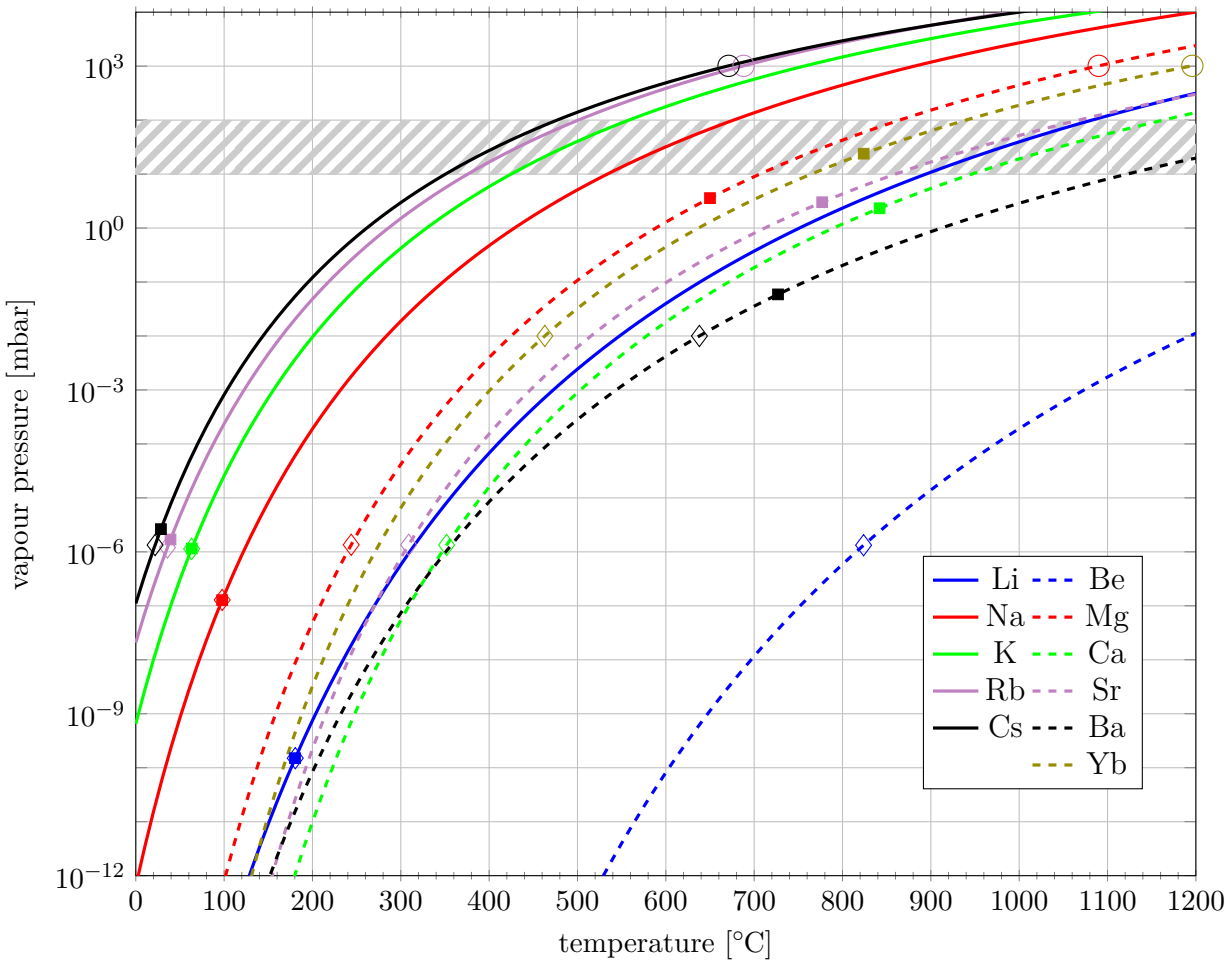

Figure 2.2: Vapour pressure curves for the first five alkali (solid lines) and alkaline earth metals and ytterbium (dashed lines). The Antoine coefficients for these curves were taken from [Yaw06] and can be found in Appendix D. A square represents an element's melting point, which is barely affected by the pressure. The diamonds and circles represent the minimum and maximum measured temperatures as given in [Yaw06]. The vapour pressure curve of Li is similar to those of most alkaline earth metals. The hatched area indicates the experimentally relevant decade.

noticeable drawback. Spectra obtained at pressures close to 80 mbar seemed to have lower intensity. However, no systematic series of experiments with quantifiable results was ever conducted to gauge the effect of the buffer gas pressure on the quality of the spectra.

During the handling of the alkali and alkaline earth metals, both argon and nitrogen were used as inert shielding gas.

2.3 Obtaining Spectra

The centre of the heat pipe was imaged into the entrance of a Fourier-transform spectrometer[b] [Gri83], which is capable of recording a broad spectral range with high resolution.

The image is fed into a Michelson interferometer that has a photodetector in the recombination arm. One mirror is moved along the optical axis and the detected intensity is recorded against the position of that mirror. The Fourier transform of this interferogram is the frequency spectrum of the light source. The resolution of the resulting spectrum

[b] IFS 120HR from Bruker with the OPUS 3.1 controlling software.

is higher with increased travelling distance of the mirror. A sketch of the spectrometer is given on the right side of Figure 2.1. The FTS was evacuated to $\leq 100\,\mu\text{bar}$ when registering spectra.

In principle, the spectroscopic method of Fourier transform allows to detect all frequencies of the light source. In reality, the frequency range is restricted to that part of the spectrum, which in the end creates an electric signal in the photodetector. The windows and mirrors of the FTS are specified for $4800\,\text{cm}^{-1}$ to $45000\,\text{cm}^{-1}$ and the beamsplitter used for the LiSr observation[c] is specified for $1000\,\text{cm}^{-1}$ to $10000\,\text{cm}^{-1}$. The detector is an near-infrared-enhanced silicon avalanche photodiode[d] which is sensitive from 500 nm to 1150 nm. The aperture size inside the FTS was set to 1.7 mm and the internal preamplifier was set to level 2.

Using two lenses and a slotted mirror (IL and SM in Figure 2.1), the hot molecular gas should be imaged as efficiently as possible into the FTS entrance. Apart from the molecular emission spectrum, this image contains also thermal radiation from the heat pipe walls. This blackbody radiation would dominate the recorded infrared LiSr spectrum if the optics are not aligned properly. The mirror was aligned to minimize the light from the heat pipe walls that is incident on the detector, while maximizing the light from the hot sample within the heat pipe. In the optimum configuration, the optical axis of the image almost coincides with the heat pipe axis. For the alignment, the detector signal can be directly monitored[e]. A approximate alignment can found with an unfilled heat pipe: first, a light is shone through the heat pipe and the detector signal is maximized by adjusting the mirror. In this configuration, the optical axis is close to the heat pipe axis. Afterwards, the light is turned off and the oven is switched on in order to get blackbody radiation from the heat pipe walls. The mirror is aligned again to minimize the detector signal. In this configuration, mainly the (empty) volume of the heat pipe is imaged. When this optimum position is reached and the mirror is tilted around any axis, a large increase of the detector voltage can be observed, as more and more of the hot wall area is imaged. The minimum of the incident light in dependence of the tilting angle is rather broad. Therefore, the experiment does not suffer if the slotted mirror is tilted a bit.

After the initial phase of testing the conditions leading to a reproducible spectrum, several spectra were recorded to improve the signal-to-noise ratio. Also, when the sample was heated up to conduct laser experiments (see Section 2.4 below), an emission spectrum was first recorded to see if the spectrum looks like expected. These spectra were all averaged and the final spectrum is the average of 1080 scans. This should nominally improve the signal-to-noise ratio by a factor of $\sqrt{1080} \approx 33$.

The relevant LiSr spectrum appears around $9400\,\text{cm}^{-1}$ [Ste16] and will be described in detail in Chapter 4. To reduce noise in the spectrum, optical[f] and electrical filters[g] were applied to limit the observed spectral range from $8000\,\text{cm}^{-1}$ to $12000\,\text{cm}^{-1}$. The light from the heat pipe went through about 80 cm of air before entering the FTS. For this reason,

[c] Si on CaF_2 from Bruker

[d] Si APD S11519 from Hamamatsu, operated at $-150\,\text{V}$ for all measurements

[e] For the alignment procedures, which take place on mesoscopic timescales, the time average of the signal is sufficient. It can be accessed directly at the detector in the FTS.

[f] FGL 850S from Thorlabs, with ca. 90 % transmision from 850 nm to 1800 nm and $< 1\,\%$ for $< 790\,\text{nm}$

[g] The transmitted spectral range is indicated as $7899\,\text{cm}^{-1}$ to $12638\,\text{cm}^{-1}$ in the OPUS software.

it cannot be ruled out that the observed spectrum shows some absorptions by the air[h], although no distinct absorption patterns were observed in the LiSr spectra. Because of this lack of observation, possible absorptions can be assumed to be at most as large as the noise of the spectra and are therefore neglected in the analysis of the spectrum.

The thermal emission spectrum was recorded with a resolution of $0.03\,\mathrm{cm}^{-1}$, which is close to the expected line width (see equation (3.1.1)).

For a well-imaged operational LiSr heat pipe, the (time-averaged) detector signal is around 200 mV with the setup described here.

2.4 Laser Setup

In addition to recording and interpreting the thermal emission spectrum of LiSr, a laser beam was used to record LIF spectra of the molecular sample. This was realized with a diode laser with a broad tuning range of 950 nm to 1110 nm ($\approx 9000\,\mathrm{cm}^{-1}$ to $10500\,\mathrm{cm}^{-1}$). The laser setup can be found in the left part of Figure 2.1. Two similar laser systems were used. Each has a different laser diode with anti-reflective coating in a Littrow configuration. Their linewidth can be expected to be below 1 MHz $\approx 10^{-5}\,\mathrm{cm}^{-1}$ [WH91]. The laser diode that was mainly used for the excitations in the LiSr spectrum[i], was placed in the laser head DL1 in Figure 2.1. The other head was used for experiments in other spectral ranges in the LiSr spectrum (see Section 4.1.1) or for the investigation of other molecules.

The red line in Figure 2.1 describes the path of the laser beams. Both lasers were set up to have the same optical path after a flippable mirror (FLM). After the mirror, the laser beam passes through an optical diode and is split in two beams by a $\lambda/2$ plate and a polarizing beam splitter. One beam is coupled into a fiber, which leads to a wavelength meter[j], win an accuracy of 10 MHz. The wavemeter was calibrated each day with a HeNe-laser stabilized within 10 kHz to a I_2 hyperfine transition. Experience shows that even with a running experiment (that is, with a hot oven on the experiment table) a recalibration once a day suffices for the required precision of a few hundred megahertz to be within the Doppler-broadening of the lines (see Section 3.1).

The main part of the beam is sent across the experimental table via various optical components in order to be shone into the heat pipe opposite to the direction of observation. This is necessary to reduce the intensity of unwanted laser light that is imaged on the detector (see Section 2.5.1 below). Over the distance between the laser diode and the heat pipe (close to 3 m), the beam widens significantly. Since the laser diode has an elliptical beam profile, the beam diameters along the axes parallel and perpendicular to the optical table grow differently. To counteract the widening of the beam diameters, a telescope consisting of two lenses (TL, at the bottom of Figure 2.1) was used. These refocus both axes of the elliptical laser beam near the slotted mirror to avoid cutoff and prevent the beam from becoming too broad before it exits the heat pipe again. The lenses are spherical, so their corrections to the laser beam are not identical for both axes, but a good compromise to fit all requirements.

[h] According to the HITRANS database [Gor+17], there are H_2O and CO_2 bands in the observed spectral range.
[i] GC-1030-160-TO-200-B from innolume
[j] WS-U from HighFinesse

After passing the telescope, the beam is directed via three mirrors through the slotted mirror and the heat pipe. Two iris diaphragms, one on each end of the telescope, help with the beam alignment. In order to observe laser-induced fluorescence, the laser beam should fall within the volume of the molecular vapour which is imaged into the FTS. The imaging of diffuse reflections, e.g. from the backside of the slotted mirror or the heat pipe wall, should be avoided, as it leads to undesirable artefacts in the recorded spectra (see Section 2.5.1). When the laser path seems suitable, the laser frequency is set to a known molecular transition line in order to record a test spectrum. If the (known) fluorescence lines in that spectrum are strong and there are no artefacts, the alignment of the laser beam is accepted. An iris diaphragm is installed on each end of the heat pipe to facilitate the reproduction of the fruitful beam path. They were set according to an already well-aligned beam. After passing the heat pipe, the laser beam is absorbed in a beam dump.

The optical elements between the beam splitter and the molecular sample[k] lead to a loss of about 35 % of the laser intensity (see Table 2.1). Because broadband optics were used, this loss rate is relatively constant for a wide range of laser wavelengths. For the laser diode used for the analysis of LiSr, the power of the laser beam measured directly before the heat pipe was around 100 mW.

The laser frequency is recorded by the wavemeter during the measurement and stabilized via a software PI controller. This setup can stabilize the frequency to ±10 MHz (about $\pm 0.00034\,\mathrm{cm}^{-1}$).

Table 2.1: Approximate losses of the used optical elements as given by the vendor. For mirrors, this refers to the reflectivity, for everything else, to the transmittance. Compare Figure 2.1

optical element	approximate loss [%]	wavelength range [nm]
laser mirror (LM)	0.05	750–1150
beam splitter	2–3	620–1050
$\lambda/2$ plate	2	690–1200
telescope lens (TL)	8	300–1800
beam mirror (BM)	3	450–10000
slotted mirror (SM)	3	450–10000
heat pipe window	8	300–1800
imaging lens (IL)	8	300–1800

2.5 Obtaining LIF spectra

Section 4.4 will explain the merits of laser-induced excitations in a molecule. To obtain the LIF spectrum for a line known from the thermal emission spectrum, the laser was tuned to the frequency of the line and the whole spectrum was recorded like the emission spectrum. The laser light greatly increases the population of the target transition's upper state, whereas the other states remain populated according to the Boltzmann distribution. Thus, all transitions from that excited state are enhanced and their corresponding spectral

[k] 2× LM, 2× TL, 3× BM, 1× heat pipe window, see Table 2.1

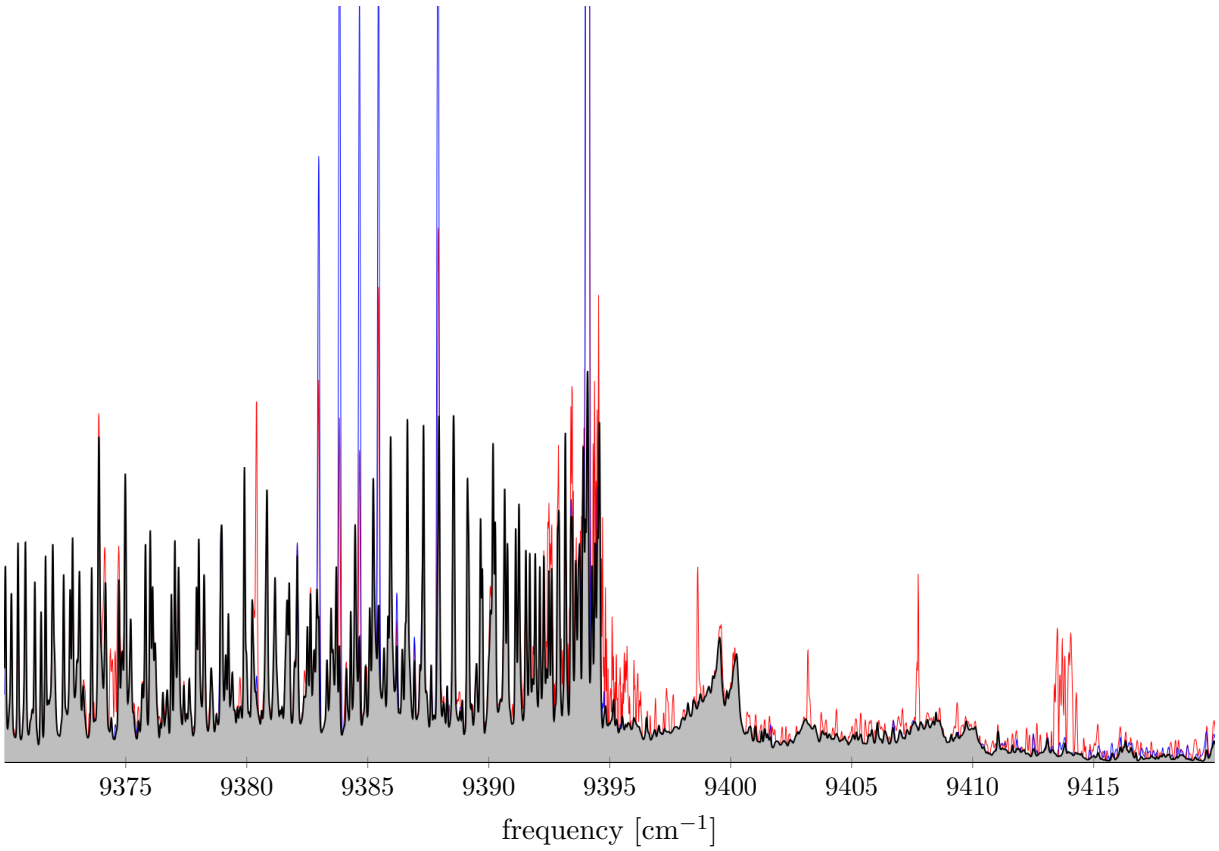

Figure 2.3: The spectrum of the thermal emission of LiSr with superimposed LIF spectra. The red LIF spectrum has many strong artefacts. The blue LIF spectrum, recorded at the same laser frequency, shows no noticeable artefacts. The thermal emission spectrum with a higher resolution is shown in black for comparison. Some of the artefacts can easily be mistaken for fluorescence lines.

lines stand out against the thermal emission spectrum. Comparing such a LIF spectrum with the thermal emission spectrum reveals all transition lines associated with the same upper state.

To economize the measuring time, the LIF spectra were recorded with a resolution of $0.05\,\mathrm{cm}^{-1}$. This resolution is lower than that used for the thermal emission spectrum but it is sufficient to relate an laser-induced fluorescence line to an emission line recorded with higher resolution. Chapter 3 will discuss the influence of the resolution as well as the expected accuracy of the recorded spectra. Typically, 10 scans were averaged for the LIF spectra. Their noise amplitudes are 8 to 10 times higher than that of the averaged thermal emission spectrum, which is in line with the estimation on page 23.

2.5.1 Artefacts

The narrow spectrum and relatively high intensity of stray light from the laser can lead to artefacts in the obtained spectrum, as illustrated in Figure 2.3. Their position in the spectrum depends on the laser frequency and their intensity as seen by the detector. They resemble fluorescence lines and thus make it arduous to gain useful information from the LIF spectra. To verify if an observed line in the LIF spectrum is indeed a fluorescence line, the laser can be tuned to the frequency of the possible artefact in order to record

a complementary LIF spectrum. When the line is indeed an artefact, the line at the original laser frequency shows no laser-induced fluorescence. With a large number of artefacts, this scheme would be very time-consuming. To reduce the artefacts, the amount of laser light scattered on the mirror, heat pipe or optical elements that are imaged on the photodetector needs to be minimized. To achieve this, the effect of the laser on the time-averaged photovoltage can be monitored when aligning the laser beam through the heat pipe. For a well-aligned beam, it is in the order of 5 % to 15 % of the voltage corresponding to the hot gas in the heat pipe without a laser beam.

Additionally, a apodization function that suppresses the artefacts and makes their form more distinguishable from proper fluorescence lines was used for the Fourier transform[1]. For consistency, this apodization function was also used for the emission spectrum. The IFS 120 HR manual states that with this function, a peak is broadened to $1.52 \times$ resolution, which would with a resolution of $0.03\,\mathrm{cm}^{-1}$ lead to about twice the value of the Doppler width calculated in equation (3.1.1). Chapter 3 will demonstrate that the actual measured line widths in the emission spectrum are indeed close to the expected Doppler width, so that the apodization function does not affect the measurements too strongly.

[1] named 'Blackman-Harris 4-term' in the OPUS software

Chapter 3

Determining Peak Frequencies

The thermal emission spectrum (as seen in Figure 4.1) is composed of numerous transition lines and the continuous blackbody radiation of the heat pipe. The registered lines are deformed according to the instrument function of the FTS. The lines themselves can overlap with other lines that are close in frequency. The most interesting information gathered from the spectrum is the transition frequencies of the emission lines. This chapter will explain how the frequencies were extracted from the recorded spectra using derivative spectroscopy.

3.1 Line Characteristics

All experiments were done with molecules in a hot vapour (see Chapter 2). The transition lines in the spectrum at around $f = 9400\,\mathrm{cm}^{-1}$ have therefore a Doppler-broadened Gaussian shape with linewidth [Dem88, p. 84, equation (3.30d)]

$$\begin{aligned}\sigma &= (f_0 = (9400 \pm 300)\,\mathrm{cm}^{-1}) \times 7.16 \times 10^{-7} \sqrt{\frac{T = 1188.15\,\mathrm{K}}{m = 7\,\mathrm{u} + 88\,\mathrm{u}}} \\ &= 0.0238(8)\,\mathrm{cm}^{-1}.\end{aligned} \tag{3.1.1}$$

The hyperfine splitting of the $^2S_{1/2}$ state of ^{7}Li is approximately $0.027\,\mathrm{cm}^{-1}$ [Sta10]. Such a splitting would lead to a line shape that differs from a simple Gaussian profile. This chapter will demonstrate that the observed rovibronic transition lines have indeed a linewidth comparable to the expected Doppler broadening. This leads to the conclusion that the hyperfine structure of ^{7}Li^{88}Sr is narrower than that of the individual atoms[a]. Also, no broadening due to possible magnetic fields in the oven, as discussed in Section 2.3, was observed. The Doppler broadening mostly allows to distinguish between the individual rotational transition lines in the thermal emission spectrum, except for lines that coincide by chance.

A spectral line has a Voigt profile that is given by the convolution of the lines' Lorentzian profile with the Gaussian profile from the Doppler-broadening mechanism. In the registered spectra, the resulting Voigt profile is further convoluted by the instrument function of the FTS. The Doppler width is much larger than the expected natural line width of the observed spectral lines, so the Voigt profile can be expected to resemble a Gaussian curve, with small deviations far from the line centre. To acquire the frequencies of the spectral

[a] ^{88}Sr does not have a hyperfine structure since its nuclear spin is zero.

lines, they were fitted to one or more Gaussian curves, which are described by

$$g(f) = A \times \exp\left(-\frac{1}{2}\left(\frac{f - f_0}{\sigma}\right)^2\right). \tag{3.1.2}$$

Here, A is the amplitude, f_0 the central frequency and σ the linewidth, which is defined by $g(f_0 \pm \sigma/2) = A/e$. The letter g will also be used to refer to a sum of Gaussian curves with different characteristics. The fit to a Gaussian curve needs only three parameters, which all encode information that is relevant to the analysis of the LiSr spectrum (the frequency of a transition, how strong the transition is and if the line width is close to the expected Doppler width). The examples later in this chapter will show that this parametrization of the spectral lines is sufficient. The instrument function of the FTS does not change the line profile noticeably from a Gaussian profile. There are deviations at the feet of the observed spectral lines. They are, however, very small and not relevant at all for the derived data.

3.2 Untangling Gaussian Curves

For superimposed line structures, the first two derivatives of the sum of several curves can help to find the peak positions and linewidths of the contributing Gaussian curves [Saa13]. Figure 3.1 illustrates this with several examples. The shape of the second derivatives g'' of the curves in Figure 3.1 (a) - (c) sets strong limits for the central frequencies f_0 of the involved Gaussian curves. Especially in the cases (b) and (c), where the total peak sum g has no distinct points apart from the maximum, g'' elucidates the underlying structure.

The concept of consulting the derivatives can be translated to peaks recorded with finite resolution, albeit with expectable limitations. For each spectral peak of interest, one or more Gaussian curves were fitted to its discrete data points. Figure 3.2 displays six exemplary peaks or peak structures that will be discussed here.

3.2.1 Background

The recorded spectrum has a background on which the lines are added (or in which they are engulfed). It originates from the imaged blackbody radiation and the presence of many small lines that are too weak or overlap too much to be properly resolved. This background cannot easily be subtracted from the spectrum because it is different over several frequency scales. To illustrate this, a curve going from one local minimum of the recorded spectrum to the next minimum can be plotted together with the spectrum itself. This curve's dynamic closely resembles that of the spectrum. If the minimum plotting is iterated, that is, if the local minima of the minima curve are taken and plotted together with the spectrum, the fine features of the background are slowly lost. Figure 4.1 illustrates the third and fourth iteration step of this procedure in the inset and the fifth and sixth step in the large figure. Comparing the iteration steps shows that there are background features on many scales. Finer features extend over only few of the larger, discernible lines, whereas the curve given by the sixth iteration approaches a reasonable parametrization of the blackbody radiation multiplied with the photodetector's response curve.

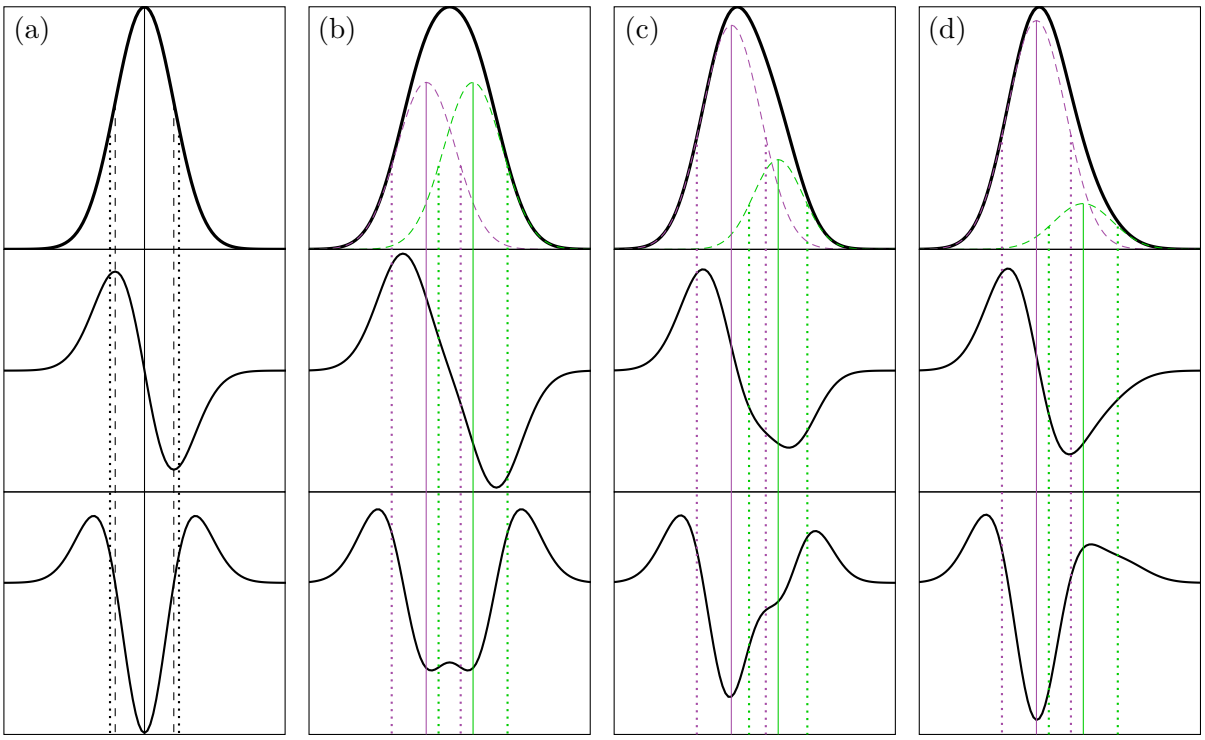

Figure 3.1: The sum $g(f)$ of two Gaussian bell curves (first row) along with their first and second derivatives g' and g'' (second and third row). (a) The derivatives of one curve can be used to infer its characteristics. At the peak position, g' is zero and g'' has a minimum. The extrema of g' and zero-crossings of g'' indicate the positions $\mathfrak{f}$, where $g(\mathfrak{f}) = \max(g)/\sqrt{e}$, indicated by thicker, dashed lines in (a). This is close to the position of $\sigma/2$ (indicated by lighter, dotted lines), with $\sigma/2 \approx 1.18\,\mathfrak{f}$. (b) With two superimposed bell curves, g'' can be used to approximate the positions of the maxima and the linewidths. (c) Even the position of small peaks can be detected with g''. (d) If one peak is too dominant, the second peak is only hinted at by the asymmetry of g'' and the sum of the curves cannot wholly be disentangled. Similarly, peaks that are too close together show no distinct features in the curve or its derivatives and cannot be singled out.

Because the background cannot easily be parametrized, a local correction is applied for every peak in the spectrum. When investigating a peak or peak structure, the two local minima to the left and right of the line are used to determine a linear slope connecting them. This slope is subtracted before applying equation (3.1.2) to the line to remedy the distortions of the background. Figures 3.2 (a), (b) and (c) give examples of spectral lines next to a large structure that adds a background slope. Most peaks, though, are far enough away from the next peak that their slope is considerably less steep.

3.2.2 Line Fit

When investigating a peak, the discrete data points between the two minima are plotted together with the slope. Their first and second derivatives, g' and g'', are plotted separately on the same frequency scale.

The software MINUIT [JR75] was used to perform a nonlinear fit of the three parameters given in equation (3.1.2) for a given number of lines in each peak or peak structure. The quality of the fit is determined by the least mean square difference of the solution to the data points g. Only the primary data g is used for fitting the lines; the derivatives are not

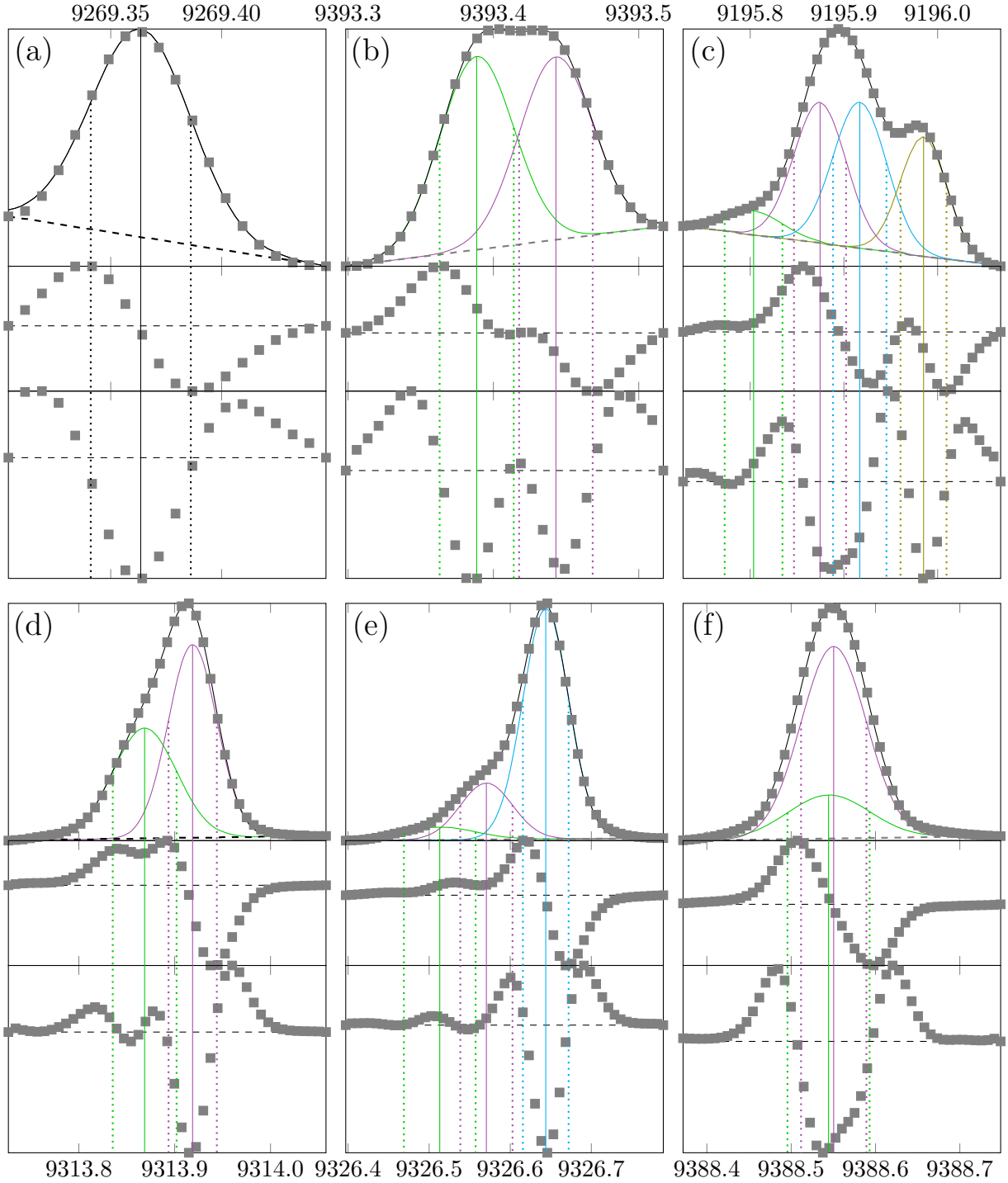

Figure 3.2: Examples of peaks described by Gaussian curves (coloured) according to equation (3.1.1). The first and second derivatives g' and g'' of the experimental data are plotted in the middle and lower parts of each graph. (a) A slope function (dashed line) is calculated from the outside-most data points to allow for the skewed background. The fitted curve (full black line) deviates noticeably from the data at the feet of the peak. (b) g'' shows the central frequencies of two peaks that form a plateau. (c) A structure with four recognizable underlying lines. The first one is weak and its determined frequency lies noticeably besides the small minimum in g''. g'' suggests the presence of two transition lines in the middle peak. (d) The position of a line in the bulge of an asymmetric peak can be narrowed down by looking at the derivatives. (e) The small curve to the left has a considerably higher σ that the other peaks. It should not be taken as a transition line but is included to accommodate the structure's left foot. This improves the fit quality of the other lines. (f) g'' indicates two lines in the peak, but they are so close together that two fitted curves are highly correlated and there is no single, clear way to disentangle them.

considered. The fit routine gives as errors for the fitted parameters one standard deviation. These errors are used for the parameters' uncertainties. The peak-to-peak amplitude of the recorded spectrum's noise is used for the intensity uncertainty of a data point. (For the averaged thermal emission spectrum, shown in Figure 4.1, this amplitude is around 3×10^{-3} of the intensity of the strongest spectral feature in the spectrum.) The frequency uncertainty of a data point was assumed to be zero for the fit since the uncertainty depends on the FTS and hence it is the same for every data point. This uncertainty of the instrument can be determined separately and it will be shown in Section 3.4 that it is well within the lines' Doppler width.

The fitted Gaussian curves and their sum are displayed together with the spectral peak and its derivatives, as in Figure 3.2. The fit is nonlinear and there is no simple way of finding a global minimum, thus good starting values are required to fit a peak with more than one line. The derivatives are used to determine a rough value for the central frequencies and, if possible, the linewidths. The most useful feature for this are the positions or shapes of g''. Figures 3.2 (b) and (d) give examples of the minima of g'' showing the approximate central frequencies of unresolved lines. The shape of a minimum of g'', as seen in Figures 3.2 (c) and (f), indicates that a peak is formed by more than one line. Because the second derivative is very useful to detect the central frequencies, it is worthwhile to calculate the discrete derivatives as accurately as possible. The FTS software offers the possibility to have a higher data point density in g (not to be confused with the resolution) by adding zeros to the ends of the recorded interferogram. The output of the Fourier transform is then padded with data points between each significant spectral data point. These additional points carry no information and merely let the spectrum appear more smooth. However, the higher point density does help to calculate more accurate derivatives. The spectra were transformed with a zerofilling factor of four, which the manual defines to mean that the number of points in the resultant spectrum is multiplied by four.

A sign of a plausible fit solution is that the sum of Gaussian curves approximates the data points. This was generally achieved, except sometimes for points near the base of a structure. Figure 3.2 (a) gives an example. This inconsistency is due to the selection of a narrow fit window and the neglect of the farther surroundings of a peak, the assumption of a pure Gaussian rather than an other profile or with pressure effects that shape the base of a spectral line (see e.g. [MW36; Kuh37]) but are neglected in the model of the line shape. If these deviations are too severe, a further Gaussian curve with small amplitude can be added to facilitate the fit. For example, the line to the left in Figure 3.2 (e) is of no further interest when examining the thermal emission spectrum due to its small size. It might belong to the background of the rather broad peak structure. Nevertheless, adding it allows the fit procedure to better approximate the data points with higher intensity.

In the case of one fitted line, σ can be verified by the derivatives as illustrated in Figure 3.1 (a). With more lines, checking the linewidths is more difficult. In a good fit, the linewidths of all lines are close together, as should happen when the lines come from a physical process such as Doppler broadening. All lines in Figures 3.2 (a) to (e) have a similar width, except the leftmost line in (e), which about 1.5 times broader. This line was only added to allow the fit to model the shape of the peak's left foot and will not

be used to determine molecular parameters. Figure 3.5 illustrates the consistency of the fitted linewidths.

The position of the central frequencies can often be checked against the position of local minima in g''. In Figure 3.2 (c), three fitted central frequencies lie either close to the discrete minimum of g'' (the rightmost frequency) or are arranged around a flat minimum. Thus, they might indeed indicate the two Gaussian curves in the middle of the graph. The leftmost frequency does not properly lie at a minimum position but the corresponding line is weak compared with the others and a deformation of g'' at this position has to be accepted.

The uncertainty of the central frequency is also taken from the fit routine. These uncertainties will later be applied in a fit of molecular parameters to weight the associated transition frequencies. For sufficiently distinct lines, the fitted frequency uncertainty can lie well below the Doppler width. The data points have an uncertainty along the intensity axis, so the frequency uncertainty depends on the amplitude of the line in question. In order to not give stronger transition lines too much weight when fitting the molecular parameters, all frequency uncertainties below the threshold of $0.02\,\mathrm{cm}^{-1}$, slightly lower than the expected Doppler width, were set to this threshold value. Each fitted line was checked for plausibility via three criteria that were discussed above: congruency with the recorded data points g, linewidth close to the Doppler width or agreement of the fitted parameters with the shape of g''. When a fitted line position remained suspect, the frequency uncertainty was manually set to a higher value. For the majority of such lines, the linewidth gave a reasonable uncertainty interval. For example, the peak shown in Figure 3.2 (f) is probably formed by at least two transition lines but they are so close together that the fit routine could find several solutions that describe the recorded data g. The solutions depend on the starting conditions. Manually fixing one line position according to the shape of g'' would lead to a different description of the peak. However, that characterization would not be any more trustworthy. For this peak, the parametrization of one large Gaussian curve was used and the assumed frequency uncertainty is given by the linewidth, which is larger than for lines from well-described peaks.

3.3 Fluorescence Lines

A recorded LIF spectrum (see Section 4.4) also shows the thermal emission spectrum with a large laser line and fluorescence lines that are stronger than the corresponding line in the thermal emission spectrum without the laser. The resolution of LIF spectra is lower than for thermal emission spectra (see Section 2.5). An example of a LIF spectrum is shown in Figure 3.3. Since less scans were averaged during fluorescence experiments than for the thermal emission spectrum, the noise amplitude is higher here. The reduced resolution and the larger noise amplitude generally lead to a higher frequency uncertainty than for the thermal emission spectrum. The noise amplitude has to be measured for each LIF spectrum before the peaks of a spectrum can be fitted. The laser lines appearing in the LIF spectrum are usually 2 to 3 orders of magnitude larger than any other spectral feature. They are also sufficiently well described by one Gaussian curve. This is not due to Doppler broadening but rather the effect of the instrument function of the FTS. Thanks to the

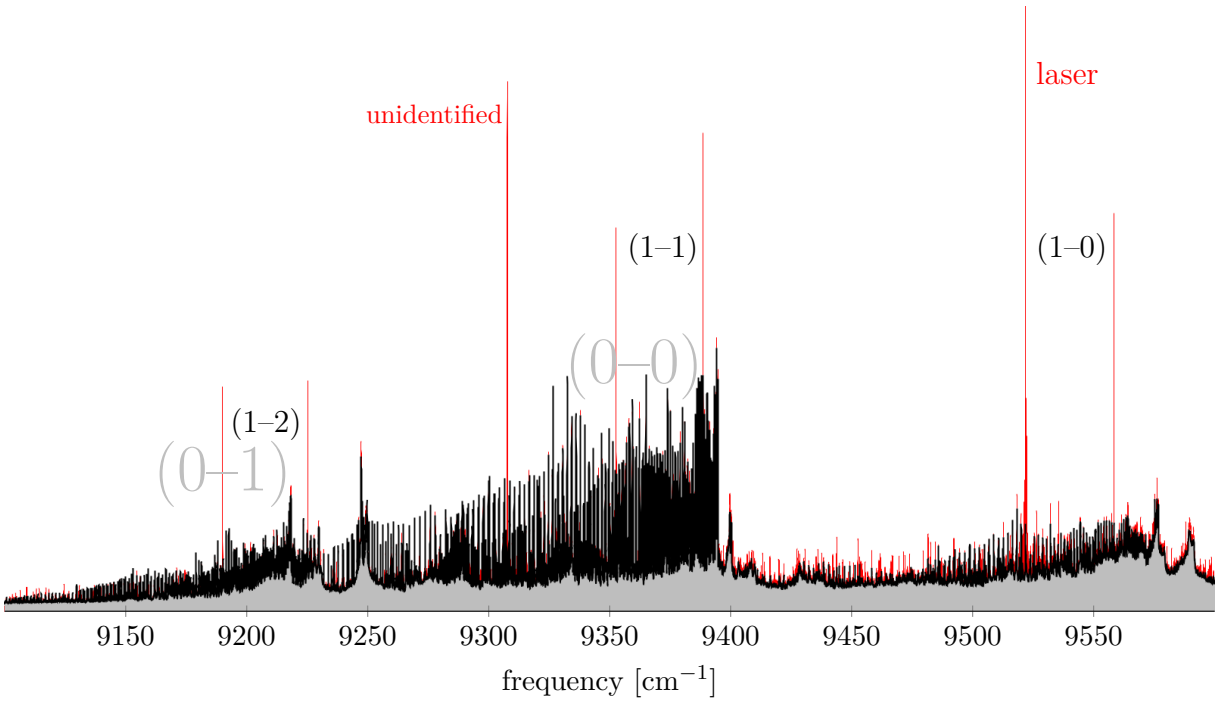

Figure 3.3: A LIF spectrum (in red) with an excitation in the (1–0) band and fluorescence lines in the (1–0), (1–1) and (1–2) bands. Each band features fluorescence of a PR pair. The thermal emission spectrum is overlaid in black for comparison. This spectrum has an unidentified line, which might come from an other molecular system or, more likely, may be an artefact. At this frequency, the thermal emission spectrum shows no peak.

laser lines' high intensity, their fitted frequency uncertainty is very low. LIF lines also have usually a much higher amplitude than the thermal emission lines and can be described with one Gaussian curve. When a LIF line is close to a strong emission line, the emission line might have to be considered in the fit.

There are cases of fluorescence lines so weak that the thermal emission spectrum, with which they are recorded together simultaneously, dominates their peak structure. This happens when a relatively weak transition is excited whose fluorescence frequencies are close to stronger transitions, for example of a vibrational band with a larger Franck-Condon factor. Two examples of this are displayed in Figure 3.4. In these cases, the fluorescence was recognizable only by comparison with the thermal emission spectrum. For both Figures 3.4 (a) and (c) and Figures 3.4 (b) and (d), there is a transition to the left that has a higher relative amplitude in the LIF spectrum than in the thermal emission spectrum. A direct comparison of fluorescence peaks and the thermal emission can also give hints at unrecognized lines in the thermal emission spectrum if the fluorescence is strong enough to elicit a line obscured by larger neighbouring lines in the thermal emission spectrum.

When comparing peaks fitted with fluorescence and thermal emission spectra, the effect of the resolution becomes noticeable. Thermal emission lines have generally lower linewidths than fluorescence lines. Figure 3.5 (a) compares the linewidths of thermal emission, fluorescence and laser lines. The latter two were recorded with a resolution of $0.05\,\mathrm{cm}^{-1}$ (see Section 2.5). Fits of the laser lines give an approximate linewidth of $0.03\,\mathrm{cm}^{-1}$. Because the actual laser is much narrower (see Section 2.4), this linewidth sets a lower limit for the expected values with the experimental parameters. Generally,

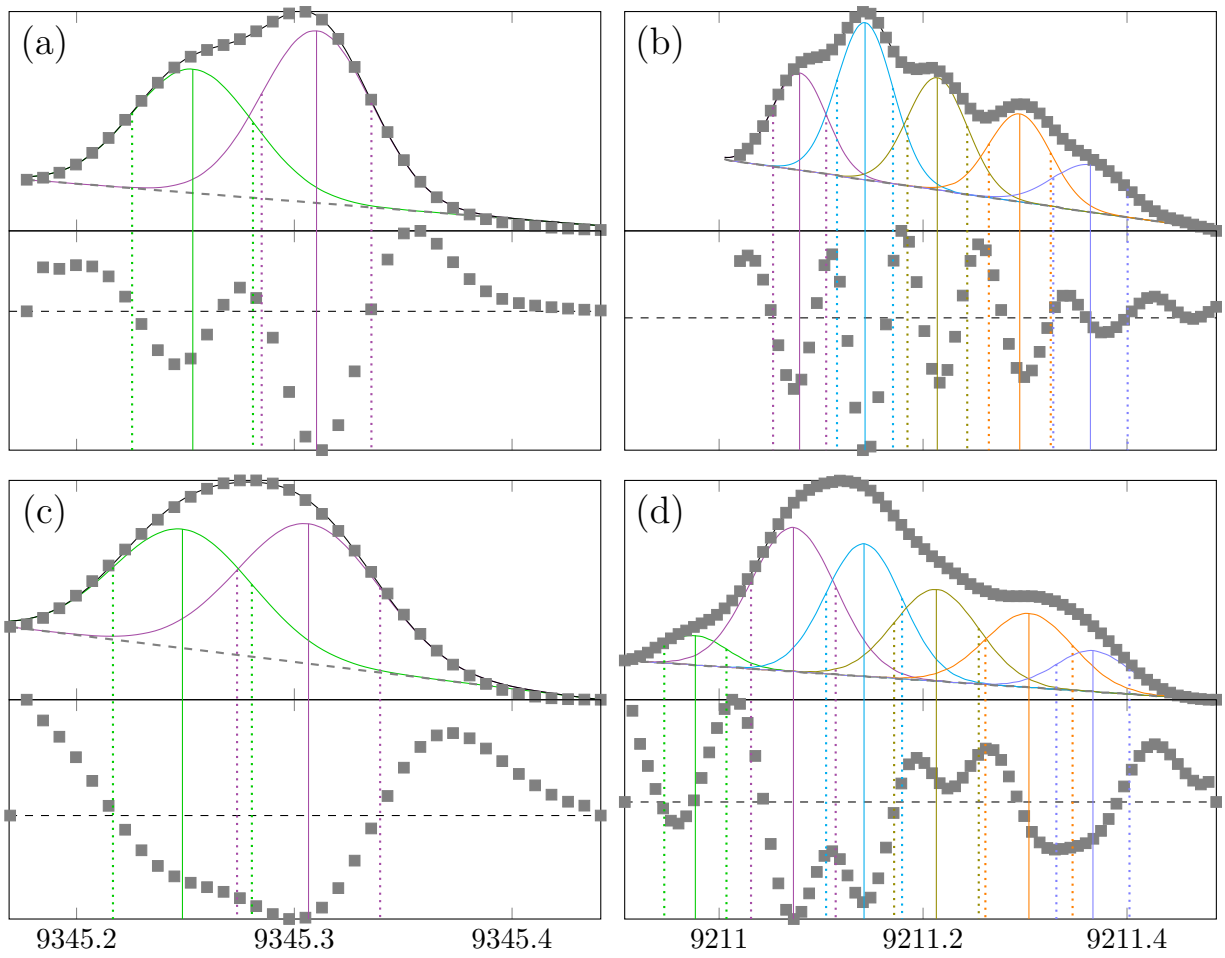

Figure 3.4: Comparison between two peak structures in the thermal emission spectrum ((a) and (b)) and in two LIF spectra ((c) and (d)). The first derivative is omitted as it usually gives no additional information. The structures in the LIF spectra look generally broader due to their lower resolution. The linewidths of the fitted lines in (c) and (d) are also noticeably larger than in (a) and (b). The fit ranges of the peak structures are different in the thermal emission spectrum and the LIF spectrum because the local minima are not at the same frequency. In (d) the fluorescence peak even alters the peak shape sufficiently to shift the left minimum beyond a neighbouring line that was fitted separately in the thermal emission spectrum.

the fitted linewidths of the fluorescence or thermal emission lines lie below the spectra's resolution. Many thermal emission lines, recorded with a resolution of $0.03\,\mathrm{cm}^{-1}$, even have linewidths comparable with the expected Doppler width given in equation (3.1.1). Based on these findings, the broadening effects of the resolution and of the window function described in Section 2.5.1 do not considerably impair the quality of the records. Figure 3.5 (b) and (c) show the frequency errors assigned by the fit. They are below $0.01\,\mathrm{cm}^{-1}$ for lines with a sufficiently large amplitude, but for weak lines or lines that needed to be fitted with several other lines, the assigned error can be higher than the linewidths. In the range of $9400\,\mathrm{cm}^{-1}$ to $9570\,\mathrm{cm}^{-1}$ the lines are less intense than in the range of $9200\,\mathrm{cm}^{-1}$ to $9400\,\mathrm{cm}^{-1}$ (compare Figure 4.1). The reduced intensity leads to larger frequency errors. The range of $9100\,\mathrm{cm}^{-1}$ to $9220\,\mathrm{cm}^{-1}$ features relatively weak lines, which also lie closer together than in the other parts of the spectrum. Here, the assigned frequency errors are very large. When it seemed reasonable from the appearance of the fitted line, the smaller linewidth was used as frequency uncertainty instead of a high frequency error.

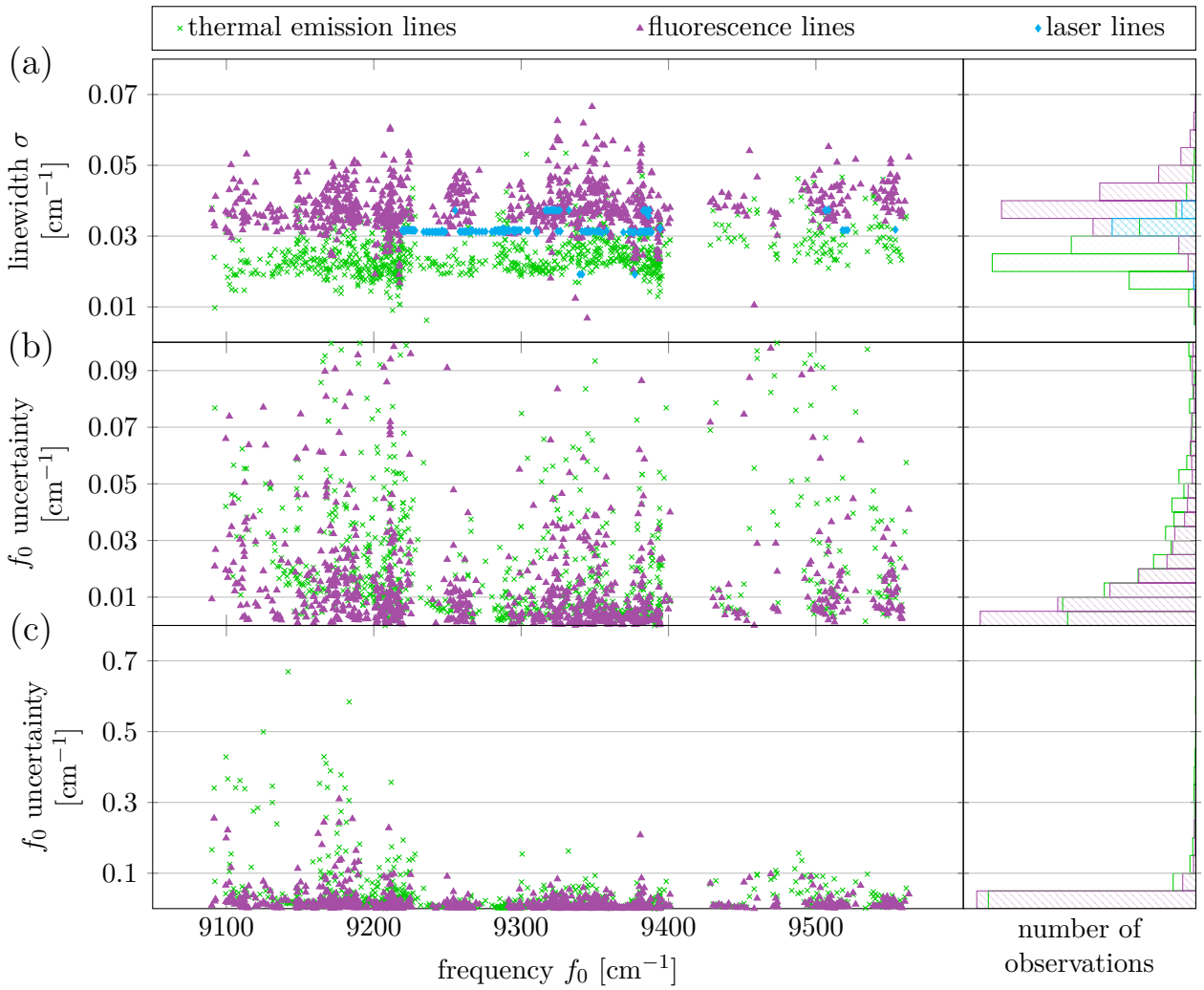

Figure 3.5: Comparisons of the linewidth (a) and frequency uncertainty ((b) and (c)) of lines from recorded thermal emission and fluorescence lines. Only lines with assigned quantum numbers are included in these plots; lines that were included to improve the description of a peak are disregarded. The frequency range of 9100 cm^{-1} to 9220 cm^{-1} has the highest frequency uncertainties. (In this range there are relatively weak bands with many coinciding lines.) The abundance of the linewidths or uncertainties is indicated on the right.

3.4 Frequency Precision

To fit the molecular parameters (see Chapter 5), the laser frequency of a LIF spectrum is required. Since the wavemeter's resolution and uncertainty is much higher than that of the recorded spectrum, the frequency value from the wavemeter was used as the frequency of the laser line. The uncertainty was set to 0.0006 cm^{-1} because the laser was stabilized within an interval of ±10 MHz during a fluorescence measurement. The laser peak in the LIF spectra was nonetheless fitted to a Gaussian curve and the difference between the frequency displayed by the wavemeter and the fitted central laser frequency was recorded for every LIF spectrum. These differences are plotted in Figure 3.6 (a) for all LIF spectra whose data was used to fit the molecular parameters. There is a spread of about 0.004 cm^{-1}, with the centre shifting by nearly 0.005 cm^{-1} over several years. The grey bar represents the 20 MHz uncertainty interval. For reference, the rovibrational states excited during fluorescence experiments are given with date in Figure 3.6 (b). The latest

measurements added transitions with upper rotational quantum numbers between ca. 70 to 120 in two vibrational levels. They expand the range of rotational energy levels that was used until then, so molecular parameters describing higher rotational levels might have a slight bias. These deviations are, however, within the assumed minimal uncertainty of $0.02\,\mathrm{cm}^{-1}$ mentioned in the last paragraph of Section 3.2.2 and thus should not affect the molecular fit.

For these reasons, the lower bound of the uncertainty value of $0.02\,\mathrm{cm}^{-1}$ is a reasonable weighting factor for the fits and captures the expected frequency variations well.

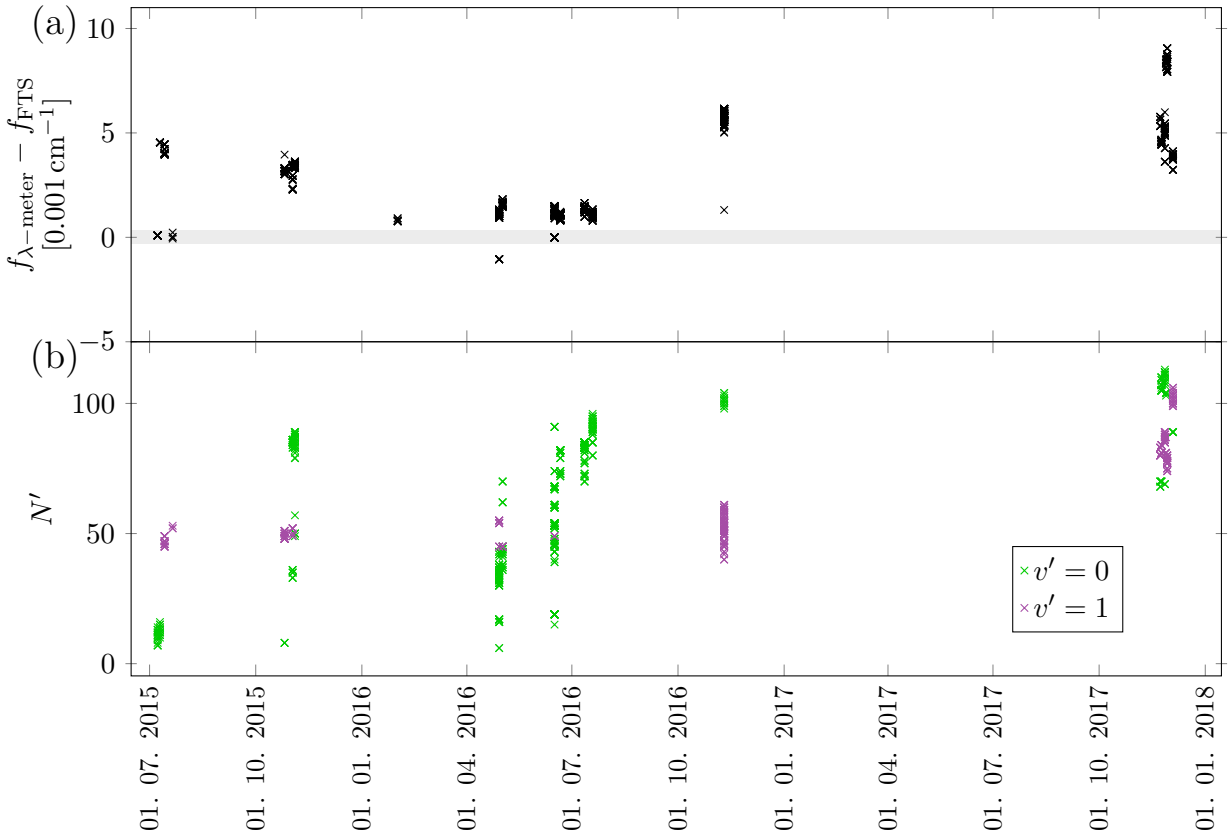

Figure 3.6: Observations regarding the frequency precision. (a) Deviation of laser frequency measured with wavemeter and FTS. The grey bar represents the 20 MHz stability interval of the laser. The centre shifts slightly over several years. (b) The quantum numbers of the excited rovibrational states are plotted over time to give a reference for how much the observed states might be affected by the drift.

Chapter 4

Interpretation of the Spectrum of LiSr

After having considered individual lines in the previous chapter, this chapter will discuss the large features of the broadband spectrum, especially the vibrational bands, and the next chapter will describe the assignment of the finer rotational structure in detail.

The recorded emission spectrum Figure 4.1 gives a broad overview over all infrared transition lines of LiSr. These lines have to be assigned to quantum states in order to find molecular parameters that describe the states' energy levels.

There are two distinct major structures in the spectrum, one from $9000\,\mathrm{cm}^{-1}$ to $10000\,\mathrm{cm}^{-1}$, the other from $10700\,\mathrm{cm}^{-1}$ to $12000\,\mathrm{cm}^{-1}$. (The spectral intensity decreases for frequencies above $11400\,\mathrm{cm}^{-1}$ due to the effects of electronic filters in the FTS. In fact, the latter structure continues to $15000\,\mathrm{cm}^{-1}$.) Using LIF spectra to find lines sharing the same upper rovibronic state greatly helped to uncover the underlying spectral order. The general layout of the spectrum can also be outlined by turning to recent ab-initio works.

4.1 Identifying the Spectrum of LiSr

The metallic sample contains Li and Sr in high purity. Besides LiSr, also Li_2 and Sr_2 could form in the heat pipe. The samples of metals also contain impurities of other alkali or alkaline earth metals and spectra of other atoms or molecular could also be recorded. A broadband absorption spectrum (Figure 10.3) contains a few undesirable atomic lines but there were no spectra from the impurities observed in the near infrared spectrum.

According to [Ste16], the spectral system of the Sr_2 molecule with the lowest frequency, $(2)^1\Sigma_u^+$–$X(1)^1\Sigma_g^+$, is not found at frequencies lower than $\approx 12800\,\mathrm{cm}^{-1}$. The occurrence of Sr_2 spectra in the recorded frequency range can be ruled out on these grounds. Atomic transition lines are not visible in the spectrum, so it can reasonably be assumed to contain only LiSr and Li_2 transitions, which will be identified in the following.

The potential curves from ab-initio calculations [Gop+13; Pot+17; Zei+18] suggest that LiSr spectra can be expected starting in the near-infrared above $6000\,\mathrm{cm}^{-1}$ (compare Figure 1.1). These works agree that the transition dipole moment for $(2)^2\Sigma^+$–$X(1)^2\Sigma^+$ transitions (expected around $10000\,\mathrm{cm}^{-1}$) is much stronger than that for $(1)^2\Pi$–$X(1)^2\Sigma^+$ transitions. The transition dipole moment of the $(3)^2\Sigma^+$–$X(1)^2\Sigma^+$ system (around $13000\,\mathrm{cm}^{-1}$) is consistently calculated to be much stronger than that of the $(2)^2\Sigma^+$–$X(1)^2\Sigma^+$ system.

4.1.1 Near-Infrared Spectra of LiSr and Li_2

A structure with clearly discernible bands is seen in the thermal emission in Figure 4.1 from $9000\,\mathrm{cm}^{-1}$ to $10000\,\mathrm{cm}^{-1}$ It lies in the spectral region of the predicted $(2)^2\Sigma^+$–$X(1)^2\Sigma^+$ or $(1)^2\Pi$–$X(1)^2\Sigma^+$ transitions of LiSr. Since the ab-initio calculations predict a much

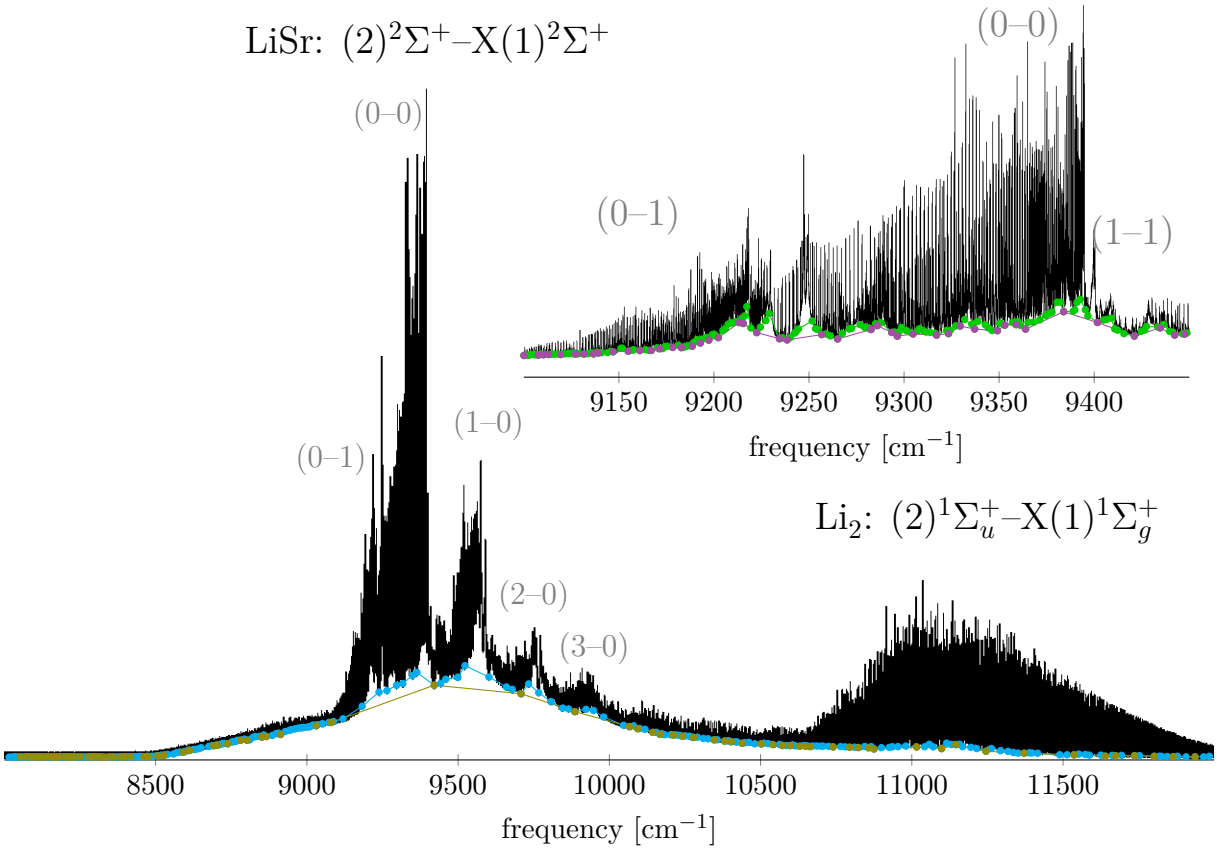

Figure 4.1: The thermal emission spectrum of the molecular gas in the heat pipe. The LiSr spectrum is in the left part of the figure and the Li_2 spectrum at higher frequency. The most prominent vibrational bands of LiSr are labeled (see text). They overlap with weaker unlabeled bands at nearly the same frequencies. The positions of local minima after three (—•—), four (—•—), five (—•—) and six (—•—) iterations of the procedure described in Section 3.2.1 are plotted to visualize the signal background. The photodetector is not sensitive for light with less than 8500 cm^{-1} and around 11700 cm^{-1} the effects of the optical and electronic filters start to attenuate the spectrum. The inset shows the strong (0–0) and (0–1) bands with their rotational structure. The weaker (1–1) band can be seen to the right. The third and fourth background iteration steps are plotted here to better show how the first iteration steps approximate the spectral structure.

larger transition dipole moment for $(2)^2\Sigma^+$–$X(1)^2\Sigma^+$ transitions than for $(1)^2\Pi$–$X(1)^2\Sigma^+$ transitions, the observed spectral system was attributed to transitions between the lowest two $^2\Sigma^+$ states of LiSr.

For frequencies above 10600 cm^{-1}, the spectrum has no clearly perceptible band structure. This part of the emission spectrum could originate from either Li_2 or LiSr. From energetic considerations alone (Figure 1.1), LiSr transitions could involve higher vibrational levels in the electronic ground state and either $(3)^2\Sigma^+$ or $(2)^2\Pi$ states with low v'. The last two states are unlikely to be involved because, according to [Pot+17], the Franck-Condon factors for high v'' and low v' are expected to be small. In order to investigate the composition of this spectrum, several fluorescence experiments were conducted in this spectral range (see Section 4.4 below). The obtained spacing of the vibrational progression was consistent with known spectroscopic constants of Li_2. To judge the amount of Li_2 transitions in this part of the recorded emission spectrum, the spectrum was compared with a simulation of a thermal emission spectrum of Li_2 that was based on electronic potentials given by

[CM06]. This simulation could adequately reproduce the recorded spectrum. There were no recorded lines or lineshapes that could not be attributed to Li_2. Any conceivable LiSr transitions in the range of $10600\,cm^{-1}$ to $12000\,cm^{-1}$ are too weak to be identified among the Li_2 lines in a straightforward way.

For these reasons, the further discussion of the thermal emission spectrum of LiSr will be restricted to the band structure from $9000\,cm^{-1}$ to $10000\,cm^{-1}$. It should be noted for the understanding of Figure 4.1 that the photodetector is not responsive for frequencies below $8500\,cm^{-1}$, while optical and electronic filters prevent the registration of a spectrum beyond $12000\,cm^{-1}$. The weakest observed emission lines are at frequencies higher than $9000\,cm^{-1}$, where the detector's response is sufficient. It is unlikely that the emission spectrum of the band system in question revives at frequencies that were not observed.

4.2 Vibrational Bands

The vibrational constants for the $X(1)^2\Sigma^+$ and $(2)^2\Sigma^+$ states from the ab-initio calculations are almost the same, namely around $180\,cm^{-1}$. Therefore, all bands ($[v' + k]$–$[v'' + k]$), for $k, \in \mathbb{N}$, should for fixed v' and v'' lie close together in the spectrum and have considerable overlap. Taking the frequencies of the band heads as an approximation, there are five clearly visible bands that are approximately $180\,cm^{-1}$ apart and thus fit well to the ab-initio calculations. These are the labeled bands in Figure 4.1, according to the following considerations:

The investigation of rotational lines by laser-induced fluorescence (see Section 4.3) also shows which vibrational bands share the same upper vibrational quantum number. Excitations in one of the bands labeled (0–0) and (0–1) in Figure 4.1 led to fluorescence in only the same or in the respective other band. The higher-energetic one of these two bands is assumed here to be the (0–0) band since the laser excitations in these two bands never led to fluorescence lines with higher frequency than the (0–0) band head. Higher frequencies would imply decay to a vibrational level with a v'' quantum number lower than that of the initial state and if the initial level is the lowest, this cannot happen.

This argument does not consider the Franck-Condon factors that might suppress fluorescence in a lower-lying band, and so the conclusion may be false. However, according to [Pot+17], the Franck-Condon factors can be expected to be highest for $v' = v''$ near the potential bottom, with Franck-Condon factors of the neighbouring bands being considerably smaller and in such a situation the above-mentioned arguments would hold. The other band is then the (0–1) band, whose transition frequency is reduced by one vibrational quantum.

A weaker, but still clearly recognizable band head lies about $6\,cm^{-1}$ higher than the (0–0) band head. It is considered here to belong to the (1–1) band which extends into the (0–0) band. Its rotational transition lines are much weaker than those of the (0–0) band and are not always visible among the stronger lines. Laser excitations in this band led to fluorescence in the band labeled (1–0) in Figure 4.1 and a band close to the (0–1) band, which is then the (1–2) band. As with the (1–1) and (0–0) bands, most of the (1–2) lines lie in the (0–1) region and are hard to discern in the thermal emission spectrum, while the (1–0) rotational branches can easily be seen.

The frequency of the band head labeled as (1–0) is about 180 cm^{-1} higher than for the (0–0) band head. This leads to the conclusion that it is the (1–0) band and that the other two bands with the same upper vibrational level are the (1–1) and (1–2) bands.

It becomes clear from these observations that the Franck-Condon factors allow only transitions to neighbouring bands, which means that advancing to higher vibrational levels in both electronic potentials can only be done in small steps.

The other bands labeled in Figure 4.1, namely the (2–0) and (3–0) bands were assigned based on their frequency distance to the (0–0) band. They likely also overlap with other bands, e.g. the (3–1) band, which should be weaker in intensity. A few laser experiments were conducted in these bands but no fluorescence could be observed. Possibly, the Franck-Condon factors for these bands are too small to see single transitions here.

4.2.1 Isotopologue

Since the sample was prepared without consideration of isotopic purity, it can be assumed that LiSr was formed according to the natural abundance of Li and Sr isotopes. These isotopologues of LiSr have slightly different molecular constants and hence spectra. This leads to several variants of one rovibrational band with the same quantum numbers. Their intensity varies according to the fraction of the corresponding isotopologue.

Table 4.1: Occurrence of different isotopologues of LiSr in percent. They were calculated from the natural abundance of isotopes of Li and Sr taken from [BW11].

isotope	Sr	84	86	87	88
Li	%	< 1	10	7	83
6	8	—	0.80	0.56	6.6
7	92	—	9.2	6.4	76

Table 4.1 suggests that the fraction of $^{7}Li^{88}Sr$ is around 3/4 and each other isotopologue makes up at most 1/10 of the LiSr molecules. Because of this disparity in occurrence, the assumption is made here that the spectrum comes from the most probable isotopologue, $^{7}Li^{88}Sr$, and that the spectra of other isotopologues are too weak to be recognized.

In the observed spectrum, there are some less intense bands near bands of higher intensity but these can be explained as different vibrational bands of the same isotopologue.

4.3 Rotational Quantum Numbers

The shape of a vibrational band is determined by the rotational spectrum added to the vibrational transition frequency. As described in Section 1.4, the rotational transition lines are arranged on the frequency axis according to equations (1.4.1). No transitions with $F_1 \rightarrow F_2$ or $F_2 \rightarrow F_1$ could be assigned (which is in line with with the expectation of weak lines discussed in Section 1.3) and the further discussion will omit them.
Figures 4.2 (a) and (b) illustrate the build-up of the (0–0) band heads near the reversal of the R branches of the F_1 and F_2 systems. The spacing of the rotational lines of one branch is in general larger than the linewidth given by equation (3.1.1), with the exception of lines near the band head. The (0–0) band, being the most prominent one, was investigated first.

The rotational constants that describe this band were then used as a basis for evaluating other bands.

4.3.1 Spin Components

There are two band heads in the experimental recording in Figure 4.2 (b) with nearly the same intensity. They could conceivably come from different vibrational transitions but, as stated in Section 1.4, it is more likely that they are formed by the two spin systems. This explanation is also in accordance with the fact that each of the studied vibrational bands appears as two systems with similar intensity. As illustrated in Figure 4.2, the transition lines of one system occur at higher frequency than the lines of the other system with the same rotational quantum number N'. This is due to the spin-rotation coupling as given in equation (1.1.3). The present experimental method cannot determine the spin state, so the transitions with the same N' at higher frequency were arbitrarily classified as F_1 lines. This would mean a positive difference of the spin-rotation coupling constants γ in both electronic states. Changing this attribution results merely in the same value for γ with negative sign.

4.3.2 Line Assignment

Many transition lines in the rotational spectrum are resolvable so that one such line can be assigned a rotational quantum number N[a]. For larger N, the distance Δf between neighbouring lines of a branch can be expected to rise linearly with N in both the P and R branch (see equations (1.4.2)). For a small enough range of N, the change in Δf is even small enough to be considered constant. As a result, it was in most cases straightforward to find neighbouring lines with $N \pm 1$, $N \pm 2, \ldots$ to an already assigned line.

By trying a few assignments of quantum numbers to several sets of neighbouring lines and comparing the implied rotational constants to the ab-initio calculations, a consistent description of the rotational spectrum soon emerged. This approach is, however, only feasible as long as the individual transition lines are easily distinguishable. For molecules with smaller rotational constants, e.g. due to a larger reduced mass, it can be problematic due to the Doppler broadening of the lines. For such molecules, fluorescence experiments provide an effective path to determine the rotational constants of the involved states.

4.4 LIF spectra

Excited rovibrational $|v', N'\rangle$ states can decay to several states with different v'' and N'' according to the selection rules for N (see Section 1.3) and Franck-Condon factors. As explained in Section 1.3, only P and R bands appear in $^2\Sigma^+$–$^2\Sigma^+$ transitions. These lines have the same frequencies as the corresponding lines in the thermal emission spectrum but are enhanced due to the laser pumping. Comparing the LIF spectrum with the thermal emission spectrum shows which transitions in each branch are connected by their upper state $\left|(2)^2\Sigma^+, v', N', {}^{F_1}/_{F_2}\right\rangle$.

[a] N will be used as shorthand for knowledge of both N' and N'' or, equivalently, N' and whether the line is a P or R line.

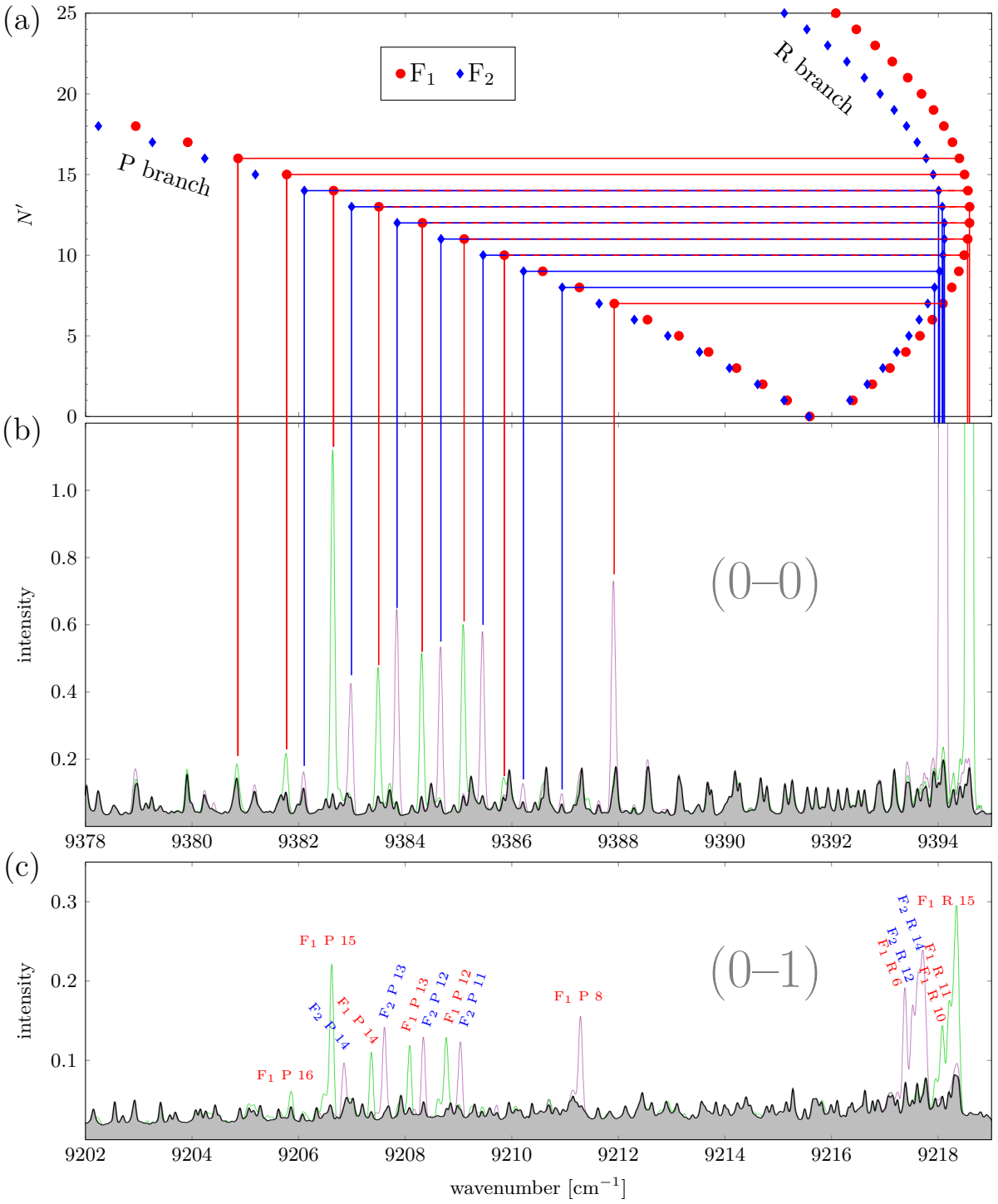

Figure 4.2: Fluorescences in the (0–0) and (0–1) band heads (a) The Fortrat parabolas for the F_1 and F_2 systems of the (0–0) band. (b) Exciting the band heads with a laser leads to fluorescence of the corresponding P lines. Their intensity depends on how much the laser overlaps with the spectral line. Two independent laser experiments are shown in different colours. (c) The same excitations also result in fluorescence in the P and R branches of the (0–1) band. The fluorescent R lines overlap too much to be all labeled here. Comparing the LIF spectra in both bands immediately shows that their rotational spectra must be different because the distance between the fluorescence lines is not the same in both bands. Since the upper states for both bands are the same, this shows that the vibrational states in the electronic ground state have different rotational constants. The labels of the lines refer to, for example, $N' = 10 \rightarrow N'' = 11$ for P 11.

The example given in Figure 3.3 shows the excitation of only one transition line in the (1–0) band and fluorescence in the (1–0), (1–1) and (1–2) bands. These fluorescence reveal a pair of P and R lines in each vibrational band.

Figure 4.2 displays the thermal emission spectrum of LiSr together with LIF spectra from an excitation in each of the (0–0) band heads. Since the heads are formed by many overlapping lines, these experiments populate several levels in $(2)^2\Sigma^+$, which leads to multiple fluorescence lines. With the exception of F_1 P 8, each LIF spectrum has fluorescence lines belonging exclusively to one of the two spin systems. The P lines from each LIF spectrum appear evenly spaced since the change in Δf is small when considering only a small N range (see Section 4.3.2). The intensity of the fluorescence lines depends on the overlap of the excited rovibronic transition line with the laser frequency.

Figure 4.2 (c) shows the laser-induced fluorescence lines of the same excitations as in Figure 4.2 (b) in the (0–1) band. Due to a smaller Franck-Condon factor, they are weaker than the (0–0) lines, hence only the more intense peaks can be distinguished from the thermal emission spectrum with certainty. It becomes clear from the laser-induced fluorescence near the band heads that the rotational parameters for the (0–1) band are different from those for the (0–0) band. Both bands have the same upper vibrational level, so the rotational energies in the $v'' = 0$ and $v'' = 1$ levels must differ[b]. This difference affects also the frequency distance of consecutive P lines (see Equations (1.4.2)), which can be seen when comparing Figure 4.2 (b) and (c).

By connecting two spectral lines with the same upper state, the upper state can be eliminated and an energy difference between the states in the lower electronic state can be determined directly. For example, the frequency difference of the F_1 P 15 lines in the (0–0) and (0–1) bands equals the spacing of the states $\left|X(1)^2\Sigma^+, v'' = 0, N'' = 15, F_1\right\rangle$ and $\left|X(1)^2\Sigma^+, v'' = 1, N'' = 15, F_1\right\rangle$, which is the vibrational spacing in the $X(1)^2\Sigma^+$ state, disregarding the anharmonicity. The same is true for all other P and R fluorescence lines that occur in more than one band[c].

Occasionally, exciting a rotational transition leads not only to fluorescence of the corresponding transition line in the other rotational branch but also to fluorescence of lines with neighbouring N in both branches. Figure 4.3 gives an example. This happens due to collisions of the excited molecule during which it loses or receives a rotational quantum. These so-called rotational satellites have lower intensity than the principal fluorescence line but are more intense than the thermal emission lines at the same frequencies. Here it has to be considered that due to the lower resolution of the LIF spectrum, its peaks are usually lower than those of the thermal emission spectrum. For example, the blue line under the label '-4' in Figure 4.3 (b) is as high as its counterpart in the black spectrum, whereas its neighbours are lower than their black correspondents. This, together with the distance between the satellite lines, leads to the conjecture that the line is a satellite. The analysis of the (0–0) band described in Chapter 5 confirms this conclusion.

Rotational satellites give unquestionable evidence concerning a sequence of lines in a rotational branch because they correspond to rotational levels that surround the excited rotational level.

[b] γ was also found to be dependent on v, but the effect is smaller.

[c] For a larger range of N or v, higher-order terms in the Dunham series become important, but here this is a good approximation.

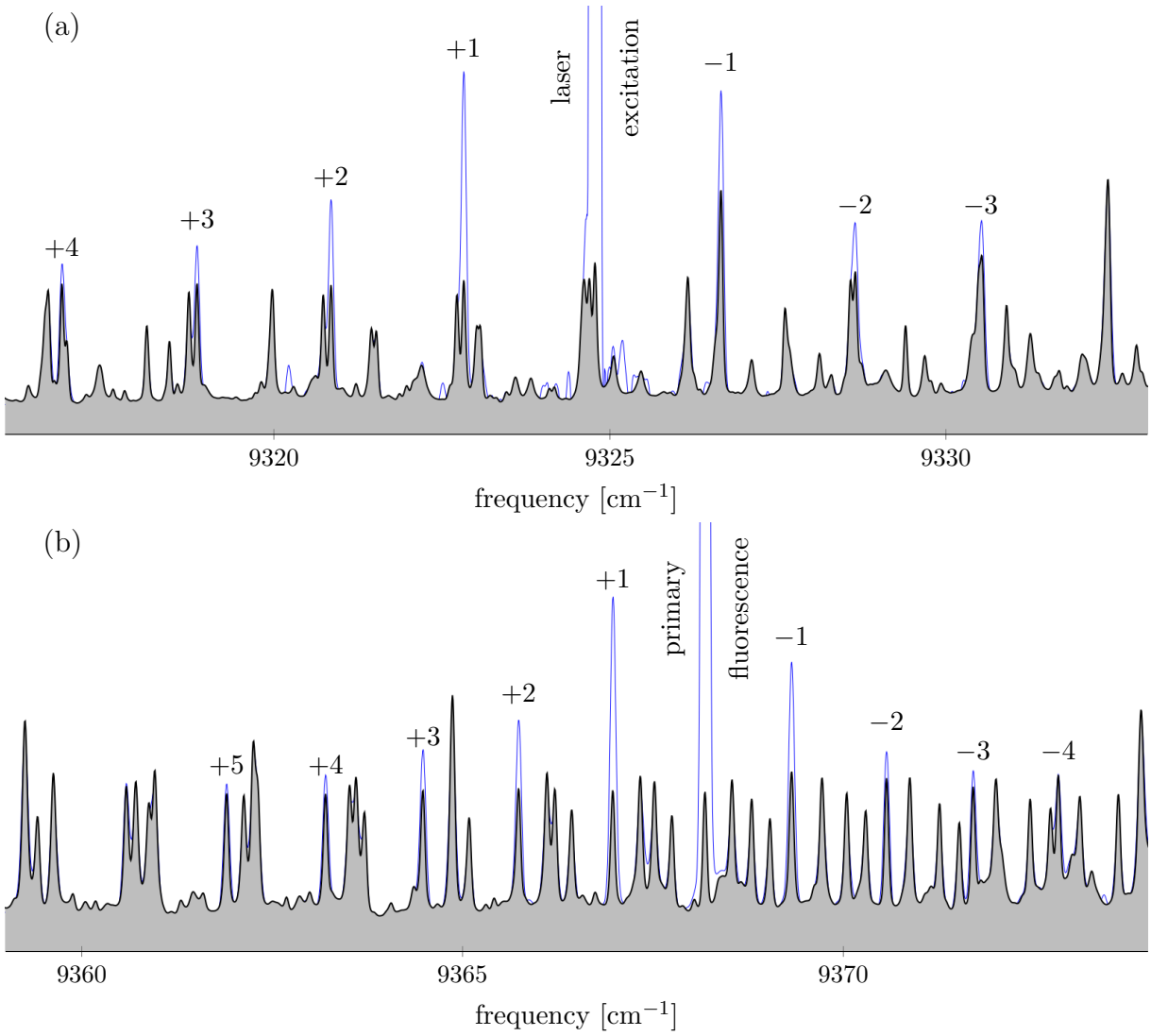

Figure 4.3: Example of a LIF spectrum (blue) featuring rotational satellites of the F_1 P 55 (a) and R 53 (b) lines in the (0–0) band. The thermal emission spectrum is displayed in black as a reference. N increases towards lower wavenumbers. The satellite lines are stronger than the thermal emission lines. There are also satellites in the (0–1) band but due to the lower overall intensity they cannot be tracked as far.

4.4.1 Determination of a First Approximation to the Rotational Constant

According to equation (1.4.4), the frequency difference Δf_{RP} between PR pairs that are known from fluorescence depends only on the rotational quantum number N' and the rotational constant B''_e in the lower electronic state. The relationship of N' and B''_e can then be parametrized for experimentally determined values of Δf_{RP}. Figure 4.4 illustrates these curves for all Δf_{RP} from the (0–0) excitations shown in Figure 4.2. Since the head is made up of several lines with consecutive N, the assumption can be made that they all share a very similar value for B''_e. This can be verified by looking for a linear factor for all observed Δf_{RP}; with the same B''_e, they should be linearly dependent on N'.

A further condition for the relation of Δf_{RP}, N' and B''_e is that N' is integer. Looking at Figure 4.4, it emerges that the only B''_e values for which all Δf_{RP} allow for integer N' are near $B''_e = 0.205\,\mathrm{cm}^{-1}$. This value is close to the rotational constant given in [Gop+13].

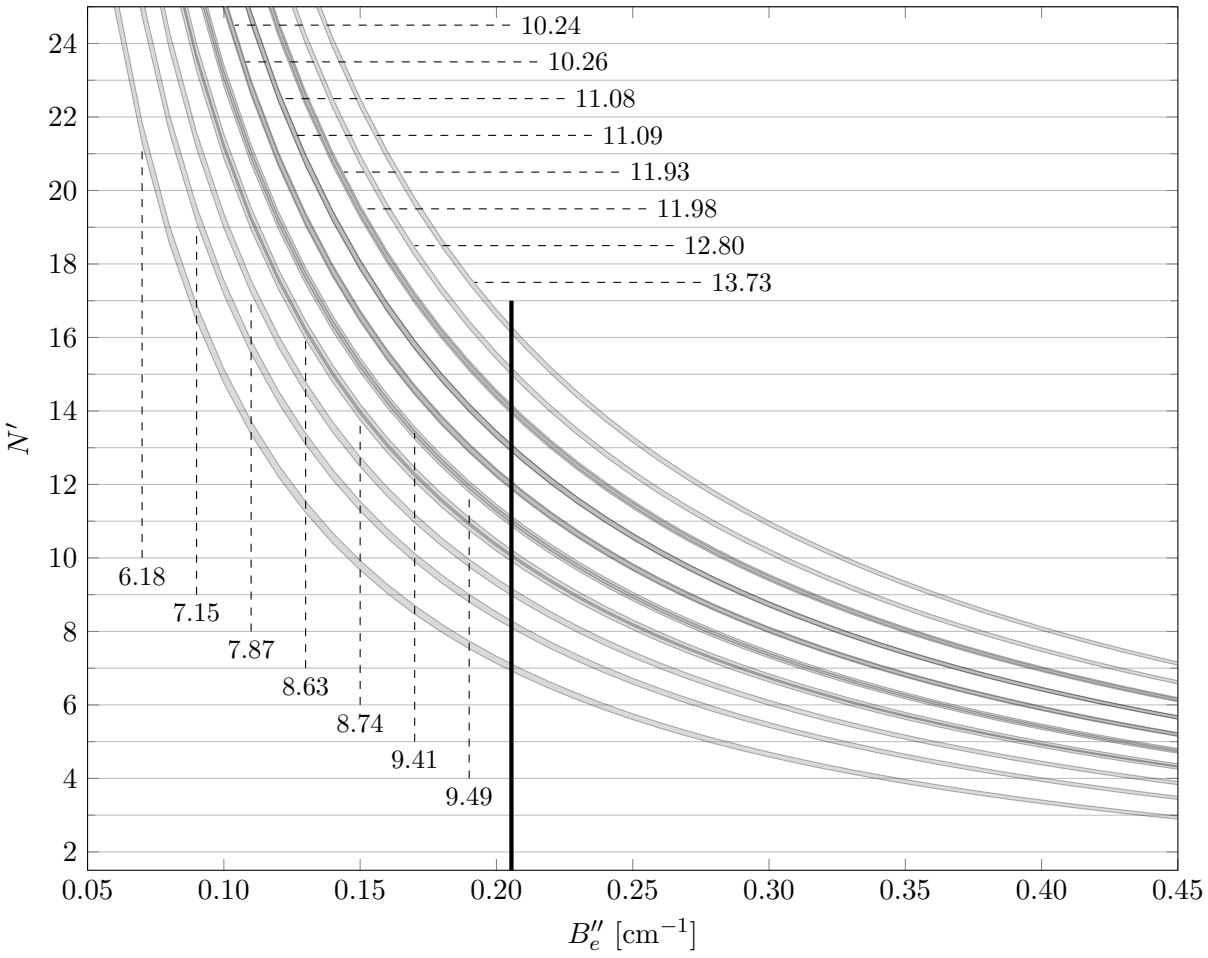

Figure 4.4: The relationship of N' and B_e'' for a given Δf_{RP} as given by equation (4.4.2). The grey curves represent $N'(B_e'')$ with different Δf_{RP} (in cm^{-1}), which were taken from Figure 4.2 (b). For the purpose of this graph, a global uncertainty of $0.04\,\mathrm{cm}^{-1}$ was assumed. Where two curves from the F_1 and F_2 systems overlap, they appear darker. Within the displayed B_e'' range, all curves intersect with integer values of N' only for values of B_e'' near the vertical black line. The exception is the line with $\Delta f_{\mathrm{RP}} \approx 7.15\,\mathrm{cm}^{-1}$ (the second curve from below). The uncertainty for that observation is in fact larger than $0.04\,\mathrm{cm}^{-1}$.

To formalize this graphical approach, equation (1.4.4) can be used to define a function $N'(\Delta f_{\mathrm{RP}}, B_e'')$ and the distance of the function value to the nearest integer is the quantity to be minimized. B_e'' can thus be narrowed down to the values for which the N' values for all plausible Δf_{RP} are closest to an integer. Mirroring a least squares fit, the expression

$$\chi^2_{N'} = \frac{1}{\#\mathrm{obs}} \sum_{i \,\in\, \mathrm{obs}} \left(\frac{N'_i(B_e'') - \mathcal{N}'_i(B_e'')}{(\delta f_{\mathrm{RP}})_i} \times 2(\delta f_{\mathrm{RP}})_{\mathrm{min}} \right)^2 \tag{4.4.1}$$

is used for this calculation, where $N'_i(B_e'')$ is obtained by rearranging equation (1.4.4):

$$N'(B_e'') = \frac{\Delta f_{\mathrm{RP}}}{4B_e''} - \frac{1}{2} \tag{4.4.2}$$

$\mathcal{N}'_i(B_e'')$ is the closest integer to $N'_i(B_e'')$ and $(\delta f_{\mathrm{RP}})_i$ is the experimental uncertainty of a measured PR distance, while #obs is the number of observations. The factor of two times the smallest uncertainty normalizes the expression.

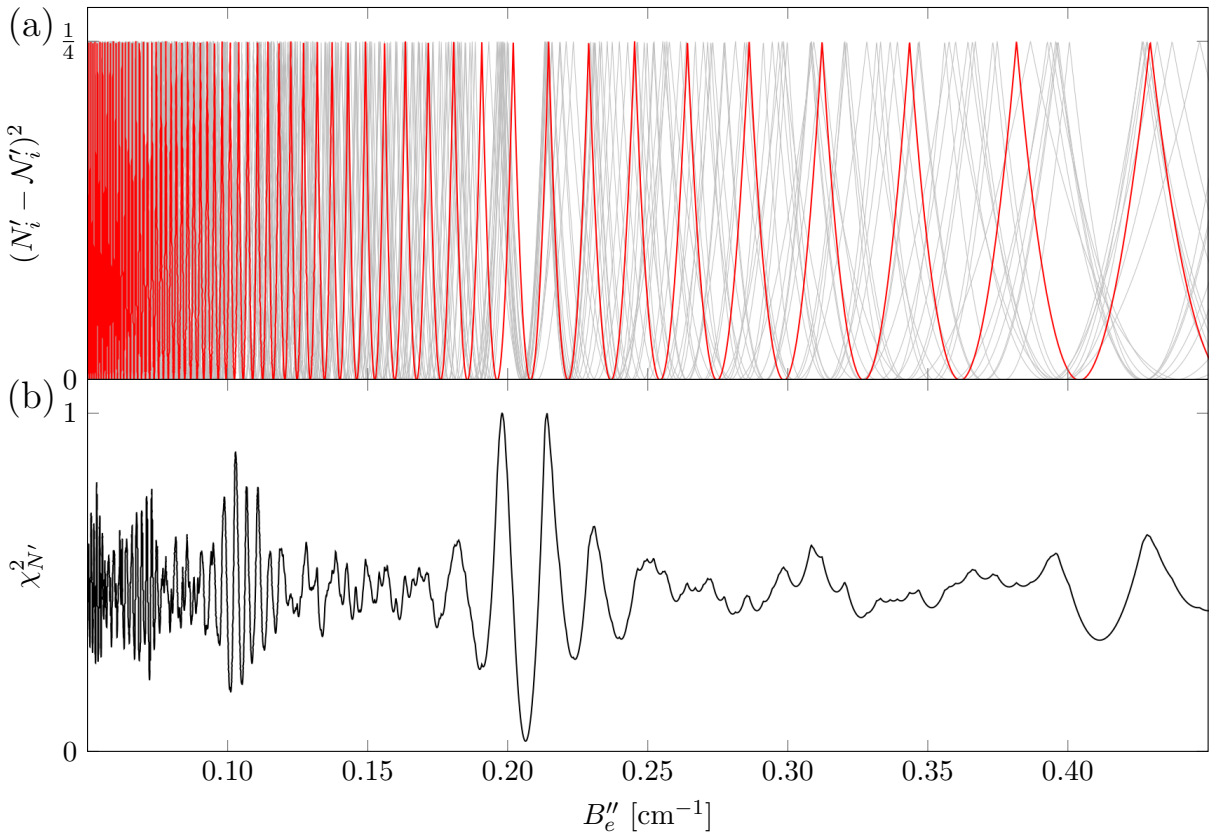

Figure 4.5: Plot of the function values given by expression (4.4.1) with the Δf_{RP} of (0–0) from Figure 4.2. The unweighted $(N_i' - \mathcal{N}_i')^2$ for each $(\Delta f_{\mathrm{RP}})_i$ are plotted in (a). One curve is highlighted in red so the parabola-like shape can be better seen. The sum $\chi^2_{N'}$ of the weighted data is drawn in (b) as a function of the rotational constant B_e''. The minimum of the curve indicates the best-fitting value of B_e''.

A visualization of this function is presented in Figure 4.5, again with the Δf_{RP} of the (0–0) band as seen in Figure 4.2. In Figure 4.5 (a), the squared distances from each calculated $N'(B_e'')$ to the nearest integer are plotted with equal weights. They describe parabolas centred around every integer when plotted over $1/B_e''$. A minimum for one $(\Delta f_{\mathrm{RP}})_i$ is not necessarily a minimum for other $(\Delta f_{\mathrm{RP}})_{j\neq i}$. Figure 4.5 (b) shows a plot of $\chi^2_{N'}$ for the 15 individual lines weighted with proper experimental uncertainties. Here, 'resonances' can be seen around $\frac{1}{2B_e''}$ and $\frac{1}{3B_e''}$ because for these values the first term of equation (4.4.2) gives almost a multiple of N' without the correction of $-1/2$. Each individual curve will therefore have a minimum close to these values but these minima do not exactly coincide.

Once B_e'' is determined, equation (4.4.2) can be used to assign reasonable N to the fluorescence lines. This information about the ground state together with the line frequencies yields B_e' in a straightforward fashion. This approach can be used to narrow down the possible values of the rotational constant of the ground states, though to what extend the constant can be identified depends on on the number of available Δf_{RP} and their uncertainty. Evaluating the expression (4.4.1) for a large range of N' can shift the obtained B_e'' due to centrifugal effects (and hence different rotational constants) for larger N. The choice of band head excitations is prudent because the head consists of transitions with consecutive N. This can easily be checked by verifying that the fluorescence in the other branch form the expected pattern of (quasi)equidistant peaks.

The method described here is of great help for molecular spectra in which the rotational transition lines are closer together so that a peak in the spectrum can consist of several lines. For such spectra, the approach described in Section 4.3.2 would be more error-prone and therefore time-consuming. As ab-initio calculations predict smaller rotational constants for most diatomic alkali-alkaline earth molecules than for LiSr, measuring the Δf_{RP} by laser excitation can be of great advantage. The advantages this LIF analysis have been demonstrated with KCa [Ger+17].

Chapter 5

Evaluation of the $(2)^2\Sigma^+$–$X(1)^2\Sigma^+$ Spectrum

With the general structure of the thermal emission and LIF spectra discussed, an attempt to find a rigorous description of the underlying molecular parameters of $^7Li^{88}Sr$ can be made. This chapter will describe how line frequencies determined with the methods described in Chapter 3 were used to find molecular parameters according to the Dunham model.

5.1 Dunham Fit

Each transition line represents an energy difference between two rovibrational levels, one in the $(2)^2\Sigma^+$ state and one in the $X(1)^2\Sigma^+$ state. The energies are approximated by equations (1.2.5) and the aim is to determine parameters Y_{mn} and γ_{mn} for both states that describe the observed lines.

In order to find these parameters, data sets with transition frequencies and quantum numbers are needed. Because only transitions of the $(2)^2\Sigma^+$–$X(1)^2\Sigma^+$ system are considered here, the parameters for the upper and lower rovibronic state in a transition belong to the $(2)^2\Sigma^+$ and $X(1)^2\Sigma^+$ states, respectively. Additionally, the LIF spectra can be used to incorporate information about only the ground state by including energy differences between the $X(1)^2\Sigma^+$ energy levels. In the latter case, the frequency difference between any two fluorescent lines with the same upper level and the quantum numbers of the two lower levels are needed. Frequency differences that incorporate the excitation frequency have generally a lower uncertainty because the laser frequency is measured with lower experimental uncertainty than the fluorescence lines. The required data are

$$\{f_0, \delta f_0, v', N', v'', N'', \mathrm{F}_i\}$$

and

$$\{\Delta f, \delta f, v_1'', N_1'', v_2'', N_2'', \mathrm{F}_i\},$$

with the frequency f_0 or frequency difference of two transition lines Δf, the frequency uncertainties δf_0 or δf, the rovibrational quantum numbers of the involved levels N and v and the index F_i, which assigns the observation to the F_1 or F_2 system.

With the frequencies and quantum numbers inserted into the energy expressions (1.2.5), all unknown parameters are factors with a linear dependence. This allows for a direct linear least squared fit to choose the appropriate molecular parameters of the infinite series in equations (1.2.5). The expansion given by equations (1.2.5) can have an unlimited number of terms in principle, but only a manageable number will be needed to describe the observed spectrum within the experimentally achievable accuracy.

5.1.1 Initial Dunham Fit

At first, only the rotational spectrum of the (0–0) band was taken into account for the fit. Because it has the highest intensity, the lines of the thermal emission spectrum can be distinguished here most clearly. Although there was also information about the (0–1) band available from LIF experiments, the approach taken was to first have a reliable understanding of the rotational branches of the (0–0) band and then to introduce corrective terms to allow for the slightly different (0–1) rotational spectrum. This approach also allows to reduce the number of fit parameters at the beginning by ignoring the vibrational dependence.

The fluorescence from the band head (see Figure 4.2) allowed to derive a value for Y''_{01} with the method described in Section 4.4.1. Rotational quantum numbers and spin states were assigned to the peaks using equation (4.4.2). This assignment immediately allowed to obtain values for Y'_{01}, γ'_{00} and Y'_{00}. In this preliminary model, the Y''_{00} and ground state vibrational parameters were set to zero, so that the energy of the $\left|X(1)^2\Sigma^+, v''=0, N''=0, F_1\right\rangle$ state was zero. The ground state energies are then only the rotational energies calculated with Y''_{01} and the three above-mentioned parameters for the upper state can be determined. The effect of the spin-rotation coupling could not be attributed to the upper or lower state with absolute certainty and so at first γ'_{00} was sufficient for the description of the lines. The effect could have equally been modelled with γ''_{00}.

These parameters were then used to predict further line frequencies in the rotational branches with quantum numbers N around the already known N numbers. Lines in the thermal emission spectrum close to these calculated frequencies were assigned the appropriate quantum numbers and with the the increased data set a new fit was performed. With the updated parameters from this fit, the added lines were checked for consistency. Usually, iteration steps of this extrapolation added about five lines in each spin system and branch. Further lines were predicted with the new parameters and new lines from the emission spectrum were assigned. Where the peaks in the thermal emission spectrum are sufficiently separated to regard them individually, this procedure yielded a large number of lines without considerable problems. Only near around the branch origin near the band head, where many lines overlap and lines with small N have low intensity (compare Figure 4.2) was the assignment more challenging. For molecules with denser spectra, more misattributions can be expected, so less new lines would be added in each iteration step.

Also, laser experiments were conducted at frequencies of arbitrarily chosen lines in the (0–0) band, further from the band head. If the assignment from the thermal emission spectrum advanced to a point where both lines from one LIF spectrum were included in the model, the fluorescence lines could be used to verify whether the assignment was consistent, i.e. if $N''_P - N''_R = 2$.

Other LIF spectra were used to accelerate the description of the (0–0) band. The known Y''_{01} parameter allowed to predict the rotational quantum numbers of the involved transitions via the observed Δf_{RP} and by assigning the lines temporarily to F_1 and F_2, it usually emerged which choice of F_i was in good agreement with the current parameters of the model. LIF spectra with transitions around $N = 55$ were used to make a leap from the lines near the band head with $N \leq 20$. The rotational branches are mostly clearly

visible in the thermal emission spectrum and the LIF spectra allowed to assign quantum numbers to random lines in these branches. When a line in a rotational branch could be identified via LIF spectra, more thermal emission lines close to the identified line were added to the data set with appropriate quantum numbers. After updating the Dunham parameters, this new range of rotational quantum numbers gave an additional starting point for characterizing the rotational spectrum.

5.1.2 Expanding the Dunham Fit

In the initial description of the (0–0) band, rotational transitions with N up to around 70 were assigned. To incorporate the centrifugal effects (see Section 1.1.3), Y_{02} was required for both electronic states. It was not necessary to include a rotational correction of γ. Later fluorescence experiments allowed to continue the description of the rotational spectrum beyond $N' = 100$ and Y_{04} was introduced during that phase.

With the P and R bands adequately characterized, the available LIF spectra were used to extend the model description from the (0–0) band to the (0–1) band. As described in Section 4.4, the rotational parameters of this band are slightly different from those of the (0–0) band. Accordingly, Y''_{11} was used in the model to allow for a vibrational dependence of the rotational constant and Y''_{10} was added to describe the vibrational energy. The thermal emission spectrum was used to assign lines around the laser-induced fluorescence lines in the (0–1) band. The process of adding emission lines was iterated as described for the (0–0) band.

With knowledge of the rotational branches of the first two vibrational levels of the ground state, new experiments were conducted with the laser tuned to frequencies of (1–0) lines. They produced fluorescence lines in the (1–0), (1–1) and (1–2) bands (see Figure 3.3 for an illustration). Similar experiments in the bands labeled (2–0) and (3–0) in Figure 4.1 yielded no perceptible fluorescence and were discontinued.

The known differences Δf_{RP} for $v'' = 0$ and $v'' = 1$, were used for the assignment of the rotational quantum numbers and spin states and more Dunham parameters were introduced. They include Y'_{10} and further corrective terms to describe the differences throughout the vibrational levels. Furthermore, γ was noticeably different in the (0–k) and (1–k) bands and for that reason, a vibrational dependence of γ, γ'_{10} , was added to the model. The spin-rotation parameters γ''_{00} and γ''_{10} needed to be introduced as well and were found to be uncorrelated to the spin-rotation constants used for the $(2)^2\Sigma^+$ state. The effect of γ is not noticeable in one Δf_{RP} observation, but due to the large number of Δf_{RP} included in the fit, an influence of the spin-rotation coupling in the $\mathrm{X}(1)^2\Sigma^+$ levels emerged.

5.2 Energy Level Coverage

The quantum number assignment of many lines from the thermal emission spectrum could be confirmed with LIF spectra. Figure 5.1 lists the energy levels that were addressed via laser experiments. This includes the excited transitions, fluorescence lines and rotational satellites. The ground state was fitted with only differences between such lines. All combinations of lines from a LIF spectrum were used to create difference data (see

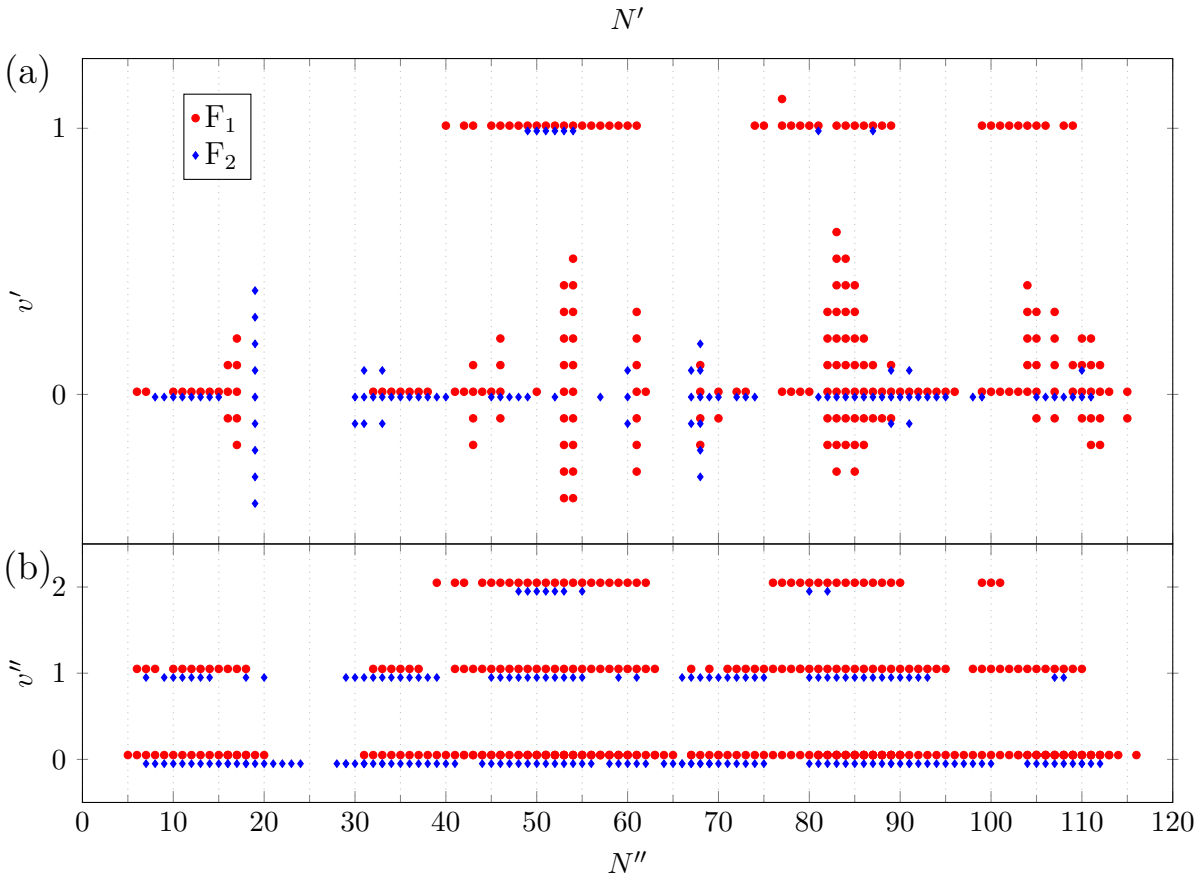

Figure 5.1: A list of all levels in the $(2)^2\Sigma^+$ state (a) and $X(1)^2\Sigma^+$ (b) states for which transitions were observed in a LIF spectrum. The F_1 and F_2 states are shifted vertically to make them all visible. For the excited states in (a), the observed rotational satellites are also listed along the vertical direction: for example, $\left|(2)^2\Sigma^+, v'=0, N'=43, F_1\right\rangle$ has one satellite point in the positive direction, so at least one transition from $|(2)^2\Sigma^+, v'=0, N'=44, F_1\rangle$ was observed in the P or R branches of the (0–0) and/or (0–1) band.

Section 5.4 below). An excitation in the (0–0) band with four relevant lines, one from each P and R branch of the (0–0) and (0–1) bands, would yield six frequency differences. They include differences Δf_{RP} for each vibrational band and the vibrational spacing of two rotational transitions in different bands and thus are distributed over a large energy range. The $v''=0$ rotational ladder is well covered with N'' ranging from almost zero to over 100. The $v''=1$ rotational ladder has more gaps, especially for low N'', and for the $v''=2$ level, a N'' range of about 60 was observed. The addressed levels with $v'=0,1$ have very similar N ranges due to the selection rule (1.3.7).

5.3 Deviations from the Dunham model in the $(2)^2\Sigma^+$ state

There are large ranges of N' for which the observed transition frequencies have considerable deviations from frequencies calculated with the Dunham model. They cannot reasonably be described by a large number of Dunham parameters. Transition lines with $v'=1, N'>70$ were not included in the fit of the $(2)^2\Sigma^+$ parameters, as will shortly be discussed. Figure 5.2 shows the difference of the observed and calculated frequencies for each assigned transition when plotted against N'. These deviations occur consistently in all bands with the same

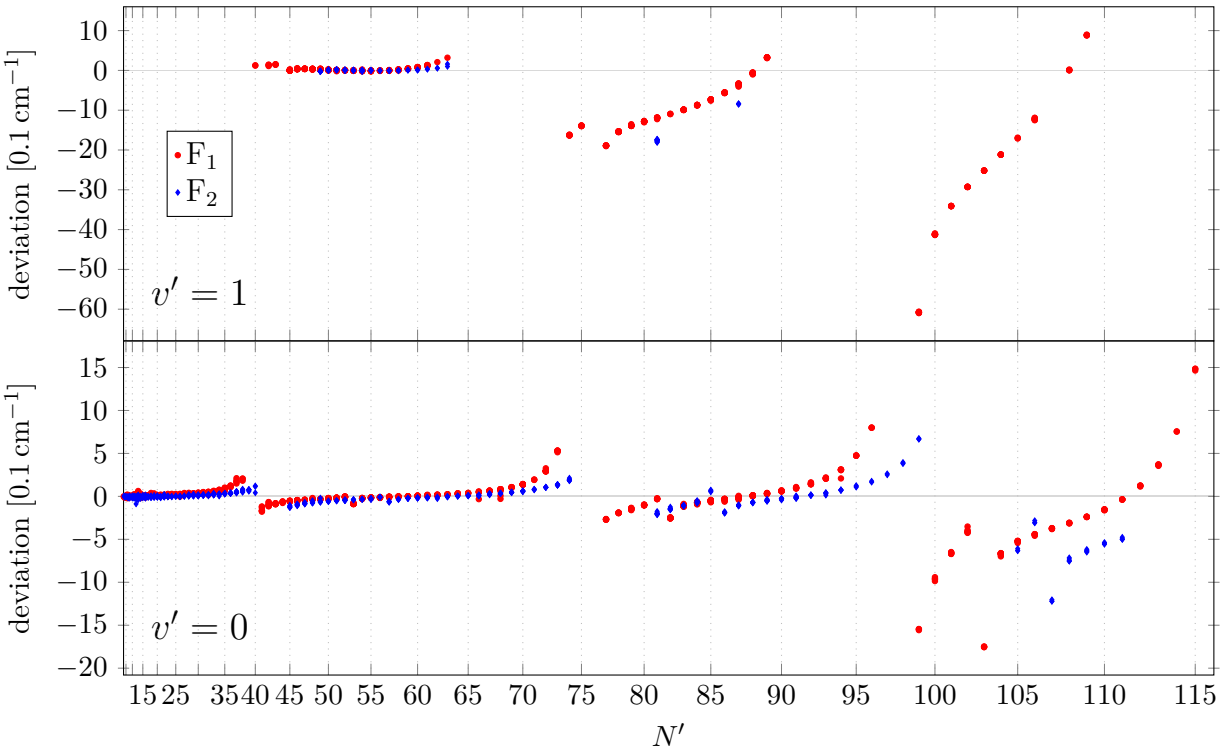

Figure 5.2: Deviations (observed frequency minus predicted frequency) from the Dunham model for transitions with $v' = 0$ and $v' = 1$. The thickness of the grey bar around zero represents an uncertainty interval of $0.02\,\mathrm{cm}^{-1}$. Large perturbations centre around different N' for F_1 and F_2. For the rotational levels with $v' = 1$, a trend to negative deviations is seen for $N' > 70$ because transitions with these N' were not be included in the Dunham fit.

quantum number v'. The upper part of Figure 5.2 shows transitions from the (1–0), (1–1) and (1–2) bands and the lower part transitions from the (0–0) and (0–1) bands.

The $v' = 0$ plot in Figure 5.2 suggests that the observed transition lines generally agree with the Dunham model up to $N' \approx 90$. The difference of the observed and modelled frequency of a transition is mostly within the uncertainty for the observed line. (The band head lines, around $N' = 12$, have a considerably higher experimental uncertainty as most lines because they cannot be disentangled.) There are, however, interruptions by several resonance-like shapes. These shapes will from here on be referred to as 'perturbations'. Likewise, the description of the $v' = 1$ bands is adequate for N' between 50 to 60. The perturbations also lack data points. There appears a larger disruption in the $v' = 1$ levels after $N' \approx 60$, which seems to resolve with even higher N'. This disruption is followed by an other perturbation. Beyond this perturbation, the Dunham model predicts higher transition frequencies in the $v' = 1$ bands than observed. According to the observed frequency differences from the LIF spectra, the electronic ground state is well described. Thus, the $(2)^2\Sigma^+$ energy levels are calculated higher by the model than observed.

The latter phenomenon can be explained because the deviant lines were not taken into account for the fit. Especially the N' between the two large perturbations around $N' = 70$ and $N' = 90$ with $v' = 1$ could not be considered to be undisrupted. Without data for the upper electronic level for this range of N', the Dunham parameters could not be adapted and the extrapolation from the available N' range proved to be insufficient to describe the high N' of the $v' = 1$ ladder. Table 5.1 lists the N' that were excluded from the Dunham

fit.

Table 5.1: Ranges of rotational quantum numbers N' that were excluded in the Dunham fit due to being perturbed. Quantum numbers in parentheses lie within sharp perturbations, the other in extended perturbations. The range of all observed N' is given for reference. Note that for F_2, the lowest assigned rotational level in $v' = 1$ has $N' = 49$ and its transitions appear not to be perturbed.

$v' = 1$	F_1	observed			40-63		74-89	99-109
		perturbed		40-48			59-109 (77)	
	F_2	observed			49-63		81,87	
		perturbed					61-87	
$v' = 0$	F_1	observed	0-38		41-73		77-96 (81,82)	99-115
		perturbed		28-50	(53)		68-84 (82)	91-115 (102-103)
	F_2	observed	2-40		45-74		81-99	105-111
		perturbed		30-51	(53-55)			94-111 (106-108)

5.3.1 Regularities of the Deviations

Following the rotational branches of the (0–0) band from low N' at $N' \approx 30$ and from high N' at $N' \approx 50$[a] towards $N' = 40$, the distance between neighbouring lines decreased in a regular fashion when approaching $N' = 40$, in contrast to the behaviour predicted by equations (1.4.2). This observation can be visualized with the lower left part of Figure 5.2. The observed transition frequencies are higher than calculated with the Dunham parameters for $N' \approx 30$ towards 40 and similarly are lower than calculated for $N' \approx 50$ towards 40.

Furthermore, the intensity of emission lines drops considerably with proximity to the centre of a perturbation. Some lines could not be found and identified in the thermal emission spectrum and there are gaps in the data set for the perturbed regions (see Figure 5.2). Figure 5.3 compares the intensity distribution of thermal emission lines from the (0–0) and (1–0) bands with the distribution calculated with equation (1.4.5). (The latter distribution is a good first-order approximation for the intensity of a rotational transition line and an average for P and R lines, as discussed in [Her50, pp. 124]) The fitted line amplitude A from equation (3.1.2) was used for the intensity. Because of this choice, intensities in Figure 5.3 tend to be overvalued for lines that could not be fitted alone. Especially lines with low N' near the (0–0) band head have too high intensity values. Nevertheless, a systematic loss of intensity can be detected in the perturbed regions, as seen in Figure 5.2.

The next perturbation of the (0–0) branches sets in at $N' \approx 68$. By tentatively extrapolating from the Dunham parameters known at that point and taking into account the systematic deviations from equations (1.4.2), the beginning of this perturbation could be mapped. Due to the decreasing intensity and stronger shift in frequency, line assignment could not be continued beyond $N' \approx 70$ without further laser experiments.

All these observations appear also in the (0–1) band; lines with a given N' deviate in the same manner as (0–0) lines with the same N'.

[a] The deviations occur at slightly different N' for the F_1 and F_2 systems.

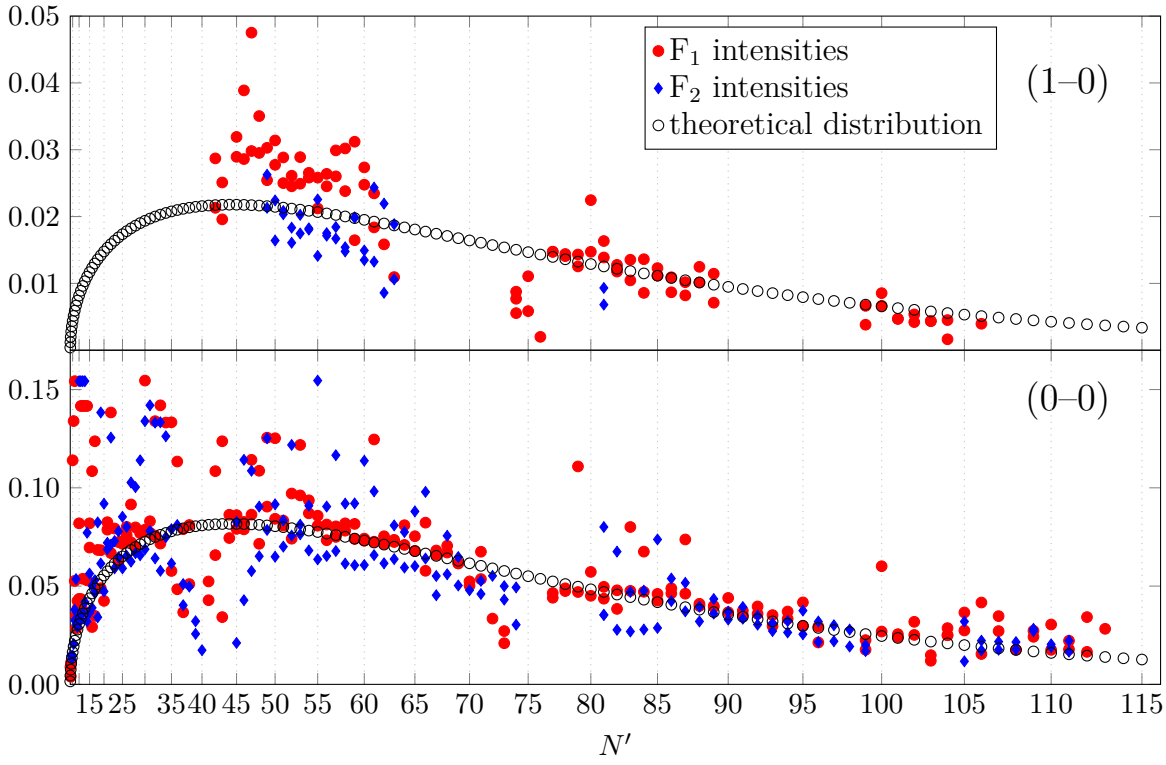

Figure 5.3: Intensities of thermal emission lines in the (0–0) and (1–0) bands compared with an ideal intensity distribution calculated with Y''_{01} (see text). Interruptions can be seen at the positions of perturbations, as seen in Figure 5.2. Line intensities can be exaggerated for lines that are superimposed with others. For high N', the (1–0) lines do not follow the calculated distribution as well as the (0–0) lines, as the calculation was done without vibrational corrections.

A similar behaviour was noticed in the (1–0) band: in this band, the starting point from LIF spectra was in the range of $N' = 50$ to 60. Proceeding to assign lines according to the Dunham model was straightforward until perturbations were encountered. This was mirrored in the other $v' = 1$ bands.

These observations lead to the conclusion that the energy levels in the $(2)^2\Sigma^+$ state are perturbed. Figure 5.2 shows the deviations plotted against $N'(N'+1)$, which gives the energy scale to first order. The perturbations appear to be evenly spaced in energy. This hints at only one perturbing electronic state whose levels regularly cross those of the $(2)^2\Sigma^+$ state.

5.3.2 Utilizing Fluorescence Experiments

The perturbations presented a substantial obstacle in the survey of the rovibrational spectrum. The combination of shifted transition frequencies and decreasing intensity made assigning the rotational lines in the thermal emission spectrum error-prone. Due to the amount of affected N', a large extrapolation step is necessary to identify lines further up the branches that seem to follow a regular pattern again. This requires a time-consuming trial-and-error approach. Furthermore, weak lines within the perturbed region can easily be mistaken for lines from other, less intense vibrational bands or from the other spin system. A misassignment would lead to a slightly shifted data point in the perturbed plot presented in Figure 5.2, the authenticity of which cannot be tested. Weak lines

that coincide with other lines can also easily elude the analyst. All of this leads to large information gaps for the perturbed regions.

In such a situation, much can be gained from LIF experiments. Since the perturbations appear to take place in the upper electronic state, the Δf_{RP} are presumably unaffected. This was utilized in two ways:
First, by looking over the thermal emission spectrum, unperturbed sequences of lines were identified by checking the intensity and spacing of the peaks. In the (0–0) band, such lines were found beyond the second large perturbation with $N' \approx 85$. Laser excitations of some of those peaks allowed to estimate the rotational quantum numbers from the known rotational constant B''_v. These new data led to improved Dunham coefficients that allowed to assign lines from the emission spectrum near the excited lines, as described in Section 5.1. With this knowledge, the second perturbation could be mapped from the other side (i.e. $N' \approx 85$ towards 75) and a new perturbation, starting at $N' \approx 90$ was encountered. This improved model describes the $v' = 0$ levels in Figure 5.2 relatively well up to $N' \approx 90$. In the (1–0) band, the same approach failed. Outside the already known part of the spectrum, no sufficiently regular patterns were found and experiments at lines with high intensity or the band head yielded no noticeable fluorescence. Also, excitations in the band head did not lead to the observation of fluorescence.

The second use of the laser experiments is the assignment of perturbed lines. By systematically addressing unknown lines in perturbed parts of a rotational branch and searching for induced fluorescence in the corresponding branch, rotational quantum numbers could be assigned to both lines simultaneously by comparing their Δf_{RP} with a calculated one. This allowed narrowing the data gap near the centre of perturbations considerably.

Because fluorescence lines also occur in other bands with the same v', several otherwise non-assignable spectral lines could be assigned at once. In accordance with the emission spectrum, the fluorescence lines get weaker, the more a line is perturbed. Occasionally it turned out that a missing line is obscured by another line from a different rotational branch or vibrational band, which would not have been noticed without the fluorescence analysis. However, for strongly perturbed lines (which are very weak and have an at that time unpredictable frequency shift), no line to excite could be found and for some very weak lines, no fluorescence was seen in the other branch of the same band.

Since the perturbations occur in the $(2)^2\Sigma^+$ state, these LIF spectra could also be used for fitting the parameters of the electronic ground state. The large deviations near the right side of Figure 5.2 represent only the deviation in the upper state, while the Dunham model for the ground state agrees well with measured frequency differences.

By cataloguing lines with N' up to about 100 in the $v' = 0$ band and $N' \approx 40$ to 65 in the $v' = 1$ bands, most of the strong lines in the spectrum from $9090\,\mathrm{cm}^{-1}$ to $9570\,\mathrm{cm}^{-1}$ were assigned. At this point, there was a number of yet unassigned lines between $9260\,\mathrm{cm}^{-1}$ to $9300\,\mathrm{cm}^{-1}$ with moderate intensity. These seemed to be either a continuation of the (0–0) band beyond the perturbation at $N' \approx 97$ or a continuation of the (1–1) band beyond the perturbation at $N' \approx 70$. Their weak intensity is consistent with that of the high N' for the (0–0) band (compare Figure 5.3) and the general intensity of the (1–1) band.

A thorough survey of the peaks in question using laser experiments yielded lines from both of these vibrational bands (with LIF lines also in other bands). They make up the

data points with $N' > 70$ in the upper part of Figure 5.2, and most of the data with $N' > 100$ in the lower part.

The deviations of these data in Figure 5.2 suggests that none of their $(2)^2\Sigma^+$ levels can be assumed to be unperturbed. Thus, they were only used to fit $X(1)^2\Sigma^+$ Dunham parameters.

5.3.3 Irregularities of the Deviations

The perturbations depicted in Figure 5.2 introduce a seemingly systematic frequency shift of the transition lines when compared with a Dunham description and get stronger for higher N', as can seen by their amplitude (magnitude of deviation) and the size of the data gaps. The next two chapters will discuss them in detail.

Apart from these observations, there are other peculiarities not so obvious from Figure 5.2. There exist smaller, more local perturbations, spanning 2 or 3 N'. This can be seen best in the $v' = 0$ part around $N' = 82$ for F_1 and $N' = 85$ for F_2. Smaller perturbations are near $N' = 55$. There are similar disruptions around $N' = 103$ for F_1 and $N' = 107$ for F_2 and around $N' = 76$ in the upper part of the figure. These latter observations have to be regarded with care, however, due to the large disruption of the plot by the neighbouring large perturbations. These local, sharp perturbations appear to follow the larger perturbations with an equidistant offset in the energy scale and their amplitude seems to correlate with the amplitude of the larger perturbations.

A curious finding was that those LIF spectra for which lines affected by the small perturbations were excited have a higher amount of rotational satellite lines than other LIF spectra (see Figure 5.1). One fluorescence line with a quantum number N' could have satellites with up to $N' \pm 5$ for these lines. Others have usually $N' \pm 1$ or $N' \pm 2$ while most LIF spectra showed no rotational satellites. This might hint at a different scattering behaviour of the $(2)^2\Sigma^+$ states near the sharp perturbations. However, this is based on a small data set and could be merely coincidental.

A further notable oddity is the discrepancy in the number of F_1 and F_2 observations. The majority of laser experiments led to an assignment of an F_1 transition. Most experiments were conducted to map the perturbed regions of the spectrum and hence this disparity is more apparent there: when comparing the gaps in the perturbations in the F_1 and F_2 systems in Figure 5.2, the F_2 gaps are noticeable larger. No lines could be found in the thermal emission spectrum that would make good candidates for the missing F_2 lines. This would imply that perturbed F_2 transitions are generally weaker that perturbed F_1 transitions and that the F_2 system is more affected by the perturbation.

For two large spectral ranges, there were almost only F_1 transitions assigned: the regions with N' between about 74 to 89 and 99 to 106 in the $v' = 1$ bands. The first range of N' has two pairs of laser experiments that yielded the same Δf_{RP} for two different excitation frequencies. These double observations of the same Δf_{RP} led to the conclusion that the excited line that is higher in frequency belongs to F_1 and the other to F_2[b].

The group of lines with $N' > 98$ and $v' = 1$ turned out to be only one spin system and the Δf_{RP} gave a consecutive series of N'. The choice of F_1 was taken here because the

[b] This convention was established in Section 4.3.1.

deviation of this group is consistent with the trend towards larger negative deviations of the aforementioned group (compare Figure 5.2). An assignment of F_2 would shift these data towards positive deviations by around $3.5\,\mathrm{cm}^{-1}$, centred around a deviation of zero. This is a possible scenario, but it would imply a more complex deviation pattern of the $v' = 1$ rotational energies.

Due to the encountered perturbations, the Dunham model proved to be insufficient for faithfully describing the $(2)^2\Sigma^+$ state and therefore the observed emission spectrum.

5.4 Fit of the Electronic Ground State

Since the deviations described in the previous section all originate from the $(2)^2\Sigma^+$ state, the $X(1)^2\Sigma^+$ state can still be described with the Dunham series. Using the LIF spectra, the frequency difference between transition lines with the same upper state describe energy differences of rovibrational levels in the electronic ground state. For example, from the six identified lines seen in Figure 3.3 the rotational constants B_0, B_1 and B_2 can be found from the three PR pairs and the vibrational energy spacing can be obtained from the frequency difference of the three P or the three R lines. For a Dunham fit of the ground state alone, only frequency differences Δf between lines with a common upper state were used. The six exemplary lines in Figure 3.3 yield $(6-1)\cdot 6/2 = 15$ frequency differences. All of them contain information of the rotational or vibrational spacing of the involved $X(1)^2\Sigma^+$ levels or a linear combination thereof.

Since the laser frequency could be measured with more accuracy by the wavemeter than the lines observed with the FTS, all Δf data were recorded using the laser frequency as reference. Most laser experiments were conducted in the (0–0) or (0–1) bands, however, and confining the data to frequency pairs containing a laser line would put a disproportionate weight on the energy distances to the $v'' = 0$ and $v'' = 1$ levels. To compensate this weighting (and because the uncertainty advantage from using only laser line frequency pairs is minor), a data set was created from the LIF spectra that contained all differences of the observed frequencies of each LIF spectrum. In order to completely eliminate any $(2)^2\Sigma^+$ information, no frequency differences including fluorescence of rotational satellites (with would mean different N') were used in this data set because they contain information about the energy splitting in the upper electronic state. The result of the linear fit is presented in Table 5.2.

Table 5.2: Dunham and spin-rotation parameters for the $X(1)^2\Sigma^+$ state of $^7Li^{88}Sr$ in Hund's case (b). The parameters allow an accurate description for levels with $N'' < 116$ for $v'' = 0, 1$ and $35 \le N'' \le 100$ for $v'' = 2$. All values are given in cm^{-1}.

Y_{0n}	Y_{1n}	Y_{2n}	γ_{0n}	γ_{1n}	n
0	$1.830781(39) \times 10^2$	$-3.1018(17) \times 10^0$	$8.18(37) \times 10^{-3}$	$-5.04(11) \times 10^{-4}$	0
$2.074024(45) \times 10^{-1}$	$-3.4164(18) \times 10^{-3}$	$-5.724(78) \times 10^{-5}$	-	-	1
$-1.08317(50) \times 10^{-6}$	$-3.540(19) \times 10^{-8}$	$-6.628(71) \times 10^{-9}$	-	-	2
-	-	-	-	-	3
$-2.309(15) \times 10^{-16}$	$-1.1953(51) \times 10^{-16}$	-	-	-	4

To correctly model the energy differences of transitions with $N' \gtrsim 100$, Dunham parameters up to $m = 2$ and $n = 4$ were necessary. Certain fit parameters were systematically

excluded while fitting the same data set to find the minimal necessary number of parameters that describe the observed frequency differences. It became apparent that the Y_{m3} parameters could be omitted, and that the Y_{m4} parameters sufficed to describe levels with high and intermediate N.

The rotational parameters Y_{01}, Y_{02} and Y_{04} are highly correlated with each other. The vibrational parameters Y_{10} and Y_{20} are also correlated. Several, but not all, of the mixed parameters have a relatively high correlation with one or more of the vibrational parameters, but only a small correlation with the rotational parameters. While the experimental uncertainty was too high to resolve the spin-rotation splitting given by equation (1.1.3) with the measured frequency differences, the large number of observations gave rise to a distinction between F_1 and F_2 lines, so that both γ_{00} and γ_{10} were required to find a satisfying description. These two spin-rotation parameters do not show correlation with each other nor with the Dunham parameters.

The uncertainties given in Table 5.2 are taken from the linear fit of the Dunham parameters. A total of 1657 frequency differences were fitted, giving one weighted standard deviation of $\overline{\sigma} = 0.25$. The maximum relative deviation of a difference (i.e. $(\Delta f_{\mathrm{obs}} - \Delta f_{\mathrm{calc}})/\delta f$) is 2, while 99.64 % of observations have a value of 1 or lower, which means that they are well described within their given uncertainty.

For a set of independent data points with appropriate uncertainties, the value of $\overline{\sigma}$ should be close to 1. Therefore, the assumption of either the independence of the data or the estimation of the uncertainties does not hold. The uncertainties were estimated with at least $0.02\,\mathrm{cm}^{-1}$[c], according to the Doppler width as discussed in Section 3.2.2 and given in Figure 3.5. However, a LIF spectrum with n lines ($n-1$ fluorescence lines and one laser line) for an upper state $|v', (2)^2\Sigma^+, N', \mathrm{F}_i\rangle$ gives $(n-1)\cdot n/2$ line pairs for the fit of the ground state. These will have different combinations of rotational and vibrational energy spacings, which means that they are not all independent of each other. To compensate the effect of the interdependent data, their uncertainties could be adjusted until their average increase in uncertainty gives a more reasonable value for $\overline{\sigma}$ and thus more realistic uncertainties of the fitted parameters, which can be expected to be about four times higher on average.

Adapted uncertainty values would give the same minimum in the parameter space of the fit and therefore the same results. The parameters found with the fit would only change if the uncertainty distribution of the data points would be changed by assuming other lower bounds for the uncertainties of the data. The data set contains indeed individual frequency difference data with a higher uncertainty than the stated lower bounds. This is due to the fact that especially weak laser-induced fluorescence lines have a higher frequency uncertainty. The majority of data have, however, an uncertainty of the lower bounds given here (see Figure 3.5 (b)) and the uncertainty distribution, and therefore the fit results, would be very similar with an other lower bound for the uncertainties.

[c] For frequency differences, $0.04\,\mathrm{cm}^{-1}$ were assumed. This is a very cautios estimation since the uncertainty for the difference of two independently measured frequencies can be assumed to be $\sqrt{2}\cdot 0.02\,\mathrm{cm}^{-1} \approx 0.028\,\mathrm{cm}^{-1}$.

Chapter 6

Coupling of Electronic States

The description of the LiSr spectrum with the Dunham model is only adequate for the $X(1)^2\Sigma^+$ state. The $(2)^2\Sigma^+$ state features systematic deviations from the Dunham model, as described in Section 5.3. These deviations assume a shape well known from the simple model of two coupled quantum states: when the matrix representation of a two-state Hamiltonian has an off-diagonal element d, i.e. when two states $|\psi_1\rangle$ and $|\psi_2\rangle$ are coupled by an interaction of strength d, the eigenstates of the system, $|\psi_+\rangle$ and $|\psi_-\rangle$, will have an energy difference of at least $2d$. The deviation of $|\psi_\pm\rangle$ from $|\psi_i\rangle$ is largest when the uncoupled states $|\psi_i\rangle$ grow close in energy. This is illustrated in Figure 6.1. Assuming

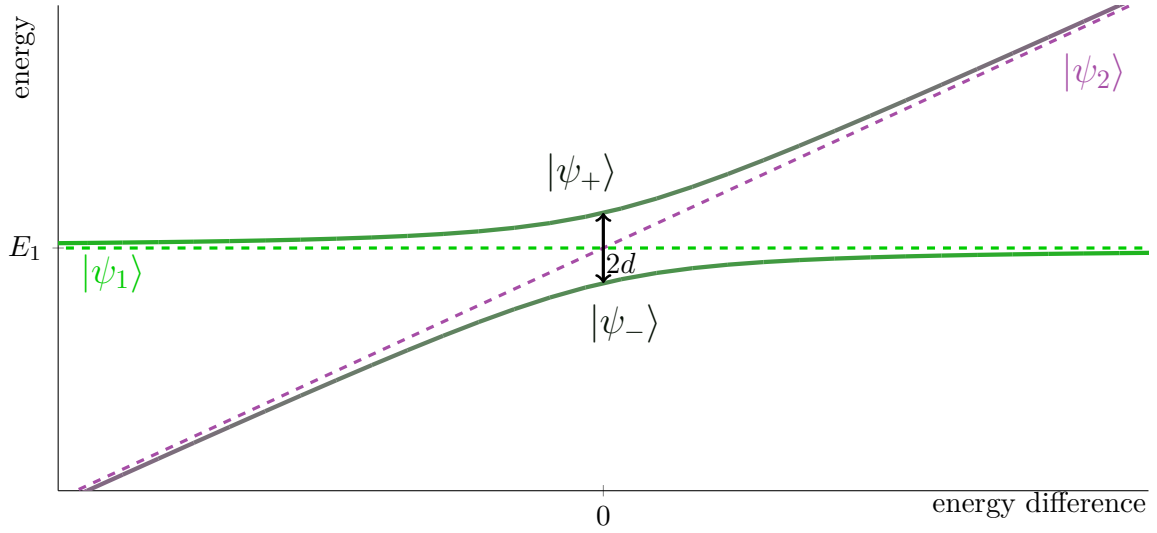

Figure 6.1: Avoided crossing of two coupled states $|\psi_1\rangle$ and $|\psi_2\rangle$ (dashed lines). The eigenstates are $|\psi_+\rangle$ and $|\psi_-\rangle$ (solid lines), with changing amplitudes of $|\psi_1\rangle$ and $|\psi_2\rangle$.

$|\psi_1\rangle$ to represent the rotational states of $(2)^2\Sigma^+$, the observed systematic perturbations in Figure 5.2 can be explained with another state that couples to $(2)^2\Sigma^+$. The positions and shapes of the (avoided) crossings are determined by the difference of the rotational constants of the two electronic states. The other state crosses from below (as $|\psi_2\rangle$ in Figure 6.1) if its rotational constant is larger than that of the $(2)^2\Sigma^+$ state. The perturbations would centre around the crossing points of the uncoupled states. Furthermore, the contribution of different electronic states to the resulting eigenstates could explain the intensity drop in the spectrum. Such a drop would occur if the state that mixes with the $(2)^2\Sigma^+$ state would have a lower transition probability to in $X(1)^2\Sigma^+$ than $(2)^2\Sigma^+$ has.

According to the ab-initio calculations (see Figure 1.1), the only state that is energetically close to the $v' = 0, 1$ levels in the $(2)^2\Sigma^+$ state around $10000\,\mathrm{cm}^{-1}$ is the $(1)^2\Pi$ state with moderately high vibrational levels v_Π. The two theoretical papers [Gop+13; Pot+17] report a small transition dipole moment for $(1)^2\Pi$–$X(1)^2\Sigma^+$. Furthermore, [Pot+17] predicts a

low transition probability for such high v_Π and low v'' levels in the X$(1)^2\Sigma^+$ state.

Figure 6.2 demonstrates how the form of a deviation plot, like in Figure 5.2, changes when a simple coupling, as in Figure 6.1, is not modelled correctly. The plotted points in Figure 6.2 represent the deviations of the observed $(2)^2\Sigma^+$ ($\widehat{=}\,|\psi_1\rangle$) levels from the eigenenergies of the coupled states with the larger $(2)^2\Sigma^+$contribution. The analogous data points corresponding to $(1)^2\Pi$ ($=|\psi_2\rangle$) deviations are not plotted because the $(1)^2\Pi$ state could not be observed. Note that the label of $(2)^2\Sigma^+$switches from the higher to the lower eigenenergies after the avoided crossing. Figure 6.2 (a) displays the deviation when no coupling is taken into account. The curve looks like the $|\psi_+\rangle$ curve to the left, and the $|\psi_-\rangle$ curve to the right of the crossing point in Figure 6.1. Figure 6.2 (b) illustrates how the form of the plot is changed when the coupled system is modelled incorrectly. The relative slope, i.e. the difference of the slope of $|\psi_1\rangle$ and $|\psi_2\rangle$ in Figure 6.1, of the coupling partner $|(1)^2\Pi\rangle$ ($\widehat{=}\,|\psi_2\rangle$) is different in each column and the crossing point of the energy levels is further shifted to the right in each row. The data is given for different assumed coupling strengths d'. The modelled deviation generally changes sign or is overcompensated when the coupling is assumed too strong. Note that the greatest differences between the graphs are near the singularity. Because of this, recognizing if and how exactly the crossing levels are modelled incorrectly is not possible when no data is available in this region.

Since a coupling between the $(2)^2\Sigma^+$ and $(1)^2\Pi$ states is the most likely explanation for the perturbations, this chapter will formulate the general coupling scheme between $^2\Pi$ and $^2\Sigma^+$ states. It is oriented on [LF86], where some of the required matrix elements are explicitly given.

The Hamiltonian of the coupled system consists of the parts

$$\hat{H}^{\text{coupl}} = \hat{H}^{\text{el}} + \hat{H}^{\text{vib}} + \hat{H}^{\text{rot}} + \hat{H}^{\text{SO}} + \hat{H}^{\text{SR}}. \tag{6.0.1}$$

The electronic part $\hat{H}^{\text{el}}$ of the Hamiltonian contributes the appropriate electronic energy T_e and the potential energy curves (see Section 1.1.1). The vibrational part $\hat{H}^{\text{vib}}$ describes the vibration of the nuclei, with the vibrational energy as discussed in Section 1.1.2. They are included in the Dunham energies as defined in equation (6.4.4) and will not be discussed separately in this chapter. The other terms represent the nuclear rotation ($\hat{H}^{\text{rot}}$), spin-orbit coupling ($\hat{H}^{\text{SO}}$) and spin-rotation coupling ($\hat{H}^{\text{SR}}$). They will be examined and evaluated separately.

The matrix elements of the operators between the electronic and rotational wave functions can be written as a product of $\alpha^{\Lambda' S' \Sigma'}_{\Lambda\ S\ \Sigma}(R)$, which depends on the internuclear distance R, and a function $f(J, S, \Sigma, \Lambda, \Omega)$ of only the angular momenta. The different rotational quantum numbers were explained in Section 1.1. The matrix elements of the different operators $\hat{H}^i$ are then a product of the form $\alpha^{\Lambda' S' \Sigma'}_{\Lambda\ S\ \Sigma}(R) \times f(J, S, \Sigma, \Lambda, \Omega)$. In the simplest case, $\alpha^{\Lambda' S' \Sigma'}_{\Lambda\ S\ \Sigma}(R)$ is given by the overlap integral of two vibrational states multiplied by the appropriate interaction strength of the electronic states under discussion. In contrast to the Franck-Condon factors introduced in Section 1.3, the overlap integral can also be negative.

The Hamiltonians will be given in units of wavenumbers, with the understanding that all obtained values need to be multiplied by hc to convert them to a dimension of energy.

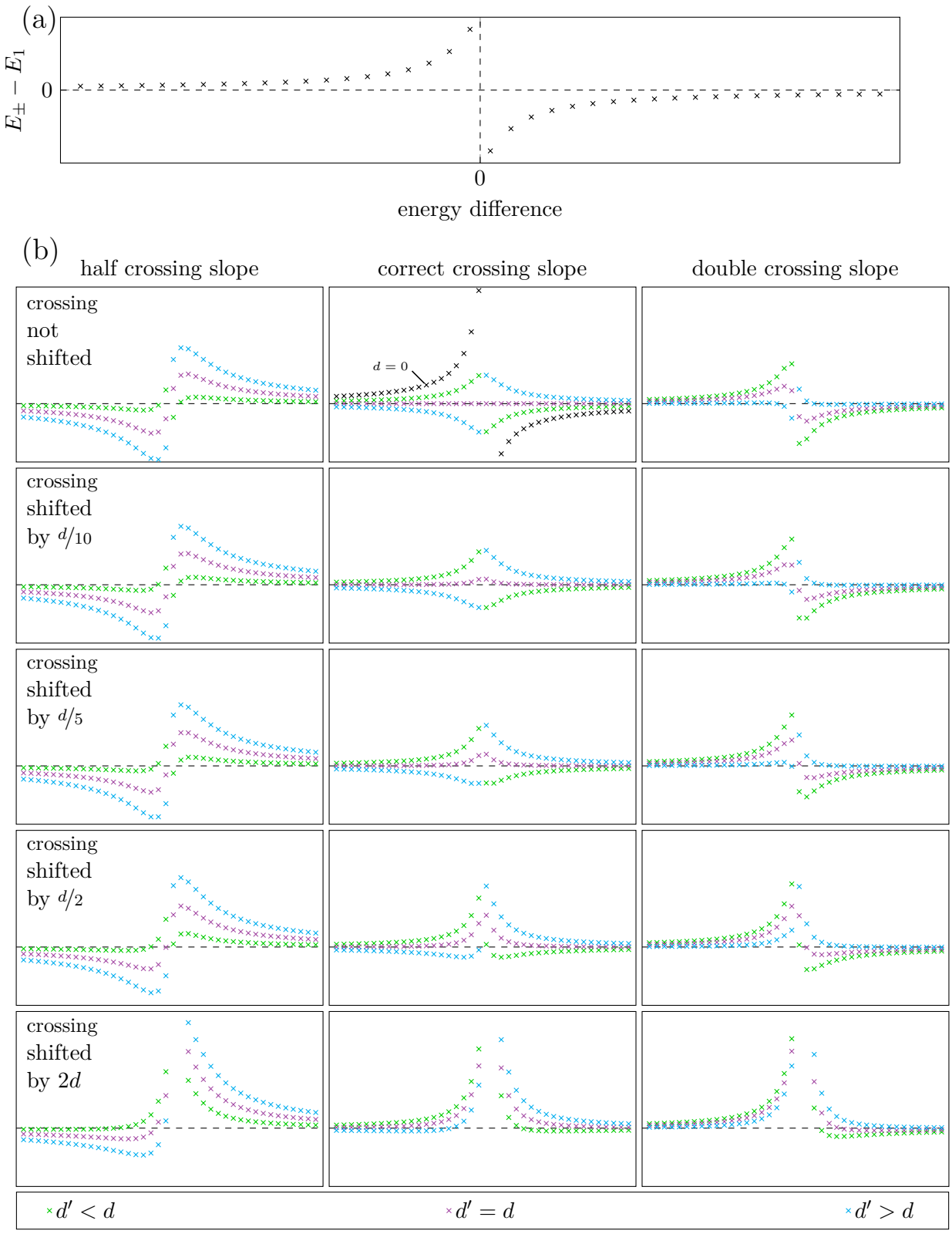

Figure 6.2: A deviation plot for one visible state $|\psi_1\rangle$ of a coupled system is strongly dependent on assumptions about the second, invisible state $|\psi_2\rangle$. (a) $E_\pm - E_1$ for states as in Figure 6.1. (b) The difference between the modelled and the correct deviation (coloured points) changes when an erroneous model is applied. Each column shows the effects on a different assumed slope for $|\psi_2\rangle$ (too low, correct, too high); the rows show the effect of shifting the assumed crossing point (correctly modelled in the first row, then with growing deviation to the correct one). The deviations are plotted for the assumed coupling strength d' set lower (green), equal to (violet) and higher (blue) than the correct strength d. The vertical scale of the graphs in (b) is different than that of (a) to better illustrate the different cases. The first graph in the middle row additionally displays the plot of (a) again for reference. All graphs in (b) have the same scale.

6.1 States

Because [LF86] discusses the coupling in Hund's coupling case (a), this basis will be adopted for the following discussion of the perturbations. The relations

$$J, e \longleftrightarrow N + 1/2 \text{ for } \mathrm{F}_1 \tag{6.1.1a}$$

$$\underbrace{J, f}_{\text{(a)}} \longleftrightarrow \underbrace{N - 1/2 \text{ for } \mathrm{F}_2}_{\text{(b)}} \tag{6.1.1b}$$

from Section 1.1.4 are used to convert between Hund's cases (a) and (b). To account for the e/f symmetry, the mapping

$$|(NS)J = N + 1/2\rangle \longleftrightarrow |J, e\rangle \qquad \text{with parity } (-1)^{J-1/2} = \quad (-1)^N \tag{6.1.2a}$$

$$|(NS)J = N - 1/2\rangle \longleftrightarrow |J, f\rangle \qquad \text{with parity } (-1)^{J-1/2} = -(-1)^N \tag{6.1.2b}$$

is used. Appropriate basis states are then

$$|v,\ J,\ S = 1/2,\ \Sigma = \pm 1/2,\ \Lambda = 0, \pm 1,\ \Omega = \pm 1/2, \pm 3/2\rangle$$

or

$$|v,\ J,\ S = 1/2,\ \Sigma = 1/2,\ \Lambda = 0, 1,\ \Omega = 1/2, 3/2,\ e/f\rangle\,.$$

The different combinations of positive and negative Σ and Λ give the following six states:

$\lvert S, \Sigma, \Lambda, \Omega\rangle$		Λ		
		-1	0	1
Σ	-1/2	$\lvert 1/2, -1/2, -1, -3/2\rangle$	$\lvert 1/2, -1/2, 0, -1/2\rangle$	$\lvert 1/2, -1/2, 1, 1/2\rangle$
	+1/2	$\lvert 1/2, \ 1/2, -1, -1/2\rangle$	$\lvert 1/2, \ 1/2, 0, \ 1/2\rangle$	$\lvert 1/2, \ 1/2, 1, 3/2\rangle$

Here, Λ, Σ and Ω in the term symbols are signed to indicate the orientation of the angular momenta $\vec{L}$, $\vec{S}$ and $\vec{J}$ with respect to the molecular axis. The physically relevant states are properly expressed as a linear combination of the basis states:

$$|^2\Sigma^+_{1/2}, J\rangle := \tfrac{1}{\sqrt{2}}\Big(|J, 1/2, 1/2, \quad 0, 1/2\rangle \pm (-1)^{J-1/2}\, |J, 1/2, -1/2, \quad 0, -1/2\rangle \Big) \tag{6.1.3a}$$

$$|^2\Pi_{1/2}, J\rangle := \tfrac{1}{\sqrt{2}}\Big(|J, 1/2, 1/2, -1, 1/2\rangle \pm (-1)^{J-1/2}\, |J, 1/2, -1/2, \quad 1, -1/2\rangle \Big) \tag{6.1.3b}$$

$$|^2\Pi_{3/2}, J\rangle := \tfrac{1}{\sqrt{2}}\Big(|J, 1/2, 1/2, \quad 1, 3/2\rangle \pm (-1)^{J-1/2}\, |J, 1/2, -1/2, -1, -3/2\rangle \Big) \tag{6.1.3c}$$

Each of these states comes as a energetically degenerate pair. The sign $\pm$ corresponds also to the eigenvalue of the parity operator, i.e. ± 1. Including the e/f index, the states can be written as:

$$|^2\Sigma^{+,e/f}_{1/2}, J\rangle := \tfrac{1}{\sqrt{2}}\Big(|J, 1/2, 1/2, \quad 0, 1/2\rangle \pm |J, 1/2, -1/2, \quad 0, -1/2\rangle \Big) \tag{6.1.4a}$$

$$|^2\Pi^{e/f}_{1/2}, J\rangle := \tfrac{1}{\sqrt{2}}\Big(|J, 1/2, 1/2, -1, 1/2\rangle \pm |J, 1/2, -1/2, \quad 1, -1/2\rangle \Big) \tag{6.1.4b}$$

$$|^2\Pi^{e/f}_{3/2}, J\rangle := \tfrac{1}{\sqrt{2}}\Big(|J, 1/2, 1/2, \quad 1, 3/2\rangle \pm |J, 1/2, -1/2, -1, -3/2\rangle \Big) \tag{6.1.4c}$$

The latter set of states obey the symmetry relations (6.1.2). As discussed in Section 1.1.4,

for a $^2\Sigma^+$ state all F_1 states have e symmetry and all F_2 states have f symmetry (see also Figure 1.2). The matrix elements need to be evaluated for all relevant combinations of the basis states. For reasons of clarity, the $|J\rangle$ part of the states (6.1.3) and (6.1.4) will be omitted in the following sections because there are no matrix elements that couple states with different J.

6.2 Spin-Orbit Interaction

The Hamiltonian describing the spin-orbit interaction is

$$\hat{H}^{SO} = A\,\vec{L}\vec{S} = \frac{A}{2}(\hat{L}^+\hat{S}^- + \hat{L}^-\hat{S}^+) + A\,\hat{L}_z\hat{S}_z, \tag{6.2.1}$$

where $\vec{L}$ is the angular momentum of the electrons and A is the interaction strength. Since A can have different values in matrix elements between different electronic states, the constants A_Σ, A_Π and $A_{\Sigma\Pi}$ are introduced, the first two for the $(2)^2\Sigma^+$ or $(1)^2\Pi$ state alone and the third for non-diagonal matrix elements evaluated with both states.

Diagonal Elements

Since Λ and Σ are the projections of $\vec{L}$ and $\vec{S}$ on the internuclear axis, their matrix elements are

$$\langle\Lambda,\Sigma|\,A\,\hat{L}_z\hat{S}_z\,|\Lambda,\Sigma\rangle = A\cdot\Lambda\Sigma, \tag{6.2.2}$$

which evaluates to the following matrix elements:

$$\langle {}^2\Sigma^{+,e/f}_{1/2}|A\,\hat{L}_z\hat{S}_z|{}^2\Sigma^{+,e/f}_{1/2}\rangle = A_\Sigma\cdot 0 \tag{6.2.3a}$$

$$\langle {}^2\Pi^{e/f}_{1/2}|A\,\hat{L}_z\hat{S}_z|{}^2\Pi^{e/f}_{1/2}\rangle = -A_\Pi/2 \tag{6.2.3b}$$

$$\langle {}^2\Pi^{e/f}_{3/2}|A\,\hat{L}_z\hat{S}_z|{}^2\Pi^{e/f}_{3/2}\rangle = A_\Pi/2 \tag{6.2.3c}$$

Off-Diagonal Elements

The coupling part $\hat{L}^\pm\hat{S}^\mp$ requires the conditions

$$\Delta\Lambda = \pm 1, \qquad \Delta\Sigma, = \mp 1 \qquad \Delta\Omega = 0 \tag{6.2.4}$$

or otherwise yields zero. The off-diagonal terms can be calculated via

$$\langle S,\Lambda,\Sigma|\,\hat{L}^\pm\hat{S}^\mp\,|S,\Lambda\pm 1,\Sigma\mp 1\rangle = \sqrt{L(L+1)-\Lambda(\Lambda\pm 1)}\sqrt{S(S+1)-\Sigma(\Sigma\mp 1)} \tag{6.2.5}$$

if L is an exact quantum number. Because only the projection of $\vec{L}$ is known, the expectation values $\langle\hat{L}^\pm\rangle$ have to be estimated. With $S = 1/2$, $\Sigma = \pm 1/2$, they are

$$\begin{aligned}\langle v_\Pi, 1/2, \Lambda, \pm 1/2|A/2\,\hat{L}^\pm\hat{S}^\mp|v_\Sigma, 1/2, \Lambda\pm 1, \mp 1/2\rangle& \\ = \langle v_\Pi|A_{\Sigma\Pi}/2|v_\Sigma\rangle\sqrt{L(L+1)-\Lambda(\Lambda+1)}\sqrt{3/4+1/4}& \\ = \langle v_\Pi|A_{\Sigma\Pi}/2|v_\Sigma\rangle\sqrt{L(L+1)-\Lambda(\Lambda+1)}\cdot 1,&\end{aligned} \tag{6.2.6}$$

but only if L is a good quantum number. In principle, the value of $A_{\Sigma\Pi}$ may change with the internuclear distance R. It is, however, doubtful that the small number of observed perturbations allows to find an adequate model for this dependency. So the assumption is made here that $A_{\Sigma\Pi}$ is independent of R and thus

$$\langle v_\Pi | A_{\Sigma\Pi} | v_\Sigma \rangle = \langle v_\Pi | v_\Sigma \rangle \, A_{\Sigma\Pi} =: V_{\Sigma\Pi} \cdot A_{\Sigma\Pi}. \tag{6.2.7}$$

Here, the symbol $V_{\Sigma\Pi}$ is defined for the overlap integral of a vibrational $(2)^2\Sigma^+$ and a vibrational $(1)^2\Pi$ state. With equation (6.2.6), a constant $p = \langle \hat{L}^\pm \rangle \, \langle \hat{S}^\mp \rangle$ is defined, so that

$$p \cdot V_{\Sigma\Pi} \cdot A_{\Sigma\Pi} = \langle \hat{L}^\pm \rangle \cdot \langle \hat{S}^\mp \rangle \cdot V_{\Sigma\Pi} \cdot A_{\Sigma\Pi}. \tag{6.2.8}$$

Because $\langle \hat{S}^\mp \rangle = 1$, p depends on $\langle \hat{L}^\pm \rangle$, which has to be determined by the experiment. Taken together, the interaction matrix has the following elements:

	$\lvert v_\Sigma, {}^2\Sigma^{+,e/f}_{1/2} \rangle$	$\lvert v_\Pi, {}^2\Pi^{e/f}_{1/2} \rangle$	$\lvert v'_\Pi, {}^2\Pi^{e,f}_{3/2} \rangle$
$\langle v_\Sigma, {}^2\Sigma^{+,e/f}_{1/2} \rvert$		$p \cdot V_{\Sigma\Pi} \cdot A_{\Sigma\Pi}/2$	
$\langle v_\Pi, {}^2\Pi^{e/f}_{1/2} \rvert$	$p \cdot V_{\Sigma\Pi} \cdot A_{\Sigma\Pi}/2$	$-A_\Pi/2$	
$\langle v_\Pi, {}^2\Pi^{e/f}_{3/2} \rvert$			$A_\Pi/2$

Couplings of the $(1)^2\Pi$ state to electronic states other than the $(2)^2\Sigma^+$ state are here ignored. Their effect can be considered negligible due to the considerable energy distance to those states, as can be seen from Figure 1.1. (In contrast, $(3)^2\Sigma^+$ levels would likely show couplings to the $(2)^2\Pi$ as well as the $(1)^2\Pi$ states, depending on the strength of the overlap integrals.) Figure 1.1 suggests furthermore that the asymptotes of the $(2)^2\Sigma^+$ and $(1)^2\Pi$ states are either $\mathrm{Li}(^2\mathrm{S}) + \mathrm{Sr}(^3\mathrm{P})$ or $\mathrm{Li}(^2\mathrm{P}) + \mathrm{Sr}(^1\mathrm{S})$, so $L = 1$ is a reasonable starting value. With this, equations (6.2.7) and (6.2.8) give

$$p = \sqrt{2}. \tag{6.2.9}$$

Because p is not precisely known, the product $[p \cdot A_{\Sigma\Pi}]$ cannot be disentangled to yield $A_{\Sigma\Pi}$. Therefore, the parameter to be determined is $[p \cdot A_{\Sigma\Pi}]$.

6.3 Spin-Rotation Interaction

The interaction of the spin $\vec{S}$ and the angular momentum of the molecular frame[a] $\vec{R}$ is

$$\hat{H}^{SR} = \gamma \vec{R}\vec{S} = \gamma(\vec{J} - \vec{L} - \vec{S})\vec{S} = \gamma \vec{J}\vec{S} - \gamma \vec{L}\vec{S} - \gamma \vec{S}^2. \tag{6.3.1}$$

This makes use of the fact that in Hund's case (a),

$$\vec{R} = \vec{J} - \vec{L} - \vec{S}. \tag{6.3.2}$$

[a] The conventional symbols for the molecular rotation $\vec{R}$ and the internuclear distance R are quite similar. The former is written as a vector operator and the latter as a scalar throughout this thesis.

The coupling constant γ can be different for the $(2)^2\Sigma^+$ and $(1)^2\Pi$ states. The last two terms in equation (6.3.1) are readily obtained: $\vec{S}^2$ gives only diagonal elements with

$$\gamma \cdot S(S+1) = \gamma \cdot {}^3/_4 \tag{6.3.3}$$

and $\gamma\vec{L}\vec{S}$ is of the same form as $\hat{H}^{SO}$ in Section 6.2, only with γ in place of A. The constants γ_Σ, γ_Π and $\gamma_{\Sigma\Pi}$ are used in analogy to A_Σ, A_Π and $A_{\Sigma\Pi}$

Diagonal Elements of $\gamma\vec{J}\vec{S}$

The projections of $\vec{J}$ and $\vec{S}$ on the internuclear axis are Ω and Σ, respectively. The matrix elements of $\gamma\,\hat{J}_z\hat{S}_z$ are then

$$\langle {}^2\Sigma^{+,e/f}_{1/2}|\gamma\,\hat{J}_z\hat{S}_z|{}^2\Sigma^{+,e/f}_{1/2}\rangle = \gamma_\Sigma/4, \tag{6.3.4a}$$

$$\langle {}^2\Pi_{1/2}{}^{e/f}|\gamma\,\hat{J}_z\hat{S}_z|{}^2\Pi_{1/2}{}^{e/f}\rangle = -\gamma_\Pi/4 \tag{6.3.4b}$$

and

$$\langle {}^2\Pi_{3/2}{}^{e/f}|\gamma\,\hat{J}_z\hat{S}_z|{}^2\Pi_{3/2}{}^{e/f}\rangle = \gamma_\Pi \cdot {}^3/_4. \tag{6.3.4c}$$

Off-Diagonal Elements of $\gamma\vec{J}\vec{S}$

The off-diagonal part $\hat{J}^\pm\hat{S}^\mp$ is only non-zero if the conditions

$$\Delta\Lambda = 0, \qquad \Delta\Sigma = \mp 1, \qquad \Delta\Omega = \pm 1 \tag{6.3.5}$$

are fulfilled. In the reference frame of a non-rotating molecule, the eigenvalues of $\hat{J}^\pm$ are like those of $\hat{J}^\mp$ in a laboratory frame ([LF86], Section 1.3.1) and therefore

$$\langle \Sigma, \Omega|\,\hat{J}^\pm\hat{S}^\mp\,|\Sigma \pm 1, \Omega \pm 1\rangle = \sqrt{J(J+1) - \Omega(\Omega \mp 1)}\sqrt{S(S+1) - \Sigma(\Sigma \mp 1)}. \tag{6.3.6}$$

Applying this to all combinations of basis vectors yields the non-zero matrix elements[b]

$$\langle {}^2\Sigma^{+,e/f}_{1/2}|\gamma/2\,\hat{J}^\pm\hat{S}^\mp|{}^2\Sigma^{+,e/f}_{1/2}\rangle = \pm\gamma_\Sigma/2 \cdot (J + 1/2) \tag{6.3.7a}$$

$$\langle {}^2\Pi^{e/f}_{3/2}|\,\gamma/2\,\hat{J}^\pm\hat{S}^\mp\,|{}^2\Pi^{e/f}_{1/2}\rangle = \gamma_\Pi/2 \cdot \sqrt{J(J+1) - {}^3/_4}. \tag{6.3.7b}$$

Together with the matrix elements (6.3.4) this gives the matrix

	$\lvert {}^2\Sigma^{+,e/f}_{1/2}\rangle$	$\lvert {}^2\Pi_{1/2}{}^{e/f}\rangle$	$\lvert {}^2\Pi_{3/2}{}^{e,f}\rangle$
$\langle {}^2\Sigma^{+,e/f}_{1/2}\rvert$	$\gamma_\Sigma/4 \cdot [1 \pm (2J+1)]$		
$\langle {}^2\Pi_{1/2}{}^{e/f}\rvert$		$-\gamma_\Pi/4$	$\gamma_\Pi/2 \cdot \sqrt{J(J+1) - {}^3/_4}$
$\langle {}^2\Pi_{3/2}{}^{e/f}\rvert$		$\gamma_\Pi/2 \cdot \sqrt{J(J+1) - {}^3/_4}$	$\gamma_\Pi \cdot 3/4$

[b] The matrix element (6.3.7a) results from a coupling between the states $\left|S = {}^1/_2, \Sigma = +{}^1/_2, \Lambda = 0, \Omega = +{}^1/_2\right\rangle$ and $\left|S = {}^1/_2, \Sigma = -{}^1/_2, \Lambda = 0, \Omega - {}^1/_2\right\rangle$.

with all diagonal and off-diagonal matrix elements of $\vec{J}\vec{S}$. The ${}^2\Sigma^+_{1/2}$ diagonal element depends on the state's e/f symmetry. The upper sign is for states with e and the lower sign for states with f symmetry.

The value of γ_Π in the matrix element $\langle v_\Pi, {}^2\Pi^{e/f}_{1/2}|\gamma\vec{J}\vec{S}|v'_\Pi, {}^2\Pi^{e/f}_{3/2}\rangle$ is considered to be independent of R, so that the overlap integral $V_\Pi = \langle v_\Pi|v'_\Pi\rangle$ can be factored out as in equation (6.2.7).

$\gamma\vec{R}\vec{S}$

The whole spin-rotation interaction is obtained by adding the various matrix elements according to equation (6.3.1):

	$\lvert v_\Sigma, {}^2\Sigma^{+,e/f}_{1/2}\rangle$	$\lvert v_\Pi, {}^2\Pi_{1/2}{}^{e/f}\rangle$	$\lvert v'_\Pi, {}^2\Pi_{3/2}{}^{e,f}\rangle$
$\langle v_\Sigma, {}^2\Sigma^{+,e/f}_{1/2}\rvert$	$-\gamma_\Sigma/2 \cdot [1 \mp (J + 1/2)]$	$-p \cdot V_{\Sigma\Pi} \cdot \gamma_{\Sigma\Pi}/2$	
$\langle v_\Pi, {}^2\Pi_{1/2}{}^{e/f}\rvert$	$-p \cdot V_{\Sigma\Pi} \cdot \gamma_{\Sigma\Pi}/2$	$-\gamma_\Pi/2$	$\frac{\gamma_\Pi/2 \cdot V_\Pi \times}{\sqrt{J(J+1) - 3/4}}$
$\langle v'_\Pi, {}^2\Pi_{3/2}{}^{e/f}\rvert$		$\frac{\gamma_\Pi/2 \cdot V_\Pi \times}{\sqrt{J(J+1) - 3/4}}$	$-\gamma_\Pi/2$

Note that, using the relations (6.1.1), the diagonal matrix element for $|{}^2\Sigma^{+,e/f}_{1/2}\rangle$ is exactly as given by equation (1.1.3).

6.4 Nuclear Rotation

The Hamiltonian for the rotation of the nuclei is

$$\hat{H}^{\text{rot}} = B\vec{R}^2 \tag{6.4.1}$$

with a rotational constant B. This was already used in Section 1.1.3. In the following, B_Λ is used to indicate the electronic state for which B is the rotational constant.

In Hund's case (b), the rotation is written as $\vec{R} = \vec{N} - \vec{L}$. Because $\hat{L}$ does not give good quantum numbers, all terms with non-zero expectation values of $\hat{L}$ are usually incorporated in the electronic energy or the Dunham parameter Y_{00}. Other terms do not affect the energy of an isolated ${}^2\Sigma^+$ state but could allow coupling to other states. The rotational energy can thus adequately be given by equation (1.1.2), with N as the rotational quantum number, when no coupling is considered.

6.4.1 $\vec{R}$ in Hund's Case (a)

In Hund's coupling case (a), using equation (6.3.2) and rearranging terms allows to merge some terms in a meaningful manner:

$$\vec{R}^2 = \vec{J}^2 + \vec{L}^2 + \vec{S}^2 + 2(\vec{L}\vec{S} - \vec{J}\vec{L} - \vec{J}\vec{S})$$

$$= \vec{J}^2 + \vec{L}^2 + \vec{S}^2 + 2(\hat{L}_z\hat{S}_z - \hat{J}_z\hat{L}_z - \hat{J}_z\hat{S}_z) + \underbrace{(\hat{L}^+\hat{S}^- + \hat{L}^-\hat{S}^+) - (\hat{J}^+\hat{L}^- + \hat{J}^-\hat{L}^+) - (\hat{J}^+\hat{S}^- + \hat{J}^-\hat{S}^+)}_{=:\hat{R}^\pm} \tag{6.4.2}$$

The operator $\hat{H}^{\mathrm{rot},\pm} \coloneqq B\hat{R}^\pm$ will be discussed in Section 6.4.2. The remaining terms describe the rotational energies that can be expressed together with the energies of the Hamiltonians $\hat{H}^{\mathrm{el}}$ and $\hat{H}^{\mathrm{vib}}$ from equation (6.0.1) by using the Dunham series:

$$\begin{aligned}\langle J,S,\Sigma,\Lambda,\Omega|\hat{R}^2|J,S,\Sigma,\Lambda,\Omega\rangle &= J(J+1) + \left\langle \hat{L}_x^2 + \hat{L}_y^2 \right\rangle + \Lambda^2 + S(S+1) + 2\left(\Lambda\Sigma - \Omega\Lambda - \Omega\Sigma\right) \\ &\overset{\Lambda=\Omega-\Sigma}{=} J(J+1) + S(S+1) - \Omega^2 - \Sigma^2 + \frac{1}{2}\left\langle \hat{L}^+\hat{L}^- + \hat{L}^-\hat{L}^+ \right\rangle\end{aligned} \tag{6.4.3}$$

The term $1/2\,(\hat{L}^+\hat{L}^- + \hat{L}^-\hat{L}^+)$, associated with the electronic angular momentum, is described by an expectation value summed over all L and depends on the electronic state. It can, like in Hund's case (b), simply be summarized with other constant energies to Y_{00}. When L is known, $(L_x^2 + L_y^2) + \Lambda^2$ can be replaced with $L(L+1)$.

For the basis states, the Dunham energies are then defined by

$$E_{\mathrm{Dun}}^{\Lambda} \coloneqq E(v,J) = \sum_{m,n} \mathrm{Y}_{mn}^{\Lambda}[v+1/2]^m[J(J+1) + S(S+1) - \Omega^2 - \Sigma^2]^n. \tag{6.4.4}$$

The rotational term $\left\langle \vec{R}^2 \right\rangle$ can be explicitly calculated with equation (6.4.3):

diagonal matrix element of $\vec{R}^2 - \hat{R}^\pm$:	$^2\Sigma^+_{1/2}$	$^2\Pi_{1/2}$	$^2\Pi_{3/2}$
L unknown	$J(J+1) + 1/4$	$J(J+1) + 1/4$	$J(J+1) - 7/4$
$L = 1$	$J(J+1) + 9/4$	$J(J+1) + 5/4$	$J(J+1) - 3/4$

The difference between unknown L and $L = 1$ is due to the term $1/2\,(\hat{L}^+\hat{L}^- + \hat{L}^-\hat{L}^+)$, as explained above. The Dunham coefficients are different for the $(2)^2\Sigma^+$ and $(1)^2\Pi$ states. Notably, the case (a)-coefficients for $(2)^2\Sigma^+$ differ from the case (b)-coefficients since they have to describe the energy dependence of other quantum numbers. Adding equation (6.4.9a) gives the same expression for the rotational term as in Hund's case (b). Accordingly, the energy of $E_{\mathrm{Dun}}^{\Sigma} \mp B_\Sigma(J+1/2)$ can be calculated with the Dunham series for case (b) without the terms for the spin-rotation coupling.

6.4.2 Rotational Coupling

The operator $\hat{H}^{\mathrm{rot},\pm}$ from equation (6.4.3) consists solely of raising and lowering operators for different angular momenta. It is a correction to the Born-Oppenheimer approximation, in which the nuclear motion is uncoupled from the electronic motion. It has three terms:

$$\hat{H}^{\mathrm{rot}\pm} = \hat{H}_{LS}^{\mathrm{rot}\pm} + \hat{H}_{L}^{\mathrm{rot}\pm} + \hat{H}_{S}^{\mathrm{rot}\pm} \tag{6.4.5}$$

Spin-Electron Interaction

The term $\hat{H}_{LS}^{\mathrm{rot},\pm} = B_\Lambda(\hat{L}^+\hat{S}^- + \hat{L}^-\hat{S}^+)$ acts like $\hat{H}^{SO}$ in Section 6.2, but without the diagonal term. The only matrix elements are

$$\langle {}^2\Pi_{1/2}^{e/f}|\, \hat{H}_{LS}^{\mathrm{rot},\pm}\, |{}^2\Sigma_{1/2}^{+,e/f}\rangle = p \cdot B_{\Sigma\Pi}. \tag{6.4.6}$$

L Uncoupling

The term $\hat{H}_L^{\mathrm{rot},\pm} = -B_\Lambda(\hat{J}^+\hat{L}^- + \hat{J}^-\hat{L}^+)$ is zero unless

$$\Delta\Lambda = \pm 1, \qquad \Delta\Sigma = 0, \qquad \Delta\Omega = \pm 1. \tag{6.4.7}$$

The eigenvalues of $\hat{J}^\pm$ and $\hat{L}^\pm$ were discussed in equations (6.2.5) and (6.3.6). The matrix elements are:

$$\langle {}^2\Pi_{1/2}^{e/f}|\, \hat{H}_L^{\mathrm{rot},\pm}\, |{}^2\Sigma_{1/2}^{+,e/f}\rangle = \mp p \cdot B_{\Sigma\Pi} \cdot (J + {}^1\!/_2) \tag{6.4.8a}$$

$$\langle {}^2\Pi_{3/2}^{e/f}|\, \hat{H}_L^{\mathrm{rot},\pm}\, |{}^2\Sigma_{1/2}^{+,e/f}\rangle = -p \cdot B_{\Sigma\Pi} \cdot \sqrt{J(J+1) - {}^3\!/_4}. \tag{6.4.8b}$$

The upper and lower signs are again for states with e or f symmetry. As in Section 6.2, the product $[p \cdot B_{\Sigma\Pi}]$ will be determined as a model parameter.

S Uncoupling

$\hat{H}_S^{\mathrm{rot},\pm} = -B_\Lambda(\hat{J}^+\hat{S}^- + \hat{J}^-\hat{S}^+)$ is the non-diagonal part of $\vec{J}\vec{S}$ and was already discussed in Section 6.3. Its only contributions are

$$\langle {}^2\Sigma_{1/2}^{+,e/f}|\hat{H}_S^{\mathrm{rot},\pm}|{}^2\Sigma_{1/2}^{+,e/f}\rangle = \mp B_\Sigma \cdot (J + 1/2) \tag{6.4.9a}$$

and

$$\langle {}^2\Pi_{3/2}^{e/f}|\, \hat{H}_S^{\mathrm{rot},\pm}\, |{}^2\Pi_{1/2}^{e/f}\rangle = -B_\Pi \cdot \sqrt{J(J+1) - {}^3\!/_4}. \tag{6.4.9b}$$

The whole rotational matrix, including the Dunham energies, is:

	$\left\lvert v_\Sigma, {}^2\Sigma_{1/2}^{+,e/f}\right\rangle$	$\left\lvert v_\Pi, {}^2\Pi_{1/2}^{e/f}\right\rangle$	$\left\lvert v'_\Pi, {}^2\Pi_{3/2}^{e,f}\right\rangle$
$\left\langle v_\Sigma, {}^2\Sigma_{1/2}^{+,e/f}\right\rvert$	$E_{\mathrm{Dun}}^{\Sigma}$ $\mp B_\Sigma(J+1/2)$	$p \cdot V_{\Sigma\Pi} \cdot B_{\Sigma\Pi}\times$ $[1 \mp (J + {}^1\!/_2)]$	$-p \cdot V_{\Sigma\Pi} \cdot B_{\Sigma\Pi}\times$ $\sqrt{J(J+1) - {}^3\!/_4}$
$\left\langle v_\Pi, {}^2\Pi_{1/2}^{e/f}\right\rvert$	$p \cdot V_{\Sigma\Pi} \cdot B_{\Sigma\Pi}\times$ $[1 \mp (J + {}^1\!/_2)]$	E_{Dun}^{Π}	$-B_\Pi\sqrt{J(J+1) - {}^3\!/_4}$
$\left\langle v'_\Pi, {}^2\Pi_{3/2}^{e/f}\right\rvert$	$-p \cdot V_{\Sigma\Pi} \cdot B_{\Sigma\Pi}\times$ $\sqrt{J(J+1) - {}^3\!/_4}$	$-B_\Pi\sqrt{J(J+1) - {}^3\!/_4}$	E_{Dun}^{Π}

The value of B_Π in the matrix elements $\langle v_\Pi, {}^2\Pi_{1/2}^{e/f}|\hat{H}^{\mathrm{rot}}|v'_\Pi, {}^2\Pi_{3/2}^{e,f}\rangle$ with different vibrational quantum numbers will be discussed on page 72.

6.5 Coupling Matrix in the Hilbert Space $v_\Sigma, v_{\Pi_{1/2}}, v_{\Pi_{3/2}}$

With all matrix elements known, they can be added together according to equation (6.0.1):

	$\left\vert v_\Sigma, {}^2\Sigma^{+,e/f}_{1/2}\right\rangle$	$\left\vert v_\Pi, {}^2\Pi_{1/2}{}^{e/f}\right\rangle$	$\left\vert v'_\Pi, {}^2\Pi_{3/2}{}^{e/f}\right\rangle$
$\left\langle v_\Sigma, {}^2\Sigma^{+,e/f}_{1/2}\right\vert$	$E^\Sigma_{\mathrm{Dun}} \mp B_\Sigma(J+1/2)$ $-\gamma_\Sigma/2\cdot[1\mp(J+1/2)]$	$V_{\Sigma\Pi}\cdot p/2\times\left[A_{\Sigma\Pi}-\gamma_{\Sigma\Pi}+\right.$ $\left.2B_{\Sigma\Pi}(1\mp[J+1/2])\right]$	$-V_{\Sigma\Pi}\cdot p\cdot B_{\Sigma\Pi}\times$ $\sqrt{J(J+1)-3/4}$
$\left\langle v_\Pi, {}^2\Pi_{1/2}{}^{e/f}\right\vert$	$V_{\Sigma\Pi}\cdot p/2\cdot\left[A_{\Sigma\Pi}-\gamma_{\Sigma\Pi}+\right.$ $\left.2B_{\Sigma\Pi}(1\mp[J+1/2])\right]$	$E^\Pi_{\mathrm{Dun}}-$ $1/2(A_\Pi+\gamma_\Pi)$	$(V_\Pi\cdot\gamma_\Pi/2-B^{(v)}_\Pi)\times$ $\sqrt{J(J+1)-3/4}$
$\left\langle v'_\Pi, {}^2\Pi_{3/2}{}^{e/f}\right\vert$	$-V_{\Sigma\Pi}\cdot p\cdot B_{\Sigma\Pi}\times$ $\sqrt{J(J+1)-3/4}$	$(V_\Pi\cdot\gamma_\Pi/2-B^{(v)}_\Pi)\times$ $\sqrt{J(J+1)-3/4}$	$E^\Pi_{\mathrm{Dun}}+$ $1/2(A_\Pi-\gamma_\Pi)$

The upper signs are to be used for states with e symmetry and the lower sign for states with f symmetry, that is, for F_1 and F_2 states, respectively. Figure 6.3 illustrates the different couplings between the $(2)^2\Sigma^{+,e/f}_{1/2}$, $(1)^2\Pi_{1/2}$ and $(1)^2\Pi_{3/2}$ states. This matrix can be used for any given $|v_\Sigma, N, (2)^2\Sigma^+, {}^{F_1}/_{F_2}\rangle$ state known from the spectrum. There are no couplings to states with other J. The coupling strength to $(1)^2\Pi$ states with a given v_Π depends on the overlap integral and the energy distance between the states.

Using this coupling scheme between $(2)^2\Sigma^+$ and $(1)^2\Pi$ states, attempts to model the perturbations observed in Section 5.3 can be made. To this extend, several parameters have to be determined such that the coupled $|v', J', (2)^2\Sigma^{+,e/f}_{1/2}\rangle$ states conform with the observed transition frequencies.

The diagonal matrix element $\langle v_\Sigma, {}^2\Sigma^{+,e/f}_{1/2}|\,\hat{H}^{\mathrm{coupl}}\,|v_\Sigma, {}^2\Sigma^{+,e/f}_{1/2}\rangle$ is equal to the energy $E_{\mathrm{Dun}}\mp B_\Sigma(J+1/2)$ from the Dunham fit described in Section 5.1 plus the term $-\gamma_\Sigma/2\times[1\mp(J+1/2)]$ from $\hat{H}^{\mathrm{SR}}$, which corresponds precisely to equation (1.1.3) in Hund's case (b). Therefore, this matrix element can be calculated by using the Dunham expansion from Section 1.2 and the hitherto obtained $(2)^2\Sigma^+$ Dunham coefficients.

The $(1)^2\Pi$ Dunham energies are unknown but highly relevant because they determine the energy difference between the coupling basis states. Only the most influential, that is Y^Π_{00}, Y^Π_{10} and Y^Π_{01}, should be estimated at the beginning of a deperturbation attempt to keep the number of parameters low. According to equation (1.2.2c), Y^Π_{01} also approximates B_Π. To keep the coupled state model simple, both the $^2\Pi_{1/2}$ and $^2\Pi_{3/2}$ states are assumed to have the same R-dependence of their potential energy curves. In this case, they have the same Dunham coefficients and the overlap integrals between $|v_\Pi, {}^2\Pi^{e/f}_{1/2}\rangle$ and $|v'_\Pi, {}^2\Pi^{e/f}_{3/2}\rangle$ are given by $\delta_{v_\Pi v'_\Pi}$. They are energetically separated by $(A_\Pi-\gamma_\Pi)$. The spin-rotation coupling is usually much weaker than the spin-orbit coupling, so this term can be merged to one parameter A_Π. The rotational constant B_Π in the matrix element $\langle v_\Pi, {}^2\Pi^{e/f}_{1/2}|\hat{H}^{\mathrm{coupl}}|v'_\Pi, {}^2\Pi^{e/f}_{3/2}\rangle$ depends on the vibrational quantum numbers of the coupling states and will be written as $B^{(v)}_\Pi$. How $B^{(v)}_\Pi$ should be chosen depending on the closest $^2\Pi$ levels will be illustrated on page 72.

The values of p (see equation (6.2.8)) and the different overlap integrals have to be determined, too. While $p\propto\langle\hat{L}^\pm\rangle$ is assumed to be independent of the molecular vibration,

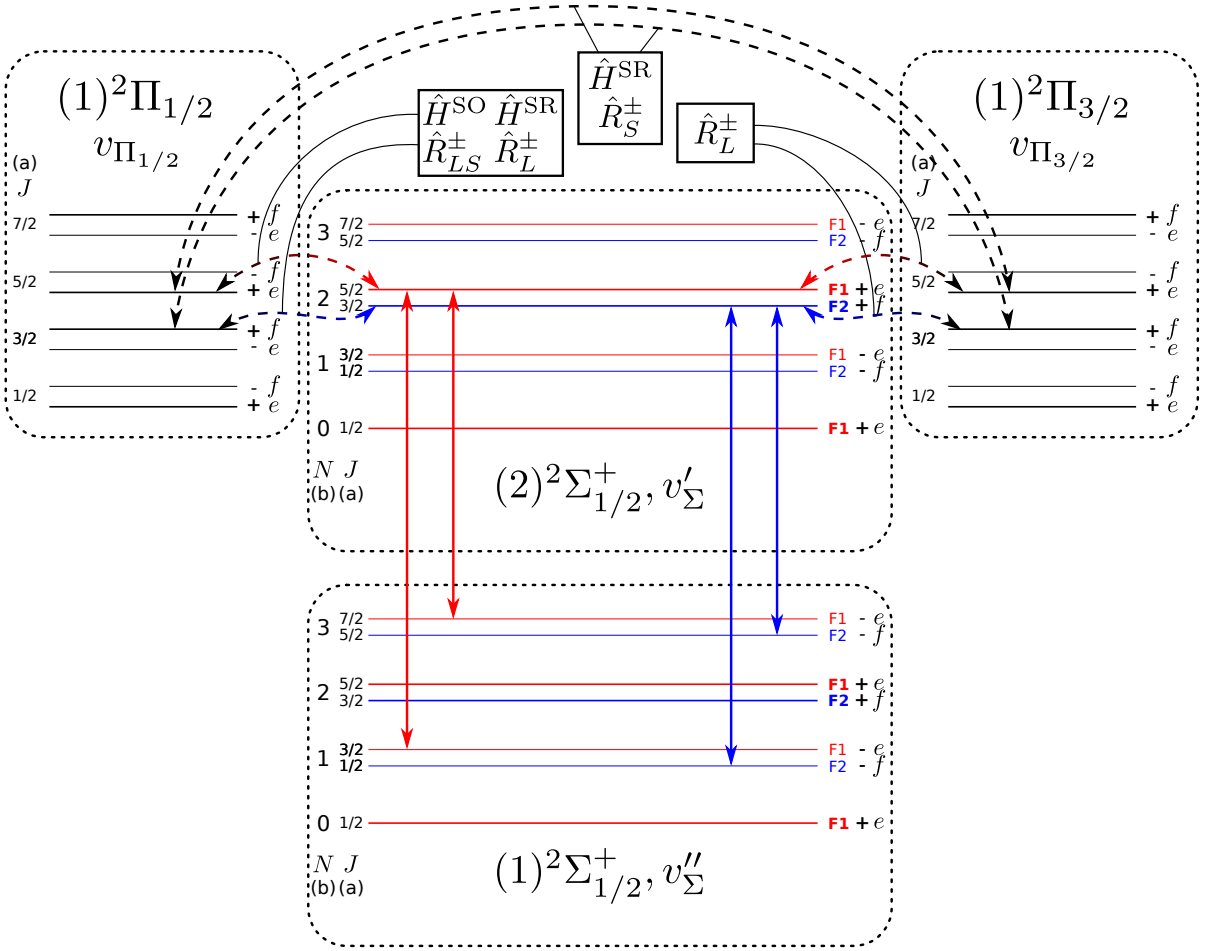

Figure 6.3: Illustration of the couplings of $|(2)^2\Sigma^+, v_\Sigma, J, {}^{e}\!/\!_{f}\rangle$ to the $|(1)^2\Pi_{1/2}, v_{\Pi_{1/2}}, J, {}^{e}\!/\!_{f}\rangle$ and $|(1)^2\Pi_{3/2}, v_{\Pi_{3/2}}, J, {}^{e}\!/\!_{f}\rangle$ states by the different operators described throughout this chapter. Quantum numbers for the $^2\Sigma^+$ states are given in Hund's cases (a) and (b). Red energy levels and arrows represent the F_1 system and blue ones depict F_2. See also Figure 1.2

the overlap integrals can differ greatly for different involved vibrational states. The perturbations seen in Figure 5.2 involve different v_Π because the rotational energies of the $(1)^2\Pi$ state rise faster with J than those of the $(2)^2\Sigma^+$ state, as was discussed at the beginning of this chapter. A reasonable value for each of these overlap integrals has to be found.

Similarly, the constants $A_{\Sigma\Pi}$, $\gamma_{\Sigma\Pi}$ and $B_{\Sigma\Pi}$, differ from those of the uncoupled states and appropriate values for them have to be determined. The first two parameters are only encountered together, so they can be combined into

$$d_{\Sigma\Pi} \coloneqq A_{\Sigma\Pi} - \gamma_{\Sigma\Pi}. \tag{6.5.1}$$

The terms $d_{\Sigma\Pi}/2$ and $B_{\Sigma\Pi}$ were fitted without the common factor of p. Neither coupling parameter is known and both have to be found by deperturbing the $^2\Sigma^+$ states. Including p would add a further fit parameter that could not easily be disentangled from the others. Accordingly, the products $[p \cdot d_{\Sigma\Pi}]$ and $[p \cdot B_{\Sigma\Pi}]$ are the parameters to be found. The remaining parameter, γ_Π in the matrix element $\langle v_\Pi, {}^2\,\Pi^{e/f}_{1/2} | \hat{H}^{\text{coupl}} | v'_\Pi, {}^2\,\Pi^{e/f}_{3/2} \rangle$, can be expected to be small compared to B_Π. It will be neglected in the following considerations.

This last step also eliminates also the need for the overlap integral V_Π.

Appendix B gives an overview of the implementation of the deperturbation model derived here.

Coupling Between $^2\Pi$ States

Couplings between the $(1)^2\Pi$ states have an indirect effect on the observed $(2)^2\Sigma^+$ levels. The model used to describe the perturbations by the $(1)^2\Pi$ state includes four $(1)^2\Pi$ states for every $(2)^2\Sigma^+$ state with given v_Σ and J: the two $|v_\Pi,^2\Pi_{1/2}, J\rangle$ and the two $|v_\Pi,^2\Pi_{3/2}, J\rangle$ states that are closest in energy to the $|v_\Sigma,^2\Sigma^+_{1/2}, J\rangle$ state (see Figure 6.4). With the

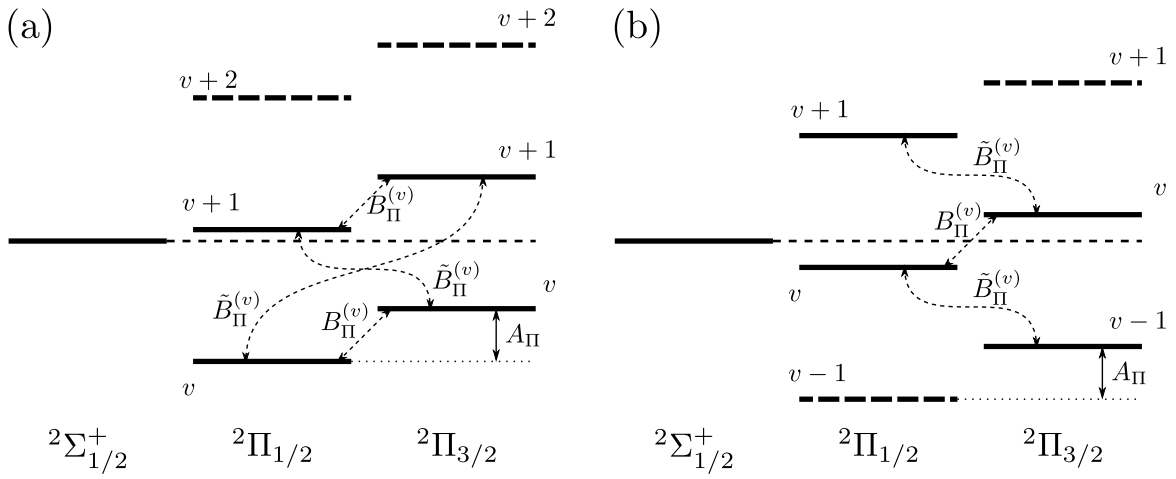

Figure 6.4: When regarding the two $|v_\Pi,^2\Pi_{1/2}\rangle$ and the two $|v'_\Pi,^2\Pi_{3/2}\rangle$ levels closest to a $|v_\Sigma,^2\Sigma^+_{1/2}\rangle$ level, there are two possible arrangements, (a) and (b). Couplings between levels with the same v are written as $B^{(v)}_\Pi$, for levels with neighbouring v they are written as $\tilde{B}^{(v)}_\Pi$. Dashed lines represent levels that are not included in the model.

choice of states employed here, the states $|v_\Pi,^2\Pi_{1/2}, J, {}^e/_f\rangle$ and $|v_\Pi \pm 0, 1,^2\Pi_{3/2}, J, {}^e/_f\rangle$ can be coupled by $(\gamma_\Pi/2 - B^{(v)}_\Pi) \cdot \sqrt{J(J+1) - {}^3/_4}$, as depicted in Figure 6.4. For the case of couplings between states with $|v,^2\Pi_{1/2}, J, {}^e/_f\rangle$ and $|v \pm 1,^2\Pi_{3/2}, J, {}^e/_f\rangle$ (Figure 6.4 (a)), an approximation $\tilde{B}^{(v)}$ for the effective rotation constant B_Π has to be found. (γ is usually much smaller than B and will be neglected.) In general, B is the expectation value $\langle v|{}^\hbar/_{(2\mu R^2)}|v\rangle$ of the radial part of the nuclear motion (compare equation (1.1.2)). In a rotating molecule with rotational quantum number J and two vibrational states, the diagonal elements of the matrix

	$\lvert v\rangle$	$\lvert v+1\rangle$
$\langle v\rvert$	$E(v) + {}^\hbar/_{(2\mu R^2)} \cdot J(J+1)$	${}^\hbar/_{(2\mu R^2)} \cdot J(J+1)$
$\langle v+1\rvert$	${}^\hbar/_{(2\mu R^2)} \cdot J(J+1)$	$E(v+1) + {}^\hbar/_{(2\mu R^2)} \cdot J(J+1)$

give the rotational energies $B_v J(J+1)$ and $B_{v+1} J(J+1)$. The actual eigenvalues of the matrix differ slightly from these energies and can be approximated by the second-order term

$$E_{\text{eig}} - E_{\text{diag}} \approx \frac{\left[\langle v|{}^\hbar/_{(2\mu R^2)}|v+1\rangle\right]^2 \cdot \left[J(J+1)\right]^2}{E(v+1) - E(v)}. \tag{6.5.2}$$

The expression (6.5.2) is proportional to $[J(J+1)]^2$. In the case of a non-rigid rotor, there is a second-order correction proportional to $[J(J+1)]^2$ (see [Her50] and equation (1.2.2d)), which can be used to get an approximate value for $\langle v|\hbar/(2\mu R^2)|v\pm 1\rangle$. By equating equation (6.5.2) with the absolute value of the Kratzer relation (1.2.2d) (expressed in proper spectroscopic notation), it follows that

$$\frac{\left[\langle v|\hbar/(2\mu R^2)|v+1\rangle\right]^2}{E(v+1)-E(v)}\cdot[J(J+1)]^2=\left|-\frac{4\,B_e^3}{\omega_e^2}\cdot[J(J+1)]^2\right|$$

$$\Leftrightarrow\qquad \tilde{B}^{(v)}:=\langle v|\hbar/(2\mu R^2)|v\pm 1\rangle\approx\sqrt{\frac{4\,B_e^3}{\omega}}, \tag{6.5.3}$$

where $E(v+1)-E(v)\approx\omega$, according to equation (1.1.1). The value of $\tilde{B}_\Pi^{(v)}$ can be used to approximate the coupling strength between $|v,^2\Pi_{1/2},J,{}^e\!/_f\rangle$ and $|v\pm 1,^2\Pi_{3/2},J,{}^e\!/_f\rangle$ states.

Couplings between states $|v,^2\Pi_{1/2},J,{}^e\!/_f\rangle$ and $|v\pm 2,^2\Pi_{3/2},J,{}^e\!/_f\rangle$ will be neglected even if both states are included in the model (see Figure 6.4 (b)) because these couplings are weak due to the large energy difference.

6.6 Simplified Coupling Model

The $(1)^2\Pi$ state is only roughly known from the ab-initio calculations, which makes the description of all perturbations challenging. For this reason, only the best-charted perturbed region, centred around $N'\approx 40$ in the $v'=0$ level of the $(2)^2\Sigma^+$ state, was approached in a first step of iterations, as will be discussed in the next chapter. To simplify the problem further, the $\Omega=3/2$ component of the $(1)^2\Pi$ state was neglected and only the two $|v_\Pi,(1)^2\Pi_{1/2},J,{}^e\!/_f\rangle$ states closest to a state $|v',(2)^2\Sigma^+_{1/2},J',{}^e\!/_f\rangle$ will be used. These simplifications greatly reduce the number of fit parameters to arrive at a first approximation of the major coupling and $(1)^2\Pi$ parameters.
Merely three overlap integrals are needed within this scope. The energetic offset given by half of the spin-orbit coupling constant A_Π can also be incorporated into the parameter Y_{00}^Π of the $(1)^2\Pi$ state. The simplified coupling matrix is:

	$\left\lvert v_\Sigma,^2\Sigma^{+,e/f}_{1/2}\right\rangle$	$\left\lvert v_\Pi,^2\Pi_{1/2}{}^{e/f}\right\rangle$
$\left\langle v_\Sigma,^2\Sigma^{+,e/f}_{1/2}\right\rvert$	$E^\Sigma_{\mathrm{Dun}}\mp B_\Sigma(J+1/2)-\gamma_\Sigma/2\times[1\mp(J+{}^1\!/_2)]$	$p/2\cdot V_{\Sigma\Pi}\cdot[d_{\Sigma\Pi}+2B_{\Sigma\Pi}(1\mp[J+{}^1\!/_2])]$
$\left\langle v_\Pi,^2\Pi_{1/2}{}^{e/f}\right\rvert$	$p/2\cdot V_{\Sigma\Pi}\cdot[d_{\Sigma\Pi}+2B_{\Sigma\Pi}(1\mp[J+{}^1\!/_2])]$	E^Π_{Dun}

Due to the lower number of parameters and states, the simplified model is more manageable than that presented on page 70. The knowledge gained by the simplified model can then be used to start the deperturbation with the extended coupling model. The next chapter will describe the steps taken to apply first the simple and then the extended models to the experimental data and discuss what can be learned about the $(1)^2\Pi$ state.

Chapter 7

Characterizing the Observed Pertubations

The coupling model from the previous chapter was applied to resolve the perturbations described in Section 5.3.

Only the perturbation, around $N' = 40$ in the $v' = 0$ level of the $(2)^2\Sigma^+$ state, was characterized at first with the simplified model discussed in Section 6.6. The thus gained parameters were used with extended transition data sets to describe several perturbations at once. The deperturbation model was iteratively extended to more perturbed regions in the spectrum until a consistent modelling of all observed was achieved.

The coupling matrix given in Section 6.5 was calculated for every observed level of the $(2)^2\Sigma^+$ state. The level energies were obtained by adding the observed transition frequencies to the energies of the corresponding (unperturbed) $X(1)^2\Sigma^+$ levels, which were calculated with the Dunham model. A non-linear least-squares fit was used to find effective parameters that parametrize the observed levels with minimal overall deviation between observed and calculated level energies. The MINUIT software [JR75] was also used for this fit. Appendix B describes the minimization procedure in more detail.

7.1 One Perturbation

The perturbation around $N' = 40$ in the $v' = 0$ level has the smallest data gap (see Figure 5.2) and was therefore the best choice for the description of a single perturbation.

The rotational levels with quantum numbers up to $N' = 65$ were used for the initial fit data set. They cover the first large perturbation but are not significantly influenced by the second large perturbation (compare Table 5.1). The deviations of the $(2)^2\Sigma^+$ energies from the Dunham fit can be seen in Figure 7.1 (a). The energies are plotted in Figure 7.2 together with the energy of their two closest $(1)^2\Pi_{1/2}$ levels. The $(1)^2\Pi_{3/2}$ states are not considered in the simple model employed here. The $(1)^2\Pi$ state was not directly observed and thus no accurate parameters for its description were available. Starting values were taken from the ab-initio parameters given by [Gop+13]. As the $(1)^2\Pi$ levels were not known precisely enough, the first step of the deperturbation process was to shift the $^2\Pi$ energies such that their rotational ladder crosses the $^2\Sigma^+$ ladder in the region of the strongest perturbation, i. e. the data gap around $N' = 40$. The ab-initio calculations suggest that the perturbing $(1)^2\Pi$ vibrational levels are around $v_\Pi = 15$. For the purpose of the deperturbation, the $^2\Pi$ levels were described with the Dunham parameters Y^Π_{00} (incorporating the spin-orbit coupling constant A_Π), Y^Π_{10}, Y^Π_{02}, Y^Π_{01} and Y^Π_{11}. The higher-order description of the vibrational levels proportional to $(v + 1/2)^m$ with $m > 2$ (see Section 1.1.2) was ignored because only a few adjacent vibrational levels are actually needed to describe the perturbation. The exact v_Π quantum numbers are not important, so v_Π was set to 15 according to the ab-initio potential energy curves. The parameter

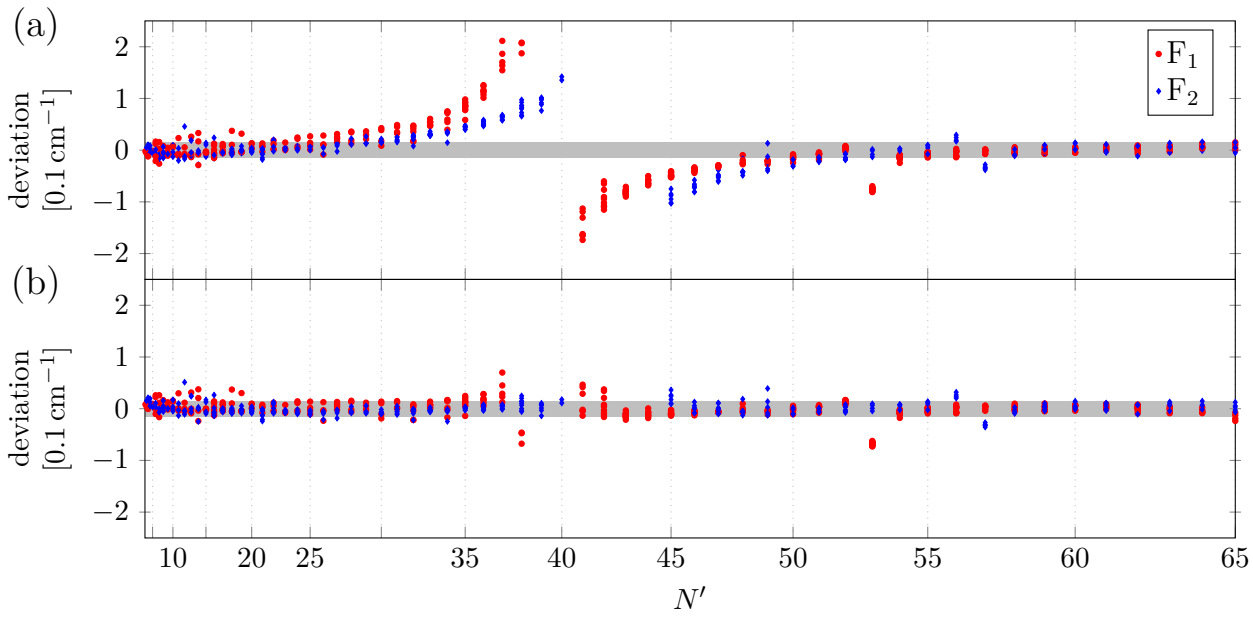

Figure 7.1: Deviations (observed frequency - modelled frequency) for $(2)^2\Sigma^+$ levels with $v' = 0$ up to $N' = 65$. The energy was calculated with the Dunham series (a) and the coupling to the $(1)^2\Pi_{1/2}$ state with the simple coupling model (b). The thickness of the grey bar represents an uncertainty interval of $0.03\,\mathrm{cm}^{-1}$. The data near the band head around $N' = 12$ have generally a higher uncertainty than $0.03\,\mathrm{cm}^{-1}$. The data around $N' = 53$ for F_1 and $N' = 55$ for F_2 are perturbed by a state not included in the model. Adapted from [Sch+17b].

Y_{11}^{Π}, taken from [Gop+13], was used to rudimentarily model the non-equal energy spacing of the relatively high vibrational states. This parameter was kept fixed during the fit procedures.

The Dunham parameters for the $^2\Pi$ state were manually adjusted to put the crossing in the right energetic vicinity. Also, only one intersection of the $v_\Sigma = 0$ rotational ladder with the chosen v_Π ladders in the desired N' interval should occur. This was the case with the rotational constant taken from the ab-initio calculations, so Y_{01}^{Π} was kept in the first step.

To completely evaluate the matrix given in Section 6.6 for every observed state $|(2)^2\Sigma^+, v' = 0, N', {}^e/_f\rangle$, the coupling parameters $[V_{\Sigma\Pi} \cdot p \cdot d_{\Sigma\Pi}]$ and $[V_{\Sigma\Pi} \cdot p \cdot B_{\Sigma\Pi}]$ needed to be determined. Because the overlap integrals and the spin-orbit parameter are unknown, the common factor $V_{\Sigma\Pi} \cdot p$ was set to $\sqrt{2}$ according to equation (6.2.8) at the beginning of the fit. Three vibrational $^2\Pi$ levels were considered in the model in total (they are shown in Figure 7.2), whereas each individual $^2\Sigma^+$ state was modelled with only two $^2\Pi$ states. Figure 7.2 shows that the involved vibrational $^2\Pi$ levels change with the crossing of the rotational ladders, which introduces an unsymmetrical effect on the $(2)^2\Sigma^+$ levels. All overlap integrals $\langle v_\Sigma = 0 | v_\Pi, v_\Pi \pm 1\rangle$ were assumed to be equal for the present case. For the greatly perturbed observed levels, the contribution of the two next-nearest levels with $v_\Pi \pm 1$ is less than that of the closest v_Π level due to the higher energetic difference. Therefore, the influence of the two overlap integrals corresponding to the next-nearest states to the fit can be expected to be small and setting them to the same value as the overlap integral of the principal perturbing state should not have a large effect on the fit quality. In that way, the number of fit parameters could be reduced by incorporating the overlap integrals in the common factor.

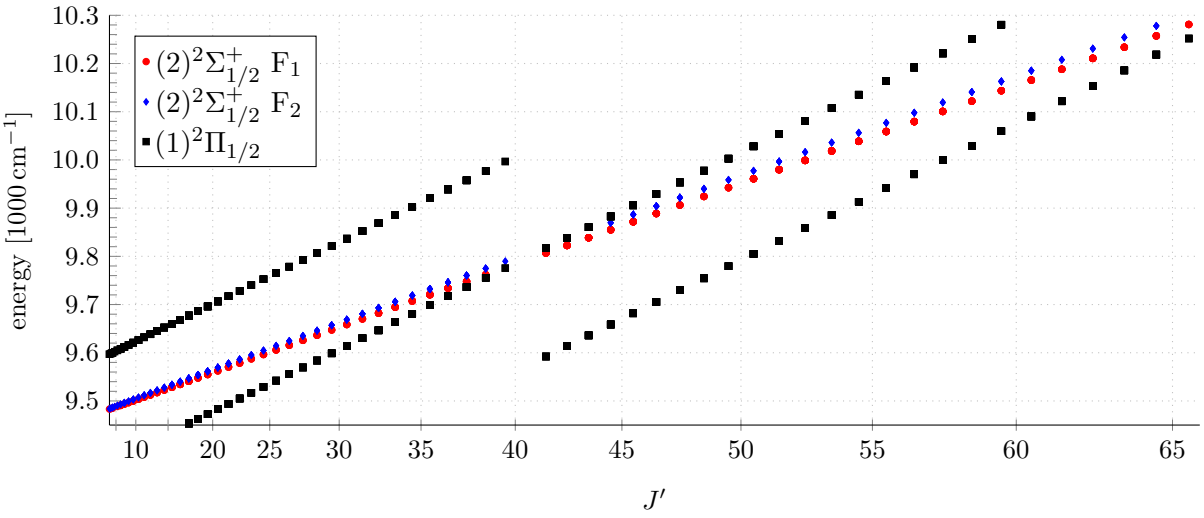

Figure 7.2: Energy levels of the $v' = 0$ rotational states of the $(1)^2\Sigma^+_{1/2}$ state with their two closest $(1)^2\Pi_{1/2}$ states. The vibrational quantum numbers of the $^2\Pi$ levels are not known. Adapted from [Sch+17b].

By alternatively fitting the Dunham parameters for the $^2\Pi$ state and the three coupling parameters, the deviation from the observation could be reduced. Subsequently fitting also the Dunham parameters for the $(2)^2\Sigma^+$ state yielded an even better description. The coupling parameter $B_{\Sigma\Pi}$ was found to not critically affect the fit quality and was set to zero. This left the product $[V_{\Sigma\Pi} \cdot p/2 \times d_{\Sigma\Pi}]$ as the only coupling parameter.

Because of the different perturbation of the F_1 and F_2 states, both systems were deperturbed independently at first. The thus derived parameters were applied to describe also the respective other system to compare the similarity of the fits. The parameters from the F_1 fit deperturbed also the F_2 system sufficiently well, hence they were used as starting points for a fit of the combined system.

New $(2)^2\Sigma^+$ levels were constructed using the unperturbed level energies from the coupling model along with deperturbed transition frequencies. These were used in a new fit of Dunham parameters for the $(2)^2\Sigma^+$-X$(1)^2\Sigma^+$ system. The new parameters were then used for a new perturbation fit. This process was iterated until the change in the new coefficients was in the order of uncertainty of the fit parameters, which means that the Dunham fits and the perturbation fits had converged. The deviations (observed frequency - modelled frequency) of the coupled system are shown in Figure 7.1 (b) and the energies of the $(2)^2\Sigma^+$ and $(1)^2\Pi$ levels are shown in Figure 7.2. The fit achieved a weighted standard deviation of $\overline{\sigma} = 0.49$. There are still small deviations around $N' = 53$ (F_1) and $N' = 56$ (F_2). These hint at a local perturbation that might come from the $^2\Pi_{3/2}$ state that was disregarded in the employed model (compare Table 5.1). For this reason, these data points were not used in the present fit.

It is possible that the coupling parameter $B_{\Sigma\Pi}$ affects the observed splitting of the $(2)^2\Sigma^+$ F_1 and F_2 levels because both $B_{\Sigma\Pi}$ and γ_Σ have the same J dependence (see the matrix in Section 6.5). As a result, the coupling to the $^2\Pi$ state could significantly influence the energy splitting when compared to an uncoupled $^2\Sigma^+$ state. Allowing combinations of $B_{\Sigma\Pi}$ and γ_Σ to be fitted while fixing the other parameters showed that γ_Σ alone is sufficient for the description of the observed transition frequencies. The introduction of $B_{\Sigma\Pi}$ does

not considerably change the magnitude of γ_Σ. According to this finding, the observed spin-rotation splitting in the $(2)^2\Sigma^+$ state can not be explained locally with the coupling to the $(1)^2\Pi$ state.

This perturbation was modelled with the coupling parameter $[p \cdot d_{\Sigma\Pi}]$, the $(2)^2\Sigma^+$ Dunham parameters including the spin-rotation coupling constant and the $(1)^2\Pi$ Dunham parameters Y^Π_{00}, Y^Π_{10} (fixed), Y^Π_{20} (fixed), Y^Π_{01} and Y^Π_{11} (fixed). The fixed parameters were taken from [Gop+13]. The effect of $B_{\Sigma\Pi}$ is negligible, as was previously discussed. Results of the deperturbation described in this section have been published together with a description of the $X(1)^2\Sigma^+$ state in [Sch+17b].

7.2 Multiple Perturbations

The whole data set contains transitions with $v' = 0, N' < 120$ and $v' = 1, N' < 110$. See e.g. Table 5.1 for an overview of the perturbed regions.

To simplify the fit procedure, the $v' = 0$ and $v' = 1$ levels were at first considered separately. The deviations, as seen in Figure 5.2, show a trend towards negative values for the $v' = 1$ levels, which means that the calculated $(2)^2\Sigma^+$ levels are too high at larger N'. To compensate this trend, every observed $v' = 1$ line was used for a fit of upper state Dunham parameters. That fit used also the lines that were excluded from the $(2)^2\Sigma^+$ fit described in Chapter 5 because they were considered perturbed (see Table 5.1). In that way, an averaged rotational constant B_1 for the $(2)^2\Sigma^+$ state was estimated.

The $(2)^2\Sigma^+$ vibrational constant needed to be adjusted to allow for the energy spacing of the perturbations. The parameter Y^Π_{02} was introduced to the model as a variable to allow a variation in the vibrational spacing in the perturbing $^2\Pi$ state. To keep the effects of the correlation of this parameter with Y^Π_{00} and Y^Π_{01} manageable, levels with low v_Π quantum numbers were chosen to cross $(2)^2\Sigma^+$, which implies that Y^Π_{00} was set much higher as in Section 7.1.

The value of the coupling parameter $[V_{\Sigma\Pi} \cdot p \cdot d_{\Sigma\Pi}]$ from the fit described in Section 7.1 was used as a starting value for that parameter. For both v' systems, the Dunham parameters for the $^2\Pi_{1/2}$ state were first changed manually to have the crossings at roughly the right positions. As can be seen from Figure 5.2, the stronger perturbations have larger data gaps. The $^2\Pi_{1/2}$ crossings and overlap integrals were chosen partially by interpolating the energy ladder of the $^2\Sigma^+$ states and partially by monitoring the effect on the deviations between the observations and the model.

Because $[V_{\Sigma\Pi} \cdot p \cdot d_{\Sigma\Pi}]$ could neither alone nor in conjunction with $[V_{\Sigma\Pi} \cdot p \cdot B_{\Sigma\Pi}]$ explain the varying coupling strengths seen in Figure 5.2, the overlap integrals $V_{\Sigma\Pi}$ were adapted manually for each perturbation while $[p \cdot d_{\Sigma\Pi}]$ was fitted. Dunham parameters for only the $(1)^2\Pi$ or the $(2)^2\Sigma^+$ state were later fitted separately along with $[p \cdot d_{\Sigma\Pi}]$ while the parameters of the other state were fixed. Both separate vibrational systems were then fitted together in order to improve the agreement in the strongly perturbed regions to improve the relative values of the overlap integrals. Only $^2\Pi_{1/2}$ parameters were used for these steps, because their large, direct influence is easier to predict than that of a $^2\Pi$ system consisting of two coupled states.

7.3 Fit of All Observed Perturbations

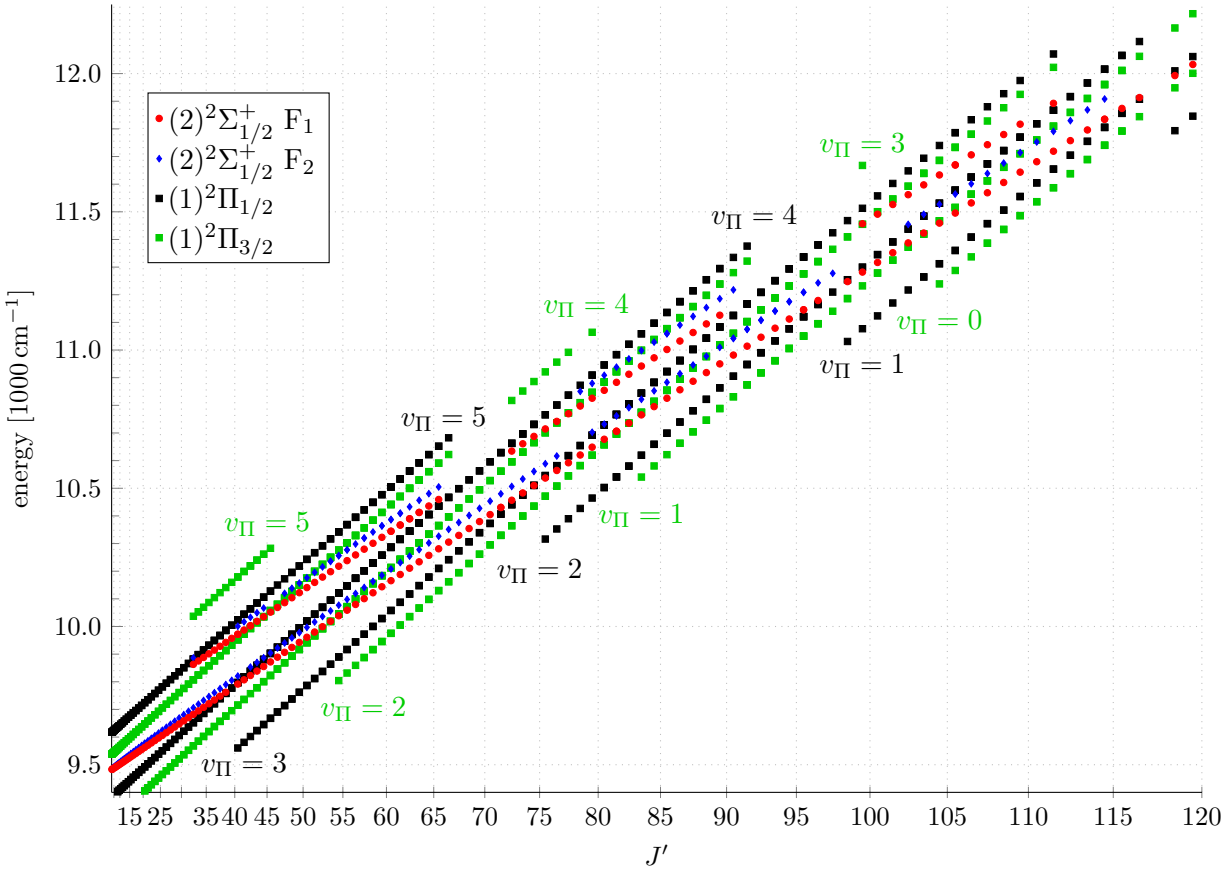

Figure 7.3: Energy levels of the rotational states of the two vibrational levels of the $(1)^2\Sigma^+_{1/2}$ state and their two closest $(1)^2\Pi_{1/2}$ and $(1)^2\Pi_{3/2}$ states. The vibrational quantum numbers of the $^2\Pi$ levels are the same as in the deperturbation model. The lowest vibrational level in the model was assigned to $v_\Pi = 0$.

The crossing points, relative overlap integrals and coupling constants found by deperturbing the individual vibrational levels were used as guidance when modelling both v' states together. The rotational and vibrational constants of the $^2\Pi$ state did not adequately connect the perturbations of both v' states with the $^2\Pi_{1/2}$ rotational ladder. Attempts to manually alter the $(1)^2\Pi$ Dunham parameters to position all crossings close to all perturbation centres proved tedious due to the correlation of the rovibrational parameters. To find an approximate parametrization of the $(1)^2\Pi$ levels, the Dunham parameters determined by the Dunham fit (see Chapter 5) were used to calculate the energies of $(2)^2\Sigma^+$ states, which, by interpolation, appear to be close to the crossings. With these energies and appropriate quantum numbers for the $(1)^2\Pi$ states, a linear Dunham fit was performed to find values for Y^Π_{00}, Y^Π_{10}, Y^Π_{20} and Y^Π_{01} that describe the rotational and vibrational energy ladders of the $(1)^2\Pi$ state in order to include all crossings. Because of the different perturbation centres of the F_1 and F_2 systems, this linear fit was conducted for only the F_1 system. For this system, the crossing positions were better known, as there were more data points available. Furthermore, the most plausible results were achieved when all $v' = 0$ crossings were used to characterize the vibrational spacing, with one $v' = 1$ crossing to find the rotational constant. Only crossings with data on both sides of the

perturbation were considered for this procedure.

With the crossings set to plausible positions to explain the shape of the larger perturbations, the $^2\Pi_{3/2}$ states were also included in the model in order to describe the smaller perturbations. The coupling matrix with all couplings described in Chapter 6 was applied from this point on. It is explicitly given in Appendix B. To proceed with the deperturbation, different groups of parameters were alternatively fitted while the others were kept fixed. This approach restricts the parameter space searched by the fit routine and avoids physically unrealistic parameter values, which leads to a faster and more reliable fit. The parameter groups are, broadly: the coupling constants $[p \cdot d_{\Sigma\Pi}]$, A_Π, $[p \cdot B_{\Sigma\Pi}]$, the overlap integrals $V_{\Sigma\Pi}$ and the $(2)^2\Sigma^+$ and $(1)^2\Pi$ Dunham parameters. If it seemed reasonable, only subsets or combinations of several parameter groups were fitted. When a fit led to an improved description of the perturbations, the fitted parameters were fixed and other parameters were set as variable in a following iteration step. It was noticed during that phase that a better description of the couplings could be achieved when the overlap integrals were allowed to be fitted automatically with the other parameters instead of being iterated by hand. Couplings to the next-nearest vibrational states are considered as well as couplings to the nearest vibrational state, so that overlap integrals of the same vibrational states, but with different J, might occur. Since overlap integrals are J-dependent, some overlap integrals (see Table 9.2) $V_{\Sigma\Pi}$ were modelled via

$$V_{\Sigma\Pi} = V_{\text{const}} + V_J \times J(J+1). \tag{7.3.1}$$

Higher-order Dunham parameters were added as fit parameters only when the description with the lower-order parameters needed to be expanded.

In this way of iteratively alternating between sets of fit parameters, the weighted standard deviation ($\overline{\sigma}$) value of the measured deviations could be reduced from $\overline{\sigma} \approx 27.10$ to $\overline{\sigma} = 0.79$. The first value represents the weighted sum-of-squares of all deviations as seen in Figure 5.2 and the latter represents the deviations of the deperturbed model as seen in Figure 7.4.

The deperturbation model greatly reduces the deviations, from several cm^{-1} (see Figure 5.2) to less than $0.3\,\text{cm}^{-1}$. As can be seen in Figure 7.4, the small deviations described in Section 5.3.3 (the N' in parentheses in Table 5.1) can adequately be modelled with couplings to the $^2\Pi_{3/2}$ states. This result grants confidence in the found spin-orbit coupling constant A_Π. The centres of the perturbations are, however, not perfectly described as they show relatively large and erratic deviations. This indicates that the model is incomplete or that the description of the crossing points could be improved. Since the shape of the deviations is greatly affected by the crossing geometry (see Figure 6.2), the parameter space might be too complex for the fit routine to sample.

A better parametrization of the perturbation centres might require a more sophisticated approach. The next chapter will describe how the depterurbation model was used to identify more lines, which were subsequently used to improve the model. In most cases, not all lines in a perturbed region could be found, and due to this lack of data it is not possible to describe the crossing points more accurately.

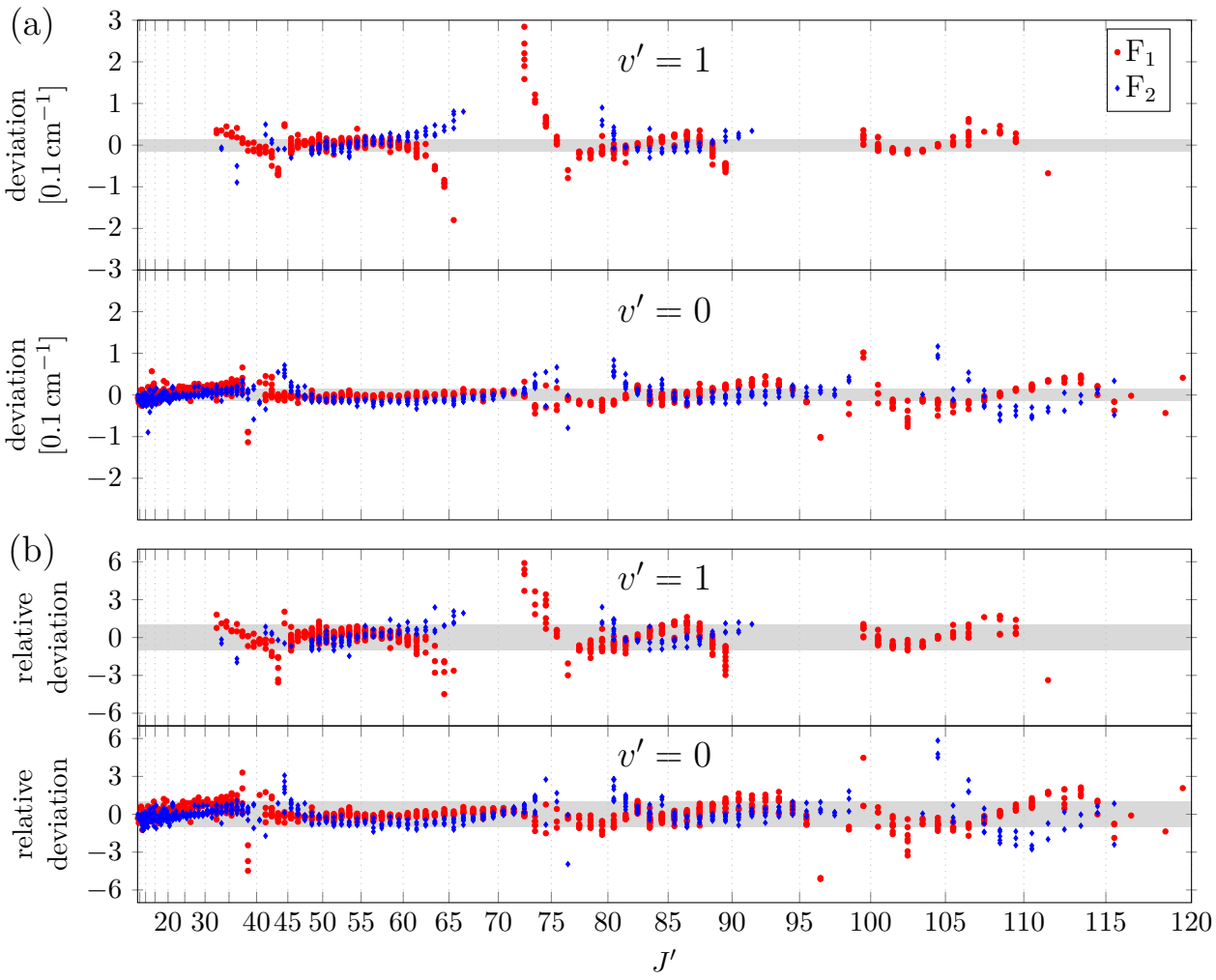

Figure 7.4: Deviations from the deperturbation model for transitions with $v' = 0$ and $v' = 1$. The perturbation centres still show noticeable deviations from the model. (a) Absolute deviations (observed frequency - modelled frequency). The thickness of the grey bar represents an uncertainty interval of 0.03 cm^{-1}. (b) Absolute deviations divided by the individual frequency uncertainty of each level's energy. The grey bar represents a ratio of 1 or lower. The plots include data that were obtained by the method described in Chapter 8.

7.4 Relative Overlap Integrals

The overlap integrals $V_{\Sigma\Pi}$ found with the deperturbation fit are only fit parameters that locally modify the global coupling strength given by $[p \cdot d_{\Sigma\Pi}]$, $[p \cdot B_{\Sigma\Pi}]$ and B_{Π}. However, they can be substantiated by comparing them with overlap integrals from ab-initio works. For this comparison, shown in Table 7.1, the variance of the fitted overlap integrals $V_{\Sigma\Pi}^{\text{fit}}$ was compared with that of ab-initio overlap integrals $V_{\Sigma\Pi}^{\text{calc}}$ via their residual sum of squares

$$\chi^2 = \sum_i \left(a \cdot V_{\Sigma\Pi,i}^{\text{calc}} - V_{\Sigma\Pi,i}^{\text{fit}} \right)^2 . \tag{7.4.1}$$

The sum was taken over the eight overlap integrals that are well described by the fit. To make the comparison for a specific choice of v_{Π}, the vibrational quantum numbers of $(1)^2\Pi$, as seen in Figure 7.3, were shifted to values around $v_{\Pi} = 11$. According to the ab-initio calculations, these vibrational levels should be energetically close to the lowest

Table 7.1: Comparison of overlap integrals between the $(2)^2\Sigma^+$ and $(1)^2\Pi$ potential curves taken from the deperturbation fit (top of the table) and from [Pot+17] (row pairs numbered with '$v_\Pi + 6, 7, ...$'). To the right, the residual sum of squares $\chi^2 = \sum_i (a \cdot V^{\text{calc}}_{\Sigma\Pi,i} - V^{\text{fit}}_{\Sigma\Pi,i})^2$ is given together with the value of a for which χ^2 is minimized. The overlap integrals $\langle v_\Pi = 0 | v_\Sigma = 0, 1\rangle$ and $\langle v_\Pi = 1 | v_\Sigma = 0, 1\rangle$ were ignored for χ^2 because the data allowed them not to be as well described as the others.

		v_Π					χ^2	a
		1	2	3	4	5		
	$v_\Sigma = 1$	0.50	5.66	3.63	2.10	0.87		
	$v_\Sigma = 0$	2.52	1.43	0.74	0.37	0.20		
$v_\Pi + 6$	$v_\Sigma = 1$		2.11E-01	3.24E-01	3.68E-01	3.51E-01	27.31	6.0
	$v_\Sigma = 0$		3.74E-01	3.09E-01	2.36E-01	1.66E-01		
$v_\Pi + 7$	$v_\Sigma = 1$		3.24E-01	3.68E-01	3.51E-01	2.92E-01	16.17	7.6
	$v_\Sigma = 0$		3.09E-01	2.36E-01	1.66E-01	1.08E-01		
$v_\Pi + 8$	$v_\Sigma = 1$		3.68E-01	3.51E-01	2.92E-01	2.16E-01	8.56	9.6
	v_Σ=0		2.36E-01	1.66E-01	1.08E-01	6.46E-02		
$v_\Pi + 9$	$v_\Sigma = 1$		3.51E-01	2.92E-01	2.16E-01	1.44E-01	3.87	12.4
	v_Σ=0		1.66E-01	1.08E-01	6.46E-02	3.56E-02		
$v_\Pi + 10$	$v_\Sigma = 1$		2.92E-01	2.16E-01	1.44E-01	8.75E-02	1.33	17.1
	$v_\Sigma = 0$		1.08E-01	6.46E-02	3.56E-02	1.81E-02		
$v_\Pi + 11$	$v_\Sigma = 1$		2.16E-01	1.44E-01	8.75E-02	4.82E-02	0.25	25.2
	v_Σ=0		6.46E-02	3.56E-02	1.81E-02	8.49E-03		
$v_\Pi + 12$	$v_\Sigma = 1$		1.44E-01	8.75E-02	4.82E-02	2.41E-02	0.07	40.1
	$v_\Sigma = 0$		3.56E-02	1.81E-02	8.49E-03	3.68E-03		
$v_\Pi + 13$	$v_\Sigma = 1$		8.75E-02	4.82E-02	2.41E-02	1.09E-02	0.53	68.9
	$v_\Sigma = 0$		1.81E-02	8.49E-03	3.68E-03	1.43E-03		
$v_\Pi + 14$	$v_\Sigma = 1$		4.82E-02	2.41E-02	1.09E-02	4.40E-03	1.41	128.6
	$v_\Sigma = 0$		8.49E-03	3.68E-03	1.43E-03	4.67E-04		
$v_\Pi + 15$	$v_\Sigma = 1$		2.41E-02	1.09E-02	4.40E-03	1.55E-03	2.60	262.0
	$v_\Sigma = 0$		3.68E-03	1.43E-03	4.67E-04	1.24E-04		
$v_\Pi + 16$	$v_\Sigma = 1$		1.09E-02	4.40E-03	1.55E-03	4.82E-04	4.15	585.7
	$v_\Sigma = 0$		1.43E-03	4.67E-04	1.24E-04	4.29E-05		
$v_\Pi + 17$	$v_\Sigma = 1$		4.40E-03	1.55E-03	4.82E-04	1.48E-04	5.86	1458.5
	$v_\Sigma = 0$		4.67E-04	1.24E-04	4.29E-05	2.40E-05		
$v_\Pi + 18$	$v_\Sigma = 1$		1.55E-03	4.82E-04	1.48E-04	4.40E-05	7.23	4143.9
	$v_\Sigma = 0$		1.24E-04	4.29E-05	2.40E-05	1.66E-06		

vibrational levels of the $(2)^2\Sigma^+$ state (see Section 7.1). The shifts are given on the left side of Table 7.1.

The magnitude of the overlap integrals is correlated with that of the coupling parameters, therefore an absolute magnitude cannot be obtained from the fit. For this reason, a global scaling factor a is introduced for the comparison. The overlap integrals depend on the rotational quantum number N. For the overlap integrals calculated with the ab-initio potential, the relative Franck-Condon factors did not vary much for different N, so the ab-initio overlap integrals shown in Table 7.1 were calculated with $N = 40$ to best fit the perturbation at $v_\Sigma = 0, J' \approx 40$. The value of a that minimizes χ^2 is shown together with χ^2 to the right of Table 7.1. According to Table 7.1, the best match is for the mapping $v_\Pi \to v_\Pi + 12 \pm 1$ and a scaling factor of 40 ± 19. For other vibrational quantum numbers, the differences become much larger. This analysis agrees with the discussion in Section 7.1, where the $(1)^2\Pi$ vibrational quantum number for the perturbation at $v_\Sigma = 0, J' \approx 40$ were estimated to be around 15. It should be noted that, while a good agreement for the variance of the overlap integrals in question can be found, the ab-initio overlap integrals decrease with increasing v_Π as well as with increasing v_Σ, whereas the fitted overlap integrals at the top of Table 7.1 show a different behaviour. When the ab-initio $(1)^2\Pi$ potential is shifted by circa 0.4 Å towards lower internuclear distance R, the overlap integrals distribution is qualitatively similar to that of the overlap integrals determined by the deperturbation fit for a shift of $v_\Pi \to v_\Pi + 12$. Table 9.4 shows that the $(1)^2\Pi$ equilibrium distance R_e estimated in this work is roughly 0.3 Å smaller than that from [Pot+17]. This analysis shows that the fitted overlap integrals are not in conflict with the ab-initio calculations, even if the actual values of the $(1)^2\Pi$ vibrational quantum numbers are not known.

An other means to corroborate the deperturbation fit is provided by the spin-orbit coupling. The value of the fitted $(1)^2\Pi$ spin-orbit coupling constant, $A_\Pi \approx d_\Pi$, is around $156\,\mathrm{cm}^{-1}$. The spin-orbit coupling constant for Sr is close to $190\,\mathrm{cm}^{-1}$ and for Li it is much smaller [San13]. According to Figure 1.1, the Sr ^{3}P state corresponds to the asymptote of the LiSr $(1)^2\Pi$ state and the coupling constant of the molecular state appears to have a spin-orbit coupling constant that is similar in magnitude, albeit smaller, to that of the asymptotic atomic state.

Furthermore, by using the approximate mapping between the vibrational quantum numbers v_Π used in the deperturbation and the quantum numbers in the ab-initio calculations [Pot+17], the ab-initio overlap integrals can be used to estimate the mixed spin-orbit coupling constant $A_{\Sigma\Pi}$. For this, the fitted parameters are equated to the product of $A_{\Sigma\Pi}$, the ab-initio overlap integrals and an estimated value of $p = \sqrt{2}$ (see equation (6.2.9)):

$$V_{\Sigma\Pi}^{\mathrm{fit}} \cdot [p \cdot d_{\Sigma\Pi}]^{\mathrm{fit}} = V_{\Sigma\Pi}^{\mathrm{calc}} \cdot \sqrt{2} \cdot d_{\Sigma\Pi} \tag{7.4.2}$$

The ab-initio potential energy curves allow to calculate overlap integrals of vibrational states in the electronic $(1)^2\Pi$ and $(2)^2\Sigma^+$ states. The choice the vibrational states with $v_\Pi^{\mathrm{fit}} + 12$ in the $(1)^2\Pi$ state and the lowest $(2)^2\Sigma^+$ vibrational states is taken here, as discussed above. With the numerical data from Tables 7.1, 9.2 and 9.3, rearranging

equation (7.4.2) yields

$$A_{\Sigma\Pi} \approx d_{\Sigma\Pi} = \frac{V_{\Sigma\Pi}^{\text{fit}}}{V_{\Sigma\Pi}^{\text{calc}}} \frac{[p \cdot d_{\Sigma\Pi}]^{\text{fit}}}{\sqrt{2}} = (196 \pm 14)\,\text{cm}^{-1}. \tag{7.4.3}$$

The large uncertainty comes mainly from the different ratios of calculated and fitted overlap integrals. For the calculation presented here, only pairs of overlap integrals from the ab-initio work and the deperturbation fit with a ratio around $a = 40.1$ (compare Table 7.1) have been used.

The mapping $v_\Pi \to v_\Pi + 11$ leads to $A_{\Sigma\Pi} \approx (131 \pm 46)\,\text{cm}^{-1}$, again only with overlap integral ratios around $a = 25$ (see Table 7.1).

These values for $A_{\Sigma\Pi}$ for both mappings have the same order of magnitude as A_Π or A_{Sr}. The ab-initio overlap integrals were used with no uncertainty limits. Since relatively high vibrational $(1)^2\Pi$ states are involved in their computation, small corrections to the potential energy curves can have a considerable effect on the the overlap integral. Thus, the $A_{\Sigma\Pi}$ values calculated here seem compatible with the other spin-orbit coupling parameters.

7.5 F_1 and F_2 Assignment

As shown in Figures 5.2 and 7.1, perturbations of the F_2 levels appear at slightly higher rotational quantum numbers N' than the perturbations of F_1 levels. Figures 7.2 and 7.3 illustrate that the reason for this finding is that the F_2 rotational ladders have a higher energy than the F_1 ladders and are therefore crossed at higher N' by the $(1)^2\Pi$ ladders. As indicated in Section 4.3.1, the spin-rotation coupling constant γ was assumed positive and, according to equation (1.1.3), the F_1 levels therefore have higher energy in Hund's case (b). The transition to Hund's case (a) switches the states' energetic order of the levels when they are plotted over J. To illustrate this: for the pair of functions

$$E_{J,\text{F}_1} = B(J - 1/2)(J + 1/2) + \gamma/2 \times (J - 1/2) \tag{7.5.1a}$$

$$E_{J,\text{F}_2} = B(J + 1/2)(J + 3/2) - \gamma/2 \times (J + 3/2), \tag{7.5.1b}$$

the following energetic order holds, since B is positive:

$$E_{J,\text{F}_1} > E_{J,\text{F}_2} \quad \text{if} \quad \gamma > 2B \tag{7.5.2a}$$

$$E_{J,\text{F}_1} = E_{J,\text{F}_2} \quad \text{if} \quad \gamma = 2B \tag{7.5.2b}$$

$$E_{J,\text{F}_1} < E_{J,\text{F}_2} \quad \text{if} \quad \gamma < 2B \tag{7.5.2c}$$

The energetic order of two states with the same N depends on the sign of γ, but the energetic order of two states with the same J depends on the magnitude of B as long as $\gamma < 2B$. The spin-rotation coupling constant γ'_{00} is considerably smaller than the rotational constant $\text{Y}'_{01} \approx B_e$. This finding is not affected by the much smaller higher-order terms of both electronic states (see Table 9.1). The appearance of the perturbation is according to the J order, which therefore allows assignment of the F_1 and F_2 labels. The initial, arbitrary, assignment of the F_1 and F_2 systems, with F_2 states having higher energy in Hund's case (a), is the correct one to explain the shifted perturbation positions.

Chapter 8

Expanding the Deperturbed Model

The perturbations seen in Figure 5.2 could be explained with the coupling between the $(2)^2\Sigma^+$ and $(1)^2\Pi$ states. The previous chapter explained how parameters were found that adequately model the positions of the observed perturbed lines due to such a coupling. The present chapter will now describe how new lines were identified with the deperturbation model and how the description of the thermal emission spectrum was further improved.

8.1 Identification of New Transition Lines

The results of the deperturbation in Chapter 7 describe the thus far assigned spectral lines reasonably well, with some exceptions near the perturbation centres (see Figure 7.4). To test the validity of the deperturbation model, the fitted parameters were used to predict previously not known $(2)^2\Sigma^+$–$X(1)^2\Sigma^+$ transition frequencies, which were compared with the thermal emission spectrum. Because there are gaps in the data used for the fit, transitions involving the missing N' near the borders of these gaps were used to check the predictive power of the model and identify new transition lines.

The data set was thus expanded towards the perturbation centres with new assigned lines, which improved the description of the perturbations. Iterating this process a few times allowed to identify heretofore unknown line series.

Figure 8.1 gives an overview of the complete data set used for the deperturbation[a]. It distinguishes the data used for the deperturbation process discussed in the previous chapter and the data added by extrapolating the model. See the figure caption for details. A comparison with Figure 5.1 reveals that most of the added lines in the perturbed regions are neighbouring other perturbed lines that are known from LIF spectra. This emphasizes how crucial the laser experiments were to assign even moderately perturbed lines by providing a reliable test of their rotational quantum numbers via equation (1.4.4). On the other hand, a strongly perturbed line could previously not be recognized and so not be targeted for a laser experiment either due to its high deviation from the regularly expected frequency or because its intensity was so low that it could only be found with the more accurate prediction of the deperturbed model.

There are several sets of newly found lines worth being discussed in order to demonstrate the limits of the identification of new lines. The line series examined in the following are partially mirrored in other bands (compare Figure 8.1). Only examples in the (0–0) and (1–0) bands will be displayed here because they are the most dominant bands in their spectral region, which facilitates tracking the rotational branches. The lines are labeled with the Hund's case (b) quantum numbers in the figures to keep the labelling concise.

[a] Compare Figure 5.1 for the previous data set.

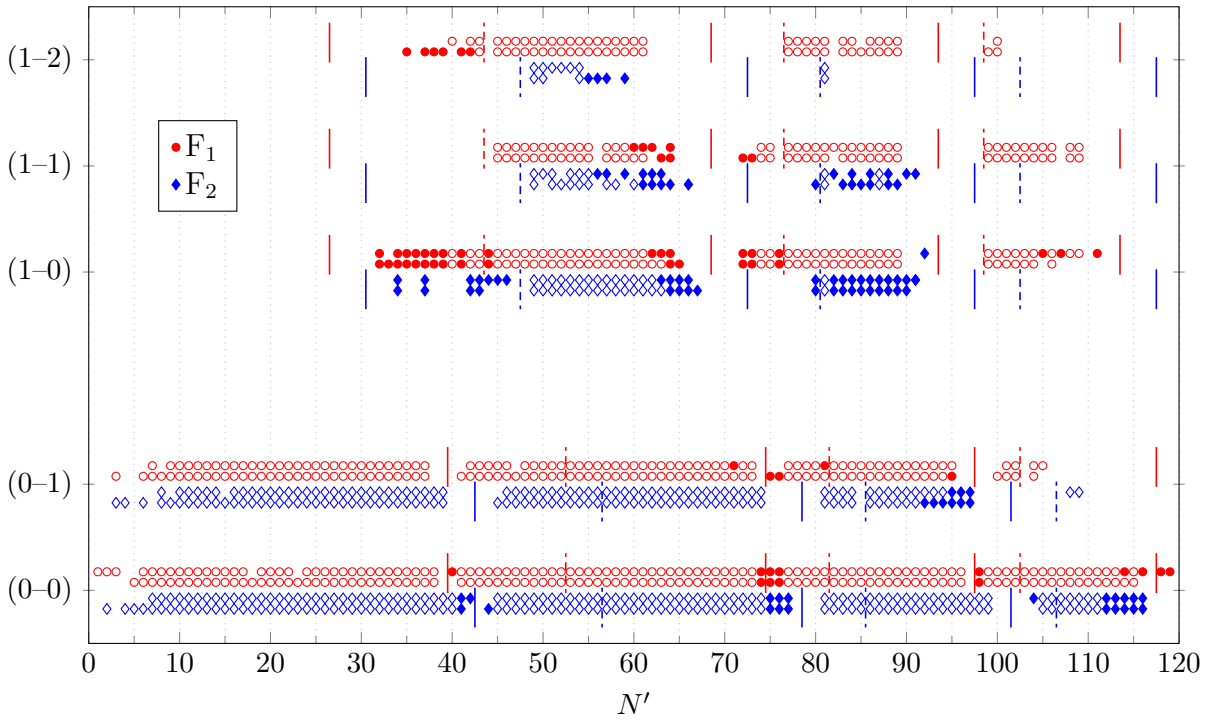

Figure 8.1: Overview of all transition lines that could be assigned to quantum numbers were used in the deperturbation fit. The upper and lower line of a single colour in a band represent the R or P line, respectively, that is associated with the indicated N'. The filled symbols indicate lines that were identified with the deperturbation model, while empty symbols represent the data set at the beginning of the deperturbation. The solid and dashed vertical lines indicate the perturbation centre of the $^2\Pi_{1/2}$ and $^2\Pi_{3/2}$ crossings, respectively.

8.1.1 Perturbation Around $v' = 0, N' = 40$

The (0–0) P and R branches around $N' = 40$ are plotted in Figure 8.2. The distance of consecutive assigned lines becomes smaller towards the perturbation centre. This can most easily be seen when tracking the F_1 R branch from the left side of Figure 8.2 (a). The line sequences on both sides of the perturbation are disrupted by a large gap in the spectrum. The calculated and observed F_2 branches in Figure 8.2 (b) illustrate this fact best in the P branch.

For the F_1 R branch, the predicted R 38 line has higher frequency than the R 37 line. They are relatively close to the band head, so the distance between two lines are smaller than in the P branch (see equations (1.4.2)). Notice how the predicted R 37 line and its counterpart, P 39, are to the right of the observed spectral lines, for which the assignments are known from fluorescence experiments. In contrast, the R 38 line is predicted at a frequency where no distinct peak could be identified in the thermal emission spectrum. The corresponding P 40 line lies in a structure that is already explained by other lines.

The F_1 R 39 line is predicted at a weak shoulder and can be assigned to a line within the peak structure with the methods from Chapter 3. The P 41 line falls between two large peaks and cannot convincingly be assigned to an observation. For these reasons, the small data gap in the F_1 rotational ladder could not be fully closed.

The larger gap in the F_2 system could also not be closed completely, although more lines were identified. The predicted R 41 line lies slightly to the right of the small peak to which it was assigned. The P 43 line is predicted to the right of a large, already assigned peak.

The correct P 43 line could be assumed to have a slightly lower frequency than predicted. In the case of the R 41 line, this assumption is not in conflict with the observed spectrum. However, no spectral peak can be found in the thermal emission spectrum for the shifted P 43 line. The other lines are likewise coinciding with stronger, already assigned peak structures and should not be assigned. The exception is P 45, which is predicted at a shoulder of the F_1 P 46 peak and was added to the data set.

8.1.2 Perturbation Around $v' = 0, N' = 75$

Figure 8.3 depicts the (0–0) P and R branches around $N' = 75$. For the F_1 system, the previously missing lines with $N' = 76, 77, 78$ were identified via the predictions by the model.

The F_2 branches were tracked up to lines with $N' = 77$. The predicted R 77 line seems to be close to the predicted R 76 line, while the P 79 line is predicted at a position where there is no discernible peak in the spectrum. Thus, the peak between the predicted frequencies for R 76 and R 77 is likely the R 76 transition line. This assumption is further corroborated by the fact that both the R 76 and the P 78 lines are predicted at slightly lower frequencies than the closest spectral peaks. The remaining F_2 transition lines are in general not predicted at spectral peaks. (Not all of the missing P lines are shown in Figure 8.3 (b).) If one of the missing lines coincides with a peak, the associated P or R line does not. Because both lines mirror the energy shift of the same level in $(2)^2\Sigma^+$, this is a clear sign of a mere coincidence of the prediction with a spectral structure. There is a peak to the left of the P 80 line and the R 78 line is predicted within an already assigned structure. However, since the $N' = 79$ level is the first after the perturbation centre (as can be seen from the gap in the predicted branches) and the modelling of the perturbation is not perfect, the P 80 and R 78 line positions were deemed not to be reliable enough to be used for further fits.

The F_1 R 74 line was added to the fit data set, even though the line coincided with a large peak that was already explained by other transition lines. The P 43 line in Figure 8.2 (b) was not added to the data set, although there the situation looks similar. This is because the former line is predicted in the middle of a peak, whereas the latter line is predicted near a peak's foot. In the former case, the transition frequency would probably lie somewhere within the peak. This could be taken into account with a larger uncertainty. In the latter case, attributing a frequency from within the peak to the transition would give a skewed data point. Furthermore, the P 43 line is directly neighbouring the perturbation gap. Because the perturbation centres are in general not modelled well, this position raises doubts regarding the quality of the prediction of this line. The R 74 transition frequency is, however, corroborated by the arguably correct prediction of the R 73 line on the other side of the perturbation gap and the P counterparts of both. Similarly, predicted lines that coincide with already well described peaks were added to the data set if they are reasonably far away from a perturbation centre, while predicted lines closer to centres are more questionable. Whether to add a line or not needs to be decided case by case, depending on their neighbouring lines or lines with the same upper quantum numbers.

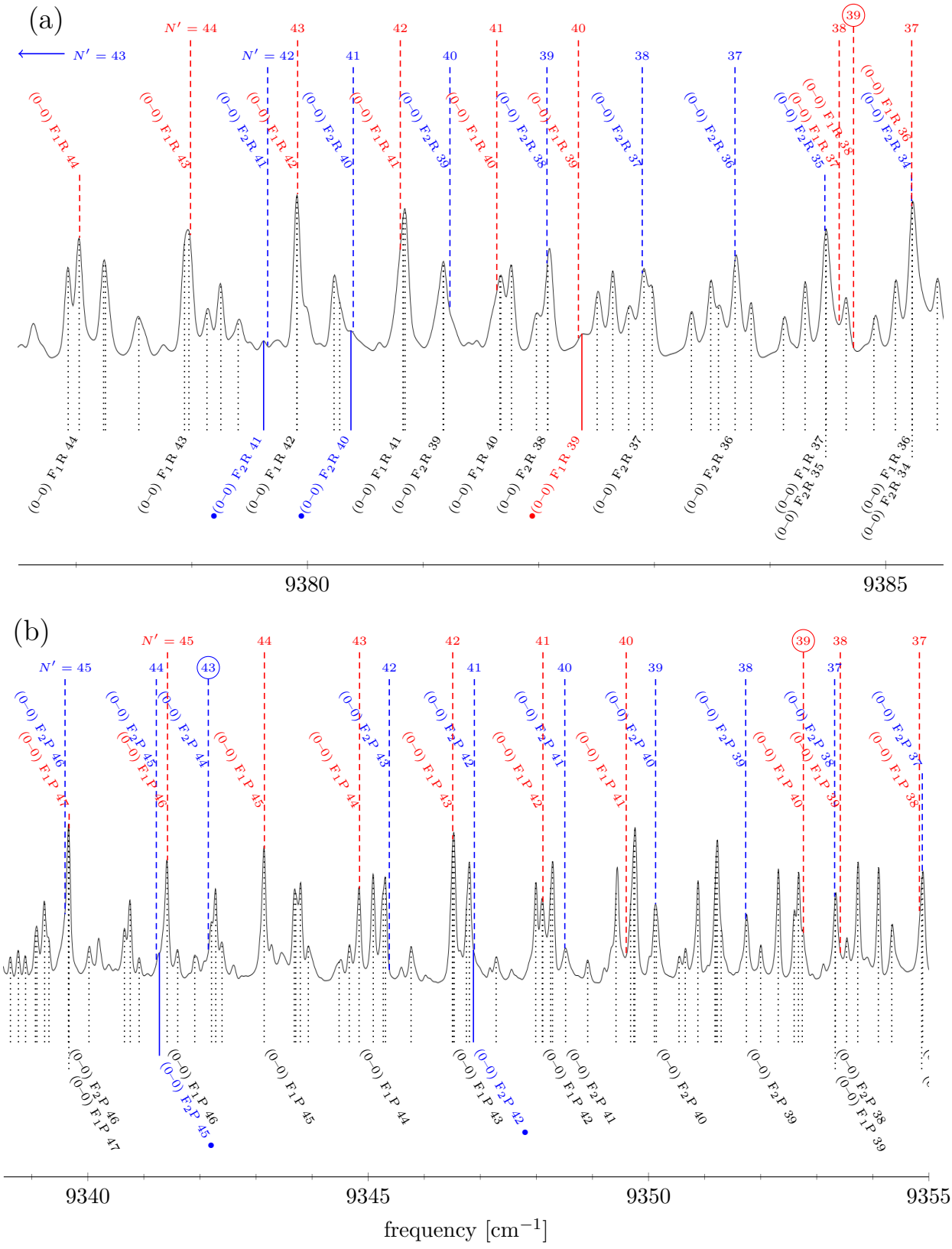

Figure 8.2: The R (a) and P (b) branches of the (0–0) band showing the perturbation at N' around 40. Assignments above the spectrum were determined with the deperturbation model; those below the spectrum were taken from the data set used for the fit. The black data were used for the deperturbation, the coloured lines with the mark (•) represent lines identified with the deperturbation model. The N' labels with the circle (◯) indicate lines with the strongest shift in a line sequence. Labels are omitted for lines that are not relevant to the discussion.

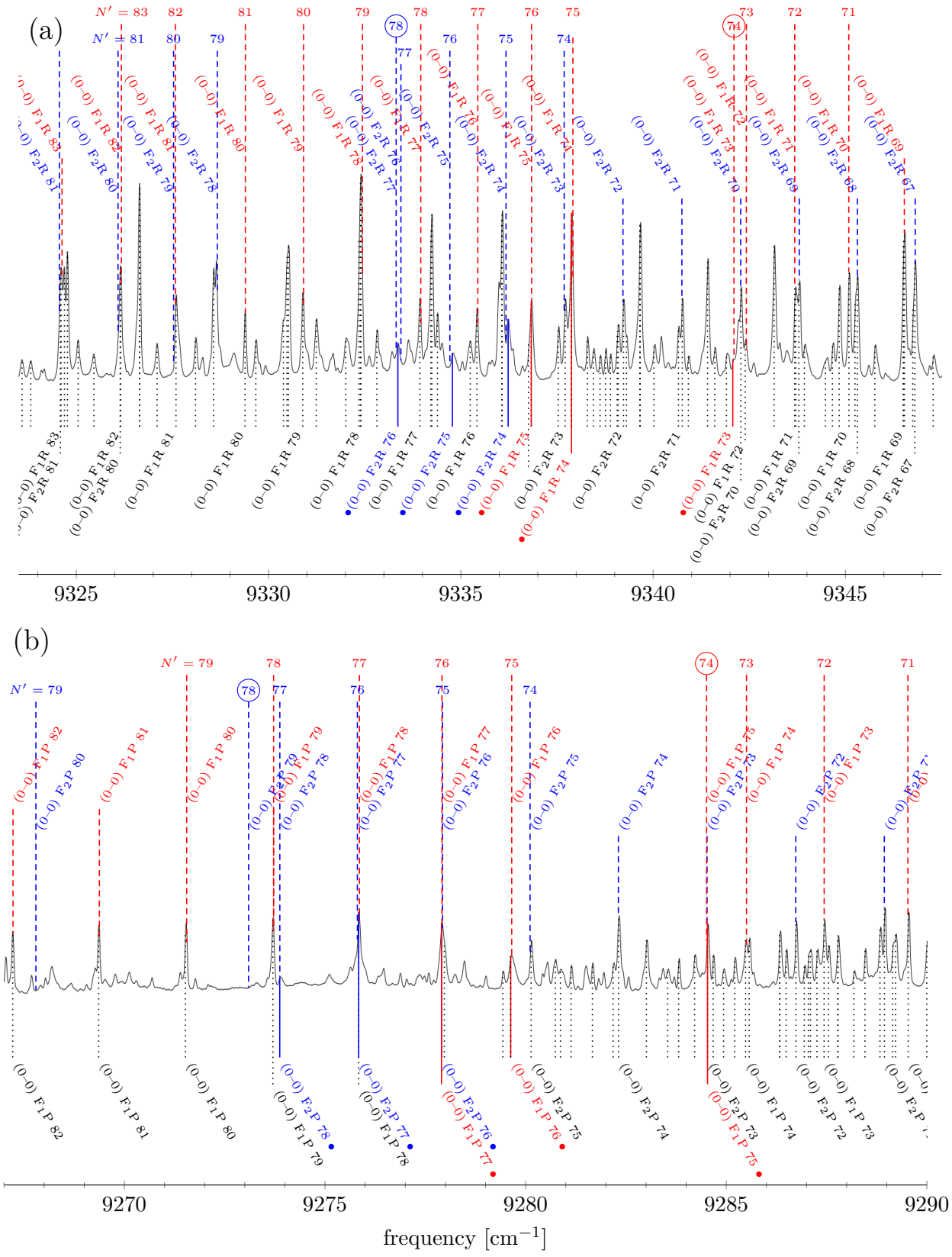

Figure 8.3: The R (a) and P (b) branches of the (0–0) band showing the perturbation at N' around 75. Assignments above the spectrum were determined with the deperturbation model; those below the spectrum were taken from the data set used for the fit. The black data were used for the deperturbation, the coloured lines with the mark (•) represent lines identified with the deperturbation model. The N' labels with the circle (◯) indicate lines with the strongest shift in a line sequence. Labels are omitted for lines that are not relevant to the discussion.

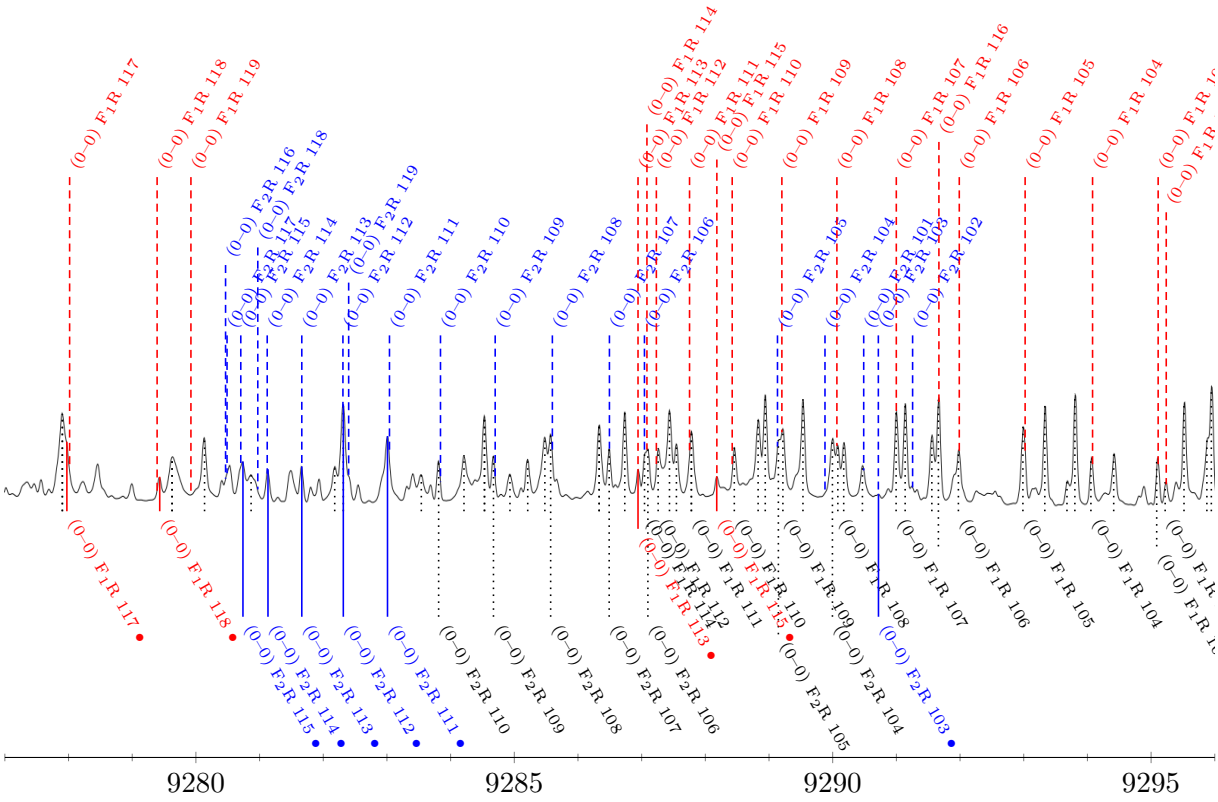

Figure 8.4: Transition lines with N' beyond 100 of the R branch of the (0–0) band. Assignments above the spectrum were determined with the deperturbation model; those below the spectrum were taken from the data set used for the fit. The black data were used for the deperturbation, the coloured lines with the mark (•) represent lines identified with the deperturbation model. Labels are omitted for lines that are not relevant to the discussion. No lines with $N' > 120$ were calculated.

8.1.3 Perturbation and Turnaround for $v' = 0, N' > 100$

Figure 8.4 displays the R branch of the (0–0) band for the highest assigned rotational quantum numbers. The corresponding section of the P branch is superimposed by the stronger (0–1) band and only a few new F_2 lines could be found (see Figure 8.1). Both the R and P branches turn back for rotational quantum numbers close to $N = 120$. This behaviour is also predicted by the bare Dunham model[b]. Only rotational lines with $N < 120$ were used to fit Dunham parameters, but with observations close to the turnaround, its position should be approximated well enough. (Like for the band head, the exact turnaround position is different in P and R branches and the F_1 and F_2 systems.) Since there is a perturbation in the $(2)^2\Sigma^+$ levels at quantum numbers near $N' = 120$, the exact turning point is different for the F_1 and F_2 branches. Because of the turnaround and the relatively strong perturbation, the line series are to some extend out of order. For example, the F_1 R 114 line has a higher frequency than the R 113 line. The R 114 line was known from a LIF spectrum, so its rotational quantum number could be assigned via the distance to the P line. The R 113 line was later known from the deperturbation model. Due to the irregular spectral structure, the LIF experiments were immensely helpful.

[b] Similar to the Fortrat parabola that depends on the difference of B' and B'', a so-called 'turnaround' of the branches can appear due to centrifugal corrections to the rotational energy.

The F_1 branch could generally be completed, except for the R 116 transition, whose predictions coincided with a strong line from the P branch (and whose corresponding P line could not be found due to the (0–1) band), and except for the R 119 transition, whose prediction does not fall near a spectral line.

In the F_2 branch, there were not so many high quantum numbers assigned prior to the deperturbation process. (Chapter 5 discussed that there were generally less observed F_2 fluorescence lines.) The added F_2 lines are well described by the model. Because the F_1 lines with the same rotational quantum numbers were already used for the deperturbation, the F_2 prediction quality indicates that the spin-orbit coupling is well described. With this coupling, the shift of the F_2 lines can be explained with the deperturbation of the F_1 system. The F_2 branch was not tracked as far as the F_1 branch since the lines move closer together due to the turnaround and, without the confirmation from the P branch, they were not deemed reliable enough to be in the data set. The addition of lines via the deperturbation model should be done very carefully because they are highly sensitive to the coupling and thus will constrain the fit significantly. In cases where only few data points are found, these might then dictate the fitted difference in the $(2)^2\Sigma^+$ and $(1)^2\Pi$ rotational ladders for a perturbation, especially with lines close to a perturbation centre.

The P and R lines with $N > 100$ have relative low intensity. This is in agreement with the calculation plotted in Figure 5.3. The (0–1) P lines, around $9100\,\mathrm{cm}^{-1}$ and lower, are not even detectable from the thermal emission spectrum without the aid of fluorescence experiments. The turning of the branches around $N = 117$ leads to lines with $N \gtrsim 120$ being harder to discover because they are dwarfed by lines with $N \lesssim 115$ of the same branches. As a consequence, a continuation of the rotational ladder beyond $N = 120$ from the present thermal emission spectrum is unlikely.

8.1.4 Perturbation and Band Head for $v' = 1, N' < 47$

The P and R lines with the lowest assigned rotational quantum numbers in the (1–0) band are shown in Figure 8.5. The line assignment in the (1–0) band started from fluorescence experiments around $N' \approx 50$ beyond the left of Figure 8.5. How far towards the (1–0) band head the assignment proceeded can be seen in Figure 8.1. The frequency shift and reduced intensity due to a perturbation did not allow to advance to the band head, however.

When first predictions of the deperturbation model became available, some lines with lower rotational quantum numbers were added to the data set. Notably, the lines belonging to $|N' = 44, \mathrm{F}_1\rangle$ were not identified before the deperturbation. This level is close to a $^2\Pi_{3/2}$ crossing, which leads to a local perturbation (compare Figure 9.1). The new lines were then used for further deperturbation fits. The thus obtained improved model could be used to identify further lines. In this way, progress was made towards lines with $N' = 32$ for the F_1 system. The F_2 branches could not be tracked as far because the intermediately predicted lines generally fell in oddly-shaped spectral structures. These are dominated by a line already assigned to a F_1 transition. There exist two solitary exceptions, for which both the predicted P and R line fell on a distinguishable peak. The previous discussion showed that the F_2 system is similarly deperturbed as the F_1 system and consequently, these predictions were deemed reliable enough for an assignment, even though there are large gaps to the next assigned F_2 lines.

The line assignment did not proceed beyond the perturbation centre. With lower N, both F_1 and F_2 lines get closer in frequency. No frequency from the thermal emission spectrum could reasonably be assigned to the predicted lines any more. The model, although not too reliable here, predicts gaps of $4\,\mathrm{cm}^{-1}$ to $8\,\mathrm{cm}^{-1}$ in the various branches. Lines with lower quantum numbers could not be identified.

In Figure 8.5 (a), also the (1–0) band heads are shown. As in the (0–0) band, the right one belongs to the F_1 R branch, the left one to the F_2 R branch. Additionally, there is a large peak at $9575\,\mathrm{cm}^{-1}$. It is likely formed by several coinciding F_1 and F_2 lines. The predicted band heads are about $0.2\,\mathrm{cm}^{-1}$ to the left from the band heads in the thermal emission. Before the extension of the deperturbation, they were approximately $0.7\,\mathrm{cm}^{-1}$ to the right of the thermal emission band heads and they drew closer in intermediate steps. This improvement substantiates the quality of the deperturbation model, although it does not adequately incorporate the low rotational levels of $v' = 1$.

To rectify the band head discrepancy, the frequency of the right band head was assigned to a F_1 line from the modelled band head. It has been given a relatively high weight and a deperturbation fit has been conducted in the hope that the added line would shift at least the F_1 band head to the observed position. This experiment did not succeed, nor did it with other lines with similar rotational quantum numbers. Consequently, the low rotational levels with $v' = 1$ are not yet correctly modelled with the available data.

8.1.5 Perturbation Around $v' = 1, N' = 70$

The R and P branches of the (1–0) band around the perturbation centred at $N' \approx 70$ are displayed in Figure 8.6. As can be seen in the plot of deviations from the deperturbation model in Figure 7.4, the F_1 lines near this perturbation seem to be overcompensated when compared to the plot of deviations from the Dunham model in Figure 5.2, which means that their deviation from the model changes sign. The deperturbed F_2 lines on the other hand still appear to be disturbed like in Figure 5.2, only weaker. The frequency gaps in the P and R branches due to the perturbation are $10\,\mathrm{cm}^{-1}$ to $15\,\mathrm{cm}^{-1}$ wide. Both sides of the perturbed regions are only shown for the F_1 branches in Figure 8.6. The F_2 branches have similar gaps, centred around lower frequencies than in the F_1 branches. It is difficult to decide on a peak to assign the F_1 R 64 line, whereas the corresponding P 66 line is likely somewhere in the peak structure to the left of its predicted frequency. The predictions of the F_1 R 71 and P 73 lines, both with $N' = 72$, fall to the right of two broader structures in the thermal emission spectrum. There exist two plausible line positions in each structure and both their positions seem in agreement with the residual perturbation shape in Figure 7.4. The (1–1) F_1 P 73 line is also predicted next to a broad spectral peak consisting of two lines. The (1–1) F_1 R 71 line cannot be located in the thermal emission spectrum with reasonable certainty. Since there are two close candidates for all three lines with $N' = 72$, it is not possible to use information from other branches to force a decision and so all six lines were added to the data set. Their spread is about $0.01\,\mathrm{cm}^{-1}$, as can be seen in Figure 7.4 (a), and they were given an appropriate uncertainty.

The F_2 lines are consistently predicted to the left of spectral peaks. Their deviation from these peaks is weaker as for the F_1 lines, but that can be attributed to the fact that the

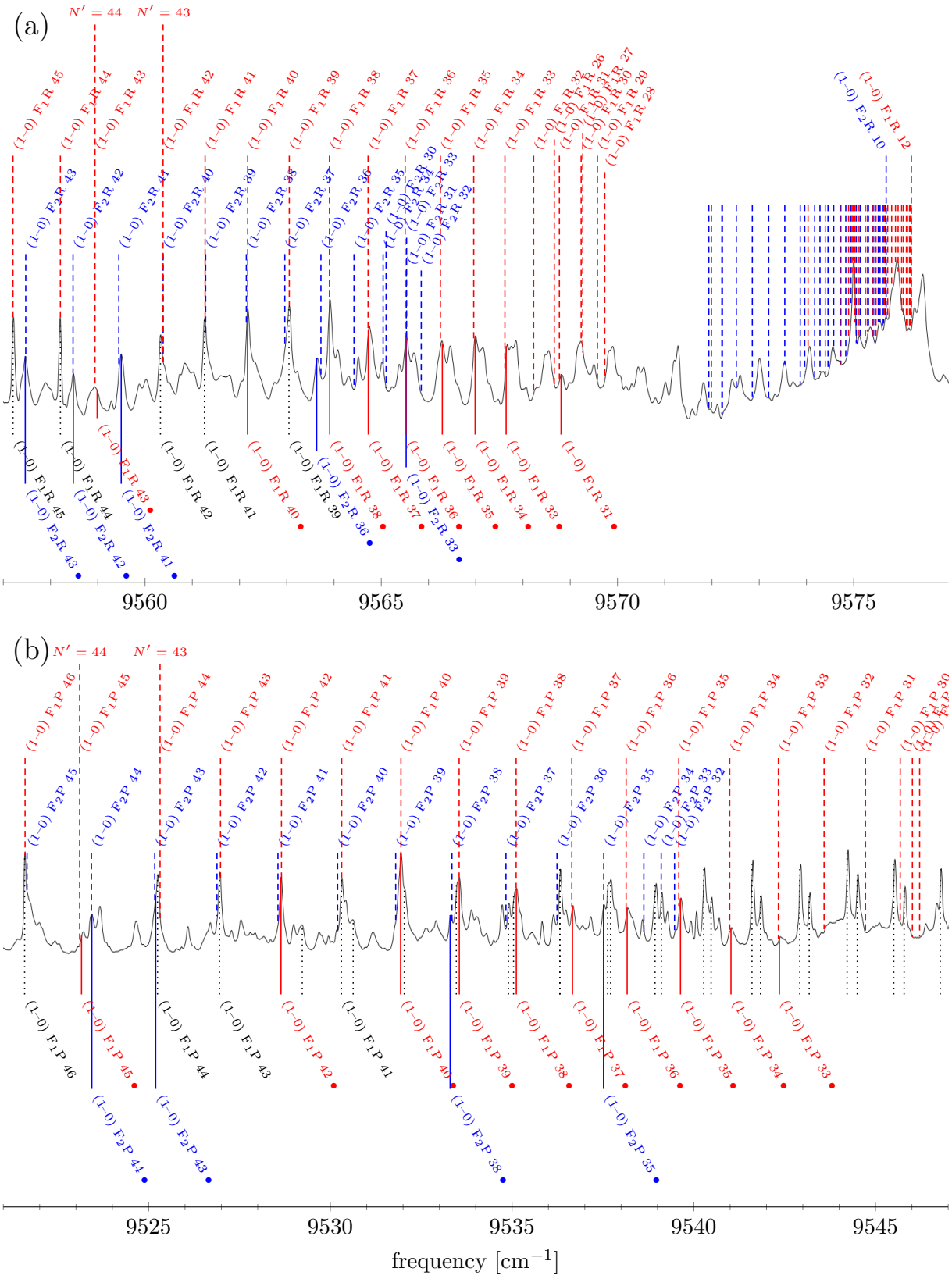

Figure 8.5: The R (a) and P (b) branches of the (1–0) band showing the perturbation at N' around 30. Assignments above the spectrum were determined with the deperturbation model; those below the spectrum were taken from the data set used for the fit. The black data were used for the deperturbation, the coloured lines with the mark (•) represent lines identified with the deperturbation model. Labels are omitted for lines that are not relevant to the discussion.

F_2 perturbation centre should be at a higher quantum number than the F_1 perturbation centre. F_2 transitions with $N' > 66$ are not predicted next to an assignable peak. An exception is the P 68 line because it can be expected to lie somewhere in the peak to the right of the predicted frequency.

The other side of the F_2 perturbation is not shown. Here, only few lines could be added that are closer to the perturbation centre than lines already known from fluorescence, as can be seen from Figure 8.1. For the other unassigned transition lines, the predictions do not fall close to spectral features.

Considering that for the F_1 and F_2 systems a clear trend towards larger deviation between the modelled and nearby thermal emission lines exists and that the two systems show incompatible behaviour, this perturbation appears to be inadequately modelled near its centre.

8.1.6 Identification of F_2 Lines Around $v' = 1, N' = 85$

Figure 8.7 shows the F_2 series of the (1–0) P and R branches between the second ($N' \approx 70$) and third ($N' \approx 95$) large perturbation in this band. Almost a dozen F_2 lines could be identified in each branch (coloured lines underneath the spectra) with the deperturbation model, which further demonstrates that the spin-rotation coupling is well described. There were also strong lines identified in the (1–1) band (see Figure 8.1). However, the overshadowing (0–0) band did not allow to find all of the (1–1) lines.

Figure 8.7 further displays the beginning of the third perturbation towards its left side. No F_1 lines could be reliably identified with the deperturbation model beyond those known from fluorescence experiments.

In conclusion, the deperturbed description of the $^7Li^{88}Sr$ spectrum allowed to substantially reduce the data gaps in the rotational branches. Due to the inaccuracy of the model near perturbation centres and random coincidences in the thermal emission spectrum, these gaps could not be fully closed. The new data were used in an iterative process to better describe the perturbations. Using the deperturbation model to identify new lines from the thermal emission spectrum allowed to increase the number of known transition lines by about 17 %. Fluorescence experiments might allow to identify a few more lines. However, the predictive quality of the model near perturbation centres is generally insufficient for targeted experiments.

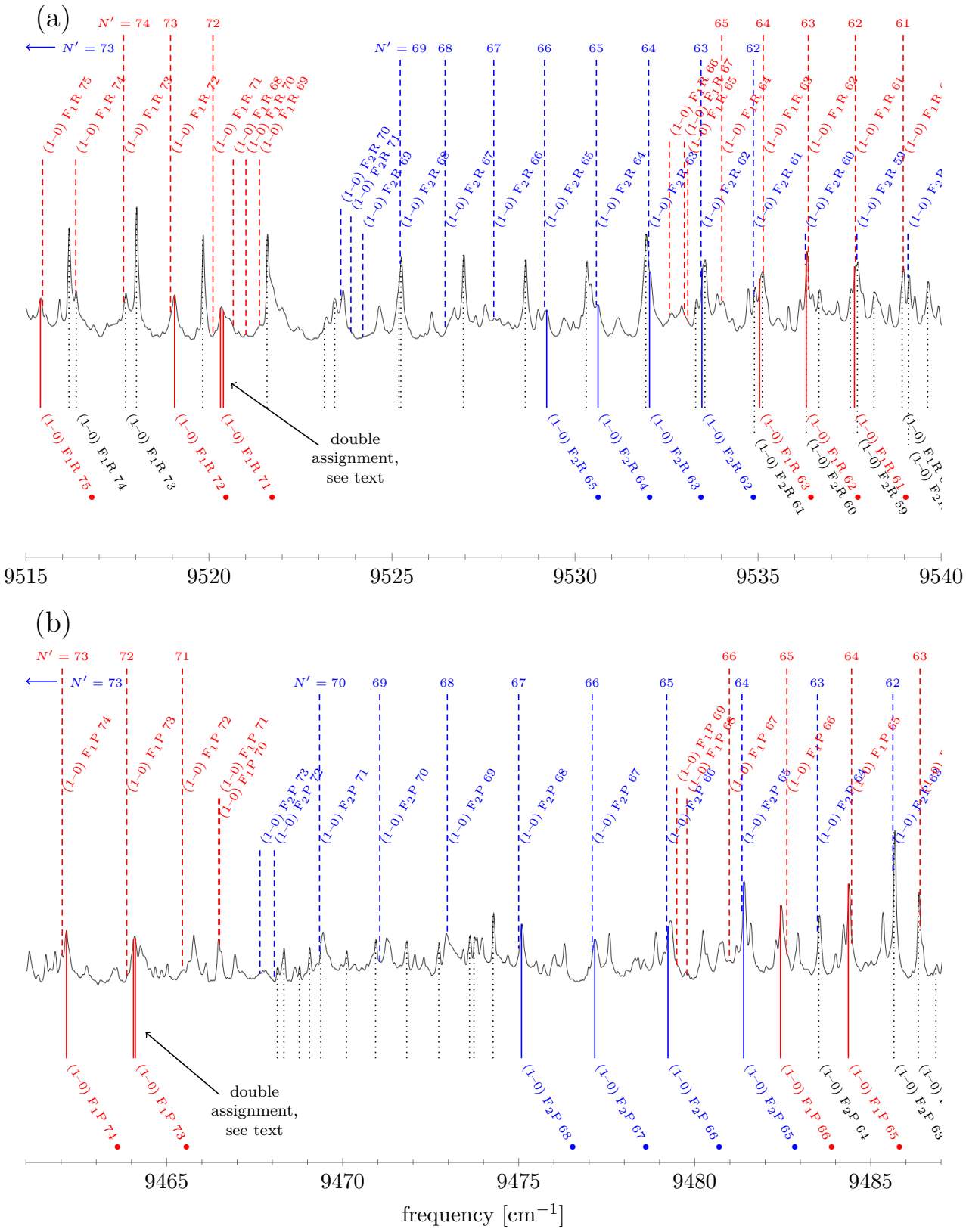

Figure 8.6: The R (a) and P (b) branches of the (1–0) band showing the perturbation at N' around 70. Assignments above the spectrum were determined with the deperturbation model; those below the spectrum were taken from the data set used for the fit. The black data were used for the deperturbation, the coloured lines with the mark (•) represent lines identified with the deperturbation model. Labels are omitted for lines that are not relevant to the discussion.

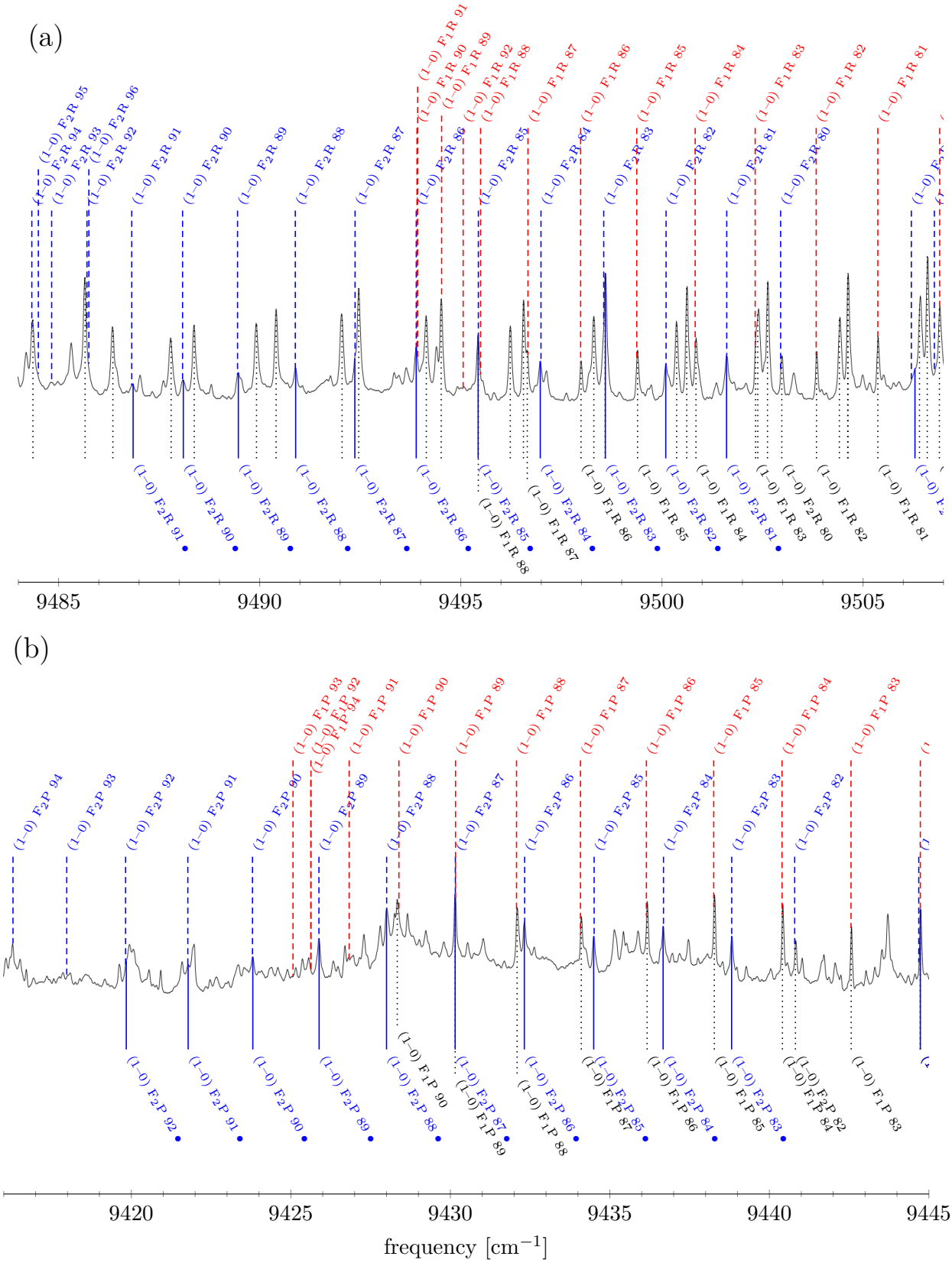

Figure 8.7: The R (a) and P (b) branches of the (1–0) band showing F_2 lines with N' beyond 79. Assignments above the spectrum were determined with the deperturbation model; those below the spectrum were taken from the data set used for the fit. The black data were used for the deperturbation, the coloured lines with the mark (•) represent lines identified with the deperturbation model. Labels are omitted for lines that are not relevant to the discussion.

Chapter 9

Discussion of the Model

The model from Chapter 6 was used to fit parameters that describe the coupling of the $(2)^2\Sigma^+$ state with the $(1)^2\Pi$ state to explain the perturbations discussed in Chapter 5. Chapter 7 and Chapter 8 explained how parameters were found that characterize not only the perturbations but also allow to predict formerly unidentified transition lines in the thermal emission spectrum. This chapter will discuss the insights gained by the description of the coupling and the limits of the model. The obtained spectroscopic constants will be presented.

9.1 Physical Considerations

The model used for deperturbing the LiSr spectrum includes the four vibrational $^2\Pi$ levels that are closest to each individual $^2\Sigma^+$ level with the same e/f symmetry. Six vibrational $^2\Pi$ states are included in total for all $^2\Sigma^+$ levels (see Figure 7.3). Figure 9.1 illustrates how the squared $^2\Sigma^+$ and $^2\Pi$ amplitudes of the eigenstates vary when the rotational ladders cross. (The plot includes only the $^2\Pi_{1/2}$ and $^2\Pi_{3/2}$ states closest to the $^2\Sigma^+$ state. The other two $^2\Pi$ amplitudes are generally too small to be recognized in the graphs.) A comparison with the list of satellite observations in Figure 5.1 (a) does not indicate a correlation of the appearance of satellites with perturbation centres. The satellites are then likely a product of fortunate experimental conditions rather than indicators of different scattering behaviour as conjectured in Section 5.3.3.

Figure 9.1 further depicts the change in energy due to the perturbation when compared with the Dunham model that was described in Chapter 1: they are larger than the deviations seen in Figure 5.2. The reason for this difference is that also the $(2)^2\Sigma^+$ Dunham parameters were changed for the deperturbation. The coupling to $(1)^2\Pi$ states has an influence even on not perceivably perturbed $(2)^2\Sigma^+$ states. The eigenstates of the coupling matrix are therefore subject to a systematic energy shift and need different Dunham parameters than the uncoupled $(2)^2\Sigma^+$ states to compensate for that shift. All observed $(2)^2\Sigma^+$ states should be regarded as perturbed by the $(1)^2\Pi$ state, with the states close to avoided crossings featuring a more perceivable energy shift.

Figure 7.4 shows how much the modelled transition frequencies deviate from the observed ones. The observations are generally well characterized, except near the perturbation centres. The only perturbation that could be completely bridged with the deperturbed model is the one in the F_1 system around $v' = 0, N \approx 75$. Since the perturbation centres indicate the closest energetic approach of the $(1)^2\Pi$ levels to the $(2)^2\Sigma^+$ levels, this exception implies that the $(1)^2\Pi$ energy levels are not modelled with sufficient accuracy to predict the energetic shift of the $(2)^2\Sigma^+$ states that are perturbed most.

With knowledge of only one side of a perturbation, the centre position and strength

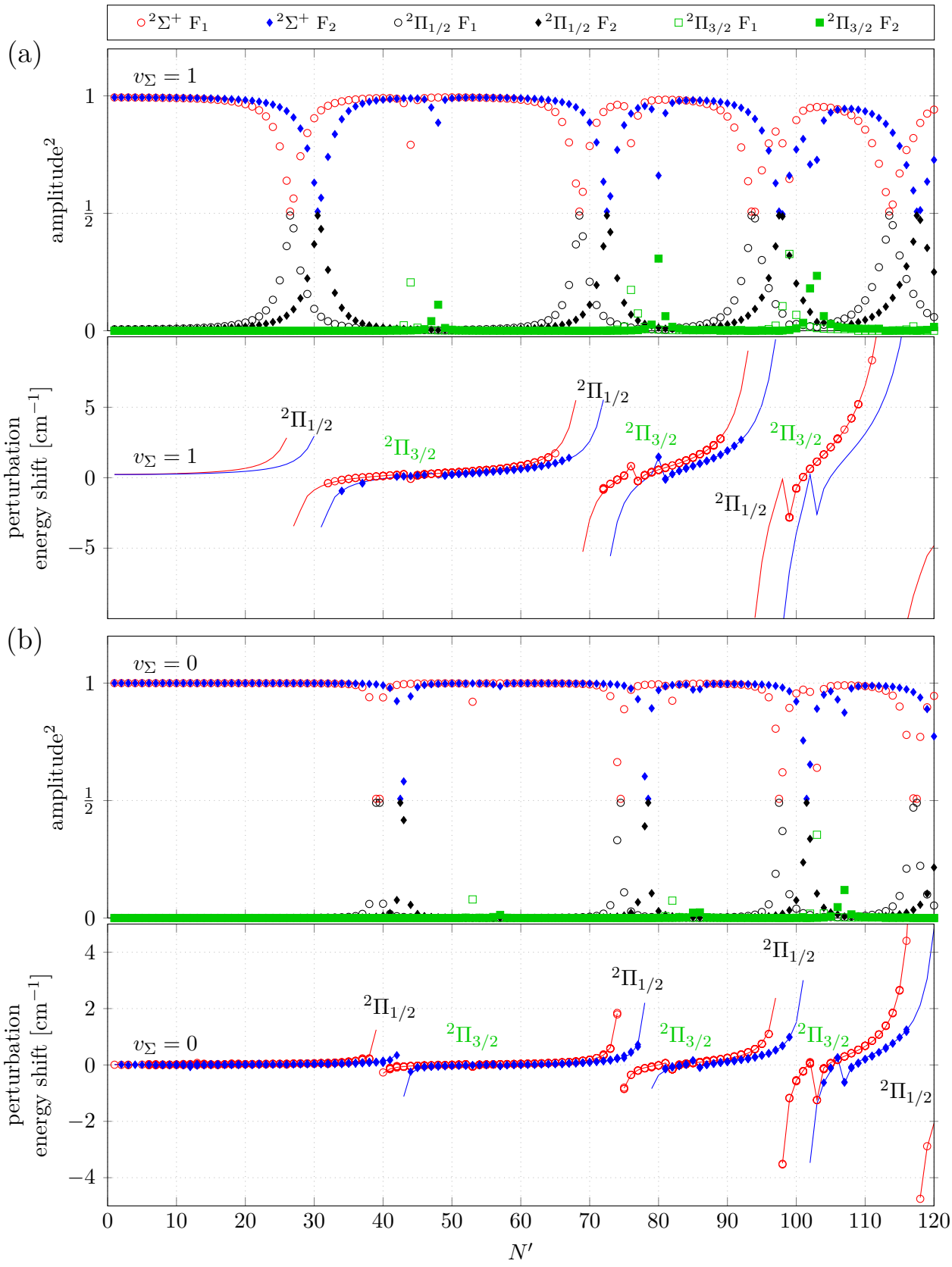

Figure 9.1: Changes in the $(2)^2\Sigma^+$ states due to the coupling to the $(1)^2\Pi$ states for the $v_\Sigma = 1$ and $v_\Sigma = 0$ levels ((a) and (b)). The upper plots in the two parts of the figure show the squares a^2, b^2, c^2 of the components of the states $a\,|v_\Sigma, {}^2\Sigma^+_{1/2}, N, \mathrm{F}_i\rangle + b\,|v_\Pi, {}^2\Pi_{1/2}, N, \mathrm{F}_i\rangle + c\,|v'_\Pi, {}^2\Pi_{3/2}, N, \mathrm{F}_i\rangle$. Only the $^2\Pi_{1/2}$ and $^2\Pi_{3/2}$ states that are energetically closest to the $^2\Sigma$ state are shown here. The lower plots illustrate the $(2)^2\Sigma^+$ energy shift due to the coupling. The lines represent modelled data and the symbols indicate observed states. The labels indicate whether the perturbation is due to a $^2\Pi_{1/2}$ or a $^2\Pi_{3/2}$ crossing.

of that particular perturbation cannot be derived reliably, making an extrapolation of the model beyond a perturbation centre difficult. For $N > 115$ in the $v' = 0$ rotational ladder, a few F_1 R lines were identified that lie beyond the perturbation centre, but the corresponding P lines could not be identified since they are surrounded by stronger (0–1) lines. The first perturbation in the $v' = 1$ rotational ladder, discussed in Section 8.1.4, hindered the description of the (1–0) band head. The (1–1) band head is visible, but the perturbation in this band is difficult to see due to the (0–0) band. Lines in the (1–2) band are very difficult to make out near the band head and the closest assigned line is F_1 R 39. Consequently, the (1–0) band head is most suitable for evaluating the quality of the deperturbation model for the $v' = 1$ levels. As described in Section 8.1.4, extending the data set towards the band head did improve its calculated frequency, although a noticeable difference between the calculation and the observed band head position remained. Because data was available for only one side of this perturbation, the extrapolation to the (1–0) band head could only give information about the lower-energetic vibrational level ($v_\Pi = 5$, see Figure 7.3) and the corresponding overlap integral. Possibly, the absence of the $v_\Pi = 6$ level in the model led to an asymmetric energy shift for the $(2)^2\Sigma^+$ states with $v' = 1, N' < 27$ (for F_1) and as a result to an insufficient description of the lower rotational levels and the band head. Extending the coupling matrix to include the three closest $^2\Pi_{1/2}$ and $^2\Pi_{3/2}$ levels, so that the $v_\Pi = 6$ level was covered for the known side of the perturbation, did, however, not improve the description of the band head position. On these grounds, the restriction of the model to only the two $\left|^2\Pi_{1/2}, v_\Pi, J, {}^e/_f\right\rangle$ and two $\left|^2\Pi_{3/2}, v_\Pi, J, , {}^e/_f\right\rangle$ states that are energetically closest to each rovibrational $^2\Sigma^+$ state seems to be a good choice. It keeps the number of model parameters low and considering more vibrational levels adds no direct benefit.

The intensity drop of the $(2)^2\Sigma^+$–$X(1)^2\Sigma^+$ transitions near the perturbations, as seen in Figure 5.3, can be explained with the smaller transition dipole moment for $(1)^2\Pi$–$X(1)^2\Sigma^+$ transitions that was also calculated by the ab-initio works. $(1)^2\Pi$–$X(1)^2\Sigma^+$ transitions could potentially have an enhanced transition dipole moment when the $(1)^2\Pi$ states are strongly coupled to a $(2)^2\Sigma^+$ state. These transitions could then be searched for in the thermal emission spectrum. However, no such lines were identified. The $^2\Sigma^+$ amplitudes fall below $\sqrt{2/3}$ for at most four states per perturbation, as can be seen Figure 9.1. These are also the states that are the least well modelled ones and could in most cases not be reliably predicted or confirmed. Accordingly, there can only be few corresponding $(1)^2\Pi$ states with a sufficiently strong transition dipole moment from their $^2\Sigma^+$ component to be expected in the thermal emission spectrum. Their identification might be as difficult as for the missing $(2)^2\Sigma^+$ levels.

9.2 Parameter Uncertainties

The Dunham parameters for the $(2)^2\Sigma^+$ and $(1)^2\Pi$ states in Hund's coupling case (a) are presented in Table 9.1. The $X(1)^2\Sigma^+$ parameters and their uncertainties were taken from Table 5.2. They are the parameters for Hund's coupling case (b). To calculate the energies in Hund's case (a) from them, see the end of Section 6.4.1. The fitted coupling parameters and overlap integrals are given in Tables 9.2 and 9.3.

Table 9.1: Modelled Dunham and spin-rotation parameters for the first two $^2\Sigma^+$ states and the first $^2\Pi$ state of $^7Li^{88}Sr$. The parameters give an accurate description for levels with $N < 116, v = 0, 1$ for both $^2\Sigma^+$ states and $40 \leq N \leq 63, v = 2$ in the $X(1)^2\Sigma^+$state. The $(1)^2\Pi$ parameters given here describe the vibrational states around the observed $(2)^2\Sigma^+$ levels. They are labeled $v_\Pi = 0$ to 5 in the deperturbation model. Their absolute vibrational quantum number is not known. The $X(1)^2\Sigma^+$ parameters were taken from Table 5.2. All values are given in cm^{-1}.

Y_{0n}	Y_{1n}	Y_{2n}	γ_{0n}	γ_{1n}	n
$X(1)^2\Sigma^+$ Hund's case (b)					
0	1.830781(39) $\times 10^2$	$-3.1018(17) \times 10^0$	$8.18(37) \times 10^{-3}$	$-5.04(11) \times 10^{-4}$	0
$2.074024(45) \times 10^{-1}$	$-3.4164(18) \times 10^{-3}$	$-5.724(78) \times 10^{-5}$	-	-	1
$-1.08317(50) \times 10^{-6}$	$-3.540(19) \times 10^{-8}$	$-6.628(71) \times 10^{-9}$	-	-	2
-	-	-	-	-	3
$-2.309(15) \times 10^{-16}$	$-1.1953(51) \times 10^{-16}$	-	-	-	4
$(2)^2\Sigma^+$ Hund's case (a)					
$9.39206(20) \times 10^3$	1.814273(39) $\times 10^2$	-	$4.55(21) \times 10^{-2}$	$7.90(17) \times 10^{-4}$	0
$1.895372(41) \times 10^{-1}$	$-7.1642(38) \times 10^{-4}$	-	$-7.96(36) \times 10^{-8}$	-	1
$-8.1774(38) \times 10^{-7}$	$3.577(19) \times 10^{-9}$	-	-	-	2
$4.536(30) \times 10^{-12}$	-	-	-	-	3
$-1.671(11) \times 10^{-17}$	-	-	-	-	4
$(1)^2\Pi$ Hund's case (a)					
$8.21144(18) \times 10^3$	2.816061(60) $\times 10^2$	$-4.7567(26) \times 10^0$	-	-	0
$2.690497(58) \times 10^{-1}$	$-4.1686(22) \times 10^{-3}$	-	-	-	1
$-2.3333(11) \times 10^{-6}$	$1.6694(90) \times 10^{-8}$	-	-	-	2
$8.506(55) \times 10^{-11}$	-	-	-	-	3
$-2.816(18) \times 10^{-15}$	-	-	-	-	4

Table 9.2: Overlap integrals $V_{\Sigma\Pi}$ between the $(2)^2\Sigma^+$ and $(1)^2\Pi$ states as used for the deperturbation. The left and right values are V_{const} and V_J according to equation (7.3.1). See the text for an estimate of the uncertainties.

v_Π	$v_\Sigma = 0$		$v_\Sigma = 1$	
	V_{const}	V_J	V_{const}	V_J
0	0.5 [a]	-	0.5 [a]	-
1	2.57	-	0.5 [a]	-
2	1.01	4.47×10^{-5}	5.66	-
3	0.689	9.05×10^{-6}	3.36	2.27×10^{-5}
4	0.326	2.00×10^{-5}	2.61	-1.13×10^{-4}
5	0.0296	-	1.05	4.03×10^{-5}
6	0.5 [a]	-	0.98 [b]	-

[a] These parameters were kept fixed during the fit.
[b] This parameter was not fitted but is an estimate from the ab-initio publication [Pot+17].

Table 9.3: Fitted coupling parameters of the $(2)^2\Sigma^+$–$(1)^2\Pi$ system in cm^{-1}. The magnitude of $[p \cdot d_{\Sigma\Pi}]$ and $[p \cdot B_{\Sigma\Pi}]$ is correlated with the overlap integrals given in Table 9.2. See the text for details.

parameter	value
$[p \cdot d_{\Sigma\Pi}]$	7.17(15)
$[p \cdot B_{\Sigma\Pi}]$	0.001228(23)
A_Π	155.52(70)

$(2)^2\Sigma^+$ Parameters

The parameters of the upper rovibronic states were obtained by fitting the $(2)^2\Sigma^+$ energies, which in turn were computed by adding the observed transition frequencies to the energies calculated with the $X(1)^2\Sigma^+$ parameters. The $X(1)^2\Sigma^+$ state is well characterized by the Dunham series, as can be read in Section 5.4. The standard deviation of the $X(1)^2\Sigma^+$ states calculated with the parameters from the linear fit is approximately $0.02\,\mathrm{cm}^{-1}$ and the observed transition frequencies have an average uncertainty of $0.02\,\mathrm{cm}^{-1}$ (see Chapter 3), so that the constructed $(2)^2\Sigma^+$ states can be expected to have an average uncertainty of about $0.03\,\mathrm{cm}^{-1}$. The relative uncertainty of the transition frequencies is approximately $10000\,\mathrm{cm}^{-1}/\,0.02\,\mathrm{cm}^{-1} = 0.00002$. In principle, this value can be taken as the relative uncertainty of the $(2)^2\Sigma^+$ Y_{00} parameter. This parameter is, however, strongly correlated with the vibrational Dunham parameters and will have a higher uncertainty because of this.

For the description of only one perturbation (see Section 7.1), the $X(1)^2\Sigma^+$ and $(2)^2\Sigma^+$ Dunham parameters[a] were fitted alternatively in an iterative process until their change from one iteration step to the next converged against the estimated standard deviation (see [Sch+17b] for details). Such an iteration was deemed unnecessary for the present model since the electronic ground state was described independently of the $(2)^2\Sigma^+$ state by using only frequency differences, thereby eliminating information about the other state. Due to the large number of fluorescence experiments (see Figure 5.1), the information about the ground state was sufficient to model it in the relevant quantum number range. Consequently, any change in the $(2)^2\Sigma^+$ description will have no effect on the $X(1)^2\Sigma^+$ parameters. To confirm this assumed independence, new frequency difference data were created from the newly identified transition lines (see Chapter 7). The amended data were then used for a new fit of the ground state parameters, but the fit quality did not change compared to that discussed in Section 5.4. Because the $X(1)^2\Sigma^+$ parameters were found independently of the observed $(2)^2\Sigma^+$ levels, nothing can be gained from iteratively fitting the parameters of the ground and excited states. The energies of the $(2)^2\Sigma^+$ and $(1)^2\Pi$ states used in the coupled model are plotted in Figure 7.3.

All Dunham parameters except Y_{00} describe the energetic differences between the rovibrational levels of an electronic state. Only the first two vibrational levels were observed and their difference is given by Y_{10}. The higher-order terms Y_{m0} with $m > 1$ were set to zero. The difference of two vibrational levels with the same N has a maximal uncertainty of $0.06\,\mathrm{cm}^{-1}$, so the vibrational spacing, and therefore the Y_{10} parameter, have a relative experimental uncertainty of around $0.06\,\mathrm{cm}^{-1}/180\,\mathrm{cm}^{-1} = 0.0003$ (see Table 9.1 for the parameter values). The situation is similar to the ground state fit portrayed in Section 5.4. For the ground state, the relative uncertainty of the vibrational parameters is around 0.0002 due to the experimental uncertainty of $0.04\,\mathrm{cm}^{-1}$ for the frequency differences. Due to the large number of observations, the linear ground state fit specified a relative statistical uncertainty that is one order or magnitude smaller. For both fits, the magnitudes of the data uncertainties and of the parameters are similar, so in

[a] Note that the parameters γ'_{00} , γ'_{10} and γ'_{01} were used for the perturbation. The reason for their inclusion is that already the Dunham model for both $^2\Sigma^+$ states required spin-rotation parameters for the $(2)^2\Sigma^+$ state (see Section 5.1.2).

general the minimal relative uncertainty for the $(2)^2\Sigma^+$ parameters can be assumed to be like in the linear fit.

In contrast, the upper state parameters were not obtained by a linear fit. They depend on the nonlinear fit strategy as well as the uncertainty of the data. For these reasons, the higher uncertainty given by the relative uncertainty of the energy levels can be an adequate choice when one wants to be cautious. The deperturbation fit has a weighted standard deviation of $\overline{\sigma} = 0.79$. This means that, albeit the perturbation centres are not well modelled, many observed $(2)^2\Sigma^+$ levels are better modelled than their experimental uncertainty. Consequently, an adequate uncertainty of a parameter will lie somewhere between one similar to the uncertainty of the same ground state parameter and the relative experimental uncertainty. For most parameters, the latter is an order of magnitude larger than the former. The former uncertainties are given in Table 9.1 for the $(2)^2\Sigma^+$ and $(1)^2\Pi$ parameters.

There are many combinations of rotational levels from which energy differences can be constructed. The higher the involved N are, the higher the energy difference used to find the rotational constant, and the smaller is the relative uncertainty of Y_{01}. The high rotational levels need the parameters Y_{02}, Y_{03} and Y_{04} (and Y_{12} and Y_{13} for the vibrational dependency) to be properly described. The relative magnitude between these higher-order parameters and the primary rotational constant Y_{01} is, however, not so large that the higher-order parameters would dominate the description of the high rotational energy levels[b]. Because of this, the fit of the rotational parameters can be expected to take many observations into account that have a relative uncertainty in the order of 0.00001 or lower. When comparing the Dunham parameters for the $X(1)^2\Sigma^+$ and $(2)^2\Sigma^+$ states given in Table 9.1, each Y'_{mn} has generally the same magnitude as its corresponding Y''_{mn}, within one order of magnitude. The range of rotational quantum numbers is more or less the same for both electronic sates, so it is a reasonable assumption that the relative uncertainties of the $(2)^2\Sigma^+$ parameters are not very different from those of the ground state parameters. This fit was not as straightforward as the linear ground state fit, though, so it seems nevertheless prudent to assume the uncertainties of the rotational parameters to be an order of magnitude higher than for the $X(1)^2\Sigma^+$ parameters, as in the case of the vibrational constant.

$(1)^2\Pi$ and Coupling Parameters

The fitted coupling parameters (and overlap integrals) are not directly grounded in frequency observations. The deviations seen in Figure 5.2, which are the primary source of information about the coupling constants, are also dependent on the energetic position of the unseen $(1)^2\Pi$ states. Because there are only discrete data points available, the energy shift from the perturbation can approximated with many similar crossing geometries (see Figure 6.2). As a consequence, the fitted $(1)^2\Pi$ state parameters may vary depending on the available data, the initially guessed parameters and the fit strategy. The crossing geometry is in principle given by the differences of the $(2)^2\Sigma^+$ and $(1)^2\Pi$ parameters that lead to a crossing of the rotational ladders. Describing several perturbations at once with a small set of parameters (see Section 7.2) does set rigid limits to the crossing parameters.

[b] $(N = 120)(N = 120 + 1) \times Y_{01} \gg \left|[(N = 120)(N = 120 + 1)]^2 \times Y_{02}\right|$

However, the description of the geometries is hindered by the density of the available discrete data points in the perturbations. Different geometries can lead to highly similar data deviations (as seen in Figure 6.2) and it is not plausible to assume to find an ideal parameterization with the few available data points.

To estimate an uncertainty for the coupling parameters, the development of their values when adding more and more data was taken into consideration. For this, the magnitudes of the fit parameters from a model that described the crossing points, coupling strength and $^2\Pi_{1/2}$–$^2\Pi_{3/2}$ splitting relatively well (see Section 7.3), over some intermediate steps to the model that incorporates the expanded data set (see Chapter 7) were compared. These different parameter sets approximate the same physical system with different amounts of available information. Since the $(1)^2\Pi$ energies are only known through the coupling to the $(2)^2\Sigma^+$ levels, the $(1)^2\Pi$ parameters result from the crossings of the two energy ladders and are additionally dependent on the coupling constants. The $(1)^2\Pi$ parameters are therefore correlated with the $(2)^2\Sigma^+$ parameters. The relative change of a parameter during these iteration steps was taken to be the parameter's uncertainty. For most of the $(2)^2\Sigma^+$ Dunham parameters, this change is one order of magnitude larger than the assumed statistical uncertainty from the ground state fit and thus consistent with the experimental uncertainty. By contrast, the changes of the $(1)^2\Pi$ Dunham parameters are about three orders of magnitude higher than the assumed statistical uncertainty. This is not surprising since the addition of more states near the perturbation centres allow to better characterize the crossing geometries. The uncertainty estimated with these considerations was applied to the coupling constants in Table 9.3. The parameter $[p \cdot B_{\Sigma\Pi}]$ is characterized mainly by the $^2\Sigma^+$–$^2\Pi_{3/2}$ coupling that is strongest at the $^2\Pi_{3/2}$ crossings. These crossings lead to sharp perturbations of the $(2)^2\Sigma^+$ rotational ladder (see Figure 9.1), so relatively few data points are available to describes these couplings. In contrast, the $^2\Pi_{1/2}$ crossings perturb more rotational $(2)^2\Sigma^+$ levels, so the fit of the stronger parameter $[p \cdot d_{\Sigma\Pi}]$ has also more data available. Since the data is quantized, a higher number of data points implies a better coverage of the observed energy range. Due to this difference in available data, the relative uncertainty of $[p \cdot B_{\Sigma\Pi}]$ should be assumed to be higher than that of $[p \cdot d_{\Sigma\Pi}]$. The uncertainties in Table 9.3 give a relative uncertainty of about 2 % for both parameters, but when the number of clearly perturbed $(2)^2\Sigma^+$ levels around the broad and sharp perturbations is considered (compare Table 5.1), the relative uncertainty for $[p \cdot B_{\Sigma\Pi}]$ is more likely around 10 % to 15 %. The identified spin-rotation coupling parameter A_Π has an uncertainty of only 0.5 %. It is derived from the energetic distance between the $^2\Pi_{1/2}$ and $^2\Pi_{3/2}$ crossings. The latter can be determined rather accurately thanks to their sharp perturbations (see Figure 5.2 for a plot over the rotational energy). The former, while having data gaps, are known well enough to interpolate the energy spacing of the $^2\Pi_{1/2}$ and $^2\Pi_{3/2}$ components to estimate A_Π.

Overlap Integrals

The overlap integrals between the $(2)^2\Sigma^+$ and the $(1)^2\Pi$ states, given in Table 9.2, are multiplied with the coupling parameters $[p \cdot d_{\Sigma\Pi}]$ and $[p \cdot B_{\Sigma\Pi}]$ to describe the coupling strength (see Section 6.5 for the derivation of the non-diagonal matrix elements). Because the magnitude of the perturbation effect depends on these products, the overlap integrals

and coupling parameters are directly correlated. The relative uncertainty of the overlap integrals is a few percent. The relative uncertainty of $[p \cdot d_{\Sigma\Pi}]$ is 2 % and the term $[p \cdot B_{\Sigma\Pi}]$ in the off-diagonal matrix element is too small compared with $[p \cdot d_{\Sigma\Pi}]$ to have a large influence on the uncertainty. The uncertainty for the overlap integrals is not explicitly given in Table 9.2.

The overlap integral $\langle v_\Sigma = 0 | v_\Pi = 0 \rangle$ influenced the fit weakly since it affects only a dozen $^2\Pi_{3/2}$ levels, which in most cases are the next-nearest state and thus have little impact. Indeed, the value of $\langle v_\Sigma = 0 | v_\Pi = 0 \rangle$ was arbitrarily set to 0.5. No adequate value was found with the fitting procedure, but a non-zero value should be assumed because otherwise there can never be a coupling to the vibrational state in question in the model. The overlap integral $\langle v_\Sigma = 1 | v_\Pi = 0 \rangle$ is not included in the fit because in the data at hand the $(2)^2\Sigma^+$ and $(1)^2\Pi$ energy levels are too far apart. The overlap integral $\langle v_\Pi = 6 | v_\Sigma = 1 \rangle$ was not fitted but taken from the ab-initio calculations for a v_Π shift of +12 (see Section 7.4) in order to model a symmetric perturbation of the $v_\Sigma = 1$ levels with low N, as described in Section 8.1.4. All overlap integrals found by the fit are positive. Since they appear in off-diagonal positions in the matrix, some of them may also have negative values. That would have no effect on the fit result. The values given in Table 9.2 can therefore only represent the absolute value of the physical overlap integrals.

The presented solution is the result of many iterative steps of a non-linear search for the minimum of the least-squares value. As such, it is most likely not the global minimum in the parameter space, but a very close local minimum. The quantitative and to a high degree the qualitative insights into the coupled $(1)^2\Pi$–$(2)^2\Sigma^+$ system would not be changed by a different parameterization of a similar or better quality.

9.3 Comparison of Spectroscopic Constants

Table 9.4 compares the spectroscopic constants for the three lowest electronic states of ^{7}Li^{88}Sr that were derived in this work with published ones. The data in the rows 'this work' are taken from Tables 9.1 and 9.3. In the case of the $(1)^2\Pi$ state, the constants T_e, ω_e and $\omega_e x_e$ are adapted for the mapping $v_\Pi \to v_\Pi + 12 \pm 1$, as discussed in Section 7.4. The value of the spin-rotation coupling constant A_Π is independent of the knowledge of the absolute vibrational quantum numbers. It could be derived with a low uncertainty, as was discussed earlier in this chapter. It amounts to broadly $^4/_5$ of the spin-rotation constant in the asymptotic (^{3}P) state of Sr (see Figure 1.1).

For the two $^2\Sigma^+$ states, the ab-initio constants are within ≈ 10 % of the experimentally determined values, but the $^2\Pi$ state shows larger disagreements. Since the survey of the $(1)^2\Pi$ state was performed indirectly via a handful of local observations and the vibrational quantum number assignment remains uncertain, this inconsistency is not surprising.

Table 9.4: Comparison of measured spectroscopic constants of ^{7}Li^{88}Sr with results of other authors. The present work is a continuation of [Sch+17b], so the comparison with [Sch+17b] is omitted here. All values are given in cm^{-1} except R_e, which is given in Å.

	Method	R_e	D_e	$\omega_e \approx \mathrm{Y}_{10}$	$\omega_e x_e \approx -\mathrm{Y}_{20}$	$B_e \approx \mathrm{Y}_{01}$	T_e	A_Π	Ref.
$\mathrm{X}(1)^2\Sigma^+$	CIPSI	3.48	2587	184.9	-	0.21	0		[GAD10][a]
	UCCSD(T)	3.55	2367	182.2	-	-	0		[Kot+11]
	CCSD(T)	3.531	2226.4	182.1	4.29	0.203	0		[Gop+11]
	SO-MS-CASPT2	3.579	2075.3	168.60	-	0.204	0		[Gop+13][b]
	MRCI	3.57	2471	181	-	-	0		[PHE16][c]
	MRCI	3.574	2483	179.1	3.22	-	0		[Pot+17][b]
	MCSCF/MRCI	3.590	2550.1	186.69	-	0.203	0		[Zei+18][a]
	spectroscopy	3.537	-	-	-	0.207	0		[Ste16]
	spectroscopy	3.540482(38)[d]	-	183.07181(39)	3.1018(17)	0.2074024(45)	0		this work
$(2)^2\Sigma^+$	SO-MS-CASPT2	3.785	6860.5	186.91	-	0.170	9488.63		[Gop+13][b]
	MRCI	3.728	7811	183.0	1.08	-	9375		[Pot+17][b]
	MCSCF/MRCI	3.874	6619.1	171.05	-	0.174	8702.25		[Zei+18][a]
	spectroscopy	3.702	-	-	-	-	9390		[Ste16]
	spectroscopy	3.703582(40)[d]	-	181.4273(39)	-	0.1895372(41)	9392.06(20)		this work
$(1)^2\Pi$	SO-MS-CASPT2	3.104	10672.3	289.68	-	0.274	5586.98	117.85	[Gop+13][b]
	MRCI	3.130	11868	269.5	1.54	-	5317	-	[Pot+17][b]
	MCSCF/MRCI	3.193	9689.2	258.37	-	0.257	5719.31	-	[Zei+18][a]
	spectroscopy	2.854463(31)[d]	-	345.3(21)[e]	4.7567(26)	0.3190727(69)[e]	4147.2(38)[e]	155.5(27)	this work
	spectroscopy	-	-	281.061(60)[f]	4.7567(26)	0.2690497(58)[g]	8211.44(18)[f]	155.5(27)	this work

[a] assuming ^{7}Li^{88}Sr, as no choice of isotopes is mentioned
[b] values were converted to ^{7}Li^{88}Sr
[c] values were converted to ^{7}Li^{88}Sr, assuming ^{7}Li^{84}Sr as in [Pot+17]
[d] calculated from Y_{01}
[e] linearly extrapolated with $v_\Pi \to v_\Pi + 12$
[f] taken from fit with low v_Π
[g] taken from fit with low v_Π; $B_{v\approx 12}$ rather than B_e

Chapter 10

Summary and Outlook

This thesis described the experimental observation and theoretical modelling of the near-infrared spectrum of $^{7}Li^{88}Sr$. The vibrational (0–0), (0–1), (1–0), (1–1) and (1–2) bands of the $(2)^2\Sigma^+$–$X(1)^2\Sigma^+$ system were observed and their rotational branches were described for rotational quantum numbers up to 119. By characterizing couplings between the $(2)^2\Sigma^+$ and $(1)^2\Pi$ states, a local description of the $(1)^2\Pi$ state, which was not directly observed from the spectrum, was also achieved. This last chapter will discuss how far the applied methods and insights can be used to further analyze LiSr and other alkali-alkaline earth diatomics.

10.1 Observed Perturbations

The perturbations in the near-infrared spectrum, caused by a coupling between the $(2)^2\Sigma^+$ state and the $(1)^2\Pi$ state, were described with a local model. This model shows consistency with published ab-initio calculations. The discussion at the end of Chapter 7 pointed out that the most perturbed $(2)^2\Sigma^+$ levels are not well modelled, however. The reasons for this shortcoming are the lack of data in the corresponding spectral regions and the complex parameter space of the local model. An iterative deperturbation allowed to obtain more data in the perturbed regions, which led to a better description of the coupling parameters and the $(1)^2\Pi$ state. As Chapter 8 exemplified, a satisfactory description of the centres of the larger perturbations, with the strongest coupling, could still not be achieved in this way. More information about the $(1)^2\Pi$ might allow to use a more global description, for example with the $(1)^2\Pi$ potential energy curve, leading to a more accurate description of the observed perturbations.

10.2 Further Vibrational Bands

Five vibrational bands, belonging to the lowest vibrational levels in the $(2)^2\Sigma^+$ and $X(1)^2\Sigma^+$ potential curves, were rigorously investigated. Other bands, with slightly higher v' levels, were tentatively assigned in Figure 4.1. Figure 10.1 displays several vibrational bands with $v \leq 3$ that were identified with the updated Dunham coefficients. Lines from these bands were not used for any fits, but their band heads are reproduced within $3\,cm^{-1}$ with the known parameters. The (2–3) band seems to be confined to a relatively large structure around $9250\,cm^{-1}$. It has a dense band head to the right which is soon followed by a turnaround to the left. Due to the spin-rotation coupling, there are two band heads that are about $2\,cm^{-1}$ apart. The spectral structure of the band heads resembles that of very strong peaks with a width of circa $1\,cm^{-1}$. The (0–0) branches are simply added on top of the (2–3) structure. These uncommon peaks were very early the target of laser

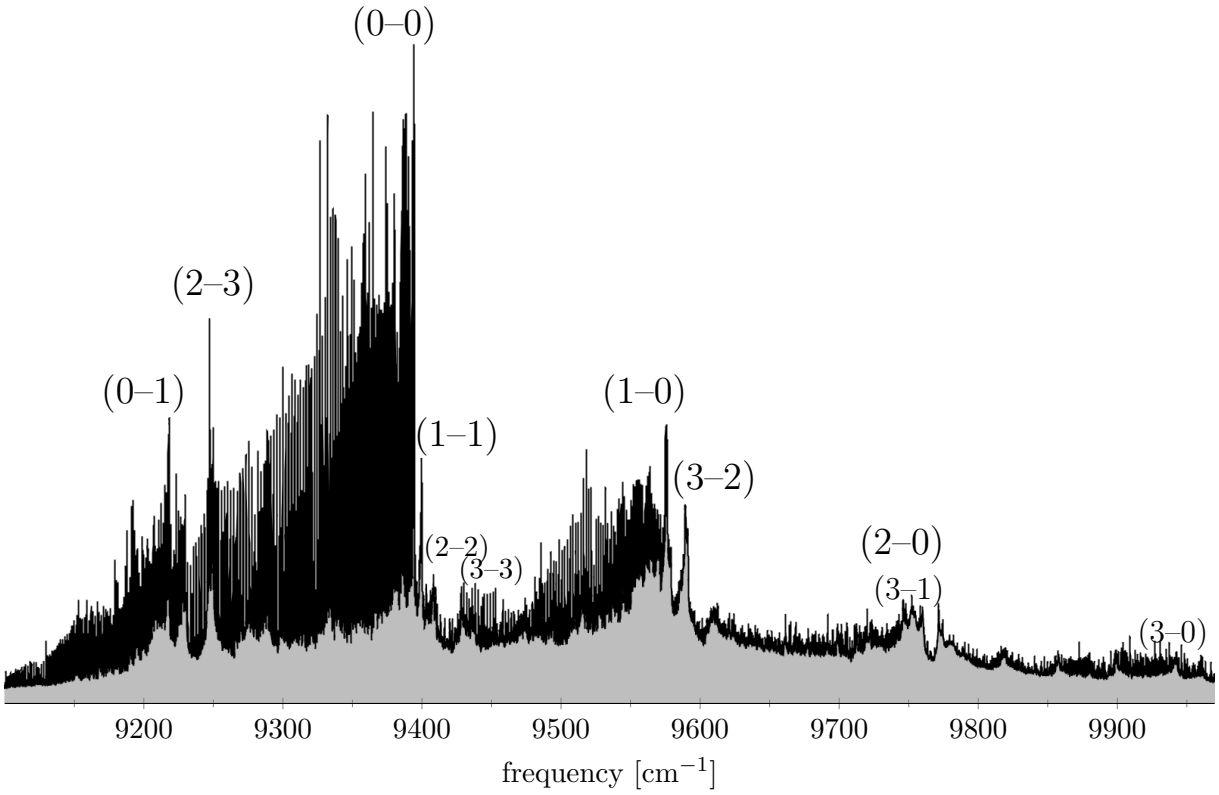

Figure 10.1: Vibrational bands of ^{7}Li^{88}Sr identified with the X(1)$^{2}\Sigma^{+}$ and (2)$^{2}\Sigma^{+}$ Dunham parameters. The (3–3) structure is a turnaround at $N \approx 60$. The (2–1) band head is close to the (1–0) band head but it is not visible in this figure.

experiments. However, these never yielded fluorescence. The individual (2–3) lines are too weak compared with (0–0) lines so that laser-induced fluorescence lines would be hard to spot. The strong structures only arise due to the sheer number of overlapping lines. For comparison, the (2–0) band is much weaker. The fluorescence lines would in most cases also occur close to the laser frequency and hence be overshadowed by the comparatively strong laser stray light.

The lack of further vibrational bands in the spectrum can be explained with weak Franck-Condon factors for transitions for which the quantum numbers v' and v'' are too far apart. Such a distribution of Franck-Condon factors has been reported to be a general feature in alkali-alkaline earth diatomics [Pot+17] and was also observed in KCa [Ger+17]. Because of such a distribution, the strongest vibrational bands would mostly overlap. According to the Boltzmann distribution, the states with lowest v are most populated and therefore their bands dominate the spectrum.

For these reasons, no long vibrational fluorescence progressions can be expected from laser experiments. Using the so far established molecular parameters to incrementally advance towards higher vibrational levels does not seem worthwhile because the extrapolation to higher bands is not precise enough to assign single transition lines and the intensity of higher vibrational bands drops rapidly.

10.3 Other Isotopologues

This work is restricted to the isotopologue $^{7}Li^{88}Sr$. No signs of other isotopologues were observed (see Section 4.2.1). On one hand, this simplified the interpretation of the thermal emission spectrum, but on the other hand it also prohibited to learn anything about the mass effects on the molecular constants. Due to the natural abundances of Li and Sr, the $^{7}Li^{88}Sr$ spectrum can be expected to dominate the spectra of natural LiSr samples (see Table 4.1). To study the mass effects, a heat pipe would need to be prepared with a sample of e.g. ^{6}Li in a high concentration and a natural Sr sample. The chemical properties should not change, so that the experimental setup presented in Chapter 2 can be used without further adaption.

10.4 Hyperfine Structure

$^{7}Li^{88}Sr$ is expected to have a hyperfine structure due to the spin of the Li nucleus. Section 3.1 discussed that the observed lines were too broad to see a hyperfine splitting of the rotational lines and that the small magnetic field measured in the oven did also not broaden the lines beyond the expected Doppler width. Recording Doppler-free spectra of spectral peaks via saturation spectroscopy [Dem88] could be a straightforward extension of the current setup. Splitting the diode laser into two counter-propagating beams, scanning the frequency and observing the absorption with photodiodes are all simple tasks. Furthermore, the plotting of absorption signals together with the frequency measured by the wavemeter is already allowed by the frequency stabilization setup. Figure 10.2 displays the absorption spectrum of two rotational lines in a narrow frequency range For these absorption spectra, the intensity of a laser beam passed through the LiSr heat pipe was measured. The setup used here was a conceptual test of the laser and cannot resolve the hyperfine structure. The low frequency uncertainty, especially of the left absorption spectrum, can be improved by transforming the photo diode current to a better dynamic range of the analog-to-digital converter. The laser frequency was set to a transition line known from the thermal emission spectrum and scanned via current modulation of the laser diode. The scan range was set as high as possible without encountering mode hopping. The figure shows that the corresponding frequency range is large enough to cover a single rotational line. The experimental resolution of the registered absorption spectra in the given examples is higher than that from the Fourier transform spectrometer[a]. The frequency resolution of such a laser registration can easily be improved further by decreasing the scan rate of the laser frequency, so that the hyperfine structure should be detectable.

If an upgraded setup should lead to the observation of a hyperfine structure in a single rotational transition line, the effect of the rotational quantum number on the hyperfine levels should be observable by comparing the hyperfine splitting of transition lines [TS55, p. 199] with low, intermediate and high rotational quantum numbers. The present work allows to easily find transition lines to almost any rotational quantum number up to 119 (compare Figure 8.1). If LiSr molecules with other isotopologues are observed, their hyperfine structure can be compared with that of $^{7}Li^{88}Sr$. Due to the different nuclear

[a] This comes at the price of a vastly decreased frequency range.

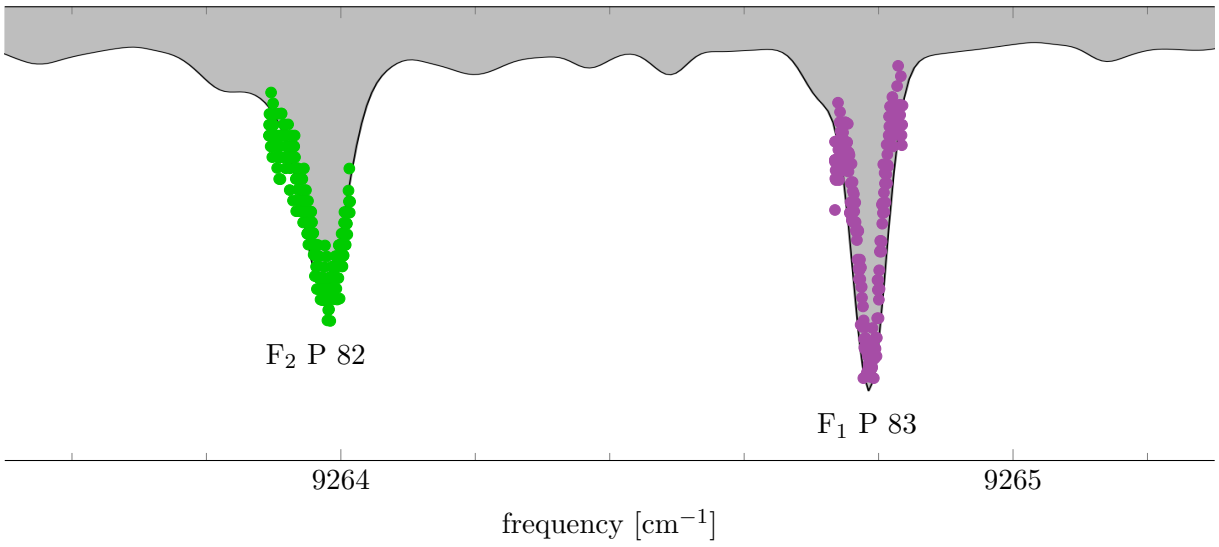

Figure 10.2: Absorption spectra (dots) of a scanned diode laser passed through a typical LiSr heat pipe. Two experiments were performed on individual rotational lines of the (0–0) band. The inverted thermal emission spectrum is shown in black for reference.

spins of other isotopologues, the hyperfine structure would be different, which would allow an independent fit of the hyperfine coupling constants. Furthermore, if a sufficiently high magnetic field can be applied to the vapour in the heat pipe, its effect on hyperfine lines could be recorded for different field strengths. The time scale for a laser scan is small enough to record many such spectra with small magnetic field strength steps, which would help the assignment of the hyperfine components.

10.5 Further Electronic Transitions of LiSr

The rotational energy ladder of the LiSr ground state was rigorously described and its lowest vibrational energy levels can be estimated. Using this knowledge, rovibronic transitions from other electronic states can readily be assigned by using frequency differences as described in Section 4.4. According to ab-initio calculations [Gop+13; Pot+17], $(3)^2\Sigma^+$–$X(1)^2\Sigma^+$ and $(4)^2\Sigma^+$–$X(1)^2\Sigma^+$ transitions have a three to four times higher transition dipole moment than $(2)^2\Sigma^+$–$X(1)^2\Sigma^+$ transitions. According to Figure 1.1, the $(3)^2\Sigma^+$–$X(1)^2\Sigma^+$ spectrum can be expected between 13000 cm^{-1} and 15000 cm^{-1}. The $(3)^2\Sigma^+$ state could conceivably couple with both the $(1)^2\Pi$ and the $(2)^2\Pi$ states, which would necessitate a more complex coupling model to explain the spectrum. However, the strength of the couplings depends on the overlap integrals, so that the perturbations may be weak.

Figure 10.3 displays high absorptions in the LiSr heat pipe at the expected transition frequencies. These appear to be molecular vibrational bands and begin at the Li $^2\mathrm{P} \rightarrow {}^2\mathrm{S}$ and/or Sr $^3\mathrm{P} \rightarrow {}^1\mathrm{S}$ transition lines near 15000 cm^{-1} [San13] at temperatures of about 600 °C. Since the near-infrared spectrum of LiSr starts to emerge at temperatures higher than 850 °C, these bands are probably Li_2 bands. They extend to 11000 cm^{-1} at 915 °C. The thermal emission spectrum at these low frequencies was explained solely by Li_2 lines (see Section 4.1.1), which indicates that the observed bands between 11000 cm^{-1} and

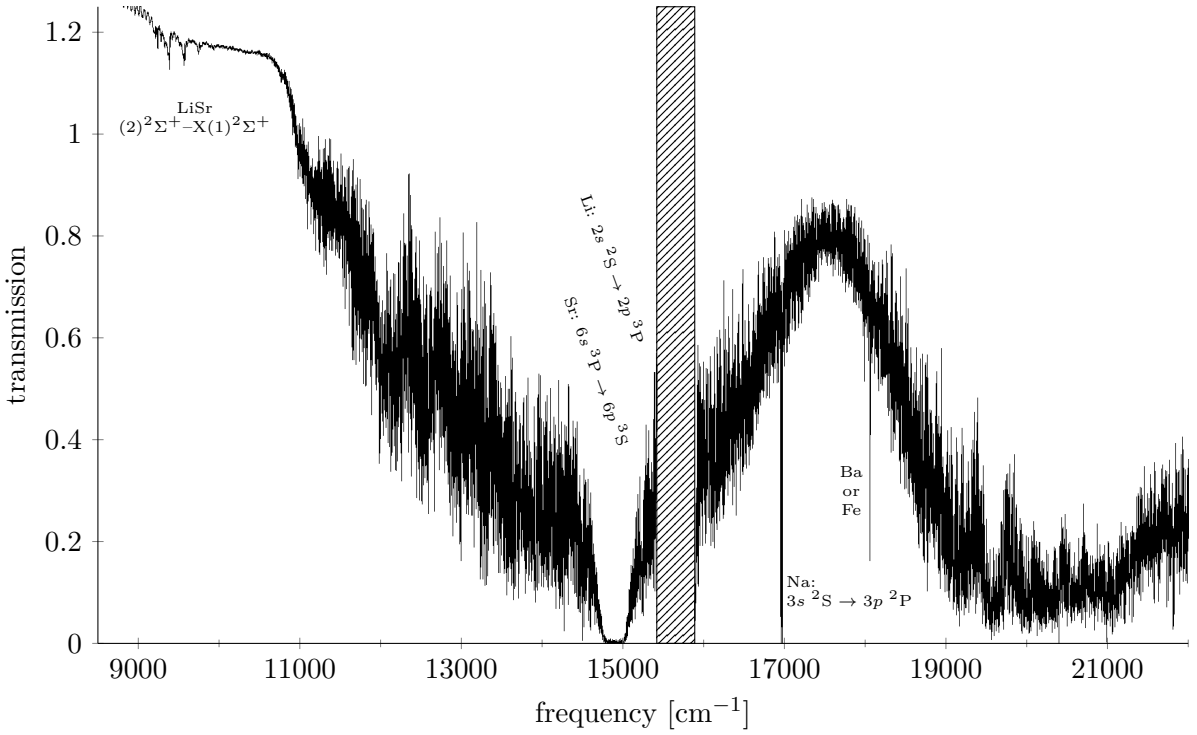

Figure 10.3: Transmission spectrum of the LiSr sample in the heat pipe at 915 °C. Due to blackbody radiation of the oven, the spectrum could not accurately be normalized to the light source but exceeds unity. Around 15600 cm^{-1}, an optical filter in the spectrometer forbids registering the spectrum.

15000 cm^{-1} are indeed Li_2 bands. The absorption around 9400 cm^{-1} in Figure 10.3 resembles the form of the thermal emission bands seen in Figure 4.1. A comparison of these LiSr absorption bands with the absorption around 14000 cm^{-1} suggests that the latter are much stronger than the LiSr transitions and will hinder the discovery of LiSr lines in the thermal emission or LIF spectra. The $(4)^2\Sigma^+$–$X(1)^2\Sigma^+$ system, at higher frequencies, can be expected to be similarly obscured. For these two higher-lying $^2\Sigma^+$ states, a search for bands by looking for fluorescence lines with the vibrational spacing of the LiSr ground state would be the first step to localize the transitions to the ground state. This approach was tested in the range above 11000 cm^{-1} for the $(3)^2\Sigma^+$ state (compare Figure 1.1), but the search was unsuccessful due to the strong overlap with the Li_2 spectrum.

The presence of Li_2, Sr_2 and possible molecules formed by impurities in the metal samples (e.g. Na) complicates finding LiSr lines. All these molecules cannot simply be removed from the heat pipe (or at least the imaged region) without also destroying the LiSr sample. The direct spectroscopic analysis of the heat pipe makes it difficult to identify LiSr lines in the dense spectra without prior knowledge. Because the Li_2 spectrum seems to be the largest obstacle in finding the $(3)^2\Sigma^+$–$X(1)^2\Sigma^+$ spectrum, a comparison of the absorption spectrum of the LiSr heat pipe with the spectrum of a heat pipe filled only with Li could help to identify extra lines in the LiSr heat pipe spectrum. Since the LiSr heat pipe is a simple single-section heat pipe without special attention to temperatures or temperature gradients, such a comparison should be reasonable, as long as the Li_2, and not Sr_2, dominates the absorption spectrum.

There are experimental schemes to record 2D spectra that allow to detect coherences between spectral lines, i.e. lines that have a common quantum state from the same molecule can be distinguished from lines that have the same frequency but come from transitions between different states (or different molecules). Chapter 3 in [Zha08] gives a well-written overview of the principles. To scan a broad spectrum in a reasonable time, the use of laser pules, providing a broad frequency range, seems necessary. Such experiments would need to be set up around the heat pipe because they are too different from the current setup.

The $(1)^2\Pi$ was only observed indirectly at vibrational quantum numbers around 15. The published ab-initio transition dipole moments for $(1)^2\Pi$–$X(1)^2\Sigma^+$ transitions in the relevant nuclear distance range are at most ten percent of those of $(2)^2\Sigma^+$–$X(1)^2\Sigma^+$ transitions. According to [Pot+17], transitions from $(1)^2\Pi$ states with $v' \approx 15$ have relatively high Franck-Condon factors for only a few vibrational $X(1)^2\Sigma^+$ states with $v'' > 3$. From the perturbations it is known that transitions from these vibrational states will lie in the $(2)^2\Sigma^+$–$X(1)^2\Sigma^+$ spectrum (because the $(1)^2\Pi$ and $(2)^2\Sigma^+$ rotational ladders are crossing). Thus, these relatively strong $(1)^2\Pi$–$X(1)^2\Sigma^+$ transitions would appear at lower frequency than the observed $(2)^2\Sigma^+$–$X(1)^2\Sigma^+$ spectrum. No $(1)^2\Pi$–$X(1)^2\Sigma^+$ transitions were identified in the thermal emission spectrum, though. If they are very weak, and added onto the $(2)^2\Sigma^+$–$X(1)^2\Sigma^+$ spectrum, the noise amplitude of the thermal emission spectrum needs to be reduced in order to detect them, i.e. more recordings of the thermal emission spectrum need to be averaged. Assuming the present signal-to-noise ratio to be just a bit too low to prevent the observation of $(1)^2\Pi$–$X(1)^2\Sigma^+$ transitions, the number of scans needs to be 100000 or more to give a sufficient signal-to-noise ratio. Even when the time is invested, the presence of the $(2)^2\Sigma^+$–$X(1)^2\Sigma^+$ spectrum would greatly hinder the identification of long $(1)^2\Pi$–$X(1)^2\Sigma^+$ series.

Transitions from low vibrational $(1)^2\Pi$ states should occur around $5000\,\mathrm{cm}^{-1}$ (see Figure 1.1). The lower vibrational states are more populated than higher states and the Franck-Condon factors are more favourable for low vibrational $X(1)^2\Sigma^+$ states. However, the low transition dipole moment, multiplied with the factor of the cube of the frequency for the transition probability, implies a relatively weak $(1)^2\Pi$–$X(1)^2\Sigma^+$ spectrum around $5000\,\mathrm{cm}^{-1}$. The Si-based photodetector used in this work has no response for frequencies below $8500\,\mathrm{cm}^{-1}$. A different avalanche photo diode[b] based on InGaAs was used to see if $(1)^2\Pi$–$X(1)^2\Sigma^+$ spectra can be recorded. The results were negative for the following reasons: The InGaAs detector is far noisier than the Si detector, thus considerably increasing the necessary number of scans. The size of its active area is also less than 1 % of that of the Si detector. According to the producer, the area cannot be increased in the foreseeable future because InGaAs detectors would then be too noisy to be useful. The smaller size worsens the signal-to-noise ratio further because less light from the experiment is registered. Moreover, the thermal background radiation is higher at these wavelengths for temperatures around 1000 °C, which leads to a larger background signal and more noise in the spectrum. In these tests, even the strongest band heads of the $(2)^2\Sigma^+$–$X(1)^2\Sigma^+$ were difficult to make out in averaged spectra, which implies that the search for weaker spectra in the farther infrared with such a detector would take much time, if it is possible at all.

[b] G8931-20 from Hamamatsu

To observe the expected $(1)^2\Pi$–$X(1)^2\Sigma^+$ spectrum around $5000\,\mathrm{cm}^{-1}$, other methods need to be applied. An absorption spectrum of the heat pipe could be recorded with the InGaAs detector and a white light source. Due to the thermal background radiation (which in the tests had a similar intensity as the $(2)^2\Sigma^+$–$X(1)^2\Sigma^+$ spectrum), a meaningful normalization of the absorption spectrum cannot be achieved. However, the absorption of a scanned laser passed through the heat pipe could be recorded with a photodiode while the background radiation is screened by an aperture. As Figure 10.2 illustrates, there can be large gaps between rovibrational lines and changing the laser frequency in small enough steps until a line is encountered can take a considerable amount of time. The approximate knowledge of the rotational and vibrational spacing for the higher vibrational levels of the $(1)^2\Pi$ state and the $X(1)^2\Sigma^+$ Dunham parameters can help to estimate the spacing of rotational lines, but the considerable offset due to the electronic energy cannot yet be guessed with high accuracy. For these reasons, such experiments should start at higher frequencies than the expected (0–0) transitions and proceed towards lower frequencies. In this way, transitions to higher vibrational $(1)^2\Pi$ states are likely to be encountered along the way, even if the estimation of the lowest transition were wrong.

Since the transition frequencies to many rotational states of the first two vibrational $(2)^2\Sigma^+$ states are known, these states can purposefully be addressed via laser light to search for transitions from the $(2)^2\Sigma^+$ state to other electronic states via two-photon excitations. Fluorescence from the higher-lying electronic states to the $X(1)^2\Sigma^+$ state induced by such a scheme would have a considerable blue-shift and would be thus easy to identify. However, the published ab-initio works only communicated $X(1)^2\Sigma^+$ transition dipole moments and none between two excited electronic states, so the prospects for such experiments remain nebulous at this point in time.

10.6 Other Alkali-Alkaline Earth Diatomics

The methods presented in this thesis were successfully used to analyze the near-infrared spectrum of LiSr and to model the lowest electronic states of the molecule.

Due to the relatively low reduced mass of LiSr, it is possible to recognize individual transition lines in the thermal emission spectrum. This facilitated the assignment of quantum numbers to spectral lines and allowed to expand the assignment using only the thermal emission spectrum. For molecules with larger reduced mass, the spectra can be expected to be more dense and the distinction between single lines becomes impossible at high temperatures. In these cases, the use of LIF spectra, as described in Chapter 4, will be greatly helpful for the assignment of quantum numbers. An example is KCa [Ger+17]. The rotational constants of KCa are about five times lower than those of LiSr and the line density in the thermal emission spectrum did not allow to resolve individual lines. The information from many LIF spectra was an immense help to find the rotational constants and quantum numbers. Fluorescence experiments in the band heads also helped to disentangle the more complex vibrational spectra.

LiSr is an experimentally uncomplicated molecule. Experiments with LiCa [Iva+11b] and KCa [Ger+17] required heat pipes with carefully designed temperature differences in order to observe the target molecules. Moreover, the heat pipes had a limited lifetime

because the material slowly left the imaged regions or because metallic structures formed in the colder parts of the heat pipes and obscured the view. In the case of KCa, there were visible vortices in the gas in the heat pipe, which suggests a dynamic state of the sample. In contrast, a heat pipe with one temperature section filled with Li and Sr in their natural abundance produces a clearly distinguishable thermal emission spectrum after a short initial waiting period. When that state is reached, the oven can simply be switched off and at a later time switched on again, without loss of quality of the spectrum. A LiSr heat pipe lasts for several months. The spectrum also reveals only the dominant lines of the most common isotopologue; other lines were not seen.

In conclusion, LiSr provides a valuable test bed for experimental methods regarding the spectroscopy of alkali-alkaline earth diatomics.

Appendix A

Dipole Transition

All spectral lines presented in this work are, in good approximation, electromagnetic dipole transitions. The presence of an electromagnetic field carrying an energy $E_{\phi'} - E_{\phi''}$ gives rise to a non-zero probability of finding a molecule in a state $|\phi''\rangle$ when it was in a state $|\phi'\rangle$. Examining the dipole matrix element between the two states gives insight to what kinds of transitions can be expected in the observed spectra. To describe the transition dipole moment in Hund's coupling case (b), the quantum numbers Λ, N, S, J and M are needed. The first four describe different rotational quantum numbers in the molecular reference frame and are known from Chapter 1. The total angular momentum, $\vec{J}$, is a constant of motion and is fixed in a laboratory reference frame. Its projection onto an axis in the laboratory frame is given by M.

This derivation will make heavy use of the book of Edmonds [Edm96]. References to equations or sections in his book are given like '$[1.7]_{\text{Edm}}$'.

Dipole Interaction

The observed strength of a dipole transition between two rovibrational states $|v', \phi'\rangle = |v', \Lambda', (N', S')J', M'\rangle$ and $|v'', \phi''\rangle = |v'', \Lambda'', (N'', S'')J'', M''\rangle$ is:

$$\left|\left\langle v', \phi' \middle| \vec{\mu} \cdot \vec{E} \middle| v'', \phi'' \right\rangle\right|^2 \quad \propto \quad \left|\left\langle v', \phi' \middle| \vec{\mu} \cdot \vec{p} \middle| v'', \phi'' \right\rangle\right|^2 \tag{A.1a}$$

$$\overset{[5.2.4]_{\text{Edm}}}{=} \left|\left\langle v', \phi' \middle| \sum_{k=-1}^{1} (-1)^k \mu^1_k \, p^1_{-k} \middle| v'', \phi'' \right\rangle\right|^2 \tag{A.1b}$$

$$\overset{[5.2.1]_{\text{Edm}}}{=} \left|\left\langle v', \phi' \middle| \sum_{k=-1}^{1} (-1)^k \left(\sum_{m=-1}^{1} \mu^1_m \mathcal{D}^1_{mk}(\omega) \right) p^1_{-k} \middle| v'', \phi'' \right\rangle\right|^2 \tag{A.1c}$$

$$= \left|\left\langle v', \phi' \middle| \sum_{m=-1}^{1} \mu^1_m \mathcal{D}^1_{m0}(\omega) \middle| v'', \phi'' \right\rangle\right|^2 \tag{A.1d}$$

$$= \left|\left\langle \phi' \middle| \sum_{m=-1}^{1} \mathcal{D}^1_{m0}(\omega) \middle| \phi'' \right\rangle\right|^2 \times \text{FCF} \tag{A.1e}$$

The interaction between an electric dipole $\vec{\mu}$ and an electric field $\vec{E}$ with polarization vector $\vec{p}$ is written in tensorial form (A.1b). The dipole moment is then rotated with a rotational operator $\mathcal{D}^1_{mk}(\omega)$, where ω represents the Euler angles, into the laboratory frame (A.1c). Since the experiment is not sensitive to different polarizations, it is assumed that only linearly polarized light is observed. Accordingly, only the component $k = 0$, representing linear polarization, is kept (A.1d). Finally, the matrix element of the transition dipole element and different vibrational states is expressed as the Franck-Condon factor (A.1e).

By using the Wigner-Eckart theorem ($[5.4.1]_{\text{Edm}}$), the M-dependency can be described by a Wigner 3-j symbol:

$$\left|\left\langle\phi'\right|\sum_{m=-1}^{1}\mathcal{D}^1_{m0}(\omega)\left|\phi''\right\rangle\right|^2 = \left|\sum_{m=-1}^{1}\begin{pmatrix} J' & 1 & J \\ -M' & 0 & M\end{pmatrix}\langle\chi'||\mathcal{D}^1_{m\cdot}(\omega)||\chi''\rangle\right|^2 \tag{A.2}$$

Here, $|\chi\rangle$ is an abbreviation for $|\Lambda(N,S)J\rangle$. Phase factors of ±1 are omitted for this whole discussion since their square is always unity.

Since the spin S is not affected by the electronic dipole moment, the relation $[7.1.7]_{\text{Edm}}$ can be used, which introduces a 6-j symbol:

$$\begin{aligned}\left|\sum_{m=-1}^{1}\begin{pmatrix} J' & 1 & J'' \\ -M' & 0 & M''\end{pmatrix}\langle\chi'||\mu^1_m\,\mathcal{D}^1_{m\cdot}(\omega)||\chi''\rangle\right|^2 &= \left|\sum_{m=-1}^{1}\begin{pmatrix} J' & 1 & J'' \\ -M' & 0 & M''\end{pmatrix}\times\right. \\ &\left.\sqrt{2J'+1}\sqrt{2J''+1}\begin{Bmatrix} N' & J' & S'=1/2 \\ J'' & N'' & 1\end{Bmatrix}\langle\psi'||\mu^1_m\,\mathcal{D}^1_{m\cdot}(\omega)||\psi''\rangle\right|^2\cdot\delta_{S'S''}\end{aligned} \tag{A.3}$$

As above, a reduced vector $|\psi\rangle = |\Lambda, N\rangle$ was introduced.

Reduced Matrix Element

The values of the 3-j and 6-j symbols can be calculated, while an expression for the reduced matrix element in equation (A.3) is still needed. According to $[4.7]_{\text{Edm}}$, the rotation operators $\mathcal{D}^l_{mq}(\omega)$ are eigenfunctions of the angular momentum operator $\hat{L}$ with

$$\hat{L}^2\cdot\mathcal{D}^l_{mq}(\omega) = \hbar\,l(l+1)\cdot\mathcal{D}^l_{mq}(\omega), \tag{A.4a}$$

$$\hat{L}^{\text{lab}}_z\cdot\mathcal{D}^l_{mq}(\omega) = \hbar\,m\cdot\mathcal{D}^l_{mq}(\omega) \tag{A.4b}$$

and

$$\hat{L}^{\text{mol}}_z\cdot\mathcal{D}^l_{mq}(\omega) = \hbar\,q\cdot\mathcal{D}^l_{mq}(\omega). \tag{A.4c}$$

Therefore, $\mathcal{D}^l_{mq}(\omega)$ can be identified with the ket $|\Lambda, N, M_N\rangle$, where M_N is the projection of N onto an axis in the laboratory frame. The normalization is given by $[4.6.1]_{\text{Edm}}$:

$$\langle\Lambda,N,M_N|\Lambda,N,M_N\rangle = \frac{2N+1}{8\pi^2}\int_0^{2\pi}\int_0^{\pi}\int_0^{2\pi}\mathcal{D}^{*N}_{\Lambda M_N}(\omega)\mathcal{D}^N_{\Lambda M_N}(\omega)\overbrace{\mathrm{d}\alpha\sin\beta\,\mathrm{d}\beta\,\mathrm{d}\gamma}^{=:\mathrm{d}\omega} = 1 \tag{A.5}$$

The matrix element of the rotation operator is the integral

$$\begin{aligned}&\left\langle\Lambda',N',M'_N\right|\mathcal{D}^1_{mq}(\omega)\left|\Lambda'',N'',M''_N\right\rangle \\ &\quad= \frac{\sqrt{2N'+1}\sqrt{2N''+1}}{8\pi^2}\int_0^{2\pi}\int_0^{\pi}\int_0^{2\pi}\mathcal{D}^{*N'}_{\Lambda' M'_N}(\omega)\mathcal{D}^1_{mq}(\omega)\mathcal{D}^{N''}_{\Lambda'' M''_N}(\omega)\,\mathrm{d}\omega \\ &\quad\overset{[4.2.7]_{\text{Edm}}}{=} \frac{\sqrt{2N'+1}\sqrt{2N''+1}}{8\pi^2}\int_0^{2\pi}\int_0^{\pi}\int_0^{2\pi}(-1)^{-\Lambda'-M'_N}\mathcal{D}^{*N'}_{-\Lambda'-M'_N}(\omega) \\ &\qquad\qquad\times\mathcal{D}^1_{mq}(\omega)\mathcal{D}^{N''}_{\Lambda'' M''_N}(\omega)\,\mathrm{d}\omega\end{aligned}$$

$$\overset{[4.6.2]_{\mathrm{Edm}}}{=} (-1)^{-\Lambda'-M'_N} \begin{pmatrix} N' & 1 & N'' \\ -\Lambda' & m & \Lambda'' \end{pmatrix} \begin{pmatrix} N' & 1 & N'' \\ -M'_N & q & M''_N \end{pmatrix} \sqrt{2N'+1}\sqrt{2N''+1}. \tag{A.6}$$

On the other hand, using again $[5.4.1]_{\mathrm{Edm}}$,

$$\left\langle \Lambda', N', M'_N \middle| \mathcal{D}^1_{mq}(\omega) \middle| \Lambda'', N'', M''_N \right\rangle = (-1)^{N'-M'_N} \begin{pmatrix} N' & 1 & N'' \\ -M'_N & q & M''_N \end{pmatrix} \langle \psi' || \mathcal{D}^1_{m\cdot}(\omega) || \psi \rangle \,. \tag{A.7}$$

Comparing equation (A.7) with equation (A.6) gives

$$\left| \langle \psi' || \mathcal{D}^1_{m\cdot}(\omega) || \psi \rangle \right|^2 = \begin{pmatrix} N' & 1 & N'' \\ -\Lambda' & m & \Lambda'' \end{pmatrix}^2 (2N'+1)(2N''+1). \tag{A.8}$$

Final Expression

Using the reduced matrix element from equation (A.8) in equation (A.3) yields

$$\left| \left\langle v', \phi' \middle| \vec{\mu} \cdot \vec{E} \middle| v'', \phi'' \right\rangle \right|^2 \propto \mathrm{FCF} \times \sum_{m=-1}^{1} (2J'+1)(2J''+1)(2N'+1)(2N''+1) \times \begin{pmatrix} J' & 1 & J'' \\ -M' & 0 & M'' \end{pmatrix}^2 \begin{pmatrix} N' & 1 & N'' \\ -\Lambda' & m & \Lambda'' \end{pmatrix}^2 \begin{Bmatrix} N' & J' & 1/2 \\ J'' & N'' & 1 \end{Bmatrix}^2 \cdot \delta_{S'S''}. \tag{A.9}$$

The 3-j and 6-j symbols in equation (A.9) represent scalar values that depend on the relation of their quantum numbers. They do not have to become quantitatively evaluated for this discussion but their properties are physically meaningful. The 3-j symbols of the form

$$\begin{pmatrix} J_1 & J_2 & J_3 \\ M_1 & M_2 & M_3 \end{pmatrix}$$

are zero, and thus describe an impossible transition $|\phi'\rangle \to |\phi''\rangle$ if one of the following conditions is violated:

$$M_1 + M_2 + M_3 = 0 \tag{A.10a}$$

$$|J_1 - J_2| \leq J_3 \leq |J_1 + J_2| \tag{A.10b}$$

$$J_1 + J_2 + J_3 \text{ even, if } M_1 = M_2 = M_3 = 0 \tag{A.10c}$$

With the conditions (A.10), the following selection rules can be derived from equation (A.9):

$$\text{(A.10a):} \qquad \Delta\Lambda = 0, \pm 1$$

$$\text{(A.10b):} \qquad \Delta J = \Delta N = 0, \pm 1$$

$$\text{but} \qquad J'/N' = 0 \nrightarrow J''/N'' = 0 \tag{A.11}$$

$$\text{(A.10a):} \qquad \Delta M = 0 \tag{A.12}$$

$$\text{(A.10a) \& (A.10c):} \qquad \Delta N = \pm 1 \quad \text{if } \Lambda' = 0 \rightarrow \Lambda'' = 0$$

The only further condition from the 6-j symbol is

$$J = N \pm 1/2. \tag{A.13}$$

Equation (A.10a) also implies that for a $^2\Sigma^+ \rightarrow^2 \Sigma^+$ transition only the $m = 0$ term does not vanish.

Evaluating the 3-j and 6-j symbols for different cases also allows to estimate the relative strength of certain transitions. For a transition with $J = N \pm 1/2 \rightarrow J = N \mp 1/2$, that is, $F_{1/2} \rightarrow F_{2/1}$, the 6-$j$ symbols grow with $1/\sqrt{N^4}$ and the 3-j symbols containing J and J' grow with $1/\sqrt{N^3}$ for large N and small M. For $J = N \pm 1/2 \rightarrow J = N \mp 1/2$, that is, $F_{1/2} \rightarrow F_{1/2}$, the 6-$j$ symbols grow with $1/\sqrt{N^2}$ and the 3-j symbols with $1/\sqrt{N}$. Therefore, $F_{1/2} \rightarrow F_{2/1}$ transitions can be expected to be considerably weaker than $F_{1/2} \rightarrow F_{1/2}$, the higher the rotational quantum number N is.

Appendix B

Deperturbation Program

The flowchart of the program used for the deperturbation (see Chapter 7) is given on the next page. The minimization steps in the grey area are handled by the software MINUIT [JR75]. The value to be minimized is calculated in the steps within the dashed border.

The matrices that are actually used to describe the coupling from Section 7.3 onwards have the following form for each observed $|(2)^2\Sigma^+, v_\Sigma, J, {}^{e}\!/\!_{f}\rangle$ state:

	$\left\vert v_\Sigma, {}^2\Sigma^{+,e/f}_{1/2}\right\rangle$	$\left\vert v^{(i)}_\Pi, {}^2\Pi_{1/2}{}^{e/f}\right\rangle$	$\left\vert v^{(ii)}_\Pi, {}^2\Pi_{1/2}{}^{e/f}\right\rangle$	$\left\vert v^{(iii)}_\Pi, {}^2\Pi_{3/2}{}^{e/f}\right\rangle$	$\left\vert v^{(iv)}_\Pi, {}^2\Pi_{3/2}{}^{e/f}\right\rangle$
$\left\langle v_\Sigma, {}^2\Sigma^{+,e/f}_{1/2}\right\vert$	$\boldsymbol{E^{\Sigma}_{\mathrm{Dun}}} - \boldsymbol{\gamma_\Sigma}/2\times$ $[1 \mp (J+1/2)]$ $\mp \boldsymbol{B_\Sigma}(J+1/2)$	$\boldsymbol{V^{(i)}_{\Sigma\Pi}}\cdot[\boldsymbol{p}\cdot\boldsymbol{d_{\Sigma\Pi}}]\cdot\frac{1}{2}$ $+\boldsymbol{V^{(i)}_{\Sigma\Pi}}\cdot[\boldsymbol{p}\cdot\boldsymbol{B_{\Sigma\Pi}}]\times$ $(1 \mp [J+1/2])$	$\boldsymbol{V^{(ii)}_{\Sigma\Pi}}\cdot[\boldsymbol{p}\cdot\boldsymbol{d_{\Sigma\Pi}}]\cdot\frac{1}{2}$ $+\boldsymbol{V^{(ii)}_{\Sigma\Pi}}\cdot[\boldsymbol{p}\cdot\boldsymbol{B_{\Sigma\Pi}}]\times$ $(1 \mp [J+1/2])$	$-\boldsymbol{V^{(iii)}_{\Sigma\Pi}}\cdot[\boldsymbol{p}\cdot\boldsymbol{B_{\Sigma\Pi}}]$ $\times\sqrt{J(J+1)-3/4}$	$-\boldsymbol{V^{(iv)}_{\Sigma\Pi}}\cdot[\boldsymbol{p}\cdot\boldsymbol{B_{\Sigma\Pi}}]$ $\times\sqrt{J(J+1)-3/4}$
$\left\langle v^{(i)}_\Pi, {}^2\Pi_{1/2}{}^{e/f}\right\vert$	$\boldsymbol{V^{(i)}_{\Sigma\Pi}}\cdot[\boldsymbol{p}\cdot\boldsymbol{d_{\Sigma\Pi}}]\cdot\frac{1}{2}$ $+\boldsymbol{V^{(i)}_{\Sigma\Pi}}\cdot[\boldsymbol{p}\cdot\boldsymbol{B_{\Sigma\Pi}}]\times$ $(1 \mp [J+1/2])$	$\boldsymbol{E^{\Pi}_{\mathrm{Dun}}}$ $-\boldsymbol{A_\Pi}/2$	0	$-\boldsymbol{B^{(i,iii)}_\Pi}\times$ $\sqrt{J(J+1)-3/4}$	$-\boldsymbol{B^{(i,iv)}_\Pi}\times$ $\sqrt{J(J+1)-3/4}$
$\left\langle v^{(ii)}_\Pi, {}^2\Pi_{1/2}{}^{e/f}\right\vert$	$\boldsymbol{V^{(ii)}_{\Sigma\Pi}}\cdot[\boldsymbol{p}\cdot\boldsymbol{d_{\Sigma\Pi}}]\cdot\frac{1}{2}$ $+\boldsymbol{V^{(ii)}_{\Sigma\Pi}}\cdot[\boldsymbol{p}\cdot\boldsymbol{B_{\Sigma\Pi}}]\times$ $(1 \mp [J+1/2])$	0	$\boldsymbol{E^{\Pi}_{\mathrm{Dun}}}$ $-\boldsymbol{A_\Pi}/2$	$-\boldsymbol{B^{(ii,iii)}_\Pi}\times$ $\sqrt{J(J+1)-3/4}$	$-\boldsymbol{B^{(ii,iv)}_\Pi}\times$ $\sqrt{J(J+1)-3/4}$
$\left\langle v^{(iii)}_\Pi, {}^2\Pi_{3/2}{}^{e/f}\right\vert$	$-\boldsymbol{V^{(iii)}_{\Sigma\Pi}}\cdot[\boldsymbol{p}\cdot\boldsymbol{B_{\Sigma\Pi}}]$ $\times\sqrt{J(J+1)-3/4}$	$-\boldsymbol{B^{(i,iii)}_\Pi}\times$ $\sqrt{J(J+1)-3/4}$	$-\boldsymbol{B^{(ii,iii)}_\Pi}\times$ $\sqrt{J(J+1)-3/4}$	$\boldsymbol{E^{\Pi}_{\mathrm{Dun}}}$ $+\boldsymbol{A_\Pi}/2$	0
$\left\langle v^{(iii)}_\Pi, {}^2\Pi_{3/2}{}^{e/f}\right\vert$	$-\boldsymbol{V^{(iv)}_{\Sigma\Pi}}\cdot[\boldsymbol{p}\cdot\boldsymbol{B_{\Sigma\Pi}}]$ $\times\sqrt{J(J+1)-3/4}$	$-\boldsymbol{B^{(i,iv)}_\Pi}\times$ $\sqrt{J(J+1)-3/4}$	$-\boldsymbol{B^{(ii,iv)}_\Pi}\times$ $\sqrt{J(J+1)-3/4}$	0	$\boldsymbol{E^{\Pi}_{\mathrm{Dun}}}$ $+\boldsymbol{A_\Pi}/2$

The bold terms are the ones to be determined by the fitting procedure. The others are given by the model introduced in Chapter 6. Some terms were fitted as a product with the factor p, which is indicated with square brackets (e.g. $[p \cdot B_{\Sigma\Pi}]$ is one fitting parameter). The off-diagonal rotational constants for the $^2\Pi$ states $B^{(v,v')}_\Pi$ depend on which vibrational $(1)^2\Pi$ states are involved. See Section 6.5 for details. The Dunham energies $E^{\Lambda}_{\mathrm{Dun}}$ depend on J and v. For $E^{\Sigma}_{\mathrm{Dun}}$, only the $(2)^2\Sigma^+$ parameters were modified during the fit, while the $\mathrm{X}(1)^2\Sigma^+$ parameters were never changed during the deperturbation. As in the matrix on page 70, upper signs are used in the e states matrices and lower signs in the f state matrices.

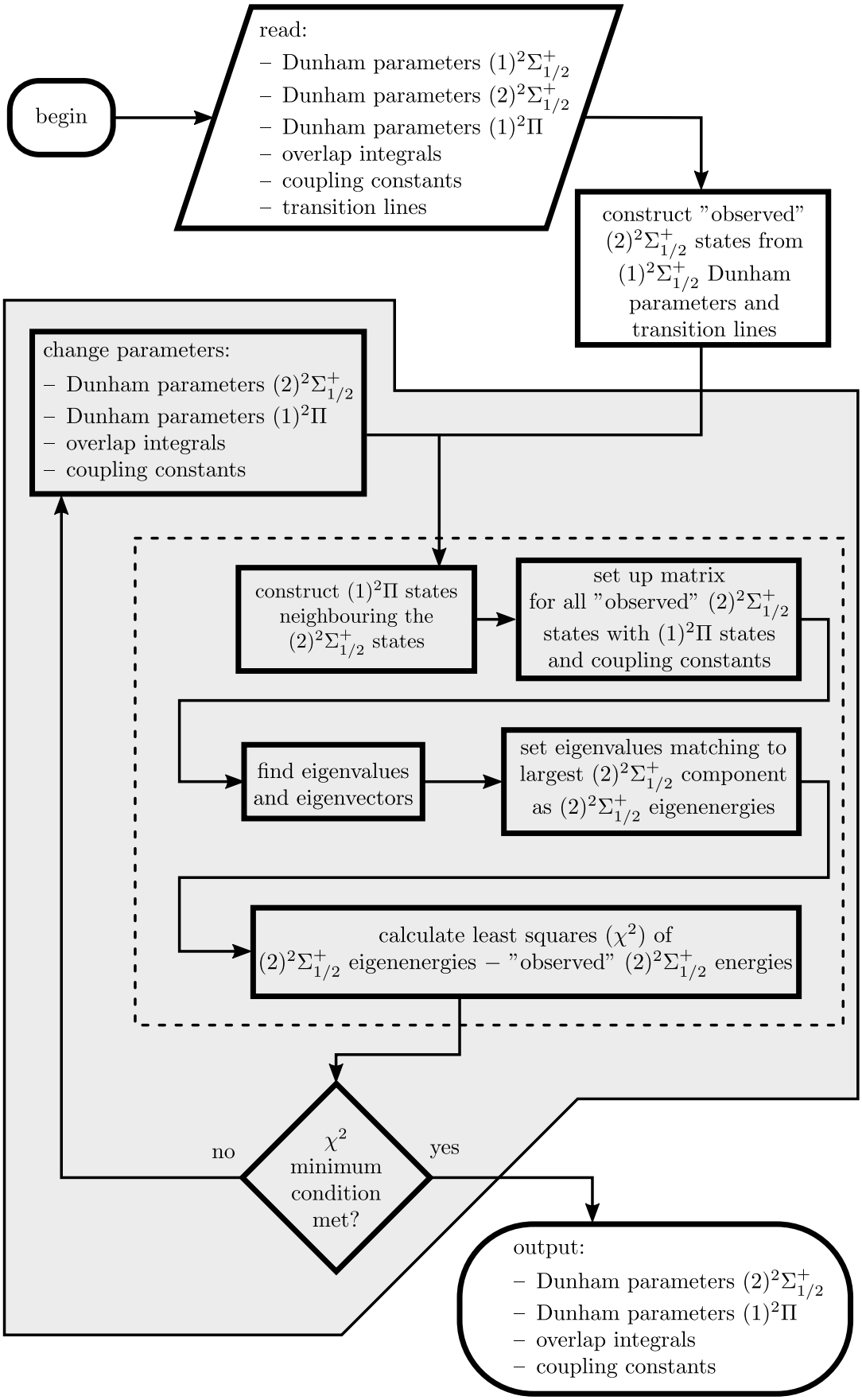
begin
read:
– Dunham parameters $(1)^2\Sigma^+_{1/2}$
– Dunham parameters $(2)^2\Sigma^+_{1/2}$
– Dunham parameters $(1)^2\Pi$
– overlap integrals
– coupling constants
– transition lines
construct "observed" $(2)^2\Sigma^+_{1/2}$ states from $(1)^2\Sigma^+_{1/2}$ Dunham parameters and transition lines
change parameters:
– Dunham parameters $(2)^2\Sigma^+_{1/2}$
– Dunham parameters $(1)^2\Pi$
– overlap integrals
– coupling constants
construct $(1)^2\Pi$ states neighbouring the $(2)^2\Sigma^+_{1/2}$ states
set up matrix for all "observed" $(2)^2\Sigma^+_{1/2}$ states with $(1)^2\Pi$ states and coupling constants
find eigenvalues and eigenvectors
set eigenvalues matching to largest $(2)^2\Sigma^+_{1/2}$ component as $(2)^2\Sigma^+_{1/2}$ eigenenergies
calculate least squares (χ^2) of $(2)^2\Sigma^+_{1/2}$ eigenenergies − "observed" $(2)^2\Sigma^+_{1/2}$ energies
χ^2 minimum condition met?
no
yes
output:
– Dunham parameters $(2)^2\Sigma^+_{1/2}$
– Dunham parameters $(1)^2\Pi$
– overlap integrals
– coupling constants

Appendix C

Physical Constants

This appendix serves as reference for the quantitative interpretation of the data presented in the work at hand. Here the numerical values of relevant natural constants and units other than from the International System of Units (SI) at the time of writing are given. Table C.1 lists all non-SI units with their conversion into SI units. Table C.2 gives numerical values of the physical constants encountered in this thesis.

Because the General Conference on Weights and Measures decided to redefine several base units of the SI [BIP] effective to 20th May, 2019, Table C.2 lists both the current constants from [MNT16] and the future ones. Since the spectral frequencies were measured in wavenumbers, and the value of the metre is not affected by the change to the SI, all presented molecular constants can be used in future. When converting them into energy units via equation (1.0.1b), there will be a small difference in the order of 10^{-9} between values calculated with old and new base units.

Table C.1: Non-SI units used in this thesis as taken from [Poi06; MNT16].

Name	Symbol	Magnitude	Dimension
Ångström	Å	10^{-10}	m
atomic mass unit	u	$1.660539040(20) \times 10^{-27}$	kg
bar	bar	10^{5}	Pa
millimetre of mercury	mmHg	≈ 133.322	Pa
electronvolt	eV	$1.6021766208(98) \times 10^{-19}$	J
wave number (frequency)	cm^{-1}	10^{2}	m^{-1}
wave number (energy)	cm^{-1}	10^{2}	m^{-1}
Gauss	G	10^{-4}	T
degree Celsius	°C	temperature [K] − 273.15	K

Table C.2: Physical constants used in this thesis in SI units.

Name	Symbol	Magnitude from [MNT16]	Magnitude [BIP]	Dim.
Boltzmann constant	k_B	$1.38064852(79) \times 10^{-23}$	1.380649×10^{-23}	$\mathrm{J\,K}^{-1}$
elementary charge	e	$1.6021766208(98) \times 10^{-19}$	$1.602176634 \times 10^{-19}$	C
Planck's constant	h	$6.626070040(81) \times 10^{-34}$	$6.62607015 \times 10^{-34}$	J s
vacuum speed of light	c	2.99792458×10^{8}	2.99792458×10^{8}	$\mathrm{m\,s}^{-1}$

Appendix D

Vapour Pressure

Here the vapour pressure data used for Figure 2.2 is given. Table D.1 lists the Antoine coefficients (A, B, C) for the first five alkali and alkaline earth metals and Yb as taken from [Yaw06]. The temperature ranges given in [Yaw06], the metals' melting points taken from [Win18] and the corresponding pressures are listed as well.

Temperatures are given in °C and pressures in mbar. Because [Yaw06] used °C as unit for temperature and mmHg as unit for pressure, the pressures P are calculated via

$$P[\text{mbar}] \approx 133.322\,\text{Pa} \times 10^{A-B/(T[^\circ\text{C}]+C)}.$$

See also Appendix C.

Table D.1: Antoine coefficients for the first five alkali and alkaline earth metals and Yb.

Element	A	B	C	T_{min}	$P(T_{\text{min}})$	T_{max}	$P(T_{\text{max}})$	T_{melt}	$P(T_{\text{melt}})$
Ba	6.477	7779.9	266.45	638.00	1.00×10^{-2}	1897.00	1.01×10^{3}	727.00	5.90×10^{-2}
Be	8.084	13697.0	148.52	823.85	1.33×10^{-6}	2483.85	1.01×10^{3}	1287.00	4.65×10^{-2}
Ca	7.118	7084.4	188.26	351.85	1.34×10^{-6}	1483.85	1.01×10^{3}	842.00	2.33×10^{0}
Cs	6.675	3515.8	255.57	21.85	1.34×10^{-6}	671.00	1.01×10^{3}	28.44	2.63×10^{-6}
K	6.974	4143.9	254.47	63.20	1.13×10^{-6}	1949.85	1.66×10^{5}	63.38	1.15×10^{-6}
Li	8.269	8884.6	307.17	180.54	1.50×10^{-10}	3811.85	1.73×10^{6}	180.54	1.50×10^{-10}
Mg	7.706	6303.0	216.22	243.85	1.35×10^{-6}	1090.00	1.01×10^{3}	650.00	3.58×10^{0}
Na	7.488	5300.1	267.61	97.82	1.29×10^{-7}	2299.85	3.54×10^{5}	97.72	1.27×10^{-7}
Rb	7.000	3926.2	265.16	35.85	1.21×10^{-6}	688.00	1.01×10^{3}	39.31	1.70×10^{-6}
Sr	6.832	6128.7	168.97	308.85	1.35×10^{-6}	1382.00	1.01×10^{3}	777.00	3.01×10^{0}
Yb	7.281	6060.2	181.30	463.00	1.00×10^{-2}	1196.00	1.01×10^{3}	824.00	2.39×10^{1}

Appendix E

Literature Overview of Alkali-Alkaline Earth Diatomics

The following pages give an tabulated overview of the existing[a] literature concerned with alkali-alkaline earth (A-AE) diatomics. There are publications which are concerned with ionized A-AE molecules (e.g. [AGD11]) but here only the neutral molecules with a doublet ground state are considered. Since Ytterbium has an electronic configuration similar to neutral alkaline earth metals, alkali-ytterbium diatomics share the same attention as A-AE molecules and are also included. There are more classes of molecules with the same electronic configuration, for example alkaline earth hydrides or alkaline earth fluorines (i.e. AE−H or AE−F diatomics). These are omitted here, in order to not stray too far from this work's topic, that is, alkali and alkaline earth metals.

Each of the possible molecules in the table is marked if a publication reports data for it. Publications presenting experimental findings are marked in the column 'exp.'. Other works give solely theoretical calculations. A comment, if deemed helpful to relate to the corpus of work on the subject or to this thesis in particular, is found to the right side of a double page.
The following abbreviations are used for the comments:

- DE: dissociation energy
- FFR: Fano-Feshbach resonances
- GS: electronic ground state
- HFS: hyperfine structure
- HP: heat pipe experiment
- ND: nanodroplets
- PA: photoassociation spectroscopy, together with the probed frequency range
- pEDM: permanent electric dipole moment, usually of the electronic ground state
- PI: photoionization spectroscopy

There are efforts by the physical community to create (A-AE) molecules from colliding ultracold atoms. This is a challenging undertaking, which produces research data concerning the trappability and inter- and intraspecies scattering behaviour of the involved elements. For the purpose of this compilation, however, only works that do present a definite observation of a bound rovibrational molecular state are regarded. For example, the publications [Iva+11a; Han+11; Khr+12; Han+13; Dow+15; Roy+16] tell successively the story of the creation of weakly-bound RbSr, but only the latter two, describing Fano-Feshbach resonances and photoassociation, will be listed in this overview.

[a] Despite best efforts to give a full overview, completeness of the list cannot be guaranteed.

Ref.	Li						Na						K					
	Be	Mg	Ca	Sr	Ba	Yb	Be	Mg	Ca	Sr	Ba	Yb	Be	Mg	Ca	Sr	Ba	Yb
[BL74]	x																	
[BLS77]														x				
[BS78]														x				
[NBM80]			x															
[NB82]		x																
[BM82]								x										
[Jon80]	x	x	x															
[NZ83]						x												
[RJ88]		x																
[PBK88]	x																	
[Fan+89]		x																
[Pic+89]		x																
[Sch+90]	x																	
[Fis+91]	x																	
[Pak+91]	x																	
[Mar+92]	x																	
[BLP92]	x	x					x	x										
[BSS93]	x	x																
[BGS94]	x	x					x	x										
[Rus+98]			x															
[DIn+94]					x													
[AA94a]					x													
[Ver+94]					x													
[Str+94]					x													
[AA94b]			x															
[BAA94]											x							
[BAA95]																	x	
[BD97]		x																
[Jan01]	x	x																
[BG02]	x	x	x				x	x	x				x	x	x			
[Rue+05]							x	x										
[Sør+09]																		
[Nem+09]																		
[Mün+11]																		
[Bor+13]																		
[BG16]																		
[ZSD10]						x												
[Gop+10]						x												
[Kaj+11]						x												
[Gop+11]		x	x	x	x													
[Gop+13]			x	x														
[Gop+14]									x	x					x	x		
[GAD10]				x						x						x		
[ŻGD14]																		
[Szc+18]																x		
[Cia+18]																		
[Bar+18]																		
[Dev+18]																		

Ref.	Rb						Cs						exp.	comment
	Be	Mg	Ca	Sr	Ba	Yb	Be	Mg	Ca	Sr	Ba	Yb		
[BL74]														
[BLS77]													x	flowing afterglow reaction
[BS78]													x	HP
[NBM80]													x	HP
[NB82]													x	HP
[BM82]													x	HP
[Jon80]														
[NZ83]													x	Knudsen cell, D_e
[RJ88]														part of a study of small heteroatomic clusters
[PBK88]														part of a study of Li_kBe clusters
[Fan+89]														LiBe calculations from [PBK88]
[Pic+89]													x	HP, exp. & theory
[Sch+90]														
[Fis+91]														
[Pak+91]														
[Mar+92]														more el. states than [Pak+91]
[BLP92]														neutral molecules and negative ions
[BSS93]														various Li diatomics and ions
[BGS94]														review of first two rows of periodic table, now new data
[Rus+98]													x	PI, exp. & theory
[DIn+94]													x	HP
[AA94a]														
[Ver+94]														
[Str+94]													x	HP
[AA94b]														
[BAA94]														
[BAA95]														
[BD97]													x	PI
[Jan01]														part of a study of GS for small molecules with atoms of H to Ar
[BG02]														also HFS
[Rue+05]														first three rows of periodic table
[Sør+09]						x								
[Nem+09]						x							x	PA, $35\,cm^{-1}$
[Mün+11]						x							x	PA, $2\,cm^{-1}$
[Bor+13]						x							x	PA, $2\,cm^{-1}$, exp.& theory
[BG16]						x							x	PA, $70\,cm^{-1}$
[ZSD10]														
[Gop+10]														
[Kaj+11]														magic frequencies for optical traps
[Gop+11]														GS only
[Gop+13]														
[Gop+14]			x	x										GS only, pEDM
[GAD10]				x										GS only, pEDM
[ŻGD14]				x										
[Szc+18]													x	HP, exp. & theory
[Cia+18]				x									x	HP, PA, $0.2\,cm^{-1}$
[Bar+18]				x									x	FFR
[Dev+18]				x										further analysis of previous calculations [GAD10; ŻGD14]

Ref.	Li						Na						K					
	Be	Mg	Ca	Sr	Ba	Yb	Be	Mg	Ca	Sr	Ba	Yb	Be	Mg	Ca	Sr	Ba	Yb
[Kot+11]	x	x	x	x		x												
[PMK15]						x												
[Dow+15]						x												
[Roy+16]						x												
[Gre+19]						x												
[Iva+11b]			x															
[Ste+13]			x															
[Ste16]			x	x														
[Sch+17b]				x														
[Ger+17]															x			
[AS12]		x						x						x				
[BH12]																		
[BH13]																		
[GH13]						x												
[AH18]						x												
[Gut+18b]																		
[Gut+18a]																		
[Xia+13]													x					
[You+15b]																		
[You+15a]	x																	
[TK13]																		
[TKA15]						x												
[TK15]												x						
[TK16]																		x
[CEK17]							x											
[Hou+17]														x				
[Zei+18]				x						x						x		
[Kro+13]			x															
[Kro+14]																		
[Lac+14]																		
[Pot+14]																		
[Pot+15]																		
[PHE16]	x	x	x	x			x	x	x	x			x	x	x	x		
[Pot+17]			x	x					x	x					x	x		
[LE18]																		
[Che+14]																		
[Sch+17a]						x												
[Sha+17]						x						x						x
[SM17]																		
[MS17b]																		
[MS17a]																		
[Li+18]								x										

Ref.	Rb						Cs						exp.	comment
	Be	Mg	Ca	Sr	Ba	Yb	Be	Mg	Ca	Sr	Ba	Yb		
[Kot+11]														GS only, pEDM
[PMK15]													x	FFR
[Dow+15]													x	FFR
[Roy+16]													x	PA, $8\,\mathrm{cm}^{-1}$
[Gre+19]													x	PA, $40\,\mathrm{cm}^{-1}$
[Iva+11b]													x	HP
[Ste+13]													x	HP
[Ste16]													x	HP, preliminary work for this thesis
[Sch+17b]													x	HP, part of work presented in this thesis
[Ger+17]													x	HP, uses ideas presented in Section 4.4.1
[AS12]		x						x						GS only, pEDMs
[BH12]						x								
[BH13]						x						x		part of study of formation by magnetoassociation
[GH13]														calculations of FFR
[AH18]				x		x								HFS
[Gut+18b]												x	x	PA, $17\,\mathrm{cm}^{-1}$
[Gut+18a]												x	x	PA, $1\,\mathrm{cm}^{-1}$
[Xia+13]														
[You+15b]	x						x							
[You+15a]														part of a study of a laser cooling scheme
[TK13]						x								
[TKA15]														
[TK15]														
[TK16]														
[CEK17]														pEDM
[Hou+17]		x						x						
[Zei+18]														
[Kro+13]													x	He ND
[Kro+14]				x									x	He ND
[Lac+14]				x									x	He ND, exp. & theory
[Pot+14]				x										
[Pot+15]			x										x	He ND, exp. & theory
[PHE16]	x	x	x	x										pEDMs
[Pot+17]			x	x										
[LE18]				x									x	He ND
[Che+14]				x										also STIRAP scheme
[Sch+17a]													x	FFR
[Sha+17]						x						x		GS only, pEDM
[SM17]						x								
[MS17b]												x		
[MS17a]						x						x		also STIRAP scheme
[Li+18]														

References

[AA94a] A.R. Allouche and M. Aubert-Frécon. 'Electronic structure of BaLi. I. Theoretical study'. In: *The Journal of Chemical Physics* 100.2 (15th January 1994), pp. 938–944. DOI: 10.1063/1.466575.

[AA94b] A.R. Allouche and M. Aubert-Frécon. 'Theoritical study of the low-lying electronic states of the CaLi molecule'. In: *Chemical Physics Letters* 222.5 (May 1994), pp. 524–528. DOI: 10.1016/0009-2614(94)00371-8.

[AGD11] M. Aymar, R. Guérout and O. Dulieu. 'Structure of the alkali-metal-atom + strontium molecular ions: Towards photoassociation and formation of cold molecular ions'. In: *The Journal of Chemical Physics* 135.6 (14th August 2011), p. 064305. DOI: 10.1063/1.3611399.

[AH18] Jesus Aldegunde and Jeremy M. Hutson. 'Hyperfine structure of $^2\Sigma$ molecules containing alkaline-earth-metal atoms'. In: *Physical Review A* 97.4 (17th April 2018), p. 042505. DOI: 10.1103/PhysRevA.97.042505.

[And+18] Loïc Anderegg, Benjamin L. Augenbraun, Yicheng Bao, Sean Burchesky, Lawrence W. Cheuk, Wolfgang Ketterle and John M. Doyle. 'Laser cooling of optically trapped molecules'. In: *Nature Physics* 14.9 (September 2018), pp. 890–893. DOI: 10.1038/s41567-018-0191-z.

[AS12] L. Augustovičová and P. Soldán. '*Ab initio* properties of MgAlk (Alk = Li, Na, K, Rb, Cs)'. In: *The Journal of Chemical Physics* 136.8 (28th February 2012), p. 084311. DOI: 10.1063/1.3690459.

[BAA94] N. Boutassetta, A.R. Allouche and M. Aubert-Frécon. 'Theoretical study of the low-lying electronic states of the BaNa molecule'. In: *Chemical Physics* 189.1 (November 1994), pp. 33–39. DOI: 10.1016/0301-0104(94)80005-7.

[BAA95] N. Boutassetta, A.R. Allouche and M. Aubert-Frécon. 'Theoretical study of the low-lying electronic states of the BaK molecule'. In: *Chemical Physics* 201.2 (December 1995), pp. 393–403. DOI: 10.1016/0301-0104(95)00301-0.

[Bar+18] Vincent Barbé, Alessio Ciamei, Benjamin Pasquiou, Lukas Reichsöllner, Florian Schreck, Piotr S. Żuchowski and Jeremy M. Hutson. 'Observation of Feshbach resonances between alkali and closed-shell atoms'. In: *Nature Physics* 14.9 (September 2018), pp. 881–884. DOI: 10.1038/s41567-018-0169-x.

[BC03] John M. Brown and Alan Carrington. *Rotational spectroscopy of diatomic molecules*. Cambridge: Cambridge Univ. Press, 2003. ISBN: 0-521-53078-4.

[BD97] K.R. Berry and M.A. Duncan. 'Photoionization spectroscopy of LiMg'. In: *Chemical Physics Letters* 279.1 (November 1997), pp. 44–49. DOI: 10.1016/S0009-2614(97)00991-3.

[BG02] Pablo J. Bruna and Friedrich Grein. 'Theoretical study of hyperfine coupling constants and electron spin g factors for X $^2\Sigma^+$ diatomics from Groups 1 and 2'. In: *Molecular Physics* 100.11 (10th June 2002), pp. 1681–1691. DOI: 10.1080/00268970110101347.

[BG16] C. Bruni and A. Görlitz. 'Observation of hyperfine interaction in photoassociation spectra of ultracold RbYb'. In: *Physical Review A* 94.2 (3rd August 2016), p. 022503. DOI: 10.1103/PhysRevA.94.022503.

[BGS94] Alexander I. Boldyrev, Nick Gonzales and Jack Simons. 'Periodicity and Peculiarity in 120 First- and Second-Row Diatomic Molecules'. In: *The Journal of Physical Chemistry* 98.40 (October 1994), pp. 9931–9944. DOI: 10.1021/j100091a001.

[BH12] Daniel A. Brue and Jeremy M. Hutson. 'Magnetically Tunable Feshbach Resonances in Ultracold Li-Yb Mixtures'. In: *Physical Review Letters* 108.4 (25th January 2012), p. 043201. DOI: 10.1103/PhysRevLett.108.043201.

[BH13] Daniel A. Brue and Jeremy M. Hutson. 'Prospects of forming ultracold molecules in $^2\Sigma$ states by magnetoassociation of alkali-metal atoms with Yb'. In: *Physical Review A* 87.5 (20th May 2013), p. 052709. DOI: 10.1103/PhysRevA.87.052709.

[BIP] BIPM. *BIPM - Resolution 1 of the 26th CGPM*. URL: https://www.bipm.org/en/CGPM/db/26/1/ (visited on 8th December 2018).

[BL74] Peter H. Blustin and John W. Linnett. 'Applications of a simple molecular wavefunction. Part 6.—FSGO open-shell calculations on first-row diatomic molecular systems'. In: *J. Chem. Soc., Faraday Trans. 2* 70.0 (1974), pp. 826–836. DOI: 10.1039/F29747000826.

[BLP92] Charles W. Bauschlicher Jr., Stephen R. Langhoff and Harry Partridge. 'Theoretical study of the BeLi, BeNa, MgLi, MgNa, and AlBe molecules and their negative ions'. In: *The Journal of Chemical Physics* 96.2 (15th January 1992), pp. 1240–1247. DOI: 10.1063/1.462160.

[BLS77] D.J. Benard, P.J. Love and W.D. Slafer. 'Energy transfer and excimer formation in a flowing afterglow of Mg metastables'. In: *Chemical Physics Letters* 48.2 (June 1977), pp. 321–326. DOI: 10.1016/0009-2614(77)80324-2.

[BM82] D.J. Benard and H.H. Michels. 'Laser-induced chemiluminescence of NaMg'. In: *Chemical Physics Letters* 86.5 (March 1982), pp. 449–452. DOI: 10.1016/0009-2614(82)80168-1.

[Bor+13] Mateusz Borkowski, Piotr S. Żuchowski, Roman Ciuryło, Paul S. Julienne, Dariusz Kędziera, Łukasz Mentel, Paweł Tecmer, Frank Münchow, Cristian Bruni and Axel Görlitz. 'Scattering lengths in isotopologues of the RbYb system'. In: *Physical Review A* 88.5 (20th November 2013), p. 052708. DOI: 10.1103/PhysRevA.88.052708.

[BRY17] John L. Bohn, Ana Maria Rey and Jun Ye. 'Cold molecules: Progress in quantum engineering of chemistry and quantum matter'. In: *Science* 357.6355 (8th September 2017), pp. 1002–1010. DOI: 10.1126/science.aam6299.

[BS78] D.J. Benard and W.D. Slafer. 'Laser induced fluorescence spectra of KMg'. In: *Chemical Physics Letters* 56.3 (June 1978), pp. 438–442. DOI: 10.1016/0009-2614(78)89010-1.

[BSS93] Alexander I. Boldyrev, Jack Simons and Paul R. von Schleyer. 'Ab initio study of the electronic structures of lithium containing diatomic molecules and ions'. In: *The Journal of Chemical Physics* 99.11 (December 1993), pp. 8793–8804. DOI: 10.1063/1.465600.

[BW11] Michael Berglund and Michael E. Wieser. 'Isotopic compositions of the elements 2009 (IUPAC Technical Report)'. In: *Pure and Applied Chemistry* 83.2 (14th January 2011), pp. 397–410. DOI: 10.1351/PAC-REP-10-06-02.

[Cai+17] William B. Cairncross, Daniel N. Gresh, Matt Grau, Kevin C. Cossel, Tanya S. Roussy, Yiqi Ni, Yan Zhou, Jun Ye and Eric A. Cornell. 'Precision Measurement of the Electron's Electric Dipole Moment Using Trapped Molecular Ions'. In: *Physical Review Letters* 119.15 (9th October 2017), pp. 153001–1. DOI: 10.1103/PhysRevLett.119.153001.

[CEK17] Wael Chmaisani, Nayla El-Kork and Mahmoud Korek. 'Theoretical electronic structure of the NaBe molecule'. In: *Chemical Physics* 491 (July 2017), pp. 33–41. DOI: 10.1016/j.chemphys.2017.04.007.

[CFK09] Cheng Chin, V.V. Flambaum and M.G. Kozlov. 'Ultracold molecules: new probes on the variation of fundamental constants'. In: *New Journal of Physics* 11.5 (14th May 2009), p. 055048. DOI: 10.1088/1367-2630/11/5/055048.

[Che+14] Tao Chen, Shaobing Zhu, Xiaolin Li, Jun Qian and Yuzhu Wang. 'Prospects for transferring ^{87}Rb ^{84}Sr dimers to the rovibrational ground state based on calculated molecular structures'. In: *Physical Review A* 89.6 (4th June 2014), p. 063402. DOI: 10.1103/PhysRevA.89.063402.

[Cia+18] Alessio Ciamei, Jacek Szczepkowski, Alex Bayerle, Vincent Barbé, Lukas Reichsöllner, Slava M. Tzanova, Chun-Chia Chen, Benjamin Pasquiou, Anna Grochola, Pawel Kowalczyk, Wlodzimierz Jastrzebski and Florian Schreck. 'The RbSr $^2\Sigma^+$ ground state investigated *via* spectroscopy of hot and ultracold molecules'. In: *Physical Chemistry Chemical Physics* 20.41 (2018), pp. 26221–26240. DOI: 10.1039/C8CP03919D.

[CM06] John A. Coxon and Todd C. Melville. 'Application of direct potential fitting to line position data for the $X^1\Sigma_g^+$ and $A^1\Sigma_u^+$ states of Li_2'. In: *Journal of Molecular Spectroscopy* 235.2 (February 2006), pp. 235–247. DOI: 10.1016/j.jms.2005.11.009.

[DeM+08] D. DeMille, S. Sainis, J. Sage, T. Bergeman, S. Kotochigova and E. Tiesinga. 'Enhanced Sensitivity to Variation of m_e/m_p in Molecular Spectra'. In: *Physical Review Letters* 100.4 (29th January 2008), p. 043202. DOI: 10.1103/PhysRevLett.100.043202.

[Dem88] Wolfgang Demtröder. *Laser Spectroscopy: Basic Concepts and Instrumentation*. 1. ed., corr. 3. print. Springer series in chemical physics 5. Berlin: Springer, 1988. ISBN: 3-540-10343-0.

[Dev+18] Adrien Devolder, Eliane Luc-Koenig, Osman Atabek, Michèle Desouter-Lecomte and Olivier Dulieu. 'Proposal for the formation of ultracold deeply bound RbSr dipolar molecules by all-optical methods'. In: *Physical Review A* 98.5 (9th November 2018), p. 053411. DOI: 10.1103/PhysRevA.98.053411.

[DIn+94] J. D'Incan, C. Effantin, A. Bernard, G. Fabre, R. Stringat, A. Boulezhar and J. Vergès. 'Electronic structure of BaLi. II. First observation of the $Ba^{6,7}Li$ spectrum: Analysis of the $(2)^2\Pi \rightarrow X^2\Sigma^+$ system'. In: *The Journal of Chemical Physics* 100.2 (15th January 1994), pp. 945–949. DOI: 10.1063/1.466576.

[Dow+15] William Dowd, Richard J Roy, Rajendra K Shrestha, Alexander Petrov, Constantinos Makrides, Svetlana Kotochigova and Subhadeep Gupta. 'Magnetic field dependent interactions in an ultracold Li–Yb($^3P_2$) mixture'. In: *New Journal of Physics* 17.5 (7th May 2015), p. 055007. DOI: 10.1088/1367-2630/17/5/055007.

[Edm96] A.R. Edmonds. *Angular momentum in quantum mechanics*. 2. ed., 4th printing. Princeton landmarks in mathematics and physics. Princeton: Princeton University Press, 1996. ISBN: 0-691-02589-4.

[Fan+89] P. Fantucci, V. Bonačić-Koutecký, W. Pewestorf and J. Koutecký. '*Ab initio* configuration interaction study of the electronic and geometric structure of small, mixed neutral and cationic $MgNa_k$ and $MgLi_k$ (k =2-8) clusters'. In: *The Journal of Chemical Physics* 91.7 (October 1989), pp. 4229–4241. DOI: 10.1063/1.456802.

[Fis+91] I. Fischer, V.E. Bondybey, P. Rosmus and H.-J. Werner. 'Theoretical study of the electronic states of BeLi and Be_2^+'. In: *Chemical Physics* 151.3 (April 1991), pp. 295–308. DOI: 10.1016/0301-0104(91)80016-B.

[GAD10] R. Guérout, M. Aymar and O. Dulieu. 'Ground state of the polar alkali-metal-atom–strontium molecules: Potential energy curve and permanent dipole moment'. In: *Physical Review A* 82.4 (15th October 2010), p. 042508. DOI: 10.1103/PhysRevA.82.042508.

[GB17] Christian Gross and Immanuel Bloch. 'Quantum simulations with ultracold atoms in optical lattices'. In: *Science* 357.6355 (8th September 2017), pp. 995–1001. DOI: 10.1126/science.aal3837.

[Ger+17] Julia Gerschmann, Erik Schwanke, Asen Pashov, Horst Knöckel, Silke Ospelkaus and Eberhard Tiemann. 'Laser and Fourier-transform spectroscopy of KCa'. In: *Physical Review A* 96.3 (6th September 2017), p. 032505. DOI: 10.1103/PhysRevA.96.032505.

[GH13] Maykel L. González-Martínez and Jeremy M. Hutson. 'Magnetically tunable Feshbach resonances in Li + Yb(^3P_J)'. In: *Physical Review A* 88.2 (23rd August 2013), p. 020701. DOI: 10.1103/PhysRevA.88.020701.

[Gop+10] Geetha Gopakumar, Minori Abe, Bhanu Pratap Das, Masahiko Hada and Kimihiko Hirao. 'Relativistic calculations of ground and excited states of LiYb molecule for ultracold photoassociation spectroscopy studies'. In: *The Journal of Chemical Physics* 133.12 (28th September 2010), p. 124317. DOI: 10.1063/1.3475568.

[Gop+11] Geetha Gopakumar, Minori Abe, Masatoshi Kajita and Masahiko Hada. '*Ab initio* study of permanent electric dipole moment and radiative lifetimes of alkaline-earth-metal–Li molecules'. In: *Physical Review A* 84.6 (28th December 2011), p. 062514. DOI: 10.1103/PhysRevA.84.062514.

[Gop+13] Geetha Gopakumar, Minori Abe, Masahiko Hada and Masatoshi Kajita. '*Ab initio* study of ground and excited states of ^{6}Li^{40}Ca and ^{6}Li^{88}Sr molecules'. In: *The Journal of Chemical Physics* 138.19 (21st May 2013), p. 194307. DOI: 10.1063/1.4804622.

[Gop+14] Geetha Gopakumar, Minori Abe, Masahiko Hada and Masatoshi Kajita. 'Dipole polarizability of alkali-metal (Na, K, Rb)–alkaline-earth-metal (Ca, Sr) polar molecules: Prospects for alignment'. In: *The Journal of Chemical Physics* 140.22 (14th June 2014), p. 224303. DOI: 10.1063/1.4881396.

[Gor+17] I.E. Gordon et al. 'The HITRAN2016 molecular spectroscopic database'. In: *Journal of Quantitative Spectroscopy and Radiative Transfer* 203 (December 2017), pp. 3–69. DOI: 10.1016/j.jqsrt.2017.06.038.

[Gre+19] Alaina Green, Jun Hui See Toh, Richard Roy, Ming Li, Svetlana Kotochigova and Subhadeep Gupta. 'Two-photon photoassociation spectroscopy of the $^{2}\Sigma^{+}$ YbLi molecular ground state'. In: *arXiv:1903.00603 [physics]* (1st March 2019). arXiv: 1903.00603.

[Gri83] P. Griffiths. 'Fourier transform infrared spectrometry'. In: *Science* 222.4621 (21st October 1983), pp. 297–302. DOI: 10.1126/science.6623077.

[Gut+18a] A. Guttridge, Matthew D. Frye, B. C. Yang, Jeremy M. Hutson and Simon L. Cornish. 'Two-photon photoassociation spectroscopy of CsYb: Ground-state interaction potential and interspecies scattering lengths'. In: *Physical Review A* 98.2 (31st August 2018), p. 022707. DOI: 10.1103/PhysRevA.98.022707.

[Gut+18b] Alexander Guttridge, Stephen A. Hopkins, Matthew D. Frye, John J. McFerran, Jeremy M. Hutson and Simon L. Cornish. 'Production of ultracold Cs*Yb molecules by photoassociation'. In: *Physical Review A* 97.6 (19th June 2018), p. 063414. DOI: 10.1103/PhysRevA.97.063414.

[Han+11] Anders H. Hansen, Alexander Khramov, William H. Dowd, Alan O. Jamison, Vladyslav V. Ivanov and Subhadeep Gupta. 'Quantum degenerate mixture of ytterbium and lithium atoms'. In: *Physical Review A* 84.1 (22nd July 2011), p. 011606. DOI: 10.1103/PhysRevA.84.011606.

[Han+13] Anders H. Hansen, Alexander Y. Khramov, William H. Dowd, Alan O. Jamison, Benjamin Plotkin-Swing, Richard J. Roy and Subhadeep Gupta. 'Production of quantum-degenerate mixtures of ytterbium and lithium with controllable interspecies overlap'. In: *Physical Review A* 87.1 (16th January 2013), p. 013615. DOI: 10.1103/PhysRevA.87.013615.

[Her50] Gerhard Herzberg. *Spectra of diatomic molecules*. 2. ed. Molecular spectra and molecular structure by Gerhard Herzberg ; 1. New York: van Nostrand, 1950. ISBN: 0-442-03385-0.

[Hil+14] Ian R. Hill, Yuri B. Ovchinnikov, Elizabeth M. Bridge, E. Anne Curtis and Patrick Gill. 'Zeeman slowers for strontium based on permanent magnets'. In: *Journal of Physics B: Atomic, Molecular and Optical Physics* 47.7 (14th April 2014), pp. 075006–. DOI: 10.1088/0953-4075/47/7/075006.

[Hou+17] Dunia Houalla, Wael Chmaisani, Nayla El-Kork and Mahmoud Korek. 'Electronic structure calculation of the MgAlk (Alk = K, Rb, Cs) molecules for laser cooling experiments'. In: *Computational and Theoretical Chemistry* 1108 (May 2017), pp. 103–110. DOI: 10.1016/j.comptc.2017.03.009.

[Iva+11a] Vladyslav V. Ivanov, Alexander Khramov, Anders H. Hansen, William H. Dowd, Frank Münchow, Alan O. Jamison and Subhadeep Gupta. 'Sympathetic Cooling in an Optically Trapped Mixture of Alkali and Spin-Singlet Atoms'. In: *Physical Review Letters* 106.15 (11th April 2011), p. 153201. DOI: 10.1103/PhysRevLett.106.153201.

[Iva+11b] Milena Ivanova, Alexander Stein, Asen Pashov, Andrey V. Stolyarov, Horst Knöckel and Eberhard Tiemann. 'The $X^2\Sigma^+$ state of LiCa studied by Fourier-transform spectroscopy'. In: *The Journal of Chemical Physics* 135.17 (7th November 2011), p. 174303. DOI: 10.1063/1.3652755.

[Jan01] Rudolf Janoschek. 'Quantum chemical B3LYP/cc-pvqz computation of ground-state structures and properties of small molecules with atoms of $Z \leq 18$ (hydrogen to argon)(IUPAC Technical Report)'. In: *Pure and Applied Chemistry* 73.9 (1st September 2001), pp. 1521–1553. DOI: 10.1351/pac200173091521.

[Jon80] R. O. Jones. 'Molecular bonding in LiBe, LiMg, and LiCa'. In: *The Journal of Chemical Physics* 72.5 (March 1980), pp. 3197–3200. DOI: 10.1063/1.439553.

[JR75] F. James and M. Roos. 'Minuit - a system for function minimization and analysis of the parameter errors and correlations'. In: *Computer Physics Communications* 10.6 (December 1975), pp. 343–367. DOI: 10.1016/0010-4655(75)90039-9. version 92.1.

[Kaj+11] Masatoshi Kajita, Geetha Gopakumar, Minori Abe and Masahiko Hada. 'Elimination of the Stark shift from the vibrational transition frequency of optically trapped $^{174}Yb^6Li$ molecules'. In: *Physical Review A* 84.2 (10th August 2011), p. 022507. DOI: 10.1103/PhysRevA.84.022507.

[Kaj+13] Masatoshi Kajita, Geetha Gopakumar, Minori Abe and Masahiko Hada. 'Sensitivity of vibrational spectroscopy of optically trapped SrLi and CaLi molecules to variations in m_p/m_e'. In: *Journal of Physics B: Atomic, Molecular and Optical Physics* 46.2 (28th January 2013), p. 025001. DOI: 10.1088/0953-4075/46/2/025001.

[Kaj+14] Masatoshi Kajita, Geetha Gopakumar, Minori Abe and Masahiko Hada. 'Characterizing of variation in the proton-to-electron mass ratio via precise measurements of molecular vibrational transition frequencies'. In: *Journal of Molecular Spectroscopy* 300 (June 2014), pp. 99–107. DOI: 10.1016/j.jms.2014.03.009.

[Khr+12] Alexander Y. Khramov, Anders H. Hansen, Alan O. Jamison, William H. Dowd and Subhadeep Gupta. 'Dynamics of Feshbach molecules in an ultracold three-component mixture'. In: *Physical Review A* 86.3 (10th September 2012), p. 032705. DOI: 10.1103/PhysRevA.86.032705.

[Kot+11] Svetlana Kotochigova, Alexander Petrov, Maria Linnik, Jacek Kłos and Paul S. Julienne. '*Ab initio* properties of Li-group-II molecules for ultracold matter studies'. In: *The Journal of Chemical Physics* 135.16 (31st October 2011), p. 164108. DOI: 10.1063/1.3653974.

[Kro+13] Günter Krois, Johann V. Pototschnig, Florian Lackner and Wolfgang E. Ernst. 'Spectroscopy of Cold LiCa Molecules Formed on Helium Nanodroplets'. In: *The Journal of Physical Chemistry A* 117.50 (19th December 2013), pp. 13719–13731. DOI: 10.1021/jp407818k.

[Kro+14] Günter Krois, Florian Lackner, Johann V. Pototschnig, Thomas Buchsteiner and Wolfgang E. Ernst. 'Characterization of RbSr molecules: spectral analysis on helium droplets'. In: *Phys. Chem. Chem. Phys.* 16.40 (8th September 2014), pp. 22373–22381. DOI: 10.1039/C4CP03135K.

[Kuh37] H. Kuhn. 'Pressure broadening of spectral lines and van der Waals forces I—Influence of argon on the mercury resonance line'. In: *Proceedings of the Royal Society of London. Series A - Mathematical and Physical Sciences* 158.893 (January 1937), pp. 212–229. DOI: 10.1098/rspa.1937.0015.

[Lac+14] Florian Lackner, Günter Krois, Thomas Buchsteiner, Johann V. Pototschnig and Wolfgang E. Ernst. 'Helium-Droplet-Assisted Preparation of Cold RbSr Molecules'. In: *Physical Review Letters* 113.15 (6th October 2014). DOI: 10.1103/PhysRevLett.113.153001.

[LE18] Florian Lackner and Wolfgang E. Ernst. 'Photoinduced Molecule Formation of Spatially Separated Atoms on Helium Nanodroplets'. In: *The Journal of Physical Chemistry Letters* 9.13 (5th July 2018), pp. 3561–3566. DOI: 10.1021/acs.jpclett.8b01530.

[LF86] Hélène Lefebvre-Brion and Robert W. Field. *Perturbations in the spectra of diatomic molecules*. Orlando: Academic Press, 1986. ISBN: 0-12-442691-3.

[Li+18] Song Li, Ming-Jie Wan, Shan-Jun Chen, Yuan-Yuan Jin, Chuan-Zhao Zhang, Peng Chen and Ning Wang. 'An ab initio investigation on the low-lying electronic states of NaMg'. In: *Spectrochimica Acta Part A: Molecular and Biomolecular Spectroscopy* 202 (September 2018), pp. 368–375. DOI: 10.1016/j.saa.2018.05.043.

[Mar+92] M.M. Marino, W.C. Ermler, C.W. Kern and V.E. Bondybey. 'Spin–orbit configuration-interaction study of valence and Rydberg states of LiBe'. In: *The Journal of Chemical Physics* 96.5 (March 1992), pp. 3756–3766. DOI: 10.1063/1.461880.

[McC18] Daniel McCarron. 'Laser cooling and trapping molecules'. In: *Journal of Physics B: Atomic, Molecular and Optical Physics* 51.21 (14th November 2018), p. 212001. DOI: 10.1088/1361-6455/aadfba.

[MNT16] Peter J. Mohr, David B. Newell and Barry N. Taylor. 'CODATA recommended values of the fundamental physical constants: 2014'. In: *Reviews of Modern Physics* 88.3 (26th September 2016), p. 035009. DOI: 10.1103/RevModPhys.88.035009.

[MS17a] D.N. Menailava and M.B. Shundalau. 'Optical Cycle Modelling for RbYb and CsYb Molecules'. In: *Journal of Applied Spectroscopy* 84.4 (September 2017), pp. 543–548. DOI: 10.1007/s10812-017-0508-1.

[MS17b] Darya N. Meniailava and Maksim B. Shundalau. 'Multi-reference perturbation theory study on the CsYb molecule including the spin-orbit coupling'. In: *Computational and Theoretical Chemistry* 1111 (July 2017), pp. 20–26. DOI: 10.1016/j.comptc.2017.03.046.

[Mün+11] Frank Münchow, Cristian Bruni, Maximilian Madalinski and Axel Görlitz. 'Two-photon photoassociation spectroscopy of heteronuclear YbRb'. In: *Physical Chemistry Chemical Physics* 13.42 (2011), p. 18734. DOI: 10.1039/c1cp21219b.

[MW36] Henry Margenau and William W. Watson. 'Pressure Effects on Spectral Lines'. In: *Reviews of Modern Physics* 8.1 (1st January 1936), pp. 22–53. DOI: 10.1103/RevModPhys.8.22.

[NB82] D.K. Neumann and D.J. Benard. 'Formation and decay kinetics of optically pumped LiMg excimers'. In: *Chemical Physics Letters* 88.4 (May 1982), pp. 429–433. DOI: 10.1016/0009-2614(82)83039-X.

[NBM80] D.K. Neumann, D.J. Benard and H.H. Michels. 'Laser chemiluminescence of LiCa'. In: *Chemical Physics Letters* 73.2 (July 1980), pp. 343–347. DOI: 10.1016/0009-2614(80)80386-1.

[Nem+09] N. Nemitz, F. Baumer, F. Münchow, S. Tassy and A. Görlitz. 'Production of heteronuclear molecules in an electronically excited state by photoassociation in a mixture of ultracold Yb and Rb'. In: *Physical Review A* 79.6 (4th June 2009), p. 061403. DOI: 10.1103/PhysRevA.79.061403.

[NZ83] A. Neubert and K.F. Zmbov. 'The dissociation energies of gaseous SmLi, EuLi, TmLi and YbLi'. In: *Chemical Physics* 76.3 (May 1983), pp. 469–478. DOI: 10.1016/0301-0104(83)85228-8.

[Pak+91] K. Pak, W.C. Ermler, C.W. Kern and V.E. Bondybey. 'Full spin-orbit configuration interaction calculations on electronic states of LiBe'. In: *Journal of Cluster Science* 2.1 (March 1991), pp. 19–28. DOI: 10.1007/BF00702932.

[PBK88] Wolfgang Pewestorf, Vlasta Bonačić-Koutecký and Jaroslav Koutecký. '*Ab initio* configuration interaction study of mixed $BeLi_k$ clusters (k = 1-9)'. In: *The Journal of Chemical Physics* 89.9 (November 1988), pp. 5794–5802. DOI: 10.1063/1.455555.

[Pet+18] M. Petzold, P. Kaebert, P. Gersema, M. Siercke and S. Ospelkaus. 'A Zeeman slower for diatomic molecules'. In: *New Journal of Physics* 20.4 (12th April 2018), p. 042001. DOI: 10.1088/1367-2630/aab9f5.

[PHE16] Johann V. Pototschnig, Andreas W. Hauser and Wolfgang E. Ernst. 'Electric dipole moments and chemical bonding of diatomic alkali–alkaline earth molecules'. In: *Physical Chemistry Chemical Physics* 18.8 (2016), pp. 5964–5973. DOI: 10.1039/C5CP06598D.

[Pic+89] G. Pichler, A.M. Lyyra, P.D. Kleiber, W.C. Stwalley, R. Hammer, K.M. Sando and H.H. Michels. 'Laser-induced chemiluminescence of the LiMg excimer'. In: *Chemical Physics Letters* 156.5 (April 1989), pp. 467–471. DOI: 10.1016/S0009-2614(89)87313-0.

[PMK15] Alexander Petrov, Constantinos Makrides and Svetlana Kotochigova. 'Magnetic control of ultra-cold ^{6}Li and ^{174}Yb($^{3}P_2$) atom mixtures with Feshbach resonances'. In: *New Journal of Physics* 17.4 (17th April 2015), p. 045010. DOI: 10.1088/1367-2630/17/4/045010.

[Poi06] Bureau International des Poids et Mesures, ed. *Le système international d'unités (SI) =: The international system of units (SI)*. 8. éd. Sèvres: BIPM, 2006. ISBN: 92-822-2213-6.

[Pot+14] Johann V. Pototschnig, Günter Krois, Florian Lackner and Wolfgang E. Ernst. '*Ab initio* study of the RbSr electronic structure: Potential energy curves, transition dipole moments, and permanent electric dipole moments'. In: *The Journal of Chemical Physics* 141.23 (21st December 2014), p. 234309. DOI: 10.1063/1.4903791.

[Pot+15] Johann V. Pototschnig, Günter Krois, Florian Lackner and Wolfgang E. Ernst. 'Investigation of the RbCa molecule: Experiment and theory'. In: *Journal of Molecular Spectroscopy* 310 (April 2015), pp. 126–134. DOI: 10.1016/j.jms.2015.01.006.

[Pot+17] Johann V. Pototschnig, Ralf Meyer, Andreas W. Hauser and Wolfgang E. Ernst. 'Vibronic transitions in the alkali-metal (Li, Na, K, Rb) – alkaline-earth-metal (Ca, Sr) series: A systematic analysis of de-excitation mechanisms based on the graphical mapping of Frank-Condon integrals'. In: *Physical Review A* 95.2 (2nd February 2017), p. 022501. DOI: 10.1103/PhysRevA.95.022501.

[RJ88] B.K. Rao and P. Jena. 'Electronic structure and geometries of heteroatomic clusters'. In: *Physical Review B* 37.6 (15th February 1988), pp. 2867–2873. DOI: 10.1103/PhysRevB.37.2867.

[Roy+16] Richard Roy, Rajendra Shrestha, Alaina Green, Subhadeep Gupta, Ming Li, Svetlana Kotochigova, Alexander Petrov and Chi Hong Yuen. 'Photoassociative production of ultracold heteronuclear YbLi* molecules'. In: *Physical Review A* 94.3 (14th September 2016). DOI: 10.1103/PhysRevA.94.033413.

[Rue+05] Fernando Ruette, Morella Sánchez, Rafael Añez, Aleida Bermúdez and Anibal Sierraalta. 'Diatomic molecule data for parametric methods. I'. In: *Journal of Molecular Structure: THEOCHEM* 729.1 (September 2005), pp. 19–37. DOI: 10.1016/j.theochem.2005.04.024.

[Rus+98] L.M. Russon, G.K. Rothschopf, M.D. Morse, A.I. Boldyrev and Jack Simons. 'Two-photon ionization spectroscopy and all-electron ab initio study of LiCa'. In: *The Journal of Chemical Physics* 109.16 (22nd October 1998), pp. 6655–6665. DOI: 10.1063/1.477317.

[Saa13] Vladimir S. Saakov, ed. *Derivative spectrophotometry and electron spin resonance (ESR) spectroscopy for ecological and biological questions*. New York: Springer, 2013. ISBN: 978-3-7091-1006-5.

[Saf+18] M. S. Safronova, D. Budker, D. DeMille, Derek F. Jackson Kimball, A. Derevianko and Charles W. Clark. 'Search for new physics with atoms and molecules'. In: *Reviews of Modern Physics* 90.2 (29th June 2018), p. 025008. DOI: 10.1103/RevModPhys.90.025008.

[San13] Jean Sansonetti. *Handbook of Basic Atomic Spectroscopic Data, NIST Standard Reference Database 108*. type: dataset. 2013. URL: http://physics.nist.gov/PhysRefData/Handbook/periodictable.htm (visited on 2nd February 2019).

[Sch+17a] F. Schäfer, H. Konishi, A. Bouscal, T. Yagami and Y. Takahashi. 'Spectroscopic determination of magnetic-field-dependent interactions in an ultracold Yb($^3P_2$)-Li mixture'. In: *Physical Review A* 96.3 (18th September 2017), p. 032711. DOI: 10.1103/PhysRevA.96.032711.

[Sch+17b] Erik Schwanke, Horst Knöckel, Alexander Stein, Asen Pashov, Silke Ospelkaus and Eberhard Tiemann. 'Laser and Fourier transform spectroscopy of ^{7}Li^{88}Sr'. In: *Journal of Physics B: Atomic, Molecular and Optical Physics* 50.23 (14th December 2017), p. 235103. DOI: 10.1088/1361-6455/aa8ca0.

[Sch+90] R. Schlachta, I. Fischer, P. Rosmus and V.E. Bondybey. 'The simplest heteronuclear metal cluster: LiBe'. In: *Chemical Physics Letters* 170.5 (July 1990), pp. 485–491. DOI: 10.1016/S0009-2614(90)87089-A.

[Sha+17] Qinqin Shao, Lijuan Deng, Xiaodong Xing, Dezhi Gou, Xiaoyu Kuang and Hui Li. 'Ground State Properties of the Polar Alkali-Metal–Ytterbium and Alkaline-Earth-Metal–Ytterbium Molecules: A Comparative Study'. In: *The Journal of Physical Chemistry A* 121.10 (16th March 2017), pp. 2187–2193. DOI: 10.1021/acs.jpca.6b11741.

[SM17] M.B. Shundalau and A.A. Minko. 'Ab initio multi-reference perturbation theory calculations of the ground and some excited electronic states of the RbYb molecule'. In: *Computational and Theoretical Chemistry* 1103 (March 2017), pp. 11–16. DOI: 10.1016/j.comptc.2017.01.008.

[Sør+09] Lasse Kragh Sørensen, Stefan Knecht, Timo Fleig and Christel M. Marian. 'Four-Component Relativistic Coupled Cluster and Configuration Interaction Calculations on the Ground and Excited States of the RbYb Molecule'. In: *The Journal of Physical Chemistry A* 113.45 (12th November 2009), pp. 12607–12614. DOI: 10.1021/jp904914m.

[Sta10] Jacob Oliver Stack. 'An Ultra-Cold Lithium Source For Investigating Cold Dipolar Gases'. Dissertation. London: University of London, October 2010.

[Ste+13] Alexander Stein, Milena Ivanova, Asen Pashov, Horst Knöckel and Eberhard Tiemann. 'Spectroscopic study of the $2^2\Sigma^+$ and the $4^2\Sigma^+$ excited states of LiCa'. In: *The Journal of Chemical Physics* 138.11 (21st March 2013), p. 114306. DOI: 10.1063/1.4795205.

[Ste16] Alexander Stein. 'Fourier-Transform-Spektroskopie and zweiatomigen Molekülen gebildet aus Alkali- und/oder Erdalkaliatomen'. Dissertation. Hannover: Gottfried Wilhelm Leibniz Universtität Hannover, 4th February 2016.

[Str+94] R. Stringat, G. Fabre, A. Boulezhar, J. D'Incan, C. Effantin, J. Vergès and A. Bernard. 'The $X^2\Sigma^+$, $(2)^2\Sigma^+$, and $(2)^2\Pi$ States of BaLi'. In: *Journal of Molecular Spectroscopy* 168.2 (December 1994), pp. 514–521. DOI: 10.1006/jmsp.1994.1298.

[SW99] William C. Stwalley and He Wang. 'Photoassociation of Ultracold Atoms: A New Spectroscopic Technique'. In: *Journal of Molecular Spectroscopy* 195.2 (June 1999), pp. 194–228. DOI: 10.1006/jmsp.1999.7838.

[Szc+18] Jacek Szczepkowski, Anna Grochola, Paweł Kowalczyk, Olivier Dulieu, Romain Guérout, Piotr S. Żuchowski and Włodzimierz Jastrzebski. 'Experimental and theoretical study of the $B(2)^2\Sigma^+ \rightarrow X(1)^2\Sigma^+$ system in the KSr molecule'. In: *Journal of Quantitative Spectroscopy and Radiative Transfer* 210 (May 2018), pp. 217–224. DOI: 10.1016/j.jqsrt.2018.02.020.

[TK13] S.N. Tohme and M. Korek. 'Electronic structure and rovibrational calculation of the low-lying states of the RbYb molecule'. In: *Chemical Physics* 410 (January 2013), pp. 37–44. DOI: 10.1016/j.chemphys.2012.10.015.

[TK15] Samir N. Tohme and Mahmoud Korek. 'Electronic structure with vibration–rotation study of the NaYb molecule'. In: *Chemical Physics Letters* 638 (October 2015), pp. 216–226. DOI: 10.1016/j.cplett.2015.08.050.

[TK16] Samir N. Tohme and Mahmoud Korek. 'Electronic structure calculation of the KYb molecule with dipole moments, polarizabilities, and ro-vibrational studies'. In: *Computational and Theoretical Chemistry* 1078 (February 2016), pp. 65–71. DOI: 10.1016/j.comptc.2015.12.022.

[TKA15] Samir N. Tohme, Mahmoud Korek and Ramadan Awad. '*Ab initio* calculations of the electronic structure of the low-lying states for the ultracold LiYb molecule'. In: *The Journal of Chemical Physics* 142.11 (21st March 2015), p. 114312. DOI: 10.1063/1.4914472.

[Tru+17a] S. Truppe, H. J. Williams, M. Hambach, L. Caldwell, N. J. Fitch, E. A. Hinds, B. E. Sauer and M. R. Tarbutt. 'Molecules cooled below the Doppler limit'. In: *Nature Physics* 13.12 (28th August 2017), pp. 1173–1176. DOI: 10.1038/nphys4241.

[Tru+17b] S. Truppe, H.J. Williams, N.J. Fitch, M. Hambach, T.E. Wall, E.A. Hinds, B.E. Sauer and M.R. Tarbutt. 'An intense, cold, velocity-controlled molecular beam by frequency-chirped laser slowing'. In: *New Journal of Physics* 19.2 (17th February 2017), p. 022001. DOI: 10.1088/1367-2630/aa5ca2.

[TS55] C.H. Townes and A.L. Schawlow. *Microwave Spectroscopy*. New York: McGraw-Hill, 1955.

[VC69] C.R. Vidal and J. Cooper. 'Heat-Pipe Oven: A New, Well-Defined Metal Vapor Device for Spectroscopic Measurements'. In: *Journal of Applied Physics* 40.8 (July 1969), pp. 3370–3374. DOI: 10.1063/1.1658190.

[Ver+94] J. Vergès, J. d'Incan, C. Effantin, A. Bernard, G. Fabre, R. Stringat and A. Boulezhar. 'Electronic structure of BaLi: the $(2)^2\Sigma^+$ state'. In: *Journal of Physics B: Atomic, Molecular and Optical Physics* 27.8 (28th April 1994), pp. L153–L155. DOI: 10.1088/0953-4075/27/8/004.

[Vit+17] Nikolay V. Vitanov, Andon A. Rangelov, Bruce W. Shore and Klaas Bergmann. 'Stimulated Raman adiabatic passage in physics, chemistry, and beyond'. In: *Reviews of Modern Physics* 89.1 (8th March 2017), p. 015006. DOI: 10.1103/RevModPhys.89.015006.

[WH91] Carl E. Wieman and Leo Hollberg. 'Using diode lasers for atomic physics'. In: *Review of Scientific Instruments* 62.1 (January 1991), pp. 1–20. DOI: 10.1063/1.1142305.

[Win18] Mark J. Winter. *The periodic table of the elements by WebElements*. WebElements. August 2018. URL: https://www.webelements.com/ (visited on 29th March 2019).

[Xia+13] Ke-La Xiao, Chuan-Lu Yang, Mei-Shan Wang, Xiao-Guang Ma and Wen-Wang Liu. 'An *ab initio* study of the ground and low-lying excited states of KBe with the effect of inner-shell electrons'. In: *The Journal of Chemical Physics* 139.7 (21st August 2013), p. 074305. DOI: 10.1063/1.4818452.

[Yan+13] Bo Yan, Steven A. Moses, Bryce Gadway, Jacob P. Covey, Kaden R.A. Hazzard, Ana Maria Rey, Deborah S. Jin and Jun Ye. 'Observation of dipolar spin-exchange interactions with lattice-confined polar molecules'. In: *Nature* 501.7468 (September 2013), pp. 521–525. DOI: 10.1038/nature12483.

[Yan+19] Huan Yang, De-Chao Zhang, Lan Liu, Ya-Xiong Liu, Jue Nan, Bo Zhao and Jian-Wei Pan. 'Observation of magnetically tunable Feshbach resonances in ultracold $^{23}Na^{40}K + {}^{40}K$ collisions'. In: *Science* 363.6424 (18th January 2019), pp. 261–264. DOI: 10.1126/science.aau5322.

[Yaw06] Carl L. Yaws. 'Antoine Coefficients for Vapor Pressure of the Elements'. In: *Chemical Engineering* (November 2006), pp. 52–54.

[You+15a] Yang You, Chuan-Lu Yang, Mei-Shan Wang, Xiao-Guang Ma and Wen-Wang Liu. 'Theoretical investigation of the laser cooling of a LiBe molecule'. In: *Physical Review A* 92.3 (8th September 2015), p. 032502. DOI: 10.1103/PhysRevA.92.032502.

[You+15b] Yang You, Chuan-Lu Yang, Mei-Shan Wang, Xiao-Guang Ma, Wen-Wang Liu and Li-Zhi Wang. 'Construction of analytic functions for the potential energy curves, dipole moments, and transition dipole moments of RbBe and CsBe molecules'. In: *Journal of Quantitative Spectroscopy and Radiative Transfer* 165 (November 2015), pp. 56–67. DOI: 10.1016/j.jqsrt.2015.06.026.

[Zei+18] Israa Zeid, Tanya Atallah, Sahar Kontar, Wael Chmaisani, Nayla El-Kork and Mahmoud Korek. 'Theoretical electronic structure of the molecules SrX (X = Li, Na, K) toward laser cooling study'. In: *Computational and Theoretical Chemistry* 1126 (February 2018), pp. 16–32. DOI: 10.1016/j.comptc.2018.01.013.

[ŻGD14] Piotr S. Żuchowski, R. Guérout and O. Dulieu. 'Ground- and excited-state properties of the polar and paramagnetic RbSr molecule: A comparative study'. In: *Physical Review A* 90.1 (9th July 2014), p. 012507. DOI: 10.1103/PhysRevA.90.012507.

[Zha08] Tianhao Zhang. 'Optical Two-Dimensional Fourier Transform Spectroscopy of Semiconductors'. PhD thesis. Colorado: University of Colorado, 2008.

[ZSD10] P. Zhang, H.R. Sadeghpour and A. Dalgarno. 'Structure and spectroscopy of ground and excited states of LiYb'. In: *The Journal of Chemical Physics* 133.4 (28th July 2010), p. 044306. DOI: 10.1063/1.3462245.

Danksagung

Dass auf der Titelseite nur mein Name steht, soll nicht zu der Vermutung verleiten, ich hätte die ganze vorgestellte Arbeit allein gemacht oder ohne die Unterstützung meiner Familie, Freunde und Kollegen machen können. Tatsächlich darf ich auf Jahre der gemeinsamen Forschung in einem angenehmen und konstruktiven Umfeld zurückblicken, das ich nicht als selbstverständlich betrachte.

Das fängt damit an, dass sowohl das Institut für Quantenoptik als auch das Laboratorium für Nano- und Quantenengineering sehr zuvorkommende und fähige technische und administrative Mitarbeiter haben, die jederzeit ansprechbar sind und sich intensiv bemühen, für jedes Problem eine Lösung zu finden.

Auch zwischen den wissenschaftlichen Arbeitsgruppen besteht ein reger Erfahrungs- und Meinungsaustausch, nicht nur zu relevanten und/oder interessanten technischen oder physikalischen Themen, sondern auch zum Dasein an der Uni, zu Kultur- und Freizeitaktivitäten, Rezepten und was das Leben sonst zu bieten hat.

In diesem Sinne möchte ich meinen Dank dafür ausdrücken, dass ich in einem so angenehmen Klima arbeiten konnte.

Ich möchte mich besonders bei meiner Arbeitsgruppe bedanken, von der ich über die Jahre so viel Unterstützung und Entgegenkommen erfahren habe. Sei es bei langen Messungen oder Reparaturen im Labor, sorgsamen Auswertungen im Büro oder dem Erarbeiten physikalischer Zusammenhänge, ich konnte mich immer an jemanden wenden, um über Schwierigkeiten zu diskutieren und andere Perspektiven oder Lösungsvorschläge zu hören.